

TiO₂ Nanotube Arrays with Engineered Geometries: Growth, Characterization
and Study of Selected Interfaces

by

Samira Farsinezhad

A thesis submitted in partial fulfillment of the requirements for the degree of

Doctor of Philosophy
[In
Microsystems and Nanodevices]

Department of Electrical and Computer Engineering Faculty of Engineering
University of Alberta

© Samira Farsinezhad, 2016

Abstract

Titanium dioxide (TiO_2) is a wide band gap, robust, n-type semiconductor whose transformation into vertically-oriented nanotube arrays makes them suitable electron percolation pathways for vectorial charge transfer together with high surface area. Growth of self-organized TiO_2 nanotube arrays as a membrane or on non-native substrates is critical for exploiting the full potential of this nanostructure in a variety of applications.

Although regular TNAs on native substrates constitute one of the most potent semiconductors for a variety of applications, to date, less research has been conducted on engineering the geometry of such structures for photon management. In this dissertation, a fundamental investigation into TNA-based photon management by periodically modulated titanium dioxide nanotube arrays (PMTiNTs) and double layer TNAs on native substrates was carried out. The present work shows that bilayer film stacks consisting of nanotubes with small (~60 nm) and large (~200 nm) diameters, respectively improve the optical absorption.

In the second part of this thesis, wherein the geometry of these unique nanostructures is engineered, galvanostatic pulse-generated modulation was used. The highly ordered PMTiNTs have been reported, which constitute bottom-up fabricated one-dimensional photonic crystals. As a last phase of the synthesis process, highly sophisticated vacuum deposition based techniques were used to investigate the influence of a variety of deposition rates and pressures at room temperature on anodic nanotube growth formation on non-native substrates.

In the third phase of the work, X-ray and ultraviolet photoelectron spectroscopic studies were used to investigate the interfacial band alignment for photocatalytic charge separation in TiO_2 nanotube arrays coated with CuPt nanoparticles. In the last phase, low energy surfaces repellent to a wide spectrum of liquids by functionalizing TiO_2 nanotubes arrays using monolayers of two different fluorinated hydrocarbon molecules were studied.

Preface

This dissertation is submitted for the degree of Doctor of Philosophy at the University of Alberta. This Ph.D. thesis contains the result of research undertaken at the department of Electrical and Computer Engineering, University of Alberta, between September 2010 and September 2015, under the supervision of Professor Karthik Shankar. Undoubtedly, I would have never gotten to the point to finishing up my dissertation without the help and support of others. These five years were an effortful trip with ups-and-downs. Mercifully, I haven't been alone all these years, and accompanied by an extended team of experts who were willing to help and motivate me. For this I would like to thank them for allowing me to realize my potential. This dissertation is ultimately based on experiments, some of which were the subject of collaborations. Most of the text of the dissertation is taken directly from previously published articles.

Some portions of the introductory text Chapter 1, are from, [*Transparent Anodic TiO₂ Nanotube Arrays on Plastic Substrates for Disposable Biosensors and Flexible Electronics*”, Journal of Nanoscience and Nanotechnology 13 (4), 2885-2891], [*The wetting behavior of TiO₂ nanotube arrays with perfluorinated surface functionalization*”, Conf paper, IMECE2014] and [*Toward single-step anodic fabrication of monodisperse TiO₂ nanotube arrays on non-native substrates*” physica status solidi (a) 211 (5), 1113-1121], and I was the first author in all of above papers.

Results of the research presented in Chapter 2 were presented as a poster and as an oral presentation at the Spring Meeting of the Materials Research Society, San Francisco, April 2013 and at Photonics North, Montreal, June 2012 respectively. Other portions of this study have been published as [Mohammadpour A, Farsinezhad S, Hsieh LH and Shankar K, “*Multipodal and Multilayer TiO₂ Nanotube Arrays: Hierarchical Structures for Energy Harvesting and Sensing*”, Proceedings of the Materials Research Society, vol. 1552: Nanostructured Metal Oxides for Advanced Applications, 2013]. In spite of the above reports, most of the data in this chapter has not been reported in publications yet and we are preparing three manuscripts on topics such as membrane PMTiNTs, double layer nanotubes, and different membrane preparation methods and

their effect on the crystal structure and optoelectronic properties. Different aspects of the study of titania nanotube membranes appear in [Zarifi M, Mohammadpour A, Farsinezhad S, Wiltshire BD, Nosrati M, Askar S, Daneshmand M, Shankar K, “*TRMC Using Planar Microwave Resonators: Application to the Study of Long-lived Charge Pairs in Photoexcited Titania Nanotube Arrays*”, The Journal of Physical Chemistry (2015)] and [Zarifi M, Farsinezhad S, Daneshmand M, Shankar K, Selective microwave sensors exploiting the interaction of analytes with trap states in TiO₂ nanotube arrays, Nanoscale (submitted)].

A version of Chapter 3 has been published as [Samira Farsinezhad, Arash Mohammadpour, Ashley N Dalrymple, Jared Geisinger, Piyush Kar, Michael J Brett, Karthik Shankar “*Transparent Anodic TiO₂ Nanotube Arrays on Plastic Substrates for Disposable Biosensors and Flexible Electronics*”, Journal of Nanoscience and Nanotechnology 13 (4), 2885-2891] and [S Farsinezhad, AN Dalrymple, K Shankar “*Toward single-step anodic fabrication of monodisperse TiO₂ nanotube arrays on non-native substrates*” physica status solidi (a) 211 (5), 1113-1121]. Some of the text and results presented in Chapter 3 are a version of manuscript [Samira Farsinezhad, Mourad Benlamri, Ashley N. Dalrymple and Karthik Shankar, “*The structure and morphology of TiO₂ nanotube arrays grown from atomically peened and non-atomically peened Ti films*”] that is currently in the final stages of preparation for submission as a journal manuscript. The first idea of using lower chamber pressures came from Prof. Brett M. J. and Prof. Shankar K. I ran the experiments and also collected most of the data that is presented in the aforementioned papers. AFM data was obtained by Benlamri M. and Dalrymple A. assisted in sample preparation. More than half of this chapter is adapted with permission from © 2014 WILEY-VCH Verlag GmbH & Co. KGaA, Weinheim.

Chapter 4 is a version of manuscript [Samira Farsinezhad, Himani Sharma and Karthik Shankar “*Interfacial band alignment for photocatalytic charge separation in TiO₂ nanotube arrays coated with CuPt nanoparticles* “]. Most of the experiments were performed by me but CO₂ reduction data and Raman spectroscopic data were obtained in the Shankar Research Lab by Sharma H. She was a postdoctoral fellow supervised by Prof. Shankar and I was trained by her for CO₂ reduction and data analysis in this paper. This chapter is adapted with permission from © 2015 The Royal Society of Chemistry.

The results of the research presented in Chapter 5 have been published as [Farsinezhad S, Prashant W, Wiltshire BD, Amiri S, Sushanta KM, Shankar K, “*The wetting behavior of TiO₂ nanotube arrays with perfluorinated surface functionalization*”, Conf paper, IMECE2014] and [Samira Farsinezhad, Prashant R Waghmare, Benjamin D Wiltshire, Himani Sharma, Saeid Amiri, Sushanta K Mitra, Karthik Shankar, “*Amphiphobic surfaces from functionalized TiO₂ nanotube arrays*”, RSC Advances 4 (63), 33587-33598]. The entire contact angle measurements in this chapter were performed by Waghmare PR. Chapter 5 is adapted with permission from © 2014 by ASME and © 2014 by The Royal Society of Chemistry.

Dedication

I would like to dedicate this thesis to my beloved parents Maryam and Javad. The completion of this works would not have been possible without their support.

Acknowledgments

My doctoral student life would never have reached its culmination without the people who have generously helped me over the past five years. I would like to thank all the people who contributed in some way to the work described in this dissertation. I feel privileged to express my thanks to them for their support, assistance and encouragement.

Foremost, I take the opportunity to express my heartfelt adoration and deep gratitude to my supervisor, Professor **Karthik Shankar** for his unreserved guidance, patience, constructive suggestions and thought provoking discussions in nurturing this research work. I am extremely indebted to him for his critical evaluation of my work and most importantly for his encouragement through the thick and thin phases of my work. His guidance helped me in performing my research and writing this thesis. His continuous support and motivation has brought this work to its fruition. I really appreciate his encouragement for working in diverse exciting projects that I believe will definitely help me to sustain my future career. I take this opportunity to express my deep gratitude to Professor **Michael Brett** for helpful discussions. I am enormously thankful to him for sharing his expertise and for valuable guidance. I would like to extend my sincerest appreciation to Professor **Thomas Thundat**, Professor **Mojgan Daneshmand**, Professor **Sushanta Mitra**, Professor **John Greer**, Professor **Robert Fedosejevs**, Professor **Natalia Semagina**, Professor **Siddhartha Das** and Professor **Prashant R. Waghmare** for their help and support during collaborative research endeavours. I place on record, my sincere thanks to Professor **Sandipan Pramanik**, a course instructor of mine and a supervising committee member. My sincere thanks also go to the rest of my committee, Professor **Xihua Wang** and Professor **José E. Herrera** for their insightful comments.

My sincere thanks and appreciation go to the **UofA NanoFab**, the National Research Council of Canada (**NRC**), the Alberta Centre for Surface Engineering and Science (**ACSES**) and **UofA Department of Earth & Atmosphere Science** for providing me with all the necessary facilities for the research. I thank the staff of the **UofA NanoFab** (Keith Franklin, Les Schowalter, Dr. Peng Li, Dr. Shiraz Merali, Scott Munro and several others), the staff of the **UofA Department of Earth & Atmosphere Science** (scanning electron microscopy and X-ray diffraction labs), the staff of **NRC-NINT** (Kai Cui, Paul Concepcion, Steve Launspach, Mike Xia,...) and the staff of **ACSES** (Dimitre Karpuzov , Shihong Xu,...) for training me on various equipment and for their technical support.

Every result described in this thesis was accomplished with the support and help of my labmates. I greatly benefited from their keen scientific insight. I was fortunate to have a chance to work with Dr. **Archana Pandey**, Dr. **Xiaojiang Zhang**, Dr. **Himani Sharma**, Dr. **Piyush Kar**, Dr. **Mohammad Hossein Zarifi** and Dr **Shyama Prasad Banerjee** who worked closely with me. I don't know how to start thanking my colleagues, I am sure to forget half of you. Thanks to my labmates and friends: **Mourad Benlamri**, **Benjamin Wiltshire**, **Yun Zhang**, **Ling-Hsuan Hsieh**, **Jing Shen**, **Shyama Prasad Banerjee**, **Ahmad Adl**, **Joel Boulet**, **Ramireddy Boppella**, **Jared Geisinger**, **Ashley Dalrymple**, **Clara Chin**, **Jordan Goldthorp**, **Nidhi Shah**, **Najia Mahdi**, **Geoffrey Casey**, **Joshua Gabriel**, **Payal Baheti**, **Bharath Bangalore**, **Arash Mohammadpour**, **Logan Snider**, **Advaita Bhatnagar**, **Abdelrahman Askar**, **Arezoo Hosseini**, **Ryan Kisslinger**, **Yutang Wang**for the good times and for all their assistance.

Some of the projects that presented in this dissertation were funded through grants from **NRC**. I thank Alberta Innovates Technology Futures (**AITF**) for scholarship support. Some device fabrication and testing used research infrastructure made possible by a Leaders Opportunity Fund grant to my supervisor, Professor Karthik Shankar, from the Canada Foundation for Innovation (**CFI**) and the Alberta Small Equipment Grants Program (**SEGP**). Most of the fabrication and characterization tests in this dissertation were made possible through the generous financial support of **CMC Microsystems**.

Finally, I would like to acknowledge my family and friends for their support during my PhD program. I would like to thank my Mom, Dad, **Maryam**, **Javad** and my siblings **Sara**, **Sepideh** and **Mohammad** for their love and support. I thank **Alexandra Savchenko**, **Himani Sharma**, **Matthew Reynolds**, **Mahshid Sharifi**, **Siamak Abdolahi**, **Shoma Sinha** for their unyielding support and friendships. Dozens of people emotionally and academically helped me through the rough road to finish this thesis. My sense of gratitude to all, who directly or indirectly, have let their hand in this endeavour.

Above all, I express my indebtedness to the “Almighty” for all His blessings and kindness.

Samira

Table of Contents

List of Tables	ii
List of Figures	iv
List of Symbols	xvii
List of Abbreviations	xxi
Chapter 1-Introduction	1
1.1 Introduction.....	1
1.2 Characterizaion of TNAs	2
1.3 Growth of TNAs on Native Substrates.....	3
1.3.1 Overview	3
1.3.2 Electrochemical Anodization	4
1.3.3 Photon Management in Titanium Dioxide Nanotube Arrays.....	6
1.3.3.1 Double layer TNAs.....	6
1.3.3.2 Pulse Modulated Nanotubular Structures	7
1.4 Growth of TNAs on Non-Native Substrates.....	8
1.5 Metal Nanoparticles Promoter TNTAs for Photocatalytic application	11
1.6 Wetting Phenomena using TNAs	12
1.7 Future work and Conclusions	15
Chapter 2- Growth of TNAs on Native Substrates	16
2.1 Introduction.....	16

2.2	Substrate Preparation for TNAs Growth	16
2.2.1	Self-Template Method by Using Two Step Pre-anodization	17
2.2.2	Electropolishing and Chemical Polishing	17
2.3	TNAs on Titanium Sheet	19
2.3.1	Single Layer TNAs by Electrochemical Anodization.....	19
2.3.2	Double layer TNAs	26
2.4	Periodically Modulated TiO ₂ Nanotubes (PMTiNTs).....	31
2.4.1	Experimental Details	35
2.4.1.1	Synthesis of PMTiNTs	35
Chapter 3-TNAs on Non-Native Substrates		41
3.1	Overview.....	41
3.2	Surface Morphology of Titanium Thin Films	42
3.3	Surface Morphology of TNAs on Non-native Substrates.....	50
3.3.1	TNAs on Flexible Substrate	51
3.3.2	TNAs on FTO, Glass and Silicon.....	60
Chapter 4-Metal Nanoparticle Promoter-Decorated TNTAs for Photocatalytic application.....		74
4.1	Overview.....	74
4.2	Experimental Details	76
4.2.1	Synthesis of transparent TiO ₂ nanotube arrays	76
4.2.2	Formation of CuPt-TTNTA hybrid structures	77
4.3	Photodeposition Mechanism.....	77
4.4	Morphology, structure and optical absorption of CuPt coated TTNTAs	80
4.5	Band alignment in CuPt coated TTNTAs.....	93
4.6	Examination of the effect of illumination in pure methanol on the TTNTAs surface.....	95
4.7	Comparison of photodeposited CuPt NPs to sputtered CuPt NPs.....	98

4.8	Work functions, Schottky barriers and surface dipoles at TTNTA surfaces	101
4.9	Schottky Barrier Electron Trapping?	104
Chapter 5-Wetting Phenomena using TNAs		106
5.1	Introduction	106
5.2	Theory behind wettability of TNAs	110
5.3	Preparation of TNAs and planar TiO ₂ thin films	112
5.3.1	Surface functionalization	114
5.3.2	Characterization	115
5.3.3	Results and Discussion	116
5.3.3.1	Verification of functionalization protocols	116
5.3.3.2	Effect of surface morphology and surface chemistry on wetting behavior	120
5.3.3.3	Explanation of observed wetting behavior	124
5.3.3.4	Analysis of wetting properties and theoretical predictions of contact angle	126
5.3.3.5	Contact Angle Sustainability	142
Chapter 6-Conclusion and Future Work		145
6.1	TNAs on non-native substrate	145
6.1.1	Future work in the area of TNAs on non-native substrates	146
6.2	Electronic Properties of the interfaces of TNAs with promoter noble metallic nanoparticles	147
6.2.1	Future work	148
6.3	Wetting properties of the interfaces of TNAs with liquids	149
6.3.1	Future work 1	150
6.3.2	Future work 2	152

References	154
Appendix A- Absorption Coefficient	172
Appendix B - (List of Publication)	176
B-1 Refereed Publications	176
B-2 Conference Papers	178
B-3 Presentations and Posters.....	179

List of Tables

Table 1-1 Textural properties of TiO ₂ nanotubes in comparison with conventional TiO ₂ nanoparticles .	3
Table 2-1. Comparing the experimental and theory for Bragg reflection wavelength and FWHM. $\lambda_{B(EX)}$ and $\lambda_{B(TH)}$ represent, Bragg reflection data from experimental data and theoretically calculated data respectively. FWHM _(EX) and FWHM _(TH) represent, full width half maximum of stop-band from experimental data and theoretically calculated data respectively.	39
Table 3-1. Statistics related to the morphology of the nanotubes on Si and FTO substrates. This data was collected from SEM (Figure 3-13).	65
Table 4-1. Binding energy of common Pt-O [171] reproduced with permission from M. Peuckert et al., Surface Science, 1984. 145 (1): p. 239-259 © 1984 Published by Elsevier B.V.	90
Table 4-2. Atom fractions and concentration ratio of CuPt deposited by photodeposition method.	93
Table 5-1. Chemical properties of organic solvents used in contact angle tests	111
Table 5-2. Identification and assignment of XPS peaks obtained from from TiO ₂ thin films and nanotubes coated by PFNA and PDPFA monolayers	118

Table 5-3. Contact angle (in degrees) for six different liquids on nine different substrates with the standard deviation determined from the average static contact angle. Also listed are the dispersive, polar and hydrogen-bonding components of the surface energy for each surface studied, calculating by the extended Fowkes method using the average contact angles for diiodomethane, ethylene glycol and water; $\gamma_s = \gamma_s^d + \gamma_s^p + \gamma_s^h$ 124

Table 5-4. The experimentally measured contact angle (θ) and deviation ($\Delta\theta$) from theoretically predicted value. The value in the parenthesis represents the percentage difference between the theoretically predicted and experimentally measured contact angle values..... 129

Table 5-5. Geometric parameters of nanotube-configurations studied here. The geometrical parameters of individual nanotube are obtained from SEM images. 134

Table 5-6. The area fraction parameter derived from experiments using Eq (5-5). And Eq (5-6). The corresponding theoretical values, are provided in parenthesis beside each different nanotube arrays..... 135

Table 5-7. Theoretically predicted contact angles (θ°) and the difference between the theory and the experimentally observed contact angle ($\Delta\theta^\circ$). Here it is assumed that the nanotubes behave like a nanorod and there is finite gap between them. 137

Table 5-8. Experimentally contact angles (θ°) hexane on three non-chemically treated surface and six fluorinated surface. In all measurement 2 μ l droplet was injected to the surface..... 138

List of Figures

Figure 1-1. Schematic view of template method, for growing TNAs.....	4
Figure 1-2. Morphology of nanotubes grown in a) aqueous electrolyte [23] adopted with permission from Gong D. et al., Journal of Materials Research, 2001. 16(12). © 2001, Research Society b) formamide electrolyte [26] adapted with permission from Yoriya, S. et al., Journal of Physical Chemistry C 2007. 111(37):p. 13770-13776 © 2007, American Chemical Society c) dimethylsulfoxide electrolyte [24] adapted with permission from Shankar K. et al, Journal of Physical Chemistry C, 2007. 111(1): p. 21-26. © 2007, American Chemical Society d) ethylene glycol (EG) electrolyte.....	5
Figure 2-1. (a, b) Titanium foil at two different magnifications. Footprints of nanotubes after (c) first step pre-anodization for 2 hours and (d) second anodization for 36 hours.	18
Figure 2-2. a) Schematic illustration of electro-polishing process. b) Electrical potential distribution on titanium surface, during electro-polishing process.	19
Figure 2-3. Optical images of a) Ti sheet before polishing b) electropolished sample c) chemically polished samples, at 50 X.	19

Figure 2-4. Illustration of anodization set up in our laboratory.	21
Figure 2-5. Current vs time behavior during anodization of Ti foil in fluoride-free electrolyte (current density respond at 10V) [95] adapted with permission from Allam, N.K., 2008. 18(20): p.2341-2348 © 2008, Royal Society of Chemistry	22
Figure 2-6. a) Current density of aqueous and organic. b) Cross-section of TNAs on aqueous base electrolyte. c) Cross-section of TNAs on organic base electrolyte [98] adapted with permission from Macak, J.M. et al. , Angewandte Chemie International Edition, 2005. 44(45): p.7463-7465 © 2005, John Wiley and Sons.....	25
Figure 2-7. (a, b) Volume ratio calculations for nanotubes and nanoparticles. FDTD results for (c) constant inner-diameters and various outer-diameters, (d) for constant volume ratio and (e) for various volume ratios.....	28
Figure 2-8. a) SEM of double layer TNAs b) experimentally observed light absorption in single layer and double layer nanotubes c) simulation result for extinction of light in single layer and double layer nanotubes.....	29
Figure 2-9. a, b) cross sectional SEM images of double layer TNAs c) top view SEM image of first layer d) diffuse reflection data from single (only small diameter nanotubes) and double layer structure.....	30
Figure 2-10. a) Schematic of PMTiNTs structure. b) Schematic of refractive index profile in PMTiNTs structure.....	32
Figure 2-11. The unit cell consists of three hollow nanotubes with radius R_0 , wall-thickness t and inter-tube spacing s	33

Figure 2-12. Effective refractive index (a) versus wavelength (b) versus porosity.34

Figure 2-13. a, b) cross sectional SEM images of PMTiNTs anodized at 120 mA, with 20 seconds cycles (2% DI water, 0.2 wt% NH₄F) with 3±0.1 cm inter-electrode separation. c) HRTEM images of notches c) diffuse reflection data (blue line was the most dominant peak- Specimen#1). ...36

Figure 2-14. Schematic of wall thickness along the length of the TNAs by controlling etching rate. SEM images in (1) corresponded to specimen#1 and (2) corresponded to the specimen#2 with more uniform electric field..37

Figure 2-15. 1 a) cross sectional SEM images of PMTiNT anodized at 120 mA, with 20 seconds cycles (1±0.1 Cm setup), b) top view SEM images with thin wall.38

Figure 2-16. a) diffuse reflection data from specimen#1 b) diffuse reflection data from specimen#2 c) diffuse reflection data (blue line was the most dominant peak- Specimen#1) e) diffuse reflection data adapted with permission from Jua Lin et al., Small, 2011. 7(13): p. 1784-1789 © 2011 WILEY-VCH Verlag GmbH & Co. KGaA, Weinheim40

Figure 3-1. Surface diffusion length versus deposition rate at 298, 320 and 498 K.44

Figure 3-2. Morphology of 500 nm-thick titanium films deposited at room temperature on FTO-coated glass using DC sputtering with a deposition rate of 0.093 nm s⁻¹ at (a) 20 mTorr, top view (b) 20 mTorr, cross section (c) 20 mTorr, top view after anodization (d) 1 mTorr, top view (e) 1 mTorr, (f) 1 mTorr, cross section after anodization. Morphology of 500nm of titanium deposited using Electron beam evaporation with a deposition rate of 0.17 nm s⁻¹ on (e) FTO (f) glass (g) after anodization..45

- Figure 3-3.** Side view and top view of 500nm Ti film on silicon (a) at 7 mTorr and (b) at 1mTorr. Side view of 2 μm (0.1175 nm s^{-1}) titanium deposited at 1 mTorr (c) on FTO (d) Kapton (e) Silicon (e) top view of titanium on Silicon, Kapton and FTO substrates.46
- Figure 3-4.** AFM data for 500 nm (0.1175 nm s^{-1}) titanium deposited on at 1 mTorr (a) on FTO with 10.49 nm rms(b) Glass with 5.1 nm rms. 0.1175 nm s^{-1} titanium deposited on silicon at (c) 1 mTorr (d) 7 mTorr.47
- Figure 3-5.** SEM of 0.23 nm s^{-1} titanium deposited on silicon (a) 7mTorr (c) 1mTorr. AFM 0.23 nm s^{-1} titanium deposited on silicon at (b)7 mTorr, with the roughness of around 17.5 nm (d) 1 mTorr, with the roughness of around 5.5 nm48
- Figure 3-6.** AFM of 500 nm titanium with a deposition rate of (c) 0.093 nm s^{-1} and (d) 0.0465 nm s^{-1} ,on FTO Morphology of 500 nm titanium with a deposition rate of (c) 0.093 nm s^{-1} and (d) 0.0465 nm s^{-1} on FTO.....50
- Figure 3-7.** (a) Top-view and (b) cross-section of $5.1 \mu\text{m}$ TNAs on $50 \mu\text{m}$ thick Kapton[®] substrate, and (c) flexible and transparent TNAs on Kapton[®] substrate.52
- Figure 3-8.** (a), (b) Top-view and cross-section respectively of a 500 nm thick film of Ti sputtered on to Kapton[®] at room temperature and 7 mtorr, and (c), (d) Top-view and (d) cross-section respectively of a 500 nm thick film of Ti sputtered on to Kapton[®] at room temperature and 1 mtorr.55
- Figure 3-9.** A 500 nm Ti film on Kapton was formed by sputtering at 1 mtorr and subjected to electrochemical anodization in a fluoride ion bearing water-ethylene glycol electrolyte to form TNAs. (a) anodization current vs. time (b) cross-sectional FESEM image showing a film thickness (i.e.

tube-length) of 870 nm (c) optical transmittance of blank Kapton substrates (blue curve) and TNAs on Kapton (black curve) with the inset showing the Fabry-Perot interference fringes of the blank Kapton substrate in more detail and (d) effective refractive index of the nanotube arrays on Kapton, calculated by applying the envelope to the transmission spectra as shown in the inset.....56

Figure 3-10. FESEM image of (a) 500 nm titanium with a deposition rate of 0.1175 nm s^{-1} on Kapton substrate (b) the investigated TNAs layer on kapton for 4% water at 40 V and $3\pm 0.1 \text{ cm}$ inter-electrode separation setup (c) 116 nm ITO and 500 nm titanium with a deposition rate of 0.1175 nm s^{-1} on Kapton substrate (d) the investigated TNAs layer on top of the ITO thin film for 4% water at 40 V and $3\pm 0.1 \text{ cm}$ inter-electrode separation setup.....59

Figure 3-11. (a, b) FESEM top view and TEM cross-section of monodisperse TNAs on silicon substrate; (c, d) FESEM top view and TEM cross-section of polydispersed TNAs on FTO:glass substrate; The anodization electrolyte contained 9 vol% H_2O and 0.3 wt% NH_4F (e, f) FESEM top view of Ti thin films DC sputtered onto Si and FTO: glass substrates respectively, at 1 mtorr chamber pressure.63

Figure 3-12. 2D-FFT images showing the effect of anodization electrolyte and substrate on the arrangement order of TNAs.....64

Figure 3-13. Images used to obtain statistics related to the nanotube morphologies a) TNAs on Si b) Magnified view of a portion of image in (a) showing how circularity and nanotube diameter were measured c) TNAs on FTO:glass and d) Magnified view of a portion of image in (c).....66

Figure 3-14. Log-log plot of the anodization current transients during the formation of TNAs on glass (black), FTO: glass (red) and two silicon substrates (cyan and olive green) magnifying the temporal region near local extreme in the current. The rise of the anodization current between the local minimum and the subsequent local maximum was fit to a straight line with a slope of 1.5 (fit not shown). Current decay following the maximum is fit to straight lines (blue) with slopes as indicated. The inset plots the currents measured over the entire anodization duration on a linear scale.....67

Figure 3-15. Effect of temperature and chamber pressure on the morphology of sputtered Ti thin films (1) and resulting anodic TNAs (2) on glass substrates (a) 1 mtorr, room temperature, (b) 1 mtorr, 250°C and (c) 7 mtorr, 250°. The scale bar at the bottom of each image corresponds to a length of 100 nm.68

Figure 3-16. Schematic illustration of the pore nucleation process on (a) smooth and (b) rough substrates highlighting the importance of film roughness on the shape and size dispersity of anodically formed TNAs.....69

Figure 3-17. FESEM images of TNAs on Si substrates formed by anodization of identical Ti thin films in different electrolytes; (a) TNAs formed in aqueous electrolyte, exhibiting a wide dispersion in shape and size, (b) TNAs formed in EG-based electrolyte containing 1% H₂O and 0.1 wt% NH₄F, (c) TNAs formed in EG-based electrolyte containing 2% H₂O and 0.3 wt% NH₄F and (d) TNAs formed in EG-based electrolyte containing 4% H₂O and 0.3 wt% NH₄F.....71

Figure 3-18. Effect of substrate on the crystallographic texture of sputtered Ti films under identical conditions. Powder mode X-ray diffractograms of Ti thin films deposited on to glass and silicon substrates using DC

magnetron sputtering at two different chamber pressures (1 mtorr and 20 mtorr).73

Figure 4-1. Band-diagram of the Schottky junction at the *n*-TiO₂/CuPt interface. The direction of the built-in field in the depletion region is such as to drive photogenerated electrons toward the TiO₂ bulk and holes toward the metal-semiconductor interface.....75

Figure 4-2. Schematic illustration of oxidation process (A: methanol) and reduction process (M⁺: Pt²⁺ /Cu²⁺).....78

Figure 4-3. (a) Effect of CuPt photodeposition on the UV-Vis spectra of annealed, crystalline TTNTAs and un-annealed, amorphous TTNTAs (b) UV-vis spectra of nanoporous anodic aluminum oxide (AAO) on glass substrates before and after being subjected to CuPt photodeposition.80

Figure 4-4. FESEM images display the morphological features of (a) TTNTAs, an inset image in the figure shows the cross-section of the arrays with the height of 1 micron and (b) CuPt-coated TTNTA hybrids. The scale bar refers to 500 nm for both the images.81

Figure 4-5. Counter-clockwise from top-left (a) Comparison of the room temperature Raman spectra of TTNTAs and CuPt-TTNTA hybrids (b) microRaman spectra of CuPt-TTNTA hybrids heated to 100°C with different light exposure times, here 2, 6 and 15 corresponds to hours of illumination; inset figure shows the broadening in the E_g peak of TiO₂ with time. (c) UV-Vis spectra of TTNTAs and CuPt-TTNTA hybrids...82

Figure 4-6. Low and high resolution transmission electron microscope images showing (a) Cu/Pt loaded TTNTAs, (b) HAADF image in STEM mode presenting the TTNTA:CuPt-NP hybrids, (c) close knit attachment of

CuPt nanoparticles along the walls of TTNTAs and (d) EDAX spectra confirming the presence of Pt	84
Figure 4-7. High-resolution autocorrelated images of (a) TiO ₂ lattice planes (b) Pt NPs (c) CuPt NPs (d) HRTEM images displaying the crystalline planes for (I) TTNTAs and (II) CuPt-TTNTA hybrids.....	85
Figure 4-8. X-ray photoelectron spectra of TiO ₂ nanotube arrays for C 1s.....	86
Figure 4-9 (a) TOF-SIMS data from TTNTA:CuPt-NP hybrids (b) ratio of Pt to Cu along the length (c) atom fraction of Cu and Pt along the length	87
Figure 4-10. TTNTA:CuPt-NP hybrids (a) XPS survey and chemical composition of Pt, Cu, O, Ti (b) Ti2p (c) O1s and (d) Pt 4f.....	88
Figure 4-11. Peak decomposed O1s core level spectra for TTNTAs (a) without an oxygen plasma cleaning treatment and (b) with an oxygen plasma cleaning treatment.....	88
Figure 4-12. Peak decomposed O1s core level spectra for TTNTAs photodeposited with CuPt compared to TTNTAs subjected to AM1.5G illumination from a solar simulator in pure methanol.	89
Figure 4-13. High resolution core level spectra showing the Pt 4f _{7/2} and Pt 4f _{5/2} peaks for (a) coated with CuPt nanoparticles by sputtering and (b) TTNTA samples coated with CuPt nanoparticles by photodeposition. ...	91
Figure 4-14. UPS data from TTNTA:CuPt-NP hybrids	94
Figure 4-15. (a) UPS spectra of Pt-TTNTA hybrids with the inset showing the secondary electron cutoff region and (b) Zoomed in view of the low binding energy edge in the UPS spectrum shown in (a). The valence band	

maximum was estimated using the intercept on the abscissa obtained by extrapolating the low binding energy edge to the baseline.....95

Figure 4-16. Ti 2p spectra for TTNTAs subjected to AM1.5G illumination from a solar simulator in pure methanol.96

Figure 4-17. Counter-clockwise from top (a) whole UPS spectra (b) magnified view of secondary electron cut-off region and (c) valence band edges of transparent TiO₂ nanotube samples following photodeposition of CuPt NPs (red curve) and subsequent to illumination under identical conditions in methanol but without the presence of metal precursors (purple curve).....97

Figure 4-18. Counter-clockwise from top-right (a, b and c) Survey and magnified UPS valence band spectra of transparent TiO₂ nanotubes (pink-colored curve), sputtered CuPt nanoparticles formed on transparent TiO₂ nanotubes subsequent to an oxygen plasma clean (green-colored curves) and sputtered CuPt nanoparticles formed on transparent TiO₂ nanotubes without an oxygen plasma clean (blue-colored curves). In (d), the high resolution XPS core-level spectra of the Ti 2p peak is shown for sputtered CuPt nanoparticles formed on TiO₂ nanotube arrays.....99

Figure 4-19. Magnified views of the low binding energy regions of the XPS spectra of TTNTAs subjected to bimetallic noble metal nanoparticle coating or ultraviolet treatment in methanol..... 100

Figure 4-20. Unlike a continuous film, a discontinuous layer of metal nanoparticles decorating a surface does not produce a planar junction. For a hemispherical Schottky point-contact with a radius of a_0 , the radius (r_0) of the hemispherical depletion region formed in the semiconductor is given by $r_0 = \left(\frac{3a_0 \epsilon_r \epsilon_0 \phi_{bi}}{eN_d} \right)^{\frac{1}{3}}$ where e is the electron charge, N_d is the carrier

density in the n -type semiconductor, ϵ_r is the relative permittivity of the semiconductor, ϵ_0 is the permittivity of free-space and ϕ_{bi} is the built-in potential of the Schottky junction. 102

Figure 4-21. Depletion region widths for a point-contact Schottky junction between n -type anatase TiO_2 and CuPt NPs. The inset is a higher magnification view of the depletion widths obtained for the commonly observed carrier concentrations in TiO_2 nanotube arrays anodically formed in fluoride-ion containing ethylene glycol electrolytes for a band bending of 0.7 V; the depletion widths for 5 nm, 2 nm and 1 nm nanoparticles are represented by red, black and green curves respectively in the inset. 103

Figure 5-1. Schematic image for contact angles versus wettability 110

Figure 5-2. FESEM images of the two TiO_2 nanotube array geometries used in this study - (a) TNAs of 100 nm average inner diameter formed by anodization at 65 V and (b) TNAs of 30 nm average inner diameter formed by anodization at 20 V. 113

Figure 5-3. The process flow for the preparation of the TNAs coated with perfluoroalkyl monolayers. A Ti foil was used to synthesize the nanotubes by electrochemical anodization. The synthesized TNAs were of two different types – large and small which are numbered as 1($TNAs_{Small}$) and 2($TNAs_{Large}$), respectively. The encircled images beside the $TNAs_{Small}$ show the SEM images of the top and bottom of the nanotubes. The encircled images at the bottom of $TNAs_{Large}$ and $TNAs_{Small}$ (image 3 and 4) are the top and side views of the large and small nanotubes. Further, PFNA and PFDA were used obtain the two different kinds monolayers by self-assembly on planar TiO_2 thin films TTF –image 5) and $TNAs$ (image 6) substrates. 115

Figure 5-4. High resolution XPS spectra of TiO₂ thin films and *TNA_{Large}* coated with PFNA and PFDPA. 117

Figure 5-5. FTIR spectra of bare TiO₂ nanotube arrays (red), and subsequent to coating (blue) with a monolayer of Perfluorononanoic acid (A) and Perfluorodecylphosphonic acid (B). 119

Figure 5-6. Equilibrium contact angles of different liquids on nine different substrates measured by the pendant drop technique are presented here. The bare TiO₂ thin film allows all liquids considered in this study, to spread easily; in nanotubular form (*TNA_{Large}* and *TNA_{Small}*), the substrates became more amphiphilic. The chemical treatment, namely functionalization by two different perfluorinated alkane chain-containing molecules (PFNA and PFDA) resulted in the bare flat TiO₂ thin films becoming hydrophobic surfaces (*TTF^{PFDPA}* and *TTF^{PFNA}*). A similar treatment was performed on two different nanotubes (*TNA_{Large}* and *TNA_{Small}*) to generate four types of functionalized nanotube array samples (*TNA_{Large}^{PFDPA}*, *TNA_{Large}^{PFNA}*, *TNA_{Small}^{PFDPA}* and *TNA_{Small}^{PFNA}*), which showed distinctly different liquid-repellent characteristics compared to the bare nanotubes. The static contact angles obtained with these functionalized nanotubes are some of the highest observed for any surface. 121

Figure 5-7. First scenario considered for the analysis: the unit cell consists of three hollow nanotubes with radius R_0 , wall-thickness t and inter-tube spacing s 127

Figure 5-8. (a) The unit cell considered for the theoretical analysis assumes that the nanotubes are closely packed in a triangular lattice (b) First scenario considered for the analysis: the unit cell consists of three hollow nanotubes with height h , radius R_0 , wall-thickness t and inter-tube spacing s . (c) Second scenario considered for the analysis: The

nanotubes are considered as solid nanorods of outer radius R_0 and there is a finite gap s in between them. 129

Figure 5-9. Possible drop configuration of liquids during the contact angle measurements. In the first case, the drop does not spread, whereas in the second and third cases the drop spreads over areas which are different from the area predicted by the contact area fraction parameter..... 132

Figure 5-10. Second scenario considered for the analysis: The nanotubes are considered as solid nanorods of outer radius R_0 and there is a finite gap s in between them. 136

Figure 5-11. Schematic of wetting configurations of liquid droplet on a substrate containing closed nanopores. Configuration 1 depicts zero imbibition into the pores (*fakir* state), configuration 2 shows imbibition into the pores, but accompanied by only a small increase in the liquid-vapor area fraction while the configuration 3 illustrates imbibition along with a substantial increase in the liquid-vapor contact area fraction. 139

Figure 5-12. Packing, orientation and exposed terminal groups for PFNA and PFDPA self-assembled monolayers on planar and nanotubular TiO_2 surfaces. 142

Figure 5-13. Static contact angles of water on large diameter nanotube arrays (a), small diameter nanotube arrays (b), and TiO_2 thin films (c) all treated with PFDPA. Images on left are pre-immersion treatment, on the right are post-immersion treatment in water. The contact angle is unchanged. 143

Figure 5-14. Static contact angles of water on large diameter nanotube arrays (a), small diameter nanotube arrays (b), and TiO_2 thin films (c) all treated with PFDPA. Images on left are pre-immersion treatment, on the right

are post-immersion treatment in ethylene glycol. The contact angle is unchanged. 144

Figure 6-1. (a, b) Process flow for making a dye-based pH-sensor with an amphiphobic surface 152

Figure A- 1. TiO₂ anatase '*n*' value versus wavelength..... 173

List of Symbols

θ_r^w	The contact angle of a liquid on a textured surface in Wenzel state
θ_{flat}^e	Equilibrium contact angle
f_{sl}^{rod}	Theoretical contact area fraction parameter
E_{VBM}^m	Position of the valence band subsequent to metal deposition
a_d	Average distance between adatoms
Al	Aluminium
Ar^+	Argon ion
Cu	Copper
$CuPt$	Bimetallic copper and platinum
D	Film thickness
d_{hkl}	Interplanar spacing
d_p	The nanotube inner diameter
E	Electric field
e	Fundamental electronic charge
E_g	Bandgap
E_h	Energy for self-diffusion
E_s	Activation energy for surface diffusion
E_{SE}	Secondary electron onset energy

F	Faraday constant
F	Fill-fraction
F^-	Fluoride ion
f_{ll}	The liquid-liquid contact fraction
f_{lv}	Area fraction of the liquid in contact with the vapor
f_{sl}	Solid area fraction
g	Gravitational acceleration
H^+	Hydrogen ion
i_+	Ionic current density
k	Boltzmann`s constant
k	Grating wavevector
K_{ads}	Adsorption rate
K_{des}	Desorption rate
k_i	incident wavevector
k_r	Reflected wavevector
l_c	Capillary length
MW	Molecular weight
N	Number of electrons involved in the electrochemical reduction process
$n(\lambda)$	Refractive index
N_a	Avogadro number
Nb	Niobium
N_c	Conduction band density of states
n_{eff}	Effective refractive index
P	Pressure
P_e	Probability of diffusion
Pt	Platinum

R	Surface roughness
R_c	Drop radius
r_d	Deposition rate
r_s	Stokes radius
S	Spreading coefficient
Si	Silicon
t	Time
T	Temperature
Ta	Tantalum
T_f	Temperature of the film
Ti	Titanium
$T_M(\tilde{\nu})$	Transmittance -upper envelope
$T_m(\tilde{\nu})$	Transmittance -lower envelope
X	Position coordinate in the direction of increasing oxide thickness
Z	Ionic charge
Zr	Zirconium
Γ	Interfacial energy of the oxide-electrolyte interface
Γ	Gibbs-Thomson coefficient
γ_i	Liquid surface tension
γ_L	Liquid surface energy
γ_{LA}	Surface tension of liquid
γ_S	Solid surface energy
γ_{SA}	Surface energy of the substrate
γ_S^d	Dispersive component of the surface energy
γ_S^h	Hydrogen bonding component of the solid surface energy
γ_{SL}	Interfacial tension
γ_S^p	Polar component of the surface energy

ΔG_D	Change in free energy associated with the chemical dissolution of the oxide
E	Effective permittivity
Θ	Surface coverage percentage
θ_{ll}	Contact angle of wetting between the liquid and itself
θ_{lv}	Contact angle of wetting between the liquid and vapour
θ_o	Equilibrium coverage
θ_r	Contact angle of a liquid drop on the heterogeneous substrate
A	Surface diffusion length
λ	Wavelength of incident light
λ^0	Ionic conductivity
λ^∞	Limiting molar conductivity
λ_B	Bragg wavelength
Λ_B	Spacing between periodic grating
πD_P	Circumference of a particle
ρ	Density of the oxide
ρ	liquid density
τ_h	Time that each adatom needs to diffuse
τ_m	Reciprocal of the Burial Rate
Φ_B	Schottky barrier height
ϕ_{bi}	The maximum band-bending
Ω	Lattice vibration
η	Solution viscosity

List of Abbreviations

AAO	Anodic Aluminum Oxide
ALD	Atomic Layer Deposition
BEM	Boundary Element Method
CVD	Chemical Vapour Deposition
DMSO	Dimethyl Sulfoxide
DSSCs	Dye Sensitized Solar Cells
EG	Ethylene Glycol
FAD	Field Assisted Dissolution
FAM	Field Assisted Migration
FAO	Field Assisted Oxidation
FTO	Fluorine Tin Oxide
FWHM	Full Width at Half Maximum
GEIS	Galvanostatic
H₂O	Deionized water
H₂O₂	Hydrogen Peroxide
HCl	Hydrogen Chloride
HF	Hydrogen Fluoride
ITO	Indium Tin Oxide
KF	Potassium Fluoride
LAHC	Laurylamine Hydrochloride
LHE	Light Harvesting Efficiency

L-TNAs	Large Diameter TiO ₂ Nanotubes
MoO₃	Molybdenum Trioxide
NaF	Sodium Fluoride
NH₄F	Ammonium Fluoride
NPs	Nanoparticles
NTs	NanoTubes
ODPA	OctaDecylPhosphonic Acid
OSPW	Oilsands Process Waters
PBGs	Photonic Band Gaps
PCs	Photonic Crystals
PEIS	Potentiostatic
PFDPA	PerFluoroDecane Phosphonic Acid
PFNA	PerFluoroNonanoic Acid
PMAAO	Pulse Modulated Anodized Aluminum Oxide
PMMA	Para-Methoxy-N-Methylamphetamine
PMTiNTs	Periodically Modulated TiO ₂ Nanotube Arrays
PTFE	Polytetrafluoroethylene
PVD	Physical Vapour Deposition
SAM	Self-Assembled Monolayer
SEM	Scanning Electron Microscope
S-TNAs	Small Diameter TiO ₂ Nanotubes
TCO	Transparent Conducting Oxide
TEM	Transmission Electron Microscope
TiF₄	Titanium Tetrafluoride
TiO₂	Titanium Dioxide
TNAs	Titanium Dioxide Nanotube Arrays
TOF-SIMS	Time of Flight-Secondary Ion Mass Spectrometry

TTF	TiO ₂ Thin Film
TTNTAs	Transparent TiO ₂ Nanotube Arrays
UHV	Ultra-High Vacuum
UPS	Ultraviolet Photoelectron Spectroscopy
XPS	X-ray Photoelectron Spectroscopy
BET	Brunauer–Emmett–Teller

Chapter 1

Introduction

1.1 Introduction

Titanium dioxide (TiO_2) has been produced in the form of thin films and in a variety of nanostructures such as nanoparticles, nanofibers [1], nanoribbons [2], nanowires [3] and nanotubes [4-6] in the past couple of decades by diverse methods. Among the various titania nanostructures, TiO_2 nanotube arrays (TNAs) have been widely investigated due to the potential applications made possible by desirable properties such as an ordered architecture, high surface area, high transparency, high refractive index, chemical inertness, mechanical robustness and one-dimensionality (which makes them suitable for electron percolation pathways for vectorial charge transfer [7]). One of the biggest advantages of nanotubes in comparison to nanowires is that nanotubes have a hollow channel that can be filled with different materials. Furthermore, nanotubes can be used as a template for the synthesis of other nanomaterials [8]. Although regular TNAs on native substrate are one of the most potent semiconductors for

photocatalytic [1] and photoelectrochemical devices, hydrogen sensing [2-4], solar cells [5, 6] and filtration applications [6], to date, less research has been conducted on engineering the geometry of such structures for photon management in the active layer of light harvesting devices. In this dissertation, we carried out a fundamental contribution to the topic of TNA-based photon management by growing periodically modulated titanium dioxide nanotube arrays (PMTiNTs) and double layer TNAs.

1.2 Characterization of TNAs

For applications such as photocatalysis, the reaction rates are related to adsorption capacity. A practical approach to achieve higher adsorption capacity is the use of unique nanotexture [7]. It is well known that commercial P25 powder is very fine with particle size of 30 nm and surface area of $\sim 50 \text{ m}^2/\text{g}$ and as reported in reference [8], anodized TNAs with appropriate texturing and dimensions can have surface areas in the range of 200-400 m^2/g that is 4-8 time higher than the P25 powder [8] (**Table 1-1**). Hence in addition to having better percolation pathways for charge transfer, TNAs also have a high surface area for various sensing, light harvesting and photocatalytic applications.

The surface area of anodized TNAs ($\sim 285 \text{ m}^2/\text{g}$) is much higher than the geometrical TNAs (100-140 m^2/g) [8]. Electrochemical anodization is known to cause the formation of double walled nanostructures that increase its surface area. Overall the surface area of TNAs can be enhanced by optimizing the geometry of anodized TNAs (e.g synthesis of small diameter nanotubes or PMTiNTs).

Table 1-1 Textural properties of TiO₂ nanotubes in comparison with conventional TiO₂ nanoparticles .

	Pore size (nm)	S _{BET} ¹ (m ² /g)
TNAs (anodization) [9]	60-100	285
TNA (AAO template method) [10]	50-150	100-140
Degussa P25 [11]	Average 30	50±15

1.3 Growth of TNAs on Native Substrates

1.3.1 Overview

During the last decade, several reports employed solution-based methods for growing TNAs. Formation of the first semiconducting titania nanotubes was reported in 1996 by P. Hoyer[12] using the template method. In this method, nanoporous aluminum oxide formed by electrochemical anodization was used as a template for the electrodeposition of TiO₂. The deposition of thin layers of gold at the top of the nanoporous alumina membranes as an electrode layer is shown schematically shown in **Figure 1-1**. In the second step, the aluminum substrate is etched and polymethylmethacrylate (PMMA) was polymerized within the porous alumina. In the third step, electroless plating was used to form a titanium dioxide layer on the wall of the porous alumina, and in the last step, the nanoporous alumina was etched away [12-14]. Although Hoyer et al [12] used the template method to make TNAs, use of electroless plating caused the formation of amorphous TNAs. Hence annealing for making them crystalline was needed, which caused deformation of the nanotubes [15]. The deformation of nanotubes in this method was the disadvantage in that study. Secondly, the use of nanoporous

¹ BET stand for Brunauer–Emmett–Teller theory: It is one of the most widely studied methods for the calculation of surface area of solid materials that is based on physical gas adsorption.

alumina and PMMA molds along with evaporated gold electrodes introduced notable costs and process complexity.

In 1999, nanoporous alumina membranes were used for the direct deposition of anatase TiO_2 . In this method, supersaturated TiF_4 was used in aqueous solution [15]. Over all, the use of templates such as nanoporous alumina, carbon nanotubes [16], $\alpha\text{-MoO}_3$ [17] and laurylamine hydrochloride (LAHC) [18] was studied to form TNAs by using sol gel [19, 20], electroplating [12, 13], chemical vapor deposition, atomic layer deposition (ALD) [21] and other methods. These methods are complicated and challenging, and none of them can offer superior control over nanotube dimensions and orientation.

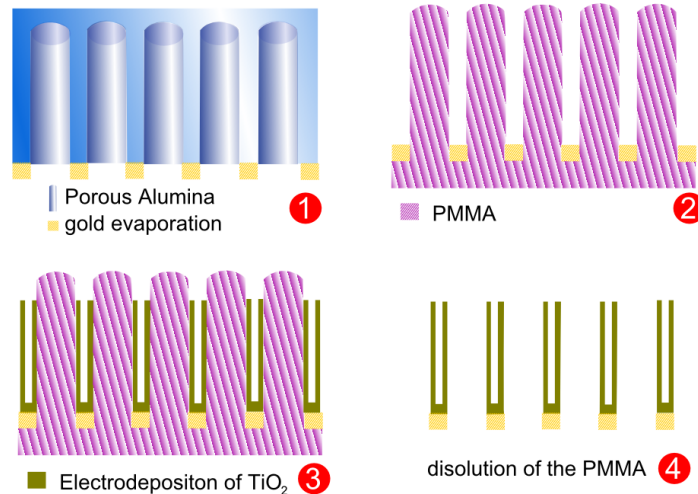


Figure 1-1. Schematic view of template method, for growing TNAs

1.3.2 Electrochemical Anodization

Anodization of Ti in hydrofluoric acid containing aqueous electrolytes to generate nanostructured TiO_2 was first reported by Zwilling, A. et al [22]. In 2001, the formation of nanotubular structures by anodization in aqueous electrolyte was reported by Gong et al. [23], which was the first report on the

anodic formation of TNAs. For synthesizing nanotubes with different pore size, wall-thickness, surface area and tube-length, different recipes have been employed such as fluoride-containing aqueous electrolytes in the first and second generation [10], and organic electrolytes based on ethylene glycol [11], N, N-dimethyl formamide [24], formamide and dimethyl sulfoxide (DMSO) in the third generation [13],[25]. Use of each recipe enables one to adjust the geometrical features of nanotubes thus allowing one to achieve nanotubes with different optical properties. Each method has some advantages and disadvantages. For instance, different recipes set different limits on the range of tunability of morphological parameter values of TNAs such as the pore size or tube-length (Figure 1-2).

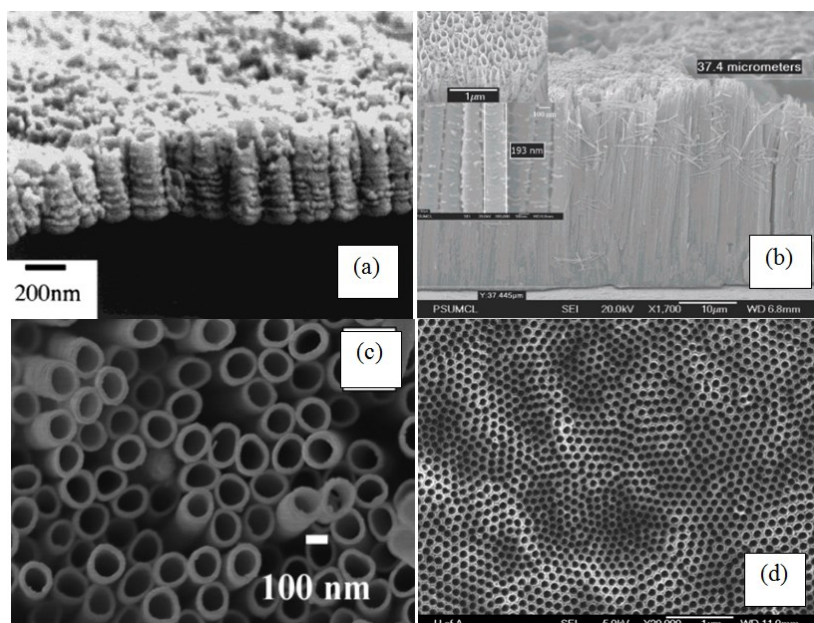


Figure 1-2. Morphology of nanotubes grown in a) aqueous electrolyte [23] adapted with permission from Gong D. et al., *Journal of Materials Research*, 2001. 16(12). © 2001, Research Society b) formamide electrolyte [26] adapted with permission from Yoriya, S. et al., *Journal of Physical Chemistry C* 2007. 111(37):p. 13770-13776 © 2007, American Chemical Society c) dimethylsulfoxide electrolyte [24] adapted with permission from Shankar K. et al, *Journal of Physical Chemistry C*, 2007. 111(1): p. 21-26. © 2007, American Chemical Society d) ethylene glycol (EG) electrolyte.

Electrochemical anodization is a single step process that does not need the assistance of a template. In addition to being highly functional and self-ordered, TNAs grown by a top-down process (electrochemical anodization) are relatively cheap to produce in comparison to standard micro- and nano-architectures requiring bottom-up lithographic techniques.

1.3.3 Photon Management in Titanium Dioxide Nanotube Arrays

Due to the unique electronic properties of TNAs such as charge carrier diffusion lengths comparable to the wall-thickness, vectorial charge percolation pathways and a large effective surface area, we paid particular attention to the tuning of the optical properties from the point of view of light harvesting applications.

1.3.3.1 Double layer TNAs

In 1997, a colloidal solution containing dye (rhodamine) and TiO₂ nanoparticles was reported to be a strongly scattering medium by E. Sauvain et al [27]. This medium is very similar to dye sensitized solar cells (DSSCs) and offers an effective way to improve optical absorption. The improvement in optical absorption comes from light scattering; it can be described in the framework of Mie theory. In 1997, boundary element method (BEM) and Monte Carlo simulation methods were conducted for simulating multiple particles with sizes comparable to the wavelength of light). Based on this theoretical study, for achieving effective scattering, the optimal diameter of particles should be about 0.65λ [28]. By using numerical methods, it was shown that using a structure of double layer TiO₂ nanoparticles (large diameter particles- $D=0.65\lambda$ along with small diameter particles), light absorption increased about 35% [28]. Overall, using large diameter nanotubes increases the optical path length, and in

conclusion improves the light harvesting efficiency (LHE) by about 35%. In recent times, various alternatives to photon management such as ‘colloidal submicron-sized ZnO particles’[29, 30], hierarchical TiO₂ nanoparticles [28, 31] and branched TNAs [32] have been proposed. While most of these structures have shown improvement in the LHE, none of them are suitable as electron percolation pathways. In **Chapter 2**, we carried out a fundamental study of the LHE in sensitized membrane-type double layer TNAs, which also constitute most suitable electron percolation pathways for vectorial charge transport [33].

1.3.3.2 Pulse Modulated Nanotubular Structures

Pulse modulated nanotubes/nanopores function as Bragg interference mirrors that manipulate the propagation of photons. PMTiNTs/PMAAO² is a functional material combined with directionality and dimension that can open up a whole range of potential applications in near future. Pulse anodization has been employed in the aluminum industry since 1960. The very first report on the pulse modulated porous anodic aluminum oxide formation was reported in 2006 by Gösele, U. et al [34]. Gösele, U. et al [26] in their work reported the use of potentiostatic anodization and mentioned that cell ordering is insensitive to anodization potential at high voltage in the range of 120-150 V. It was reported by Gösele, U. et al in 2008 that galvanostatic anodization provides better control over ‘current density/high periodicity’ in comparison to potentiostatic anodization [35]. In 2004, a 2-D photonic crystal (PC) structure consisting of highly ordered AAO was studied by Tomasiunas, R; et al. [36]. In 2007, photonic crystals made-up of periodic modulated aluminum oxide were reported by Minet et al [37]. In 2011,

²Pulse modulated anodized aluminum oxide

PMAAO with uniform narrow photonic band gaps (PBGs) (FWHM in the range of 60 nm to 80 nm) was reported. It was shown that PBGs of PMAAO are tunable in the range of 350 nm to 1330 nm [38]. Recently, in 2013, this structure was used as a sensitive sensor [39, 40].

Although, reasonably periodic nanostructures of AAO have been fabricated in combination with high and mild anodization, this structure is far from satisfactory for photon management due to lack of adequate control over the refractive index contrast along the length (i.e. axial direction) of the cylindrical channels. On the other hand, due to the low refractive index of AAO² (~1.7), it is impossible to produce a complete band gap for photons in the visible wavelength regime. However, titanium dioxide with a refractive index in the range of 2.7 can be thought of as a better candidate for PC applications. In 2011, 1D-PC films made from anodic TiO₂ nanotubes were reported [41, 42]. The minimum FWHM was reported in the range of ~100 nm to ~150 nm. **Chapter 2** of this dissertation focuses more on improving the FWHM of reflected light for PMTiNTs and achieving greater control over the periodicity in order to control the refractive index contrast and tune the stop-band wavelength.

1.4 Growth of TNAs on Non-Native Substrates

TNAs grown on titanium foils have been successfully employed in a wide range of applications due to the unique combination of properties such as *n*-type semiconducting behavior, a wide electronic band gap³[43, 44], high surface area

³The band gaps of rutile and anatase titanium oxide are 3.03 eV and 3.2 eV respectively.

[14, 43], high refractive index⁴[45, 46], large capacitance [13] and moderate electron mobility⁵[14, 47]. It is expected that highly ordered and vertically oriented titanium dioxide nanotube arrays grown on transparent substrates are more advantageous [43, 48-50], particularly for optical and optoelectronic applications. Another problem with native substrates is that titanium (Ti) sheet as a substrate can sometimes result in the formation of a Schottky barrier between the Ti film and TiO₂ barrier layer that can limit the application of TNAs in applications such as resistive gas sensors, electrochemical biosensors and photovoltaics where an ohmic contact is desired [51]. Ti foil based membranes are more vulnerable to mechanical shock and/or vibrations that can produce membrane delamination and cause the device to fail. Another problem with Ti foil based membranes in electronic devices is that Ti³⁺ and Ti⁴⁺ cations can diffuse outward from the Ti foil into the TiO₂ nanotubes at elevated temperatures and cause electrical shorting or else change the composition of the nanotubes [52],[53]. Therefore, it is more desirable to grow this nanostructure on non-native substrates (Chapter 3) or to make free-standing membrane TNAs (**Chapter 2**).

The length and pore size of TNAs on native Ti foil substrates and the effect of various electrolytes such as organic and aqueous recipes on the morphology, ordering and surface area of TNAs have been extensively investigated [48, 54]. The Ti foils used in such studies are hot-rolled uniform substrates with flat grains 10-100 μm in size. In contrast, the grain size in thin films of Ti on non-native substrates is at least two orders lower in magnitude. Very few studies have

⁴ Refractive index of anatase TiO₂ is polarization-dependent and it is in the range of 2.33 to 2.56.

⁵The mobility of pure single-crystal *n*-type TiO₂, has been measured to be 10-15 cm²/V s for a carrier density of 10¹⁸ cm⁻³.

examined the process of formation of TNAs on Ti thin films deposited on conductive glass [55], silicon [52, 56] and flexible polymeric substrates [57, 58].

In 2005, the successful formation of vertically oriented TNAs on a non-native substrate, namely borosilicate glass, was reported by Mor et al [53]. Studies conducted by K. Kalantar-Zadeh and colleagues [59], Grimes and colleagues [60, 61] and Schmidt-Mende and colleagues required elevated substrate temperatures (up to 600 °C) during Ti deposition in order to achieve TNAs on glass and transparent conductive oxide (TCO) coated glass substrates using Ti films deposited by magnetron sputtering. In **Chapter 3**, we conduct a fundamental study of the effect of the deposition parameters of the Ti thin films on the morphology of the resulting TNAs. Previous reports indicated that Ti thin films with larger sized grains and more uniform surfaces are more suitable for nanotubes formation [62]. However, our results show that smoothness is significantly more important than grain-size in order to obtain ordered nanotubes as opposed to a disordered nanoporous structure. A large grain-size, especially when randomly oriented, is associated with a larger dispersity in the shape and size of the nanotubes. Almost monodispersed TNAs are formed on silicon and ITO-coated polyimide substrates, which not coincidentally, also result in Ti thin films with the minimum surface roughness. Furthermore, TNAs can be achieved using simple, high-throughput DC sputtering at room temperature by performing the deposition at low chamber pressures, thus benefiting from the atomic peening mechanism. The effect of thin film quality on the formation of highly ordered TNAs on a variety of substrates including, glass, FTO coated glass, silicon wafer, stainless steel, and Kapton® polyimide film at room temperature is presented in **Chapter 3**. The anodization process is analyzed at different phases in detail using a current-time anodization plot. It is shown that by specifying the sputtering rate

and pressure during deposition, the adhesion and morphology of Ti film on a variety of substrates is controllable.

1.5 Metal Nanoparticle Promoter-Decorated TNTAs for Photocatalytic Application

The *n*-type semiconducting anatase phase of titanium dioxide (TiO₂) is one of the most widely used semiconductors for photocatalytic and photoelectrochemical device applications owing to its various advantageous properties such as the strong oxidizing power of photogenerated holes, nontoxicity, high resistance to photocorrosion, high chemical stability and low cost [63]. Compared to photovoltaic cells, where sunlight is converted into electricity, photocatalytic cells where sunlight is converted into fuels such as hydrogen, methane, methanol, etc. have the distinct advantages that the photocatalysts can be easily deployed either in a suspension or on a surface that receives sunlight and the products of the photoconversion reaction being fuels are easy to store and transport, and therefore simpler to deploy at remote locations or where scale-up of production capacity is not an option [64-66]. However, most photocatalytic reactions are multi-step electron transfer reactions due to which electron-hole pair recombination losses, activation barriers at each step and back-reaction of intermediate products can have a catastrophic effect on overall reaction yields [67-70]. Furthermore, because of the way in which photocatalysts are deployed, an external bias to drive the separation of charge carriers is not present. The sunlight-driven conversion of CO₂ to light hydrocarbons is particularly challenging since it is recognized to require a minimum of eight electron-transfer steps [71]. In this context, nanostructuring the TiO₂ is highly effective for improving photocatalytic action because of the resulting high surface-to-volume ratio and the proximity of carrier

photogeneration to carrier utilization. Coating wide bandgap semiconductor photocatalysts with noble metal nanoparticles is a widely used approach toward producing a built-in potential to enhance the separation of photogenerated charges and to use the promoting action of the noble metals on the catalyzed reactions. However, the interfacial band-alignment in such heterojunctions is often poorly understood. We present the electronic properties of the heterointerface formed by TiO₂ nanotubes grown on a non-native substrate (TCO-coated glass) coated with CuPt nanoparticles in **Chapter 4** [72].

1.6 Wetting Phenomena using TNAs

Surface wettability is a significant phenomenon influencing performance in many microfluidic, electrochemical, biosensing and photocatalytic applications. The structure and morphology of a material play an important role in controlling the wetting characteristics. The achievement of surfaces that completely repel a wide range of polar and non-polar liquids is a highly desirable goal in fluidics, but such superamphiphobic surfaces are exceedingly rare. Multiple studies have recommended that superamphiphobicity can be achieved by governing topographical micro/nano structure of surface and surface chemistry, which can lead to sophisticated phobicity [73]. Controlling the wettability of any nano- or micro-structured surface requires knowledge of the underlying chemistry, physics and geometry.

A true indication of amphiphobic or superamphiphobic behavior [74-76] is only obtained by demonstrating liquid repellence of the surface in a broad spectrum of solvents where dispersion-based, dipole-based and hydrogen-bonding-based interactions are involved. The few extant fundamental studies of wetting behavior on TiO₂ nanotube arrays (TNAs) are either limited to a narrow

range of solvents (mostly from the polar, protic solvent family) [77-79] and/or utilize nanotubes with visible surface debris [78, 80], pore clogging or tangled, randomly oriented morphologies [77, 81]. Superhydrophobic nanotubes have received far more attention than either oleophobic or amphiphobic nanotube surfaces. Different methods have been used to generate the desired lyophobic behavior. Brush-coating anodized Ti with fluoropolymers has been reported to result in contact angles with water of up to 122° [82]. Dip-coating anodized Ti with a perfluoroalkylsilane followed by curing resulted in optimized water contact angles of 150° [83]. Superior performance was obtained by forming a monolayer of a perfluoroalkyltrichlorosilane on the exposed surfaces of TNAs by immersion self-assembly, which resulted in contact angles as high as 163° with water and 157° with ethylene glycol [84]. Balaur et al reported water contact angles of 165 - 167° by coating TiO_2 nanotube arrays with self-assembled monolayers of octadecylphosphonic acid (ODPA) [78]. In the same study, diameter dependence of the superhydrophobic behavior was also studied and it was found that the largest diameter (100 nm) nanotubes provided the highest water contact angles and smallest diameter (20 nm) the lowest contact angles in accordance to the area fraction calculation with Cassie-Baxter theory [78].

The wetting of pristine or functionalized TNA surfaces by liquids, gases, biomolecules and polymers play a key role in the previously mentioned device applications [78]. Lately, diverse methods have been developed for making artificial superhydrophobic/amphiphobic surfaces such as electrodeposition, electrospinning, chemical vapor deposition, sol-gel method, hydrothermal method, etc. These methods are difficult to control and in some of them, the surfaces are fragile [85]. Therefore, electrochemical anodization, which is a

simple and economical approach for growing robust TNAs, is a remedy to the above discussed problems.

The main focus of **Chapter 5** is on studying the static wetting properties of perfluorinated monolayer-coated TNAs with various polar and nonpolar solvents. The superamphiphobic aspect of derivatized TNAs makes them suitable coatings for a variety of sticking-free applications.

Using ethylene glycol in electrochemical anodization results in the formation of TNAs in triangular lattice. The contact area fraction parameter needs to be calculated in the theory part to be able to compute Fakir/ Cassie-Baxter [86] contact angles. In **Chapter 5**, the contact area fraction parameter was calculated by considering triangular lattice unit cell. Pendant drop dynamic contact angle measurement system was used for recording the contact angles. Contact angle data was systematically collected from chemically treated and non-treated surfaces. Overall, extremely liquid repellent surfaces were achieved by the combination of chemical heterogeneity and surface nano-asperities. Contact angles (θ) in the range of 5° to 31° were measured on non-chemically treated planar TTF surfaces (where no nanostructuring was present) that were amplified to 42° (Toluene) and 110° (DI water) after surface treatment. The same data analysis was performed on non-chemically treated and perfluorinated TNAs in two different configurations. In bare small diameter TiO_2 nanotubes (S-TNAs) and bare large diameter TiO_2 nanotubes (L-TNAs), ' θ ' was less than 5° indicating superhydrophilicity. Afterwards S-TNAs and L-TNAs were chemically treated by PFNA and PFDPA. Experimentally measured contact angles (θ_{Large} and θ_{small}) and deviation from Cassie-Baxter contact angles ($\Delta\theta_{\text{Large}}$ and $\Delta\theta_{\text{small}}$) were tabulated. High contact angles ($>165^\circ$) for DI water was observed on all four types of

perfluorinated nanotubes (S-TNAs_{PFNA}, L-TNAs_{PFNA}, S-TNAs_{PFDPA} and L-TNAs_{PFDPA}).

1.7 Future work and Conclusions

The n-type semiconducting TNAs with vertically oriented tubular structure and high surface area possess transparency, high refractive index, chemical inertness and mechanical robustness is a part of the present study. These unique properties make them a highly promising nanoarchitecture for devices such as gas sensors [87], biomarker assays, drug-eluting coatings, flow-through membranes, stem-cell differentiators, photovoltaics and photocatalysis [88]. In spite of the significant works that have been conducted for anodization process there is still room for improvement in this vertically oriented structure and **Chapter 6** includes the conclusions of present dissertation and suggestion for future works.

Chapter 2

Growth of TNAs on Native Substrates

2.1 Introduction

In the anodization process, surface preparation is the most challenging part for growing highly ordered TNAs. The roughness of the Ti thin films or foil substrate plays a key role in attaining monodisperse nanotubes with maximum two-dimensional pattern order. Different methods like pre-anodization [43], chemical polishing [89, 90] and electropolishing [91] have been used for surface preparation.

2.2 Substrate Preparation for TNAs Growth

When the surface is smoother, the fluoride ions will reach the surface concurrently. If a conductive substrate is used, the current flows uniformly and will cause uniform pitting. On the other hand, when the surface is rough the fluoride ions will reach the surface at different times resulting in non-uniform pitting. The next section details about various methods for substrate preparation for the growth of nanotubes.

2.2.1 Self-Template Method by Using Two Step Pre-anodization

In this method Ti sheets are anodized using a solution of 4 % DI water and 0.3 wt% NH_4F in ethylene glycol for 2 hours. The samples are then rinsed in water and immersed in methanol overnight. The TNA film fully delaminated due to surface tension and/or etching of the barrier layer by H^+ and F^- ions that are present at the bottom of nanotubes (having migrated there in the course of the anodization process) [43]. Methanol, due to its low surface tension, will infiltrate into the interface of the barrier layer and Ti film. By so doing, the first step anodization native oxide layer will be removed from the surface. On the other hand, by performing the anodization for 2 hours and then removing the film, the Ti film will be smoother due to electrochemical etching that takes place during the first step of anodization. In the second step pre-anodization, since the sample is more uniform due to first step anodization, pitting will be more monodispersed compared to the first step, following which, anodization causes formation of very nice foot prints, which can be used as a template for nanotube growth in subsequent steps.

2.2.2 Electropolishing and Chemical Polishing

Since 1977, these methods (electropolishing and chemical polishing) have been used to smoothen and clean the surface of titanium sheets. As shown in **Figure 2-2a**, electropolishing is based on reduction at cathode, oxidation at anode and dissolving titanium dioxide in the electrolyte.

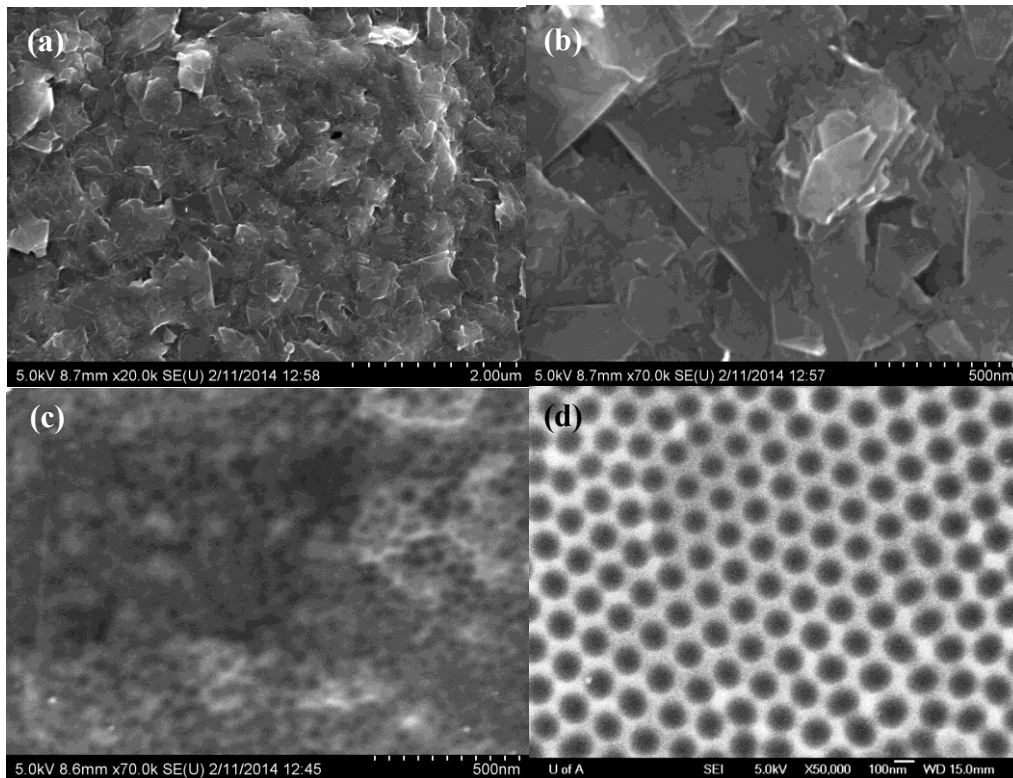


Figure 2-1. (a, b) Titanium foil at two different magnifications. Footprints of nanotubes after (c) first step pre-anodization for 2 hours and (d) second anodization for 36 hours.

In this process, the removal of titanium from the surface is due to the conversion of Ti atoms into Ti^{4+} ions that will be accelerated toward the cathode. The most important feature of electropolishing is the faster dissolution rate on asperities (peaks) compared to “micro-valleys” due to the concentration of electric fields at notch-like surface features. As depicted in **Figure 2-2b**, electropolishing results in a more uniform surface due to faster dissolution of Ti at surface asperities. Chemical polishing is a simpler process as compared to electrochemical polishing and uniformity results due to faster etching of high index crystal planes of Ti exposed at surface asperities. For polishing titanium, very diluted hydrofluoric acid (HF) was used. Since HF is very corrosive, it should be mixed with the other chemical.

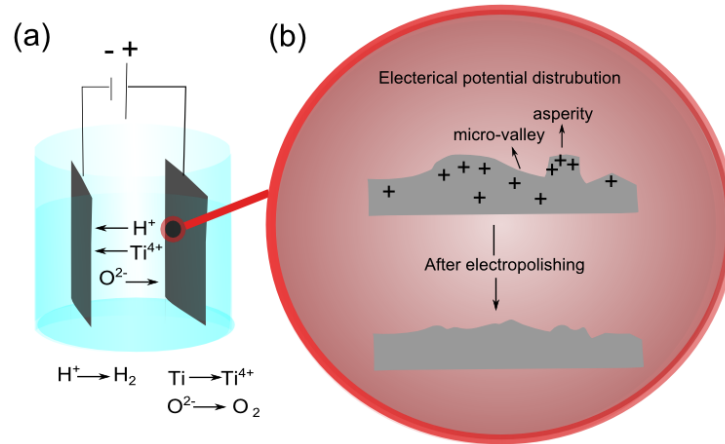


Figure 2-2. a) Schematic illustration of electro-polishing process. b) Electrical potential distribution on titanium surface, during electro-polishing process.

In **Figure 2-3**, the surfaces of titanium sheets before and after electro-polishing and chemical polishing are shown. It can be seen from the figures that the grain boundaries become more prominent after polishing the substrates.

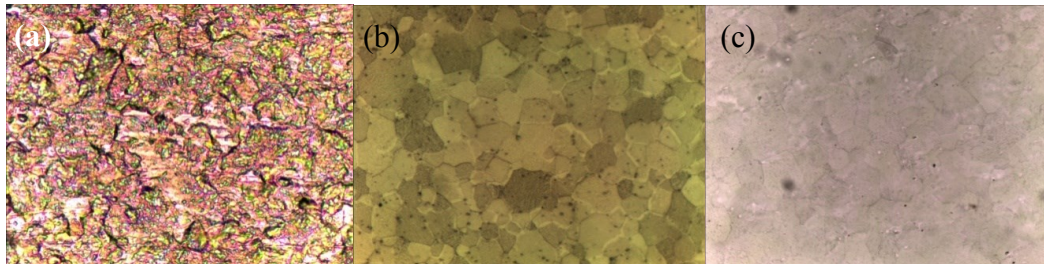


Figure 2-3. Optical image of a) Ti sheet before polishing b) electropolished sample c) chemically polished samples, at 50 X.

2.3 TNAs on Titanium Sheet

2.3.1 Single Layer TNAs by Electrochemical Anodization

The formation of anodic TiO_2 compact film was reported by Mizushima W. in 1961. In this paper, the relation between the current density ' i_+ ' and electric field ' E ' in the formation of anodic compact TiO_2 planar films was investigated [92].

This paper showed that the ionic current density increases exponentially under the influence of electric field. In this process ethylene glycol/DI water and 10% ammonium borate was used for anodization. If the same process occurs in the presence of fluoride ions, a completely different morphology (vertically oriented titanium dioxide nanotubes or a disordered nanoporous structure) will be obtained. The formation of self-organized, vertically oriented metal oxide nanotubes by the electrochemical anodization method was straightforward as compared to the template or hydrothermal methods but the length of the nanotubes was limited due to the chemical dissolution process; consequently, the process did not attract significant interest from 1999 to 2004.

In 2005, high aspect ratio TNAs were reported by Macak et al [93] and by Cai et al [94] in aqueous electrolytes by using buffers to maintain a stable concentration of protons in the electrolyte. These papers claimed that by adjusting the pH, the process of chemical dissolution could be controlled and they achieved self-organized TNAs with a film thickness (i.e. nanotube length) as high as 6.6 μm in aqueous electrolytes [93] [94]. In the anodization process, an oxide layer is grown on the surface of metallic film. To accomplish this, a conductive plate of valve metal (e.g. Al, Ti, Hf, Nb, Zr, Ta, etc.) is connected to the positive terminal of a power supply, and a counter-electrode consisting of another conductive plate/rod (typically low overpotential materials such as platinum, graphite, etc.) is connected to the negative terminal. Both terminals are immersed in the electrolytic bath (shown in **Figure 2-4**).

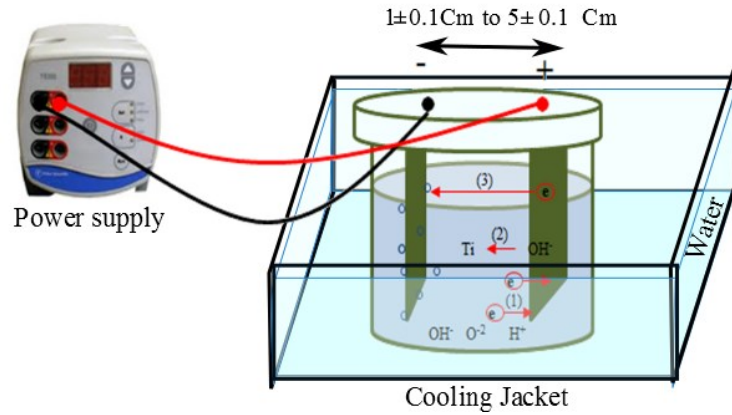
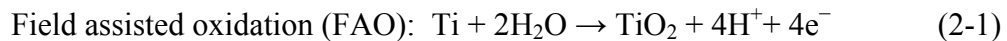


Figure 2-4. Illustration of anodization set up in our laboratory.

Sometimes, additional electrodes are present such as a reference electrode to measure absolute potentials and a pH electrode to measure pH. A thermometer to measure bath temperature is also used occasionally. As shown in **Figure 2-5a** when a potential difference is applied across the electrolyte with the polarity indicated, negative ions are forced to move towards the anode, and due to the field assisted oxidation, Ti reacts with OH^- and a thin blanket oxide layer of Ti is created according to the reaction listed below.



This oxide layer is called barrier layer that is created over the entire metallic sheet and the thickness of barrier layer is primarily determined by the electrolyte and the potential difference applied.

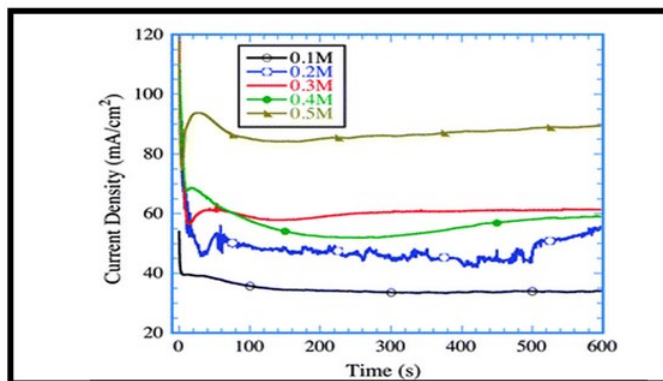
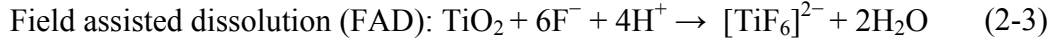
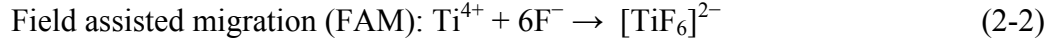


Figure 2-5. Current vs time behavior during anodization of Ti foil in fluoride-free electrolyte (current density response at 10V) [95] adapted with permission from Allam, N.K., 2008. 18(20): p.2341-2348 © 2008, Royal Society of Chemistry

As depicted in **Figure 2-5b**, during the process, initially the electronic component of the current decreases drastically due to the increased thickness of the insulating barrier layer. In this regime, which is typically a few seconds into the anodization process, the ionic component of the current is limited by the solid-state transport of ions through the barrier layer and also drops steeply with time. Next, oxide layer pitting by F^- ion results in a decrease in the oxide layer thickness, as a result of which current starts to increase thus generating a local minimum in the current along the way. As the reaction proceeds, TNAs will grow that will saturate the current further resulting in a local current maximum. In the anodization process, F^- ions play an essential role in comparison to the other components [9].

After creating the oxide layer due to the field assisted migration and dissolution, TiO_2 will be dissolved in the pitted regions and a nanoporous structure will be created [96]. Chemical dissolution of TiO_2 is the distinguishing reaction that results in nanotubes as opposed to nanopores. Chemical dissolution is field-independent and etches TiO_2 not merely in the pitted regions but

everywhere, thus also shortening the nanotube length [6, 14]. These chemical reactions are as listed below.



Initially, TNAs are amorphous after anodization and are annealed at temperatures exceeding 350° C to induce crystallinity [97]. HF, KF and NaF aqueous recipes were used in the synthesis of first-generation nanotubes [94]. HF-based aqueous recipe consists of a mixture of H₂O, HF and acetic acid with a pH < 1. This recipe limited the length of the nanotube to 500 nm because of the high rate of chemical dissolution of the titanium dioxide. The use of pH controlled KF/NaF-based aqueous electrolytes in the second generation extended the length (up to 6.6 μm) of the NTs due to reduction in the chemical dissolution of the oxide [94], [15]. Changing the experimental set-up has an effect on the nanotube features. For example, use of Fe instead of Pt as a cathode (Ti sheet [15]) during anodization increased the nanotube length from 500 nm to 2.5 μm [6]. Although the pH buffered aqueous electrolyte recipe was promising, the length of the nanotubes could not be extended beyond ~6.6 μm because the barrier layer thickness in aqueous electrolytes could not be reduced below 50 nm, and solid-state transport of reactant ions (Ti⁴⁺, OH⁻, F⁻) through the barrier layer eventually reduced to almost zero. Apart from that, polydispersity in size and shape was also one of the disadvantages for these nanotubes due to the highly conductive and relatively non-viscous electrolyte.

The solution to the problem of limited nanotube length resulted from using organic electrolytes. In 2005, an organic electrolyte based on glycerol was used for growing smoother nanotubes [98]. Electrolytes based on organic solvents such as formamide, glycerol, ethylene glycol and dimethyl sulfoxide are more viscous. Based on Walden's rule, by increasing the electrolyte viscosity, conductivity will be decreased [24], as mentioned in equation (2-5):

$$\eta \times \lambda^{\infty} = \text{Constant} \tag{2-5}$$

Where η is solution viscosity and λ^{∞} is the limiting molar conductivity of the particular ion. The higher viscosity of glycerol- and ethylene glycol-based organic electrolytes suppresses local fluctuations in the current density (**Figure 2-6**) as well as local concentrations of reactant species and thereby produces nanotubes with smoother walls, in contrast to the highly scalloped walls obtained in aqueous electrolytes. In aqueous electrolytes, water and the products of the dissociation of water (OH^- ions) are the primary oxidizers.

Organic electrolytes contain a much smaller concentration of water due to which oxidizing species are scarcer and thinner barrier layers result. For the same anodization voltage, a thinner barrier layer results in much faster solid-state transport of ions and as a result, thinner barrier layers enable the formation of longer nanotubes. The use of organic electrolytes constitutes the third generation of nanotubes. In the third generation, organic electrolytes such as dimethyl sulfoxide (DMSO), formamide [24], ethylene glycol [99] were used to control chemical dissolution and nanotubes up to 1000 μm in length were achieved. In 2006, recipes based on formamide, containing KF, NaF, NH_4F , Bu_4NF , and BnMe_3NF with a comprehensive description of the anodization process, were

published by K. Shankar et al [24] and the effect of using different cations was investigated.

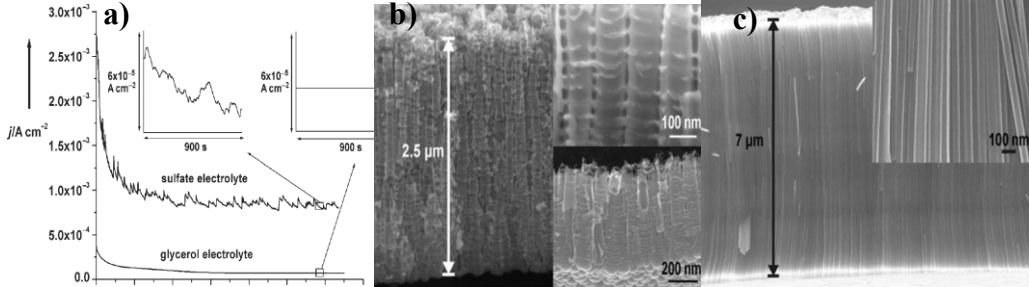


Figure 2-6. a) Current density of aqueous and organic. b) Cross-section of TNAs on aqueous base electrolyte. c) Cross-section of TNAs on organic base electrolyte [98] adapted with permission from Macak, J.M. et al., *Angewandte Chemie International Edition*, 2005, 44(45): p.7463-7465 © 2005, John Wiley and Sons.

Small counterions such as protons and ammonium ions had relatively large solvation shells resulting in a lower ionic mobility while larger ions such as tetrabutylammonium and benzyltrimethylammonium were nearly unsolvated, and solutions containing them were significantly more conductive. Based on the following equation, the Stokes radii (a measure of the size of the solvation shell) is inversely related to the product of the conductivity and viscosity:

$$r_s = \frac{|z|f^2}{6\pi N_a \eta \lambda_i^0} \quad (2-6)$$

where ' λ_i^0 ' is limiting ion conductivity, ' Z ' is the charge on the ion, ' f ' is the Faraday constant and ' N_a ' is Avogadro number. Having a smaller Stokes radii means the ions have a smaller solvation shell and are therefore more conductive with a higher mobility since the motion of ions is accompanied by the drag of fewer solvent molecules [24]. As a result, when the electrolyte is less conductive,

the anodization current will be limited by the electrolyte conductivity instead of the solid-state transport of ions through the barrier layer and the nanotube growth rate will be slower. The fourth synthesis generation used non-fluoride-based anodization chemistries based on perchloric acid (HClO₄), hydrochloric acid (HCl) and HCl in combination with hydrogen peroxide (H₂O₂). Using hydrogen peroxide increases the oxidation reaction rate [5]. All these kinds of nanotubes are hexagonal closed-packed that makes them suitable for waveguide, photocatalytic nanotemplate[1], hydrogen sensing [2-4], solar cell [5, 6] and filter applications [6].

2.3.2 Double layer TNAs

Anodically formed TNAs are being actively researched for their use as electron collecting scaffolds in excitonic solar cells, as photo-catalysts for sunlight-driven CO₂ reduction and water-splitting. Engineering the optical properties of TNAs for such light harvesting applications has received less attention but is much needed. In 1995, the effect of random scattering of light in double layer TiO₂ nanoparticles (NPs) was investigated by Monte Carlo simulation method [28], according to which, when the diameter of particles is in the range $0.8 \times \pi/k$ to $1.3 \times \pi/k$ (k being the wave number), it leads to robust scattering of light [28]. This method has not only been used for TiO₂NPs, but also for broadband absorption in silicon solar cells [100] and for ZnO films in dye-sensitized solar cells [101, 102]. The mode of scattering can be distributed into three domains base on ' α ' parameter.

$$\alpha = \frac{\pi D_p}{\lambda}$$

(2-7)

Where ' λ ' is wavelength of incident light, and ' πD_p ' is circumference of a particle. Three different domains of scattering may be defined based on ' α ' (a dimensionless parameter).

1. Geometric scattering: Particle size is much larger than the wavelength of light ($\alpha \gg 1$).
2. Mie scattering: Particle size is about the same size as wavelength of light ($\alpha \approx 1$).
3. Rayleigh scattering: Particle size is much smaller (~ 10 times) than wavelength of light ($\alpha \ll 1$).

The principal disadvantage of using NPs in solar cells is that the random walk-type hopping transport in nanoparticulate films negatively impacts charge collection. In order to remedy this problem, nanotubes have been studied instead of NPs. In this dissertation, the optical properties of films composed of TNAs are studied since these structure offer a better pathway for carrier charge transport in comparison to sintered films of nanoparticles.

The one-dimensional structure of nanotubes imposes a direction (along the nanotube axis) upon the transport of charge carriers and mitigates the random walk to a great extent. As indicated in **Figure 2-7 (a-b)**, volume ratios of nanotubes are adjustable based on outer and inner diameters. This gives us the opportunity to not only modify the scattering but also tune the effective refractive index of the nanotube array. OptiFDTD 9.0 (Optiwave Inc.) was used for simulation of TNAs with respect to the various dimensions; the barrier layer was considered to be air. The simulation results are reported in **Figure 2-7(c-e)**.

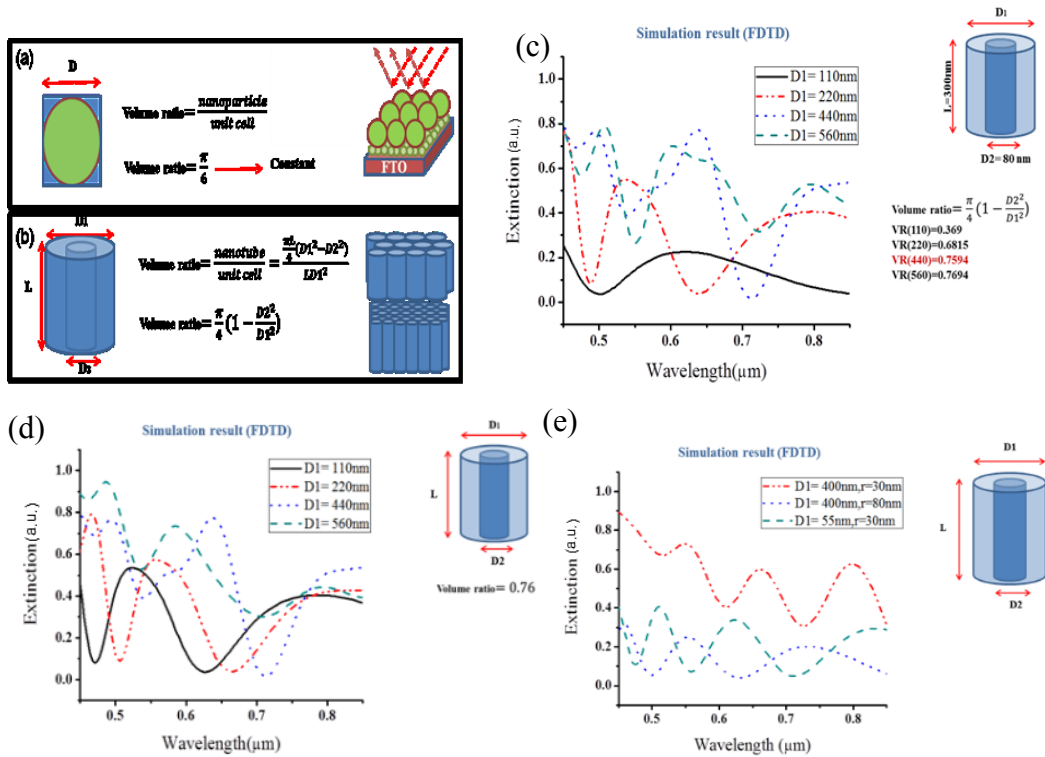


Figure 2-7. (a,b) Volume ratio calculations for nanoparticles and nanotubes. FDTD results for (c) constant inner-diameters and various outer-diameters, (d) for constant volume ratio and (e) for various volume ratios.

Using a combination of experiments and simulations, we explore the use of multilayer nanotube array architectures for engineering the optical properties of TNAs. In a bilayer array consisting of TNAs of diameter *ca.* 50 nm and 250 nm respectively, Mie back-scattering from the larger TNAs increased the optical path-length and improved the absorption of blue photons near the band-edge of TiO₂ (**Figure 2-8b**). Ti³⁺ absorb light in the spectral range 380 nm to 480 nm and the light absorption improvement that has been observed in **Figure 2-8b** proved the activation of Ti³⁺ and effect of light trapping. This is also confirmed by 3D-FDTD simulations (**Figure 2-8c**). In conclusion, multilayer TNAs offer an attractive route for management of light in the active layer of light harvesting devices.

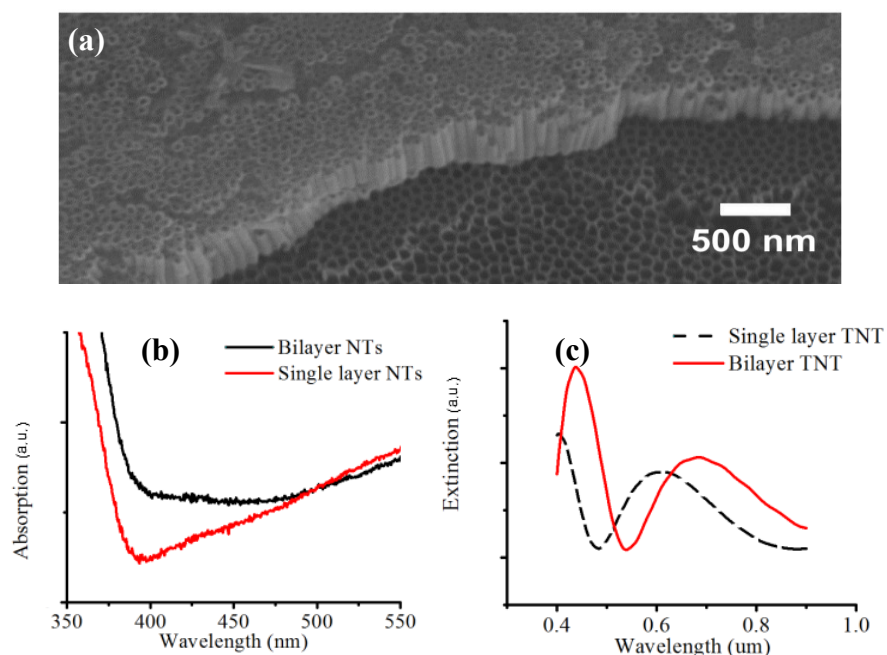


Figure 2-8. a) SEM of double layer TNAs b) Experimentally observed light absorption in single layer and double layer nanotubes c) simulation result for extinction of light in single layer and double layer nanotubes

As depicted in **Figure 2-8a** double layer TNAs was successfully grown on titanium foil. However, the presence of an opaque layer of titanium sheet behind the nanotubes limit the optical applications of this structure. Herein we present a simple method for the delamination of TNAs from the substrate. This process includes five steps. First, titanium foil was decreased ultrasonically in acetone, methanol and DI water 10 min each. Anodization process was conducted on organic electrolyte (98% Ethylene glycol, 2% DI and 0.3wt% NH_4F) at 20 volt for 72 hours at 5 ± 0.1 cm inter-electrode separation setup. After cleaning the sample ultrasonically in Methanol bath, second anodization process was conducted at 60 volt for 30 min in an organic electrolyte with 4% DI water. It well known that the anodization voltage has a direct effect on the diameter and growth rate of the nanotubes, with bounds on the maximum and minimum anodization voltages placed by the dielectric breakdown field of the barrier layer and the onset of

nanotube formation respectively. As reported by Shun et al [103] in 2010, TNAs' diameter and growth rate can be tuned based on the amount of the DI water concentration on the electrolyte. As shown in this paper, the growth process will be faster at lower water concentrations and the nanotube diameter will be larger at higher DI water concentration. In the present work, a lower water concentration has been used to achieve a faster growth rate while for achieving nanotubes with larger diameter, higher water concentrations in the range of 4% to 10% were used.

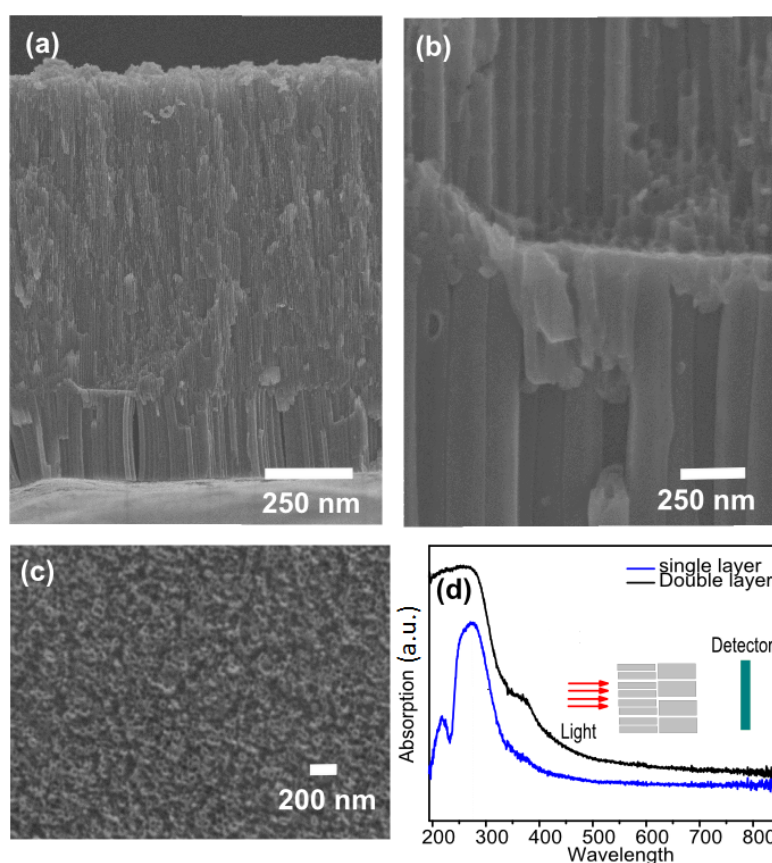


Figure 2-9. a, b) cross sectional SEM images of double layer TNAs c) top view SEM image of first layer d) diffuse reflection data from single (only small diameter nanotubes) and double layer structure.

In order to separate the TNA membrane from the Ti metal substrate, anodized sample was ultrasonically washed in methanol bath to remove ethylene glycol,

followed by annealing at 300-450 °C for 1-2 hours. Since using H₂O₂ produces more selectivity in etching amorphous TiO₂, a second step anodization was carried out on annealed samples for 8 hours at 12 V, then it was immersed in 10% H₂O₂ to etch the amorphous layer. As a result membrane TNAs was detached from the Ti Substrate. As depicted in **Figure 2-9** double layer TNAs membrane is produced with a length of about 15 μm (10 μm: large diameter nanotubes and 5 μm:small diameter nanotubes) by anodizing at 20 V (72 hours, 2 % DI water and 0.3 wt % NH₄F) and 60 V (72 hours, 4 % DI water and 0.3 wt % NH₄F) respectively. As expected, this improved the absorption of blue photons near the band-edge of TiO₂ was observed due to scattering of light from the second layer TNAs with larger outer diameter **Figure 2-9d**).

2.4 Periodically Modulated TiO₂ Nanotubes (PMTiNTs)

Insufficient research has been conducted on the potential of TNA-based nanostructures for photon management. For achieving the maximum light trapping for various applications, we need to manage photon propagation while not negatively affecting electronic transport. In this dissertation, scattering and diffraction gratings have been used in order to increase the optical path length of light [104]. As shown in **Figure 2-10** PMTiNTs structure is a series of horizontal nanotube layers arranged in a vertical stack with a periodic spacing (or alternated with nanotubes with a smaller outer diameter) that function as Bragg interferences mirrors to manipulate photon propagation. The fundamental principles of PMTiNTs' operation are based on Fresnel law where light will be refract or reflect between interfaces with different refractive index.

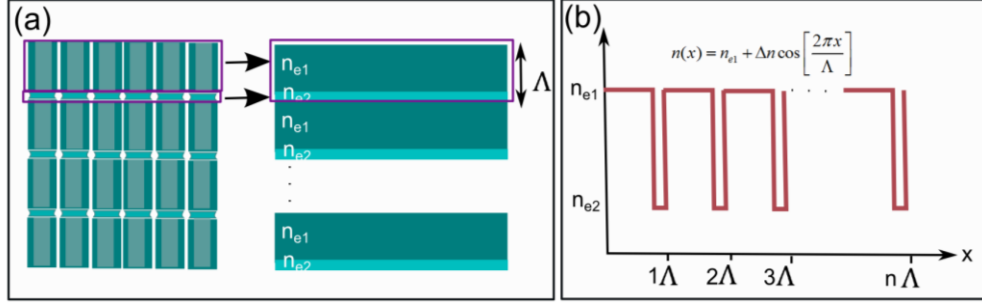


Figure 2-10. a) Schematic of PMTiNTs structure. b) Schematic of refractive index profile in PMTiNTs structure.

By considering the principle of momentum and energy conservation, summation of incident ' k_i ' and grating wavevector ' k ' should be equal to reflected wave ' k_r ', since there can be no change in frequency:

$$k_i + k = k_r \quad (2-8)$$

By considering Bragg condition ($k_i = -k_r$):

$$\frac{2\pi}{\lambda_B} n_{eff} + \frac{2\pi}{\Lambda_B} = -\frac{2\pi}{\lambda_B} n_{eff} \Rightarrow \lambda_B = 2n_{eff}\Lambda_B \quad (2-9)$$

Where λ_B is Bragg wavelength and Λ is spacing between periodic grade and n_{eff} is defined as the effective refractive index. Equation (2-9) is known as the first order Bragg condition. In designing 1D-PBG structure, the first order Bragg condition needs to be met so that the contribution of all the reflected photons add constructively toward the opposite side of light propagation. Notice importantly that the effective refractive index ' n_{eff} ' is related to the porosity ' P ' and can be estimated using the Maxwell Garnett formula [105]:

(2-10)

$$n_{eff}^2 = \epsilon_{eff} = \epsilon_{TiO_2} \frac{2\epsilon_{TiO_2} + \epsilon_{air} + 2P(\epsilon_{air} - \epsilon_{TiO_2})}{2\epsilon_{TiO_2} + \epsilon_{air} - 2P(\epsilon_{air} - \epsilon_{TiO_2})}$$

Where ' ϵ_{eff} ' is effective dielectric constant, ' ϵ_{TiO_2} ' is dielectric constant of TiO₂, ' ϵ_{air} ' is dielectric constant of air, ' n_{eff} ' is effective refractive index, ' n_{TiO_2} ' is refractive index of TiO₂ and ' n_{air} ' is refractive index of air, ' P ' is porosity where describe by following equation [106]:

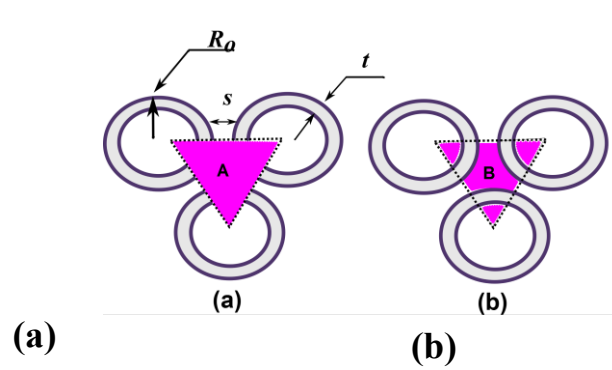


Figure 2-11. The unit cell consists of three hollow nanotubes with radius R_0 , wall-thickness t and inter-tube spacing s .

$$P = \frac{Area(B)}{Area(A)} = \frac{\frac{\pi}{2}[(R_0 - t)^2] + \frac{\sqrt{3}}{4}(2R_0 + s)^2 - \frac{\pi}{2}(R_0)^2}{\frac{\sqrt{3}}{4}(2R_0 + s)^2}$$

$$P = \frac{\frac{\pi}{2}[R_0^2 - 2tR_0 + t^2 - R_0^2] + \frac{\sqrt{3}}{4}(2R_0 + s)^2}{\frac{\sqrt{3}}{4}(2R_0 + s)^2}$$

(2-11)

$$P = 1 + \frac{2\pi t [t - 2R_0]}{\sqrt{3} (s + 2R_0)^2}$$

Where ' R_0 ' is outer radius ' t ' is wall thickness and ' s ' is inter-tube spacing. In this study, an equilateral triangle lattice has been used for theoretical analysis of

porosity ' P ' (**Figure 2-11**). To quantify the porosity parameter ' P ' has been calculated by using equation (2-11) and the value of outer diameter ' R_o ', wall thickness ' t ' and inter-tube spacing ' s ' were extracted using scanning electron microscopy. As depicted in **Figure 2-12**, the effective refractive index of TNAs with respect to wavelength and porosity has been calculated by applying equations (2-10) and **Error! Reference source not found.**

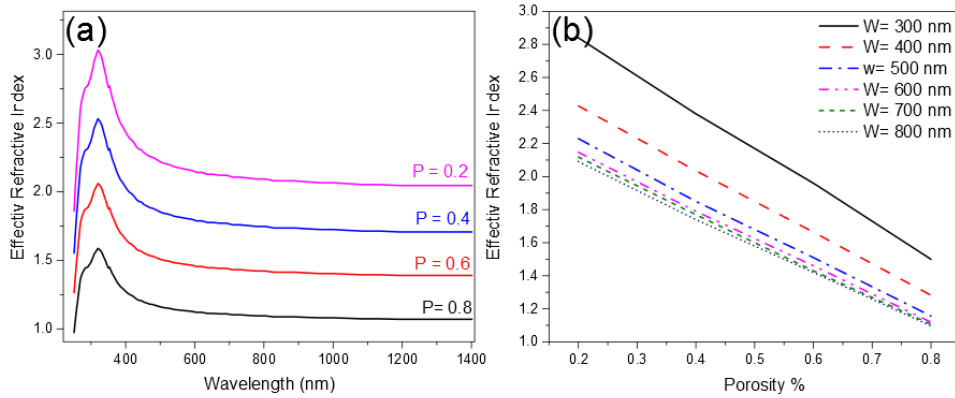


Figure 2-12. Effective refractive index (a) versus wavelength (b) versus porosity.

By calculating the effective refractive index for each layer, PMTiNTs can be considered as alternating layers of transparent materials with two different refractive indices as shown in **Figure 2-10**. Follow up Equation (2-9) the first order Bragg condition can be described by following equation:

$$\lambda_B = 2[n_{eff1}d_1 + n_{eff2}d_2]; \Lambda_B = d_1 + d_2 \quad (2-12)$$

And width ' W ' of the PBG defined by following question [39]:

(2-13)

$$W = \frac{4}{\pi} \lambda_B \left[\frac{1 - \frac{n_{1eff}}{n_{2eff}}}{1 + \frac{n_{1eff}}{n_{2eff}}} \right]$$

where ' n_{1eff} ' and ' n_{2eff} ' are effective refractive index of notches and nanotubes layer, respectively. ' n_{1eff} ' and ' n_{2eff} ' can be calculated by equations (2-10), **Error! Reference source not found.) Error! Reference source not found.) and Error! Reference source not found.)**.

2.4.1 Experimental Details

2.4.1.1 Synthesis of PMTiNTs

Pulse generated modulations have been used for growing PMTiNTs. Since the function of PMTiNTs is based on Bragg interference mirrors, the growth process is very sensitive to local surface inhomogeneities. Using chemical polishing or electrochemical polishing results in specularly reflecting Ti substrates. In this study, in order to eliminate effect of local substrate morphology, Ti substrate was chemically polished in hydrofluoric acid (HF), nitric acid (HNO₃), and glacial acetic acid with the ratio of (3:1:1) respectively, followed by ultrasonic cleaning in methanol for 10 min. Then the anodization process was conducted in a two-electrode cell with 3±0.1 cm inter-electrode separation at room temperature using solutions which consist of a mixture of 1-5% DI water, 0.1 wt %–0.4 wt % NH₄F and ethylene glycol. These unique structures formed by a sequence of current pulses 20 seconds in duration (sequence times were varied from 5 to 20 seconds in order to control the refractive index of each layer). The anode and cathode in two-electrode cell act as a capacitor plate that will be charged for 20 sec and discharges during zero cycles, and this process will be repeated in each cycle.

During the zero cycle the gradient in concentration of negatively charged ions (OH^- and F^-) are higher than the bulk electrolyte, due to limited diffusion, mass transport anodization voltage does not drop speedily and end up continuing the field-assisted processes to form the notches. Using viscous electrolyte can play an important role in controlling the mass transport. As depicted in **Figure 2-13**, the best result was observed in a specimen anodized at 120 mA, with 20 second alternating cycles (2% DI water, 0.2 wt% NH_4F). As shown in **Figure 2-13d** we observed slightly shifted different diffuse reflection patterns at different sample spots. One of the main sources of non-uniformity can be effect of local substrate morphology of the polished Ti substrate and a second source can be the wall thickness variation along the nanotube length due to chemical etching gradients.

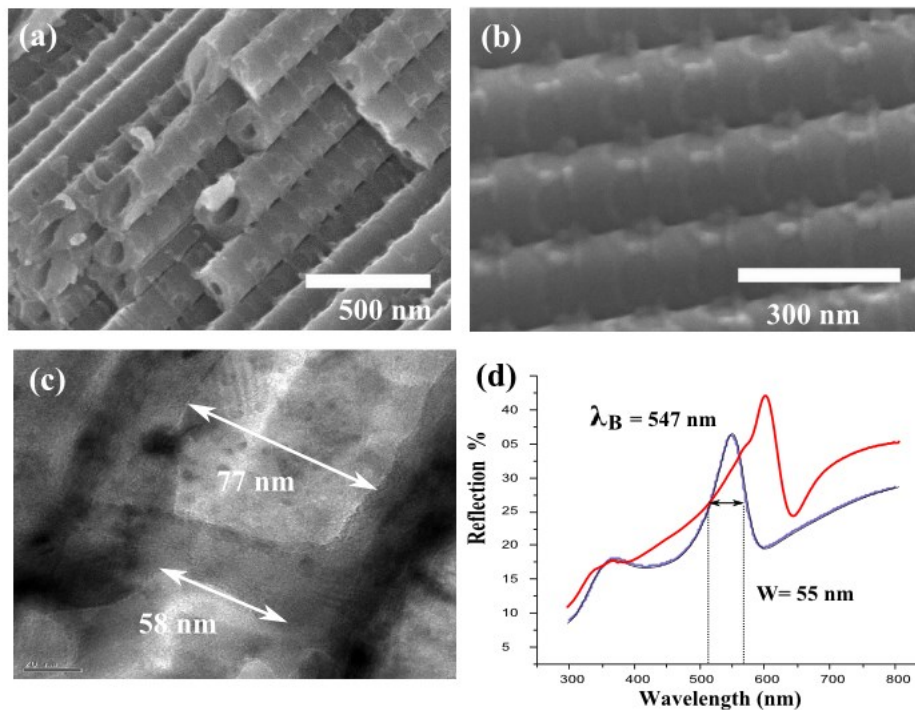


Figure 2-13. a,b) cross sectional SEM images of PMTiNT anodized at 120 mA, with 20 seconds cycles (2% DI water, 0.2 wt% NH_4F) with $3 \pm 0.1 \text{ cm}$ inter-electrode separation. c) HTEM imaged of notches c) diffuse reflection data (blue line was the most dominant peak- Specimen#1).

As depicted in the literature, it is very common for the nanotube wall thickness to vary along the length due to a higher etching rate near the mouth of the nanotubes at the top surface. As shown in **Figure 2-13a** we achieved PMTiNTs with a thick wall in the middle of the nanotubes and a much thinner wall at the top surface of the samples (opening or mouth of the nanotubes as shown in **Figure 2-14(1)**). Non-uniformity in the electric field during anodization can cause formation of non-homogeneous surface. In order to overcome this issue, we covered the back side of the anode and cathode and optimized the process of chemical polishing by using less HF (HF(1),HNO₃(2), glacial acetic acid (1)). On the other hand one of the main contributions of the current density of ions is related to Joule heating that will affect both the wall thickness and the barrier layer thickness.

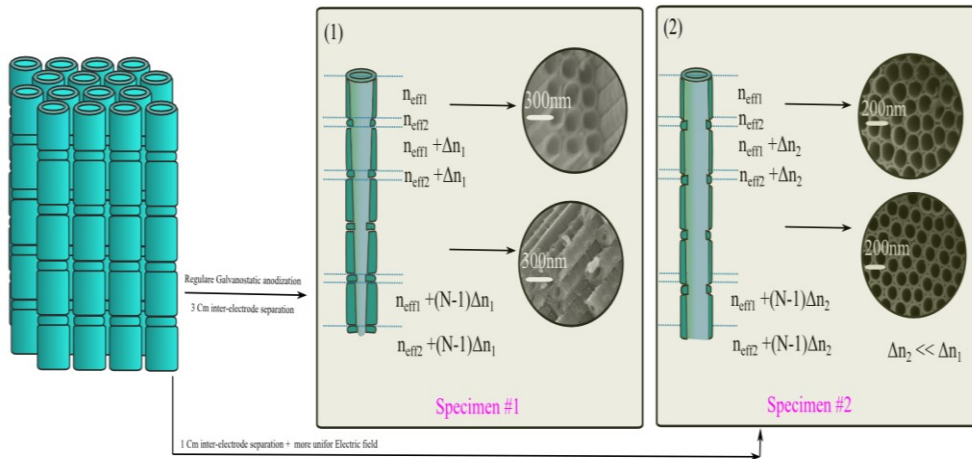


Figure 2-14. Schematic of wall thickness along the length of the TNAs by controlling etching rate. SEM images in (1) correspond to specimen#1 and (2) correspond to the specimen#2 with more uniform electric field

As a second part of this project, a 1 ± 0.1 cm inter-electrode separation (distance between anode and cathode) was used. Joule heating is proportional to $\sim J^2 t$ where J is current density and t is time. Hence by using a higher current

density, the effect of time can be made negligible and we expect to achieve nanotubes with a uniformly thinner wall thickness and a higher etching rate in notch regions (as depicted in **Figure 2-14(2)** thinner and more controllable wall thickness has been observed along the length of TNAs).

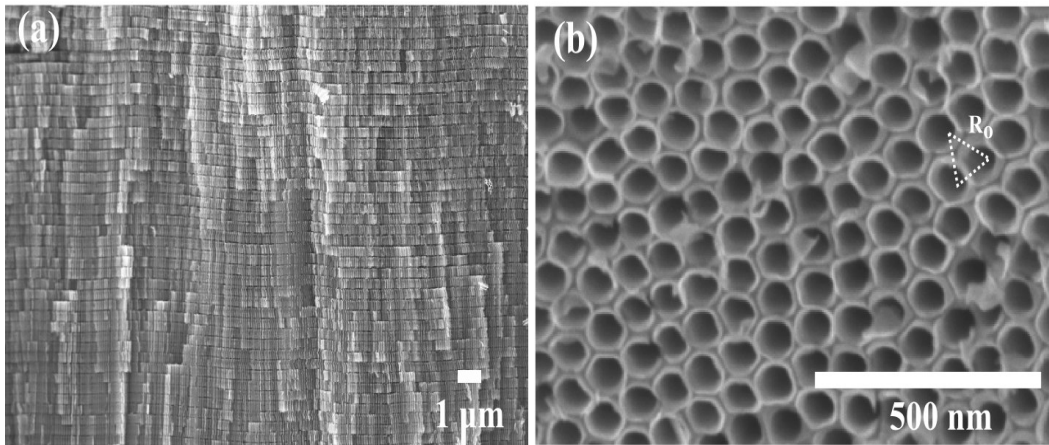


Figure 2-15. 1 a) cross sectional SEM images of PMTiNT anodized at 120 mA, with 20 seconds cycles (1 ± 0.1 cm setup), b) top view SEM images with thin wall.

By using equations (2-10), (2-11), (2-12) and (2-13), effective refractive index, porosity, Bragg wavelength and FWHM of stop-band have been calculated as shown in Error! Not a valid bookmark self-reference.. In the following calculation, the dimensions of nanotubes have been measured in TEM. Based on the results that have been reported in Error! Not a valid bookmark self-reference., theory and experimental result are in close agreement. The experimental results that have been reported in Error! Not a valid bookmark self-reference. are extracted from **Figure 2-16**.

Table 2-1. Comparing the experimental and theory for Bragg reflection wavelength and FWHM. $\lambda_{B(EX)}$ and $\lambda_{B(TH)}$ represent, Bragg reflection data from experimental data and theoretically calculated data respectively. $FWHM_{(EX)}$ and $FWHM_{(TH)}$ represent, full width half maximum of stop-band from experimental data and theoretically calculated data respectively.

	$\lambda_{B(EX)}$ (nm)	$\lambda_{B(TH)}$ (nm)	$FWHM_{(EX)}$ (nm)	$FWHM_{(TH)}$ (nm)
Ref [41]	657 _[41]	_____	92 _[41]	_____
Ref [41]	500 _[41]	_____	103 _[41]	_____
Ref [41]	439 _[41]	_____	102 _[41]	_____
Specimen#1	547	538	55	33
Specimen#2	403	400.9	78	68

In conclusion, by using Maxwell Garnett and Bragg condition, it is shown that we achieved highly uniform PMTiNTs with fewer defects. Our results indicate that we achieved lower FWHM in designed stop-band comparable with theory. We achieved 50% reduction in the spectral linewidth of bottom-up fabricated PMTiNT 1D photonic crystals in comparison with the literature (**Figure 2-16c**). In this dissertation PMTiNTs are produced by a programmed sequence of pulse anodization of chemically polished titanium sheets, where the pulse duration and distance between anode and cathode define the length of the nanotubes and notches. It worth mentioning here that no changes were observed in the length of the notches in the 3 ± 0.1 cm setup by changing the zero stage duration.

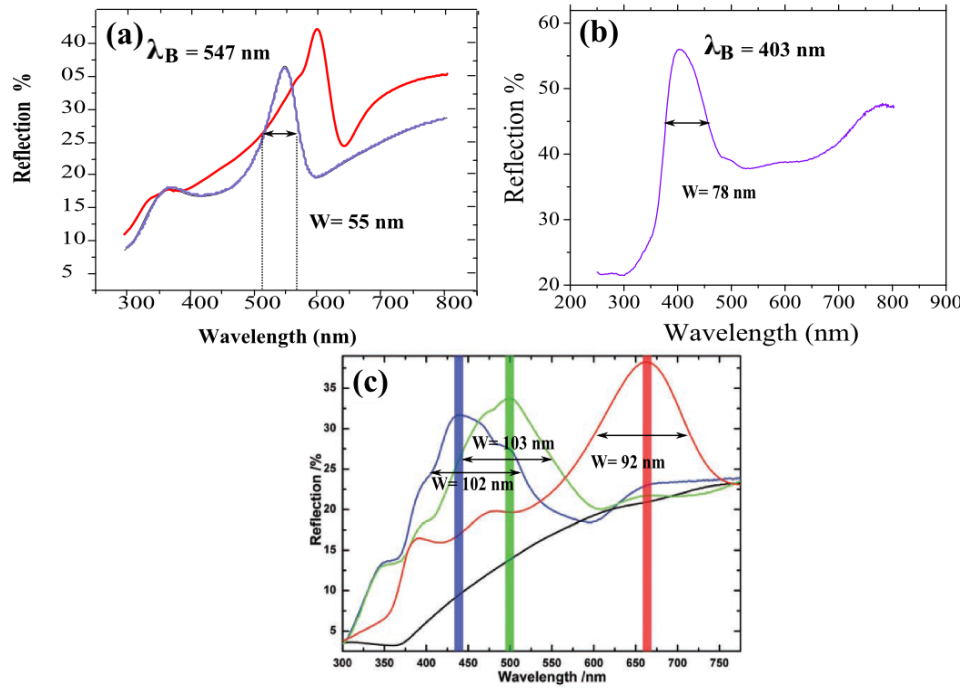


Figure 2-16. a) diffuse reflection data from specimen#1 b) diffuse reflection data from specimen#2 c) diffuse reflection data (blue line was the most dominant peak-Specimen#1) e) diffuse reflection data adopted with permission from Jua Lin et al. , Small, 2011. 7(13): p. 1784-1789 © 2011 WILEY-VCH Verlag GmbH & Co. KGaA, Weinheim

Chapter 3

TNAs on Non-Native Substrates

3.1 Overview

The formation of anodic TNAs on non-native substrates requires the vacuum deposition of a thin film of titanium on the substrate followed by subsequent electrochemical anodization of the film. In this chapter, we study the physics of formation of Ti thin films on technologically important non-native substrates. The influence of the substrate and Ti film deposition process are still not completely understood. We compared the structure and morphology of evaporated and sputtered Ti films, and correlated them to the morphology of the vertically oriented TiO₂ nanostructures that resulted subsequent to anodization of those films. Previous approaches relied on substrate heating to elevated temperatures during Ti thin film deposition at 7 mTorr or ion-beam assisted Ti thin film deposition as a prerequisite to form TNAs.

In the range of 1-10 mTorr we expect to get stable plasma given the size of our sputtering chamber. In the literature, plasma at 4-7 mTorr is used most frequently to sputter Ti thin films for TiO₂ nanotube formation. In this study we

demonstrate TNAs on silicon, glass, stainless steel, fluorine doped tin oxide coated glass (FTO), polyimide and indium tin oxide coated polyimide substrates at room temperature at 1 mTorr using sputtered Ti films, and also using electron-beam evaporated films without recourse to ion-beam sources.

3.2 Surface Morphology of Titanium Thin Films

Surface diffusion, self-diffusion and the level of stress in the thin film are the main parameters that must be optimized in order to achieve smooth films over large areas and good adhesion to the substrate during thin film deposition. These three processes are defined by deposition conditions as well as the nature of the film and substrate material. Surface diffusion in a sputtering process is controlled by the angle of the gun, substrate temperature, burial rate and deposition pressure. When atoms ejected from the target reach the surface of the substrate at normal incidence, they lose their energy in the ns timeframe via Lennard-Jones interactions.⁶ On the other hand, ejected atoms incident on the substrate at oblique angles conserve parallel momentum [60, 107], and therefore the angle of the sputter gun plays an important role in surface diffusion. In this work, the magnetron sputter gun was directed at the substrate at an angle of 10.2° from the substrate normal.

Surface diffusion and self-diffusion during film growth are key parameters that control the morphology, crystallographic orientation and surface roughness of the final thin films. If adatoms and adparticles possess the necessary energy to move on the substrate surface and rearrange themselves, a minimized surface tension

⁶ Lennard-Jones potential: mathematical model for approximating the potential between pair of neutral atoms.

results and the tendency toward three-dimensional columnar growth is constrained. Ti films follow the Stranski-Krastanow growth mode and there is strong bonding between the film and substrate. At high temperatures, adatoms and adsorbate species have high mobility and the probability of diffusion will be increased [107] due to which film roughness is decreased. Studies conducted by K. Kalantar-Zadeh and colleagues [62] and Mor et al and Paulose et al [60, 108] required thermally activated growth during Ti deposition of around 500°C in order to achieve TNAs using Ti films deposited by magnetron sputtering. On the other hand, since the activation energy for surface diffusion varies between different substrates (E_s), applicable temperatures also vary. In other words, some materials are not able to support the surface stress applied during deposition at high temperature. Hence application of this method will be limited by this phenomenon for some substrates, such as Kapton[®]. The surface diffusion length is given by:

$$\Lambda = \frac{1}{2} \sqrt{\frac{a^3 \omega}{r_d} \exp\left(\frac{-E_h}{kT_f}\right)} \quad (3-1)$$

where ' a_d ' is the average distance between adatoms (approximated by the lattice constant of Ti that is equal to 0.2951 nm at 298 K), [109] ' r_d ' is the deposition rate, ' ω ' is the lattice vibration frequency, ' E_h ' is the energy for self-diffusion, k is the Boltzmann constant and T_f is the temperature of the film. From the enthalpy of vaporization of Ti at room temperature (7.097×10^{-19} J/atom), ' E_h ' is estimated to be 0.88 eV. The vibrational frequency (kT_f/h) is taken to be 0.63×10^{13} s⁻¹.

The burial rate is controlled by changing the pressure inside the chamber⁷ and applied DC power (sputter rate):

$$\theta = \theta_0 \left\{ 1 - \exp \left[-K_{dep} (1 + KP)t \right] \right\} \quad K = \frac{k_{ads}}{k_{des}} \quad (3-2)$$

Where θ is surface coverage percentage, θ_0 is the equilibrium coverage, K_{ads} is adsorption rate, K_{des} is desorption rate, t is time and P is pressure. If we assume that K_{ads} and K_{des} are constant while decreasing the pressure, it takes more time to reach the maximum surface coverage and it means that at low pressure, burial rate will be decreased. By changing the sputtering rate, deposition pressure [110], and incident angle of adatoms on the substrate, we have achieved control over the burial rate and the diffusion length and therefore surface tension.

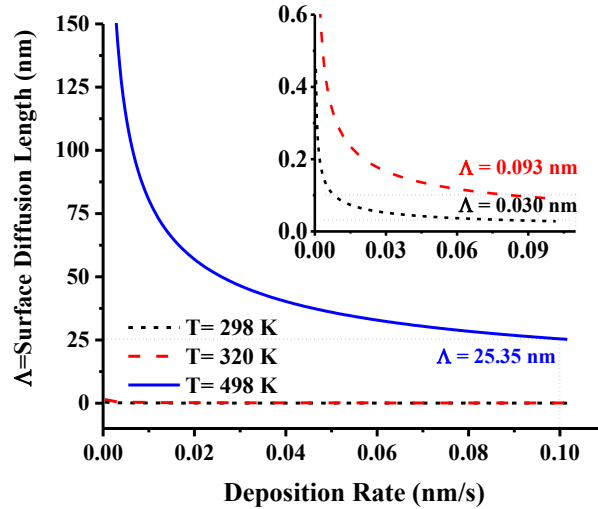


Figure 3-1. Surface diffusion length versus deposition rate at 298, 320 and 498 K.

⁷ http://users.wfu.edu/ucerkb/Nan242/L11-Thin_Film_Growth.pdf

As depicted in **Figure 3-1** for transition between various thin film growth modes, it is not only the surface diffusion length that is key but the burial rate plays an important role as well. It is worth mentioning here that the substrate surface charge cannot have an effect on the quality of the Titanium film in our case since the sample holder (anode) is grounded and will be discharged during the deposition process. For studying the effect of pressure and sputtering rate, the following experiments have been conducted. 500 nm and 2 μm of Ti were each sputtered on to various substrates at 20 mTorr, 7 mTorr and 1 mTorr at room temperature. As expected, we observed a very rough surface at 20 mTorr and 7 mTorr (**Figure 3-2a**) and (**Figure 3-3a.**), a smooth surface at 1 mTorr (**Figure 3-2b**) and (**Figure 3-3d.**)

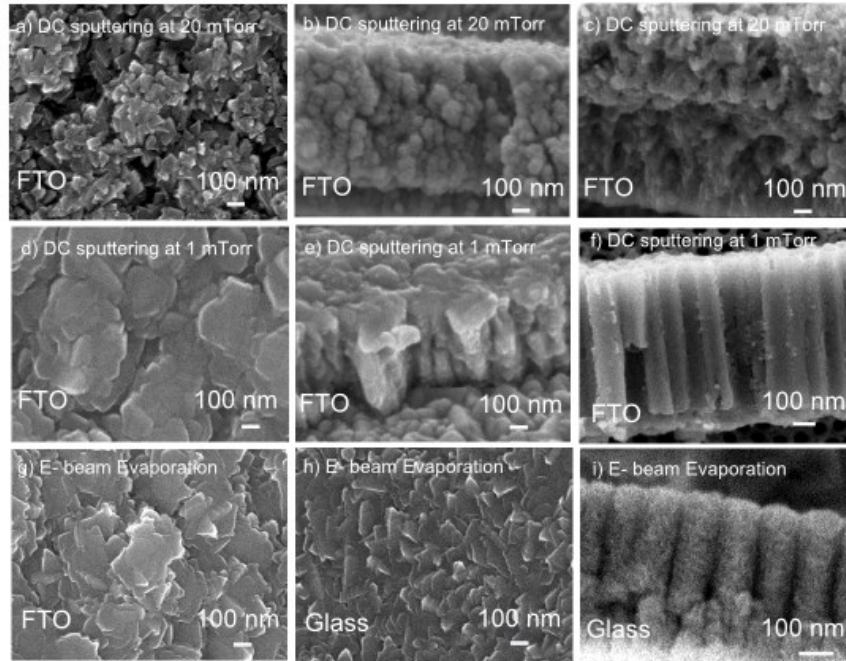


Figure 3-2. Morphology of 500 nm-thick titanium films deposited at room temperature on FTO-coated glass using DC sputtering with a deposition rate of 0.093 nm s^{-1} at (a) 20 mTorr, top view (b) 20 mTorr, cross section (c) 20 mTorr, top view after anodization (d) 1 mTorr, top view (e) 1 mTorr, (f) 1 mTorr, cross section after anodization. Morphology of 500nm of titanium deposited using Electron beam evaporation with a deposition rate of 0.17 nm s^{-1} on (e) FTO (f) glass (g) after anodization.

When Ti atoms are ejected from the target at low pressures, adatoms on the surface of the growing Ti film have larger diffusion lengths due to atomic peening from energetic neutrals (Ar^+ ions neutralized at the cathode and reflected from the same) as well as because the sputtered Ti atoms are less slowed down by collisions due to their longer mean free paths. This means that adatoms at the surface of the substrate have a higher kinetic energy (at 1mTorr the kinetic energy is ~ 415 eV and at 20 mTorr it is ~ 289 eV). The main concern with room temperature deposition is film delamination due to poor adhesion and high local surface roughness due to small columnar grain growth based on studies conducted by Kalantar-Zadeh et al [62] and Grimes et al [60, 108]. In the study by us, both DC sputtering and electron beam evaporation at room temperature as well as at 250°C were found to have a good adhesion at 1 mTorr, but not at 20 mTorr.

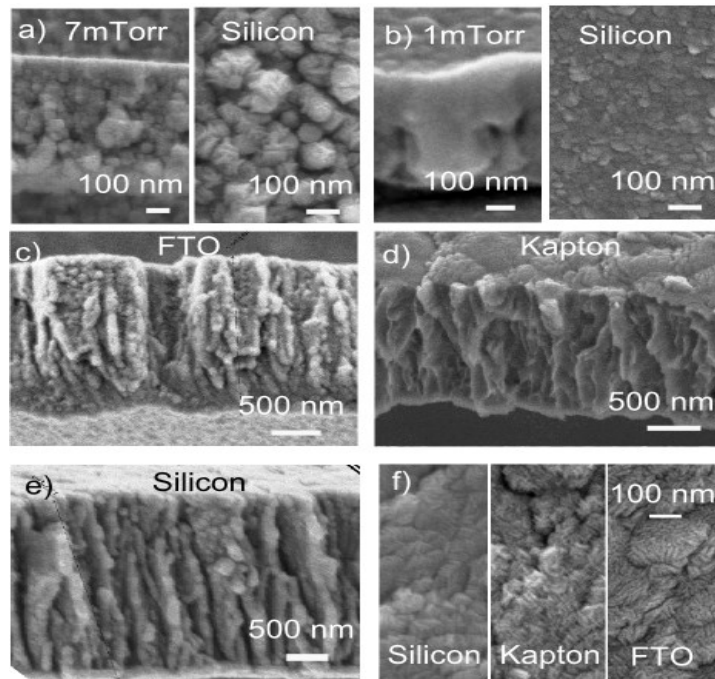


Figure 3-3. Side view and top view of 500nm Ti film on silicon (a) at 7 mTorr (b) at 1mTorr. Side view of $2\ \mu\text{m}$ ($0.1175\ \text{nm s}^{-1}$) titanium deposited at 1 mTorr (c) on FTO (d) Kapton (e) Silicon (e) top view of titanium on Silicon, Kapton and FTO substrates.

At low pressures the films were so well-adhered that when immersed in an electrolyte they did not delaminate, even for room temperature deposited samples. In other works reported so far, the adhesion of deposited titanium thin films was improved at high temperatures, whereas in our work the 1 mTorr sample had a well-adhered thin film at room temperature due to higher kinetic energy of adatoms during deposition. As indicated in **Figure 3-2** and **Figure 3-3**, 500 nm and 2 μm titanium films were sputtered on different substrates. The physical properties of the thin film are influenced not only by the deposition pressures but also the sputtering rates. To test the influence of FTO roughness, 500 nm of titanium was sputtered on glass and FTO substrates at 1 mTorr with a sputtering rate of 0.1175 nm s^{-1} . Based on AFM data the root mean squared (rms) roughness of the Ti thin film on glass was 5.11 nm and the roughness of the Ti thin film on FTO was around 10.3 nm, as shown in **Figure 3-4a** and **Figure 3-4b**.

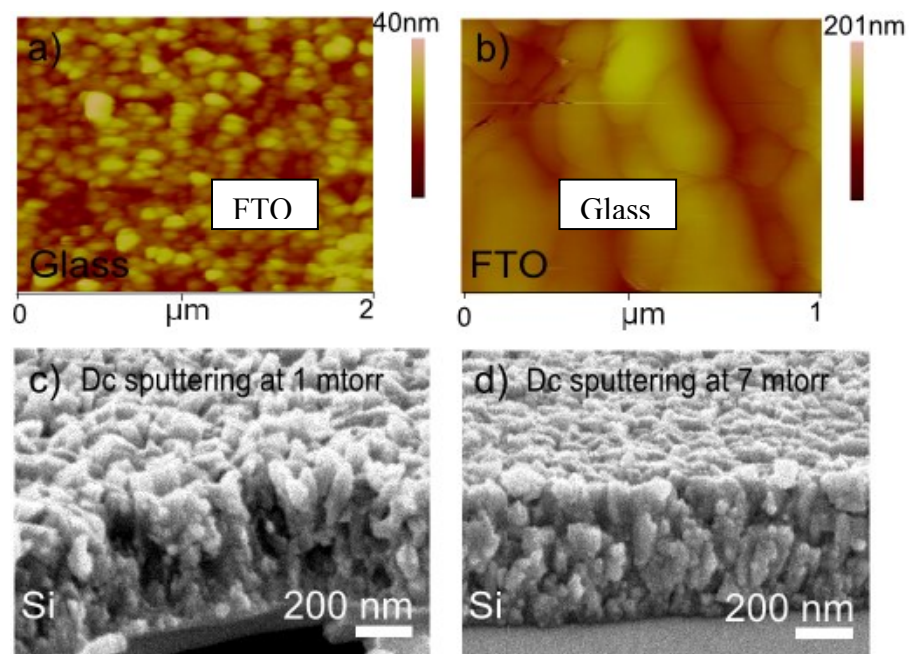


Figure 3-4. AFM data for 500 nm (0.1175 nm s^{-1}) titanium deposited on at 1 mTorr (a) on FTO with 10.49 nm rms (b) Glass with 5.1 nm rms. 0.1175 nm s^{-1} titanium deposited on silicon at (c) 1 mTorr (d) 7 mTorr.

As shown in **Figure 3-5**, the sputtering rate is a key factor in order to get a 2D-hillock in the S-K model. When 0.23 nm s^{-1} and 0.1175 nm s^{-1} of Ti were sputtered onto silicon at 1 mTorr and 7 mTorr (**Figure 3-4c** and **Figure 3-4d**), the samples sputtered at 0.23 nm s^{-1} displayed a 3D-hillock which after anodization resulted in some porosity; however no nanotubes were observed. Using low pressures during sputtering does not necessarily ensure a smooth film. As shown in **Figure 3-5a**, if a high sputtering rate is used, fast diffusing adatoms on the surface will still be buried under the newly deposited adatoms—and will limit the hopping distance. The time required for the growth of one atomic layer is given by [111]:

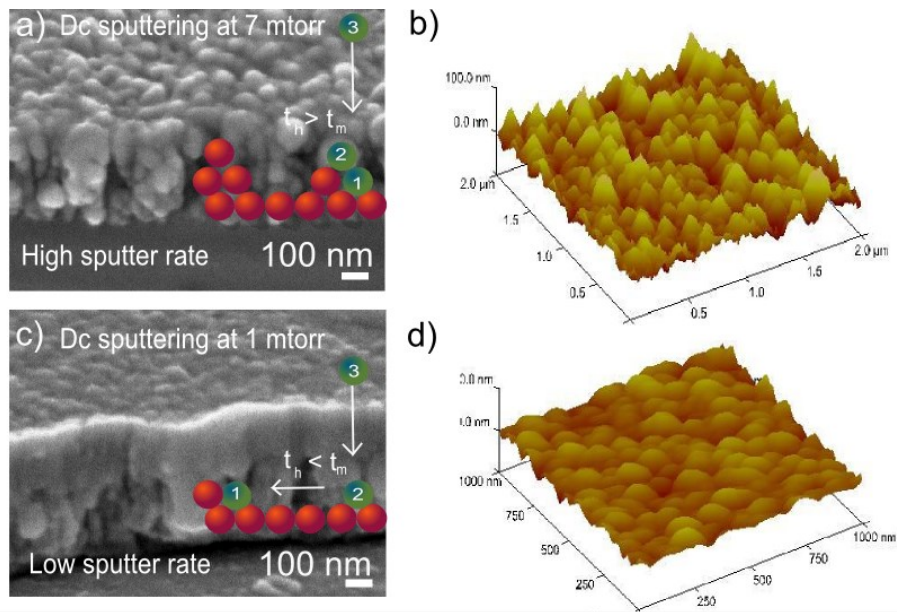


Figure 3-5. SEM of 0.23 nm s^{-1} titanium deposited on silicon (a) 7mTorr (c) 1mTorr. AFM 0.23 nm s^{-1} titanium deposited on silicon at (b)7 mTorr, with the roughness of around 17.5 nm (d) 1 mTorr, with the roughness of around 5.5 nm

(3-3)

$$\tau_m = \frac{a_d}{r}$$

where a_d is the average distance between adatoms (approximated by the lattice constant of Ti that is equal to 0.29511 nm for a temperature of 25 °C [112]) and r is the sputtering rate. When the sputtering rate is around 0.23 nm s⁻¹ and 0.1175 nm s⁻¹, the time required for the corresponding growth of one atomic layer are 1.28 s and 2.5 s respectively. Each adatom needs τ_h seconds to diffuse. Only if τ_h is smaller than τ_m will the adatoms get a chance to diffuse, otherwise they will be buried under the newly arriving adatoms and the probability of diffusion will be decreased [111]:

$$P_e \sim \exp\left(-\frac{[E_a - E_i(T)]}{K_B T}\right) = \exp\left(-\frac{N[E_a - E_i(T)]}{PV}\right) \quad (3-4)$$

where P_e is the probability of diffusion. According to equation (3-4), and the ideal gas law, the probability of diffusion varies with temperature, pressure and relation between E_a and E_i . When we are working at higher chamber pressures (pressures in the range of 20 mTorr to 7 mTorr), $E_a - E_i$ is larger than zero hence the probability of diffusion by increasing the temperature will also increase, but when we are working at low pressures due to the atomic peening and reflected and neutralized Ar⁺ (less than 2 mTorr) $E_a - E_i$ is smaller than zero; hence by decreasing the pressure, adatom surface diffusion length will be increased. In the other words, using high temperatures has the same effect on the quality of the sputtered thin films as ambient temperatures at low pressures. At lower chamber pressure, τ_h increases and consequently adatoms have more time to diffuse; if the diffusion length is high enough thin film growth results in a relatively smooth surface. The surface diffusion length is defined by equation (3-5):

(3-5)

$$\Lambda = a \sqrt{\frac{\left[\frac{K_B T}{h} \right] n_0}{r}} \exp\left(-\frac{[E_a - E_i(T)]}{2RT} \right)$$

As shown in **Figure 3-6(a-d)**, deposition at room temperature at 1 mTorr gives us a closely packed granular structure with deposition rates of 0.093 nm s^{-1} and 0.0465 nm s^{-1} . As expected, with a deposition rate of 0.0465 nm s^{-1} , the film is smoother. Based on the AFM data (**Figure 3-6a**, **Figure 3-6b**) the sample with the deposition rate of 0.0465 nm s^{-1} is much smoother when compared to the sample with a deposition rate of 0.093 nm s^{-1} .

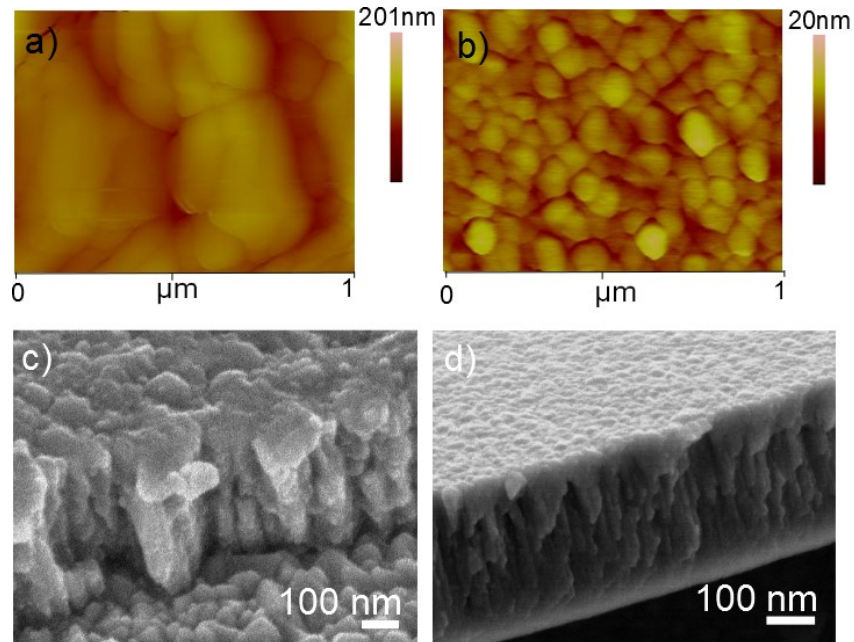


Figure 3-6. AFM of 500 nm titanium with a deposition rate of (c) 0.093 nm s^{-1} and (d) 0.0465 nm s^{-1} , on FTO Morphology of 500 nm titanium with a deposition rate of (c) 0.093 nm s^{-1} and (d) 0.0465 nm s^{-1} on FTO.

3.3 Surface Morphology of TNAs on Non-native Substrates

Several specific applications for titania nanotube arrays rely on the propagation of light through the nanotubes. In this regard, native titanium metal foils, which

are the most commonly used substrate for the growth of TNAs are severely limiting due to their non-transparency. For instance, backside illumination is inefficient in TNAs based dye-sensitized (bulk heterojunction) solar cells due to optical absorption losses through the counter-electrode (anode) and redox electrolyte (hole transporter). Front side illumination uses light more efficiently and requires TNAs on a transparent substrate. For the first time in 2002, TNAs were grown on non-native and conductive substrates by using aluminum anodization to form a nanoporous alumina template followed by a sol-gel process to form TiO₂ [115]. In 2003, TNAs on non-native substrates were used as gas sensors, photocatalysts and in solar cells where efficiency of ~5% was reported [5, 55, 116]. In 2006, the nanoporous titania on silicon was reported by Kalantar Zadeh et al [56] and in 2006, polydisperse nanotubes on silicon substrate were reported [52].

3.3.1 TNAs on Flexible Substrate

For low-cost applications in sensing and organic electronics, flexible polymeric substrates are highly desirable; among plastics, polyimide substrates (e.g. Kapton®) are popular for their relatively high temperature resistance. Previous studies have investigated the effect of process variables that directly affect the quality of the nanotubes formed, namely the substrate temperature during deposition, the stress mismatch of the substrate and Ti films and the film thickness. Based on these studies, current methods for generating highly ordered transparent TNAs with unclogged pores on non-native substrates rely on substrate heating during the vacuum deposition of thin films of titanium, which are subsequently anodized to form TNAs [12].

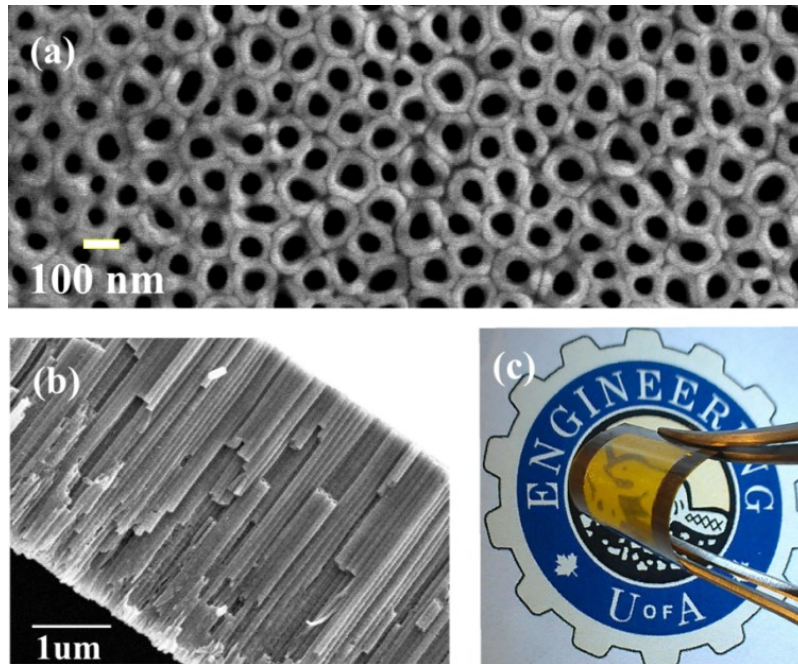


Figure 3-7. (a) Top-view and (b) cross-section of 5.1 μm TNAs on 50 μm thick Kapton[®] substrate, and (c) flexible and transparent TNAs on Kapton[®] substrate.

The use of substrate heating in these reports to temperatures of 300 °C - 500°C precludes the use of flexible polymeric substrates. **Figure 3-7** shows self-organized TNAs with open pores on bendable Kapton films, obtained by anodizing Ti films deposited by direct current magnetron sputtering at room temperature. The nanotubes are ordered and similar in quality to nanotubes obtained on Ti foil substrates.

Using Auger electron spectroscopy and other techniques, the Ti film growth mode on a variety of surfaces including polyimide, single-crystal silicon, tungsten, etc has been determined to be of the Stranski-Krastanov type consisting of the formation of a complete first monolayer of Ti atoms is followed by the growth of three-dimensional islands [13]. The low adatom mobility of Ti atoms on oxygen-terminated surfaces such as glass and tin oxide derivatives as well as

on carbonyl group-terminated surfaces such as polyimide limits the surface diffusion of Ti atoms in the growing Ti film. The resulting columnar growth consists of grain growth primarily in the direction perpendicular to the substrate with a much smaller increase in lateral dimensions of the grains. Columnar growth is also characterized by the build-up of only tensile stress which increases with film thickness and results in the adhesion problems noted by several researchers, particularly for thick Ti films. Substrate heating provides more adatom mobility to Ti atoms and allows for the formation of platelets and better filling of the inter-island spaces. In a series of studies, Kalantar-Zadeh et al [14] have clearly shown using deposition pressures of 20 mTorr and radio-frequency sputtering, that Ti films deposited at high temperatures form ordered flatter hexagonal grains conducive to uniform pitting during the early stages of the anodization process to form TNAs while Ti films deposited at room temperature form columnar grains that nucleate pits inhomogeneously and with random orientations, and are furthermore subject to lateral etching at the grain boundaries during anodization. Films deposited at room temperature were also found to have poor adhesion and delaminated soon after immersion in the anodization electrolyte. [12].

To obtain Ti films with a uniform morphology and good adhesion, we used low-pressure DC magnetron sputtering of titanium in argon ambient on to substrates held at room temperature. **Figure 3-8** shows the morphologies of 500 nm-thick Ti films deposited at room temperature on Kapton by direct current magnetron sputtering at two different argon pressures, 7 mtorr and 1 mtorr. The films deposited at 7 mtorr possess high porosity and surface roughness due to the growth of large columnar three-dimensional grains. The films deposited at 1 mTorr, on the other hand, are relatively smooth and uniform due to the positive

effect of atomic peening. At low deposition pressures, the Ti atoms ejected from the target have longer mean free paths and arrive at the substrate with greater kinetic energy. Simultaneously, Ar^+ ions are neutralized at the cathode and reflected from it. The reflected neutrals collide more frequently with the substrate. Both processes increase adatom mobility in the growing film and simulate the effect of substrate heating, while also improving intermixing between the uppermost atomic layers of the substrate and the first few atomic layers of the growing film, thus inducing superior adhesion.

Atomic peening also densifies the films by packing them more closely into the film and by forcing atoms into tiny, hard to reach spaces, a process otherwise impossible under conditions of thermal equilibrium.[15] The microstructure and compactness of the Ti film improves due to the energetic ion bombardment and the pressure of the ambient gas normal to the film surface. Consequently, the void portion is decreased and the resulting films are more uniform as in **Figure 3-8b**. During electrochemical anodization of the vacuum deposited metal film, the interplay between the three competing processes of field-assisted oxidation of the Ti, field assisted dissolution of the oxide and chemical dissolution of the oxide, determines the evolution of the morphology and the formation of TNAs.

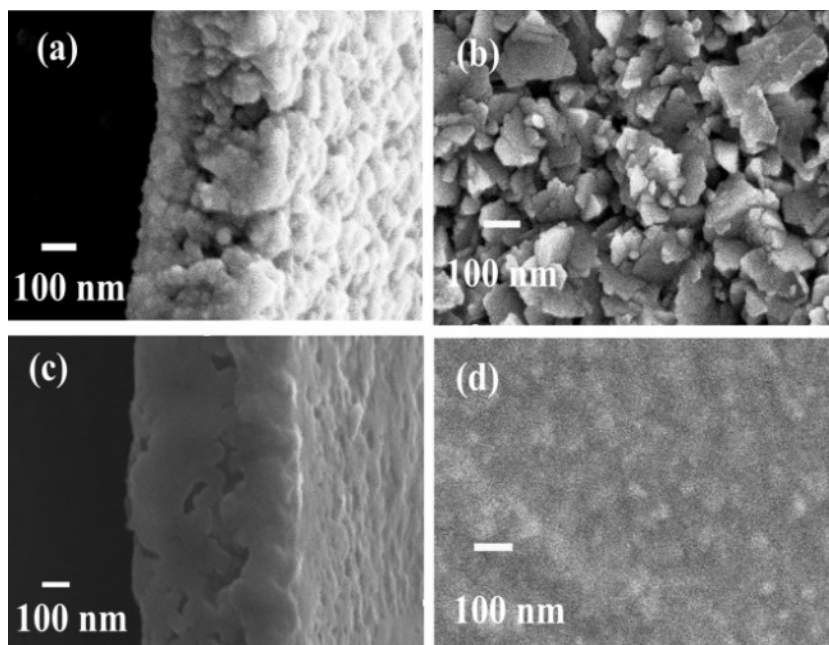


Figure 3-8. (a), (b) Top-view and cross-section respectively of a 500 nm thick film of Ti sputtered on to Kapton[®] at room temperature and 7 mtorr, and (c), (d) Top-view and (d) cross-section respectively of a 500 nm thick film of Ti sputtered on to Kapton[®] at room temperature and 1 mtorr.

The two field-assisted processes have currents associated with them that are observable in the anodization current transient (**Figure 3-9**) while chemical etching is much weaker and has a relatively minor effect in the organic anodization electrolytes used by us in this work. In **Figure 3-9a**, the sharp decrease in current at the onset of anodization is due to the formation of an insulating barrier layer of TiO₂ by field-assisted oxidation.

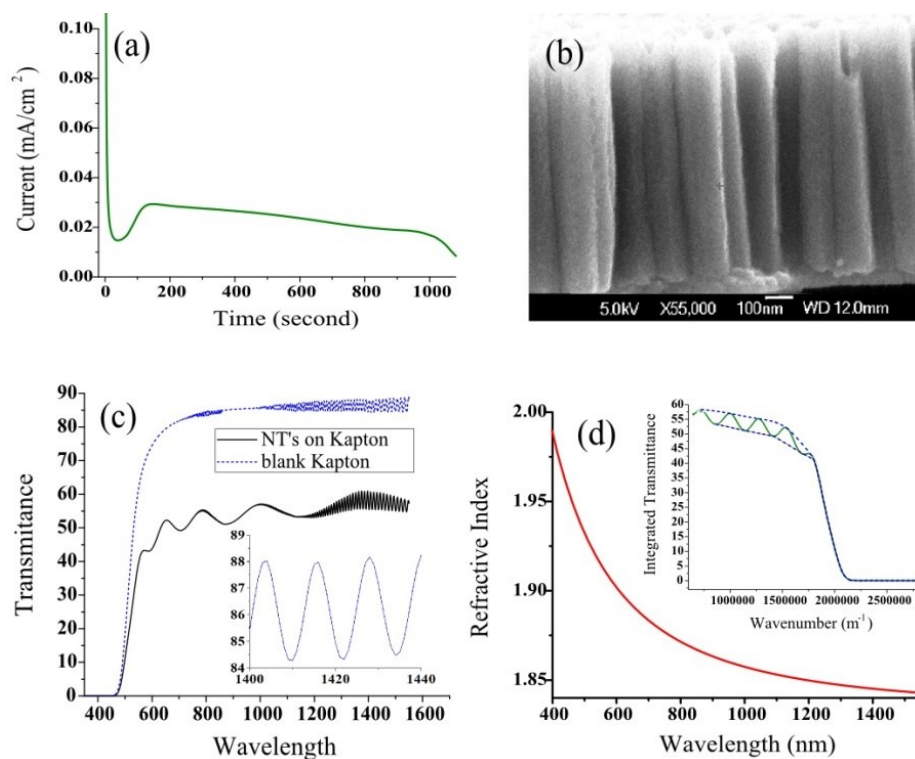


Figure 3-9. A 500 nm Ti film on Kapton was formed by sputtering at 1 mtorr and subjected to electrochemical anodization in a fluoride ion bearing water-ethylene glycol electrolyte to form TNAs. (a) anodization current vs. time (b) cross-sectional FESEM image showing a film thickness (i.e. tube-length) of 870 nm (c) optical transmittance of blank Kapton substrates (blue curve) and TNAs on Kapton (black curve) with the inset showing the Fabry-Perot interference fringes of the blank Kapton substrate in more detail and (d) effective refractive index of the nanotube arrays on Kapton, calculated by applying the envelope to the transmission spectra as shown in the inset.

In films deposited by a peening-assisted process, field-assisted dissolution nucleates uniform pits in the compact insulating oxide causing an increase in the anodization current until a local maximum is reached. Subsequently, the barrier layer thickness increases very slowly as the processes of pore self-organization and propagation occur during a steady decrease of the anodization current with time. In highly porous, non-uniform Ti films consisting of three-dimensional grains, pits oriented in several different directions are nucleated as opposed to only pits orthogonal to the substrate, and therefore interferes with the self-

organization process to yield less ordered poorer quality nanotubes, and in some cases a mere irregular nanoporous structure is obtained. As the anodization process reaches completion (defined by the near complete conversion of the Ti film into a TNAs), the conductive Ti film at the bottom of the nanotube array thins out and the anodization current undergoes a steep decrease due to the concomitant increase in resistance.

For light propagation, the titanium dioxide nanotube array may be modeled as an effective medium consisting of TiO₂ with air inclusions. Due to the difference in optical path length between light reflected at the TNAs barrier layer interface and the TNAs air interface, Fabry-Perot interference fringes are expected in the reflectance and transmission spectra, given by:

$$d = \frac{\lambda_1 \lambda_2}{2(\lambda_1 n_2 - \lambda_2 n_1)} \quad (3-6)$$

where ‘*d*’ is the film thickness and the refractive indices of the film corresponding to adjacent maxima (or minima) at points 1 and 2 are given as ‘*n*₁’ at ‘*λ*₁’ and *n*₂ at ‘*λ*₂’. Non-uniformities in the TNAs film such as high surface roughness or differences in the height of individual nanotubes generate optical scattering, which reduces the distinctness of the fringe pattern. **Figure 3-9c** shows that room-temperature fabricated TNAs show a clear pattern of interference fringes at visible wavelengths, indicating the high quality of the nanotubular film. Due to the small optical thickness of the Kapton substrates (47.5 μm thick), the substrate also produces interference fringes at infrared wavelengths (inset of **Figure 3-9c**) which complicates the analysis of the optical properties of the film. Furthermore, Kapton substrates strongly absorb photons of wavelengths 500 nm and below. We first obtained the wavelength-dependent complex refractive index (*n_s=s-ik_s*) of

the Kapton substrates and then used Manifacier's envelope method, modified by Swanepoel and others to account for optically thin and slightly absorbing substrates.[16] The resulting envelope function with an upper envelope $T_M(\tilde{\nu})$ and a lower envelope $T_m(\tilde{\nu})$ is shown in the inset of **Figure 3-9d** and was used to calculate the effective refractive index $n(\lambda)$ of the nanotube array film in the weak absorption and transparent regions of the transmission spectrum per the relations :

$$n = \sqrt{N + \sqrt{N^2 - s^2}} \quad (3-7)$$

where N is defined by

$$N = 2s \left[\frac{T_M - T_m}{T_M T_m} \right] + \frac{s^2 + 1}{2} \quad (3-8)$$

The calculated values of n were then fit to a Cauchy dispersion model for extrapolation to shorter wavelengths ; these results are shown in **Figure 3-9d**. A film thickness of 940 nm was obtained by application of Eqn. (3-6) , which agrees closely with the 870 nm tube-length estimated from the cross-sectional SEM image of **Figure 3-9b**. Using the morphological parameters of the nanotube arrays estimated from the SEM image, we calculate a purely geometrical fill-fraction of 63.7 % for the TiO_2 phase in the nanotube arrays. For such a two component medium consisting of air and TiO_2 , the effective permittivity is given by the Bruggeman effective medium model :

$$f \frac{\epsilon_{\text{TiO}_2} - \epsilon}{\epsilon_{\text{TiO}_2} + 2\epsilon} + (1-f) \frac{1 - \epsilon}{1 + 2\epsilon} = 0 \quad (3-9)$$

where f is the fill-fraction of TiO_2 and $\epsilon=n^2$ is the effective permittivity of the nanotube array. By substituting the values of the fill-fraction and the calculated effective refractive index of the TNAs shown in **Figure 3-9d**, we obtained a value of 2.4 for the refractive index of the TiO_2 skeleton, which is close to the value for bulk TiO_2 . This indicates that the walls of TNAs on Kapton substrates are highly compact and free of air inclusions [17].

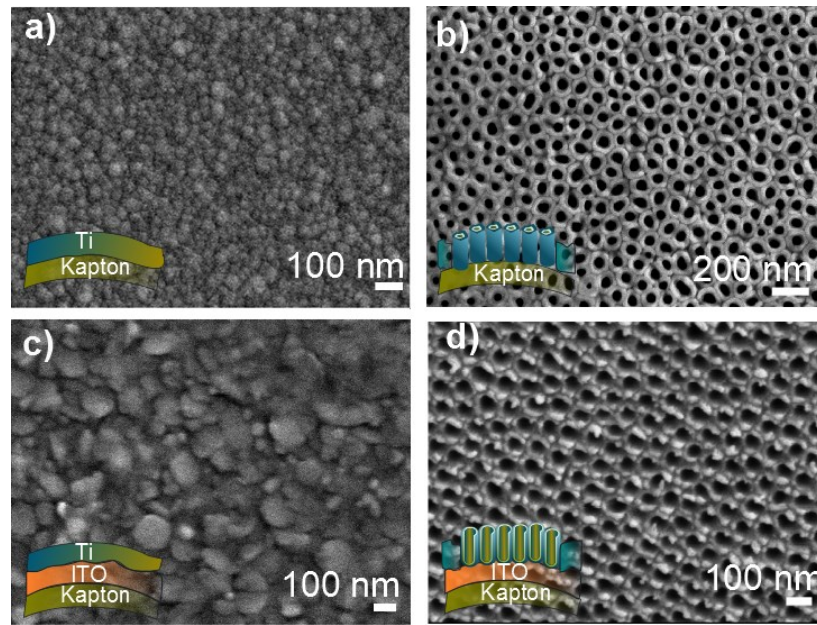


Figure 3-10. FESEM image of (a) 500 nm titanium with a deposition rate of 0.1175 nm s^{-1} on Kapton substrate (b) the investigated TNAs layer on kapton for 4% water at 40 V and $3\pm 0.1 \text{ cm}$ inter-electrode separation setup (c) 116 nm ITO and 500 nm titanium with a deposition rate of 0.1175 nm s^{-1} on Kapton substrate (d) the investigated TNAs layer on top of the ITO thin film for 4% water at 40 V and $3\pm 0.1 \text{ cm}$ inter-electrode separation setup.

To improve the dispersity of nanotubes and study the effect of chemisorption bonding on Kapton[®], 116 nm of ITO was sputtered onto it at 150 °C followed by sputtering of 500 nm of Ti thin film. Due to the stronger chemical interactions between the deposited Ti and the oxygen terminated ITO (in comparison with Ti and Kapton[®]), we expected to reach monodisperse nanotubes on ITO sample

compare to the bare Kapton. As shown in **Figure 3-10a** and **Figure 3-10c**, using ITO grain size was improved and it resulted in the growth of a more monodisperse nanotube array (**Figure 3-10b**, **Figure 3-10d**).

3.3.2 TNAs on FTO, Glass and Silicon

Since the first reports of electrochemically synthesized nanoporous and nanotubular TiO₂ by Zwilling et al [22] and Gong et al [23] respectively, the science and technology surrounding the growth of TNAs has grown enormously. TNAs have been fabricated on a range of non-native substrates including silicon, glass, transparent conducting oxide (TCO)-coated glass, polyimide and stainless steel [59, 60, 117-121]. Nanotube diameter is tuneable from 10 nm to 1 μm. Tube length, which was initially limited to a few hundred nanometers, now extends to millimeters. Bamboo-type, lace-like, multilayer, multipodal, bimodal pore- and hierarchical nanotubes have also been fabricated [122-128]. Specularly reflecting TNAs with clearly defined interference fringes have been fabricated [120, 129]. The periodic modulation of the nanotube diameter has been used to create one-dimensional photonic crystals [130-133]. The formation of metallodielectric metamaterials looks highly promising [134]. The range of potential applications has likewise undergone vast expansion, encompassing gas sensors, biosensors, supercapacitors, drug eluting biomedical implants, stem cell differentiators, photocatalytic membranes, nanostructured excitonic solar cells, etc [54, 63, 123, 135, 136]. Yet, understanding and control of the nanotube shape and size dispersity on non-native substrates has been lacking. Monodispersity in pore size and shape is desirable for small molecule filtering, drug delivery and osmotic membrane applications. For photonic applications, dispersity in shape and size, non-uniform tube-length and random variations of diameter along the tube axis are sources of defects and scattering.

It is important to note here that the improvement of hexagonal pattern order is distinct from the achievement of a narrow shape and size dispersion, although the two often coincide. On foil substrates, the most ordered pores in terms of both size/shape dispersion and medium-range pattern order have been observed by two-step anodization in F⁻ ion bearing ethylene glycol-based electrolytes wherein the concave pore footprints left by the first anodization process following nanotube removal act as nucleation sites for the formation of ordered pores in the second step [137]. Due to the convex nature of footprints on non-native substrates, a simple bottom-up method to apply the two-step anodization-based ordering technique to the formation of ordered nanopores from vacuum deposited thin films of Ti has not been found for TNAs. Furthermore, the microstructure of vacuum deposited films which typically consist of grains 1-100 nm in size, differ considerably from hot-rolled Ti foils consisting of flat grains 5-100 μm in size. In this dissertation, we demonstrate methods to control the dispersity in the shape and size of TNAs on non-native substrates.

Before titanium deposition, the substrates were degreased by sequential ultrasonication in a Micro-90 solution, DI water, and isopropanol for 10 min each. In order to remove any organic residue, substrates were further cleaned in a piranha solution comprising a 3:1 mixture of sulfuric acid and hydrogen peroxide for 15 min followed by rinsing and drying. Direct current (DC) magnetron sputtering on to substrates at temperatures ranging from room temperature to 250°C and chamber pressures from 1-7 mTorr were used to deposit the Ti thin films 250 nm to 500 nm in thickness from a 99.99 % pure Ti target at a power of 150-300 W using 50 sccm of argon flow.

Thin-films of Ti deposited on non-native substrates, namely [001] oriented single crystal wafers, borosilicate microscope glass slides and Tec-15 fluorine-

doped tin-oxide (FTO) coated glass substrates, were anodized at room temperature in an ethylene glycol (EG)-based electrolyte containing 0.1-0.3 wt% NH_4F and 1 to 10 vol % deionized water at 40 V using graphite counter electrodes and a 3 ± 0.1 cm inter-electrode separation setup. The top-view and cross-section of the deposited films and anodic nanotubes were imaged using JEOL6301F and Hitachi S4800 field emission scanning electron microscopes (FESEM), and a JEOL2200FS transmission electron microscope (TEM). X-ray diffractograms of thin films were obtained in powder mode using a Bruker D8 Discover instrument with a sealed Cu tube X-ray source. Anodization current transients were measured using a Keithley 4200-SCS parameter analyzer.

Figure 3-11 shows the morphology of TNAs formed on Si and FTO substrates under identical anodization conditions (40 V, 9 vol% H_2O +0.3 wt% NH_4F in EG and 3 ± 0.1 cm inter-electrode separation setup) using Ti films deposited under identical conditions. It is evident from **Figure 3-11** that nanotubes formed on Si are clearly more uniformly circular and almost monodisperse in diameter while the nanotubes on FTO show a broad range of shapes and sizes. Without the use of polishing, pre-texturing or a two-step anodization process, nanotubes on Si exhibited a high degree of hexagonal ordering consisting of only pentagonal and heptagonal defects. A closer examination of **Figure 3-11a** reveals 48 nanotubes possessing six nearest neighbours (hexagons), 21 pentagons and 16 heptagons. The cross-sectional TEM images also show uniform straight cylindrical channels in the nanotubes on Si while the nanotubes on FTO show considerable variation and undulation in the channel cross-section and orientation. The principal difference existed in the morphology of the Ti films on Si and FTO substrates. Sputtering Ti under atomic peening conditions [120] on atomically flat single crystal Si wafers resulted in extremely smooth films while the Ti films sputtered

on FTO substrates under identical conditions were much rougher due to the high FTO substrate roughness (**Figure 3-11e** and **Figure 3-11f**).

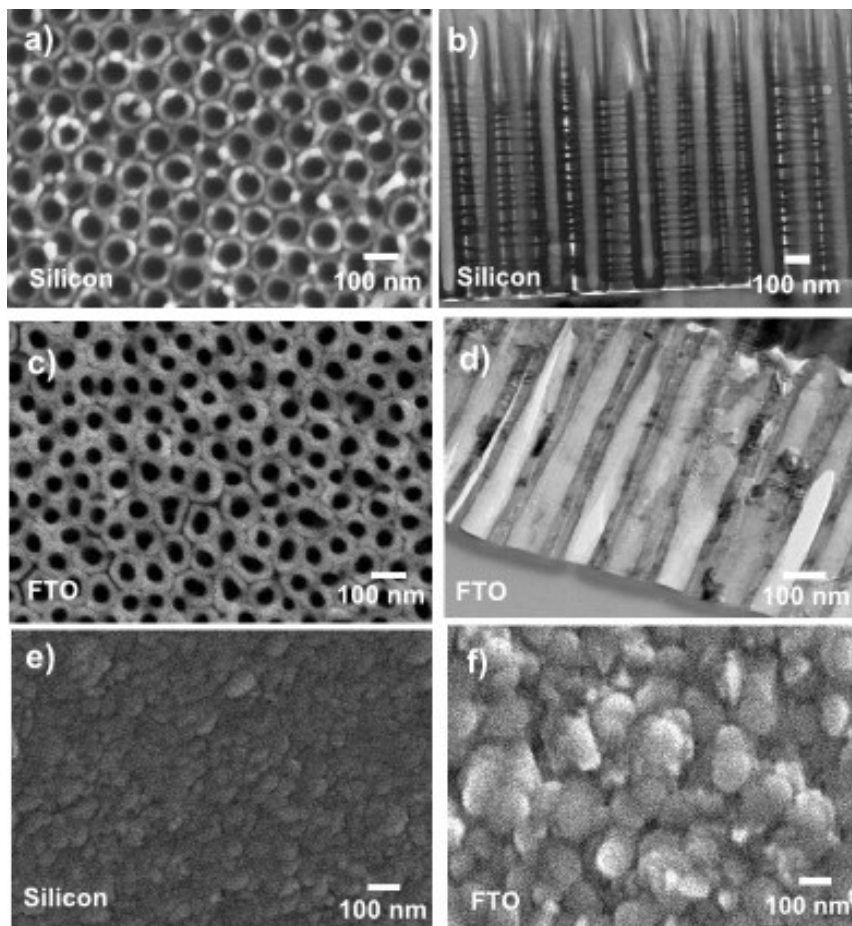


Figure 3-11. (a, b) FESEM top view and TEM cross-section of monodisperse TNAs on silicon substrate; (c, d) FESEM top view and TEM cross-section of polydispersed TNAs on FTO:glass substrate; The anodization electrolyte contained 9 vol% H₂O and 0.3 wt% NH₄F (e, f) FESEM top view of Ti thin films DC sputtered onto Si and FTO:glass substrates respectively, at 1 mtorr chamber pressure.

Two-dimensional Fast Fourier Transform (2D-FFT) images (**Figure 3-11**) were used to analyze the arrangement of nanotubes that resulted under different film formation and anodizing conditions. TNAs formed on FTO by anodization in aqueous electrolyte are disordered as evidenced by the completely blurred 2D-FFT image with no discernible ring. A high intensity narrow circular ring is

evident in the FFT image of TNAs formed on Si by anodization in EG-based electrolyte, which is indicative of the preservation of short-range periodicity and moderately disturbed long-range periodicity [138-140]. TNAs on FTO anodized in EG-based electrolytes show an intermediate level of disorder between the above mentioned cases.

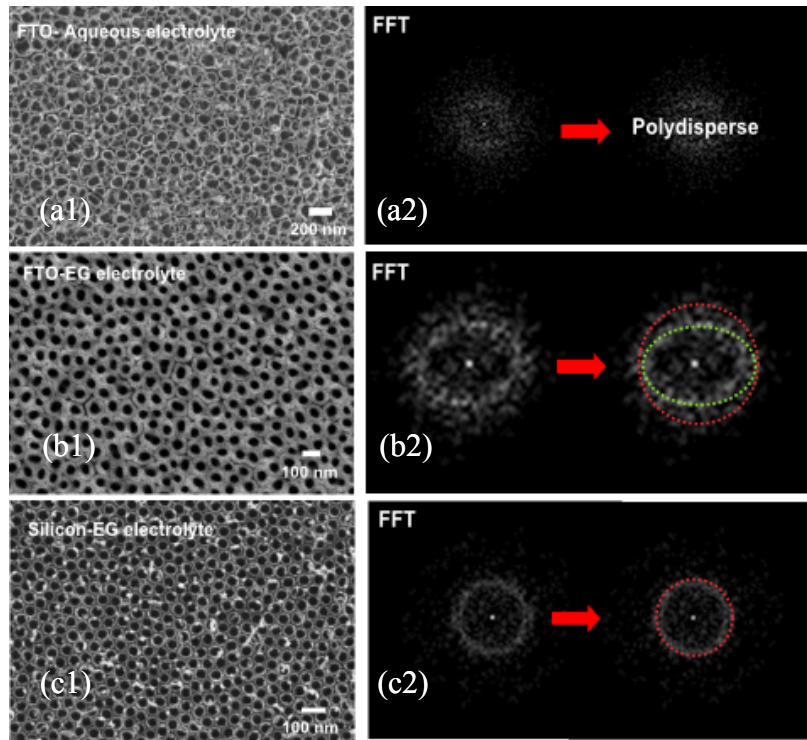


Figure 3-12. 2D-FFT images showing the effect of anodization electrolyte and substrate on the arrangement order of TNAs.

To quantify the dispersion in shape and size, the morphological parameters of 300 nanotubes each on FTO and Si, were measured. The resulting statistics are shown in Table 1. Nanotubes on Si exhibit a preponderance of circular tube-shapes (>95%) and a standard deviation in outer diameter of 10.1 nm. On FTO, the preponderance of irregular shapes rendered measurement of the inner diameter less meaningful. Instead, two values for the outer diameter - the minimum and maximum tube-widths were measured for nanotubes on FTO. The images used to

measure the statistics in **Table 3-1** are shown in **Figure 3-12** along with the methodology used to determine circularity. If more than 80 % of the annular area of a nanotube could be exactly enclosed by two concentric circles, such a nanotube was deemed to be circular. In **Table 3-1**, the size dispersity of TNAs on Si is about half that of TNAs on FTO anodized under identical conditions.

Table 3-1. Statistics related to the morphology of the nanotubes on Si and FTO substrates. This data was collected from SEM (**Figure 3-13**).

Nanotube parameter	TNAs on Si	TNAs on FTO
Size of distribution	300	300
Fraction of circular nanotubes	95 %	12 %
Average inner diameter (nm)	78.4	–
Std. Dev. of inner diameter distribution (nm)	4.7	–
Average max. outer diameter (nm)	116.0	130.9
Average min. outer diameter (nm)	116.0	104.8
Std. Dev. of max. outer diameter distribution (nm)	10.1	20.1
Std. Dev. of min. outer diameter distribution (nm)	10.1	17.0

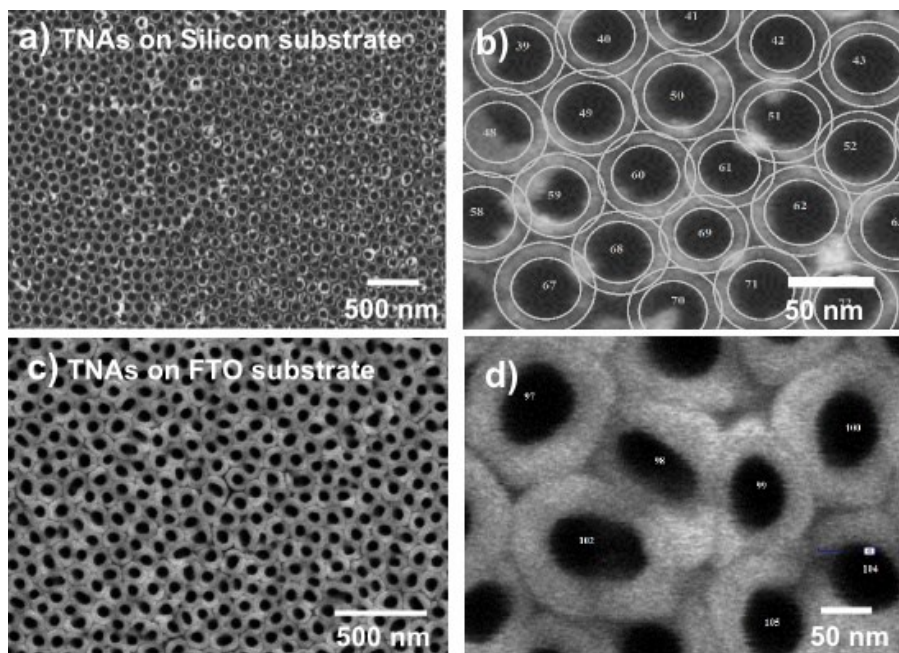


Figure 3-13. Images used to obtain statistics related to the nanotube morphologies a) TNAs on Si b) Magnified view of a portion of image in (a) showing how circularity and nanotube diameter were measured c) TNAs on FTO:glass and d) Magnified view of a portion of image in (c).

The reduction in the dispersity in shape is more dramatic, as evidenced by an 8-fold higher occurrence of circular nanotubes on Si. A narrower dispersion in nanotube diameters also produces a higher pattern order through a more uniform distribution of inter-tube centre-to-centre distances.

The anodization current transients in **Figure 3-14** for Ti anodization on different substrates show a featureless monotonic decrease in the FTO case and a clearly defined peak with a right shoulder in the case of silicon, which is known to be correlated with pitting. For glass substrates, a weak peak is seen and the behavior is intermediate between FTO and silicon. To confirm the structure of the transient on silicon substrates, results from a second silicon sample are also shown with near identical features to the first. The rise of the anodization current from the local minimum at *ca.* 200 s to the local maximum at *ca.* 510 s was

found to follow the $t^{3/2}$ relation [141]. This fact, coupled with the large amplitude of the pitting currents for the anodization of Ti on Si, together with the reproducible shape of the anodization transient, is indicative of stable pitting due to uniform hemispherical pits that confine the aggressive H^+ ions required for the electrochemical dissolution of TiO_2 in close proximity with the active etching front [142]. We surmise that the peak pitting current coincides with injection of anions from the electrolyte into the oxide which transit through the barrier layer. The post-peak currents are fit to straight lines in the log-log plot (**Figure 3-14a**) with slope $1-\alpha=0.33$ and $1+\alpha=1.54$. The sum of the slopes is ≈ 2 , and is typical of dispersive charge transport (of ions in this case) through the barrier layer with a transit time corresponding to the knee of the curve where the fit lines meet [143].

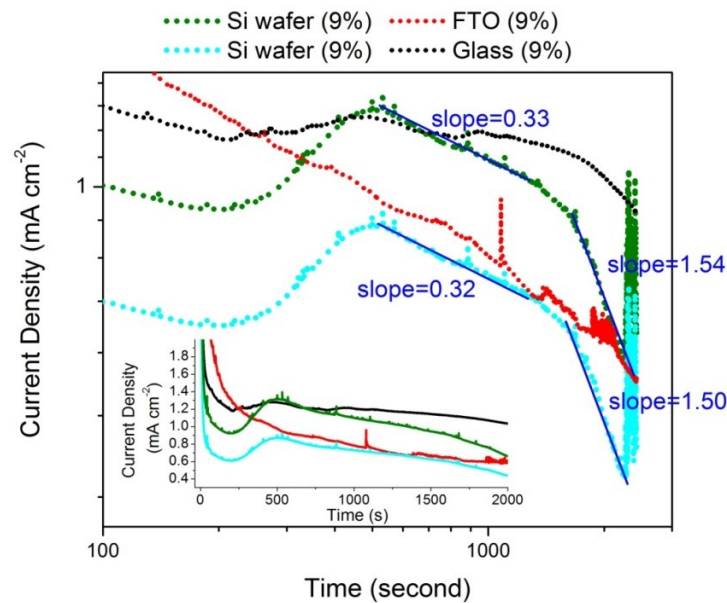


Figure 3-14. Log-log plot of the anodization current transients during the formation of TNAs on glass (black), FTO: glass (red) and two silicon substrates (cyan and olive green) magnifying the temporal region near local extreme in the current. The rise of the anodization current between the local minimum and the subsequent local maximum was fit to a straight line with a slope of 1.5 (fit not shown). Current decay following the maximum is fit to straight lines (blue) with slopes as indicated. The inset plots the currents measured over the entire anodization duration on a linear scale.

Since fluoride ions are known to be fast diffusing species in anodic TiO₂ [144], the dispersive transit is likely due to O²⁻ ions, which react with Ti at the oxide-metal interface to increase the barrier layer thickness. The post-transit decrease in anodization current below the level of the previous local minimum is supportive of this idea. **Figure 3-15** shows the effect of the morphology of the precursor Ti film on the morphology of the nanotubes that result upon anodization and demonstrates that the best quality nanotubes result from use of the smoothest Ti films. Substrate heating, which is often resorted to, in order to obtain large-grained films, can reduce the quality of the nanotubes resulting from anodization. When the Ti films are rough and composed of 3-dimensional grains, as in **Figure 3-13c**, the structure transitions from nanotubes toward irregular nanopores.

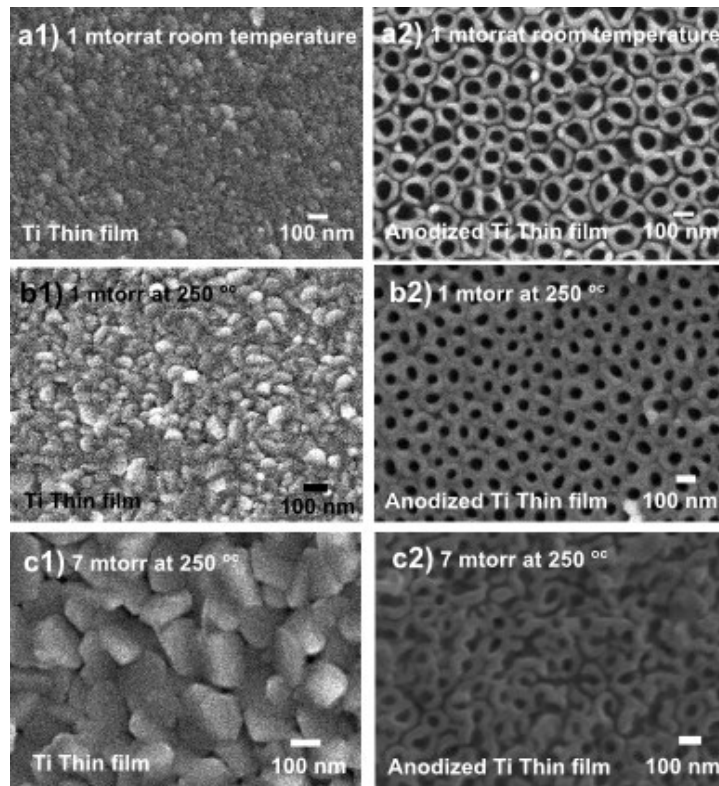


Figure 3-15. Effect of temperature and chamber pressure on the morphology of sputtered Ti thin films (1) and resulting anodic TNAs (2) on glass substrates (a) 1 mtorr, room temperature, (b) 1 mtorr, 250°C and (c) 7 mtorr, 250°. The scale bar at the bottom of each image corresponds to a length of 100 nm.

A planar interface between the anodic oxide and the liquid electrolyte enables uniform, homogeneous nucleation by electrochemical and chemical pitting of the oxide. The grain structure at the interface assumes significance in the context of pore nucleation and growth processes. When a grain with pointed crystal facets comparable in size to the amplitude and spacing of the pits presents itself to the etch front, the pit formed on the particular grain is not circular but of a more irregular shape. Fluoride ions strike the oblique faces of the grain and carve out a pit whose projection onto the substrate plane is non-circular. A second reason for the said irregularity in shape is the difference in etch rates of various crystal planes. The above processes are schematically depicted in **Figure 3-16**. When chemical etching is significantly involved in pit nucleation, the inter-pore spacing is also affected by crystal plane dependent etch rates. According to the recently developed Planar Interface Instability Criterion (PIIC) [145, 146], the dominant inter-pore spacing is slightly larger than the:

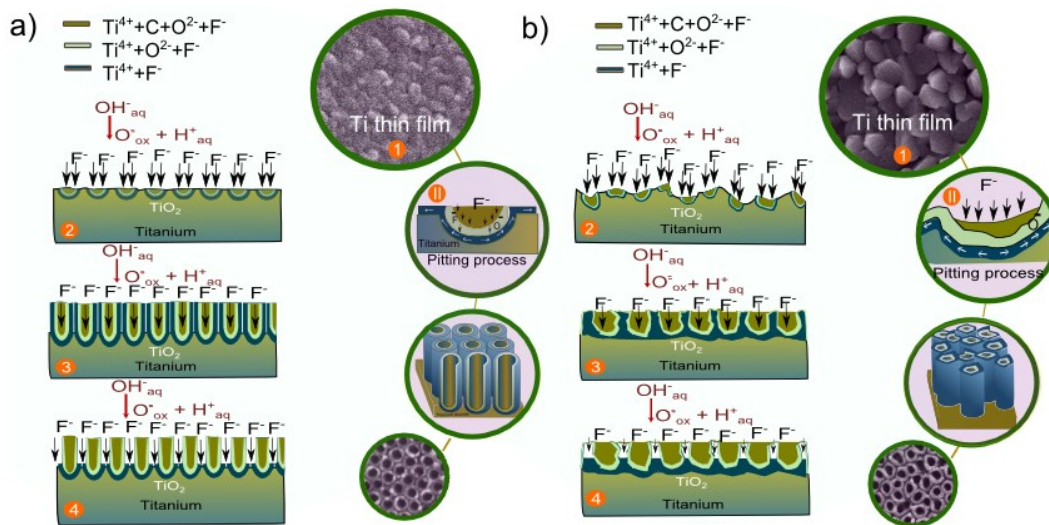


Figure 3-16. Schematic illustration of the pore nucleation process on (a) smooth and (b) rough substrates highlighting the importance of film roughness on the shape and size dispersity of anodically formed TNAs.

(3-10)

$$\left(\frac{\lambda_p}{2\pi}\right)^2 \approx \frac{\Gamma}{kT \frac{\partial \Delta G_D}{\partial x}}$$

where k is Boltzmann's constant, T is the temperature, ΔG_D is the change in free energy associated with the chemical dissolution of the oxide, x is a position coordinate in the direction of increasing oxide thickness and Γ is the Gibbs-Thomson coefficient given by :

(3-11)

$$\Gamma = \frac{\gamma \cdot MW}{\rho n e}$$

where γ is the interfacial energy of the oxide-electrolyte interface, MW is the molecular weight of the oxide, ρ is the density of the oxide, n is the number of electrons involved in the electrochemical reduction process and e is the fundamental electronic charge.

When multiple crystal planes are present on the Ti surface in the form of domains comparable to the size of the pits, and exposed to chemical dissolution with their respective orientation-dependent etch rates, it can be seen from equation (3-10) that multiple dominant pore spacings could be present. This is one source of dispersion in pore size. A second source of dispersion is the nature of the pitting process. When electrochemical dissolution is strong, high pit densities of 10^{12} cm^{-2} occur which combine during the process of pore formation to result in decreased pore densities. If the pits are large enough, then their combination results in an irregular non-circular pore. Thus a low microscopic surface roughness is a necessary condition for the formation of monodisperse pores but not a sufficient one, and careful balance needs to be struck in the composition of the anodization electrolyte between the pitting and oxide growth

mechanisms (see **Figure 3-17** It is for this reason that although the formation of TNAs from Ti films deposited on Si substrates has been studied in several articles [117, 147, 148], none report the type of uniformly circular, monodisperse nanotubes we do in this report.

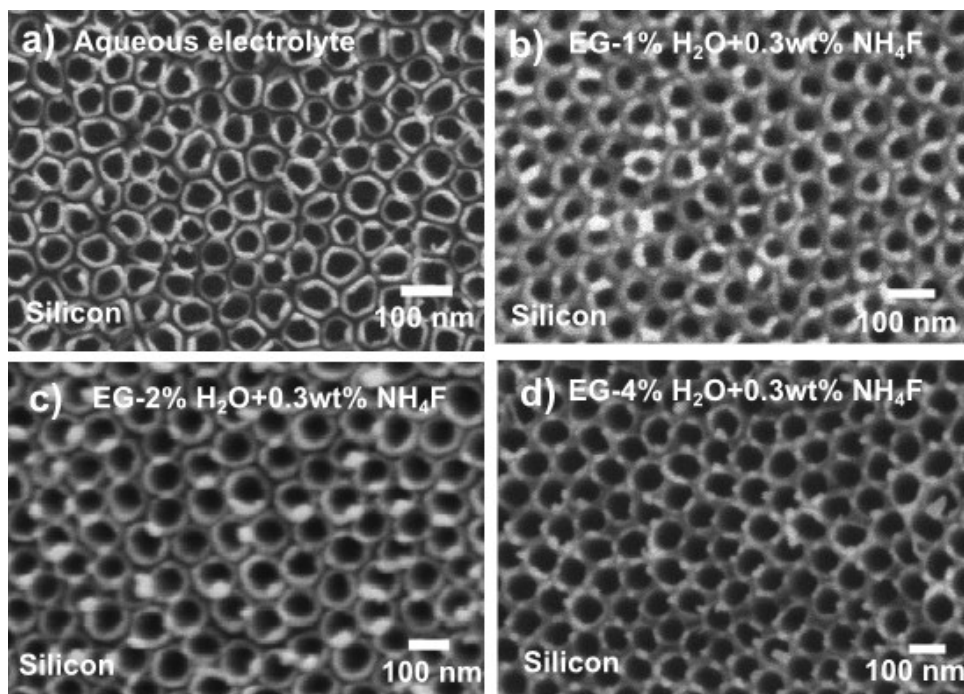


Figure 3-17. FESEM images of TNAs on Si substrates formed by anodization of identical Ti thin films in different electrolytes; (a) TNAs formed in aqueous electrolyte, exhibiting a wide dispersion in shape and size, (b) TNAs formed in EG-based electrolyte containing 1% H₂O and 0.1 wt% NH₄F, (c) TNAs formed in EG-based electrolyte containing 2% H₂O and 0.3 wt% NH₄F and (d) TNAs formed in EG-based electrolyte containing 4% H₂O and 0.3 wt% NH₄F

Our insight into the importance of surface topography for nanotube formation on non-native substrates is in line with studies of nanotube growth on foil substrates where smooth, electropolished surfaces have been observed to result in the most uniform nanotube growth [149]. Fluoride ions are highly solvated in protic solvents due to hydrogen bonding and consequently, their ionic mobilities and nucleophilic action are much weaker than in aprotic solvents where this is not

the case. Therefore, all else being equal, it is reasonable to expect stronger electrochemical etching and weaker electrochemical oxidation in polar aprotic electrolytes, and the slower oxide growth at the very beginning of the oxidation process simulates conditions similar to electropolishing of Ti. The pore shapes are nearly uniformly circular and of similar size in nanotubes formed in electrolytes containing dimethylsulfoxide and suitable concentrations of fluoride ions (see for instance Fig. 14 in Ref [53]). On the other hand, nanotubes formed in polar protic solvents have a significant dispersion in order, shape and diameter with the largest dispersions occurring in purely aqueous media.

Crawford and Chawla [150], and Leonardi et al [151] have pointed out the difference in nanotube formation rates on different Ti crystal planes owing to differences in atomic densities and oxidation rates. The effect of the crystallographic orientation of the Ti films on pore dispersity cannot be excluded but certainly does not account for all the observations. Even under similar conditions of vacuum deposition, Ti films of varying texture are deposited on different substrates, indicating a strong substrate dependence of the crystallographic orientation (**Figure 3-18**). On silicon substrates, both the absolute and relative intensity of peaks are strongly influenced by chamber pressure during sputtering. On glass substrates, the peaks are broader and shifted to higher 2θ values, likely due to stresses accumulated in the film during sputtering. However, chamber pressure has very little effect on the Ti film texture on glass since essentially the same peak structure is obtained at both 1 mtorr and 20 mtorr. However, identical Ti films deposited on Si substrates can still generate TNAs with widely differing shape and size dispersity in different electrolytes (**Figure 3-17**), pointing to the importance of uniform and stable pitting. Furthermore, Ti films of similar crystallographic texture sputtered on to glass

substrates at different chamber pressures and temperatures, differing only in surface topography, exhibit dramatically different morphologies upon anodization such as well-defined nanotubes in the case of room temperature low pressure sputtered Ti precursor films and a disordered nanoporous structure in other cases (Figure 3-15).

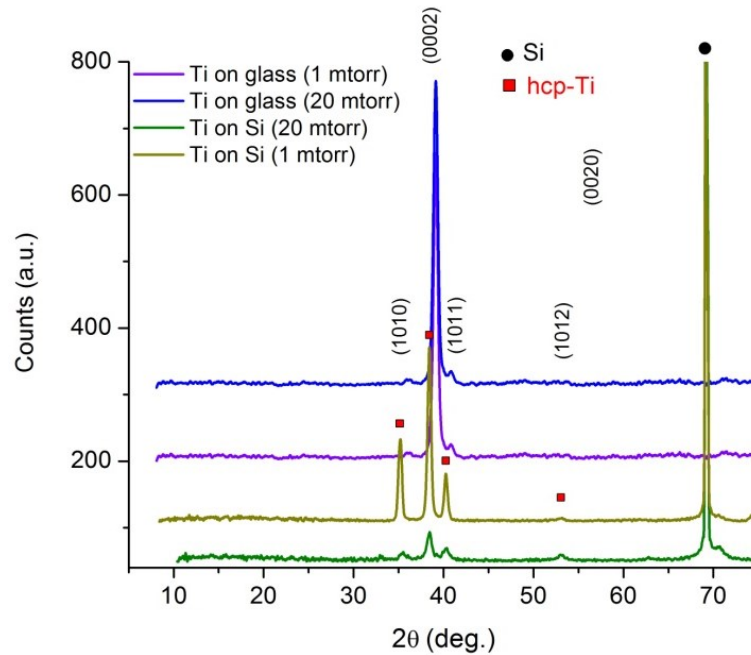


Figure 3-18. Effect of substrate on the crystallographic texture of sputtered Ti films under identical conditions. Powder mode X-ray diffractograms of Ti thin films deposited on to glass and silicon substrates using DC magnetron sputtering at two different chamber pressures (1 mtorr and 20 mtorr).

Prior reports indicated that smooth surfaces with large grains are favorable for nanotube formation. Our results show that highly smooth, fine grained Ti films produce stable and uniform pitting due to which film smoothness is significantly more important than grain-size in order to obtain highly ordered nanotubes. A large grain-size, especially when randomly oriented, is associated with a larger dispersity in the shape and size of the nanotubes. Almost monodisperse nanotube arrays are formed by anodizing Ti films on silicon substrates.

Chapter 4

Metal Nanoparticle Promoter-Decorated TNTAs for Photocatalytic Application

4.1 Overview

The interactions of light with spherical and rod-type structures are different owing to the scattering of nanoparticles governed by the exact solutions given by Mie theory [152] and that of nanorods/nanotubes affected by optical anisotropy and approximately described by Gans theory [153]. While the co-catalysts in nanoparticulate photocatalysts are also nanoparticles of roughly the same size and present a single length scale, co-catalyst NPs are much smaller than the length of NRs/NTs resulting in multiple length scales, a desirable feature for high performance photocatalysis [154].

When 1-D anatase-phase TiO₂ nanostructures are combined with a suitable co-catalyst, efficient CO₂ photoreduction capability results. The highest reported values of CO₂ photoreduction ($\sim 0.5 \mu\text{mol cm}^{-2} \text{hr}^{-1}$) for broad-band illumination in the scientific literature for any catalyst have been obtained using 1-D TiO₂ loaded with a nano-sized platinum-containing co-catalyst [155-160]. However, the exact electronic band-alignment at the Pt-TiO₂ interface is unknown. The Shockley-Anderson model [161] for band-alignment at a semiconductor heterojunction,

suggests the formation of a Schottky barrier between TiO_2 and high work-function noble metals resulting in a carrier-depleted interfacial region with an electric field that causes photogenerated holes to transfer to the noble metal and photogenerated hot and equilibrated electrons to be injected into or retained in the TiO_2 (Figure 4-1). There is some evidence in the scientific literature that TiO_2 forms Schottky junctions with noble metals such as Au and Pt [162, 163].

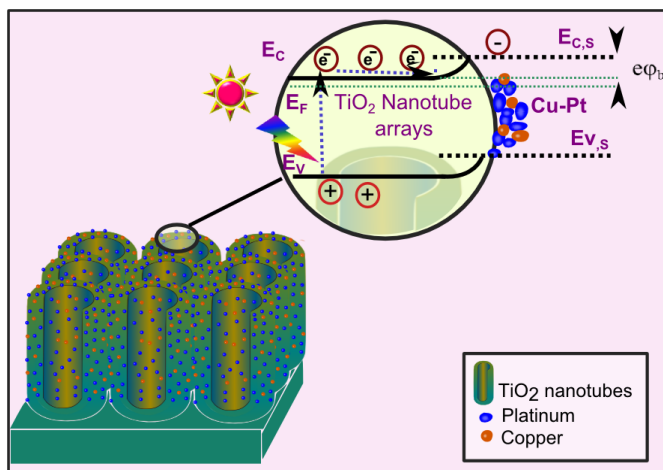


Figure 4-1. Band-diagram of the Schottky junction at the $n\text{-TiO}_2/\text{CuPt}$ interface. The direction of the built-in field in the depletion region is such as to drive photogenerated electrons toward the TiO_2 bulk and holes toward the metal-semiconductor interface.

On the other hand, femtosecond transient absorption spectroscopy and electron spin resonance studies suggest transfer of the photoexcited electron to the noble metal leaving the photogenerated hole in TiO_2 [157, 164]. Thus there exists a fundamental contradiction between the above two scenarios that needs resolving. Some reports claim (incorrectly, in our opinion) that Pt NPs on $n\text{-TiO}_2$ act as electron sinks through Schottky barrier electron-trapping [165, 166], which represents an obfuscation or misunderstanding of the difference between the two scenarios outlined. The electronic properties of the metal-support interface are also key toward understanding the nature of sub-bandgap absorption in Cu-TiO_2 and Pt-TiO_2 photocatalysts [167, 168], and its effectiveness in driving

photocatalytic reactions are also unknown. Furthermore, the photocatalytic activity is highly sensitive to the method of formation and deposition of the noble metal NPs. Since NTs differ in structure and properties from NPs, investigations on electronic interactions and charge transfer at the co-catalyst-TiO₂ interface specific to 1-D nanostructures and type of co-catalyst loading are quite important from the point of view of understanding and improving photocatalytic performance. The present study investigates the structure and electronic interactions at the CuPt NP-TiO₂ hybrid interface wherein the CuPt NPs are photodeposited onto the nanotube walls. Transparent nanotubes on FTO-coated glass substrates are used in this study since they allow clear and quantitative measurement of the effect of CuPt loading on the optical absorption of the photocatalyst.

4.2 Experimental Details

4.2.1 Synthesis of transparent TiO₂ nanotube arrays

Transparent TiO₂ nanotube arrays (TTNTAs) were synthesized by electrochemical anodization of thin Ti film deposited on fluorine doped tin oxide (FTO) coated glass substrates (glass:FTO) purchased from Hartford Glass Co., by direct current (DC) sputtering from a Ti target of 99.995 % purity (Kurt J. Lesker Co.); further details regarding the details of the vacuum deposition and nanotube growth processes are provided in prior work [120, 169]. Prior to depositing Ti films, FTO substrates were cleaned in an ultrasonicated bath with soap solution, deionized water and methanol, consecutively for 10 minutes each. Electrochemical anodization of the Ti-coated glass:FTO substrates was carried out at room temperature using an organic electrolyte containing 0.3 wt % NH₄F (> 98 % purity, Fisher Chemical) and 4% deionized water in ethylene glycol (> 99 %

purity, Fisher Chemical). A constant potential of 40 V was applied across the two electrodes (3 ± 0.1 cm inter-electrode separation setup) by using a DC power supply.

4.2.2 Formation of CuPt-TTNTA hybrid structures

Cu/Pt-TTNTA hybrids were formed by photodeposition of bimetallic alloys over TTNTAs. To prepare these hybrid catalysts, annealed and oxygen plasma treated TTNTAs were soaked in a methanolic solution of methanol, [Pt(acac)₂], [Cu(acac)₂] (2:2:1) for 60 minutes under the irradiation of a 4 W UV lamp and a 150 W solar simulator equipped with an AM1.5 filter at an intensity of 1 sun⁸. [Pt(acac)₂] was of 98 % purity and purchased from Strem Chemicals Inc., [Cu(acac)₂] was of 98 % purity and purchased from Acros Organics, Inc and the methanol was of 99.8 % purity and purchased from Fisher Chemical. The samples were placed in a teflon reaction cell. After photodeposition, TTNTAs were taken out from the solution followed by rinsing in methanol and drying in air.

Photodeposition method is one of most cost effective and simple methods for synthesis of CuPt catalysis. Titanium dioxide is a favorable candidate as a host substrate in the photodeposition process since it is chemically and photochemically stable in comparison to most other semiconductors such as CdS and ZnO. In this process each nanotube can be considered as a microphotoelectrochemical cell, that absorbs photons with energy higher than its bandgap ($h\nu > E_g$) and electron-hole pairs will be generated. This electron hole pairs may recombine due to trap

⁸ Most of the data that is present in this dissertation are from the samples that were exposed to solar simulator unless otherwise mentioned.

states or may move from the bulk to the surface due to diffusion and react with $[\text{Pt}(\text{acac})_2]$ and methanol. As a result of this reaction, oxidation (of methanol) and reduction (of $\text{Pt}(\text{acac})_2$) will take place on the surface of TiO_2 nanotubes and $\text{Pt}(\text{acac})_2$ will reduce to Pt metal [170]. This process is schematically illustrated in **Figure 4-2**.

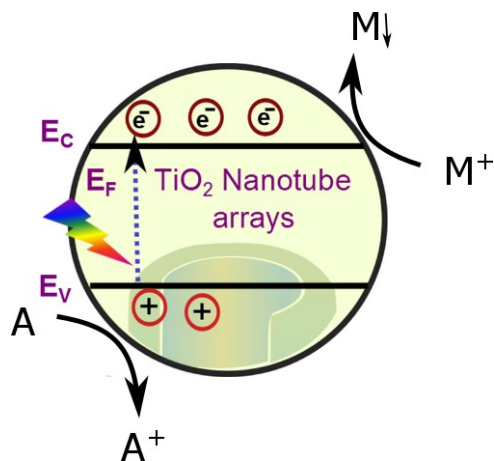


Figure 4-2. Schematic illustration of oxidation process (A: methanol) and reduction process (M^+ : $\text{Pt}^{2+}/\text{Cu}^{2+}$).

4.3 Photodeposition Mechanism

Under the conditions used by us for photodeposition, the mechanism of deposition could be either photochemical reduction (a.k.a. photo-induced reaction) or photocatalytic deposition. It is well-known that metal ions with relatively positive values of the standard electrochemical redox potential (w.r.t. NHE) are able to easily receive photogenerated electrons from the conduction band of TiO_2 in neutral as well as acidic conditions. For such metals (a list that includes Cu and Pt), photocatalytic deposition is more facile than photochemical reduction, and is the dominant mechanism of photodeposition. This is also supported by specific and relevant reports regarding acetylacetonates, where

photocatalytic deposition is favored over photochemical depositions for illumination by near-ultraviolet photons (i.e. 350-400 nm) [171]. In addition, we performed simple experiments to confirm the nature of the photodeposition process. These experiments relied on the differences in electronic properties between the amorphous and crystalline forms of TiO₂. It has been shown by us and others in numerous reports that anatase-phase anodic TiO₂ nanotube arrays annealed at temperatures higher than 350°C are an *n*-type semiconductor while as-anodized amorphous anodic TiO₂ nanotube arrays (i.e. not subjected to thermal annealing) are insulating with semiconducting behavior either very poor or absent. Therefore, photocatalytic deposition would be possible in the case of the anatase-phase TTNTAs while the same would not be possible in the case of amorphous TTNTAs. Keeping this in mind, we subjected both anatase-phase TTNTAs and amorphous TTNTAs to photodeposition under identical conditions. The results are shown below in **Figure 4-3**. In **Figure 4-3a**, anatase-phase TTNTAs exhibit a much larger increment in optical absorption at visible wavelengths following photodeposition compared to amorphous TTNTAs under identical conditions of photodeposition, pointing to a difference in mechanism - the more efficient photocatalytic deposition for the anatase nanotubes and less efficient photochemical reduction for the amorphous TTNTAs. We also verified this effect for nanoporous anodic alumina (indisputably an insulator) on glass substrates (**Figure 4-3** below) where once again the samples showed very little change in optical absorption after being subjected to photodeposition, thus confirming the CuPt nanoparticle deposition process to be primarily photocatalytic in nature.

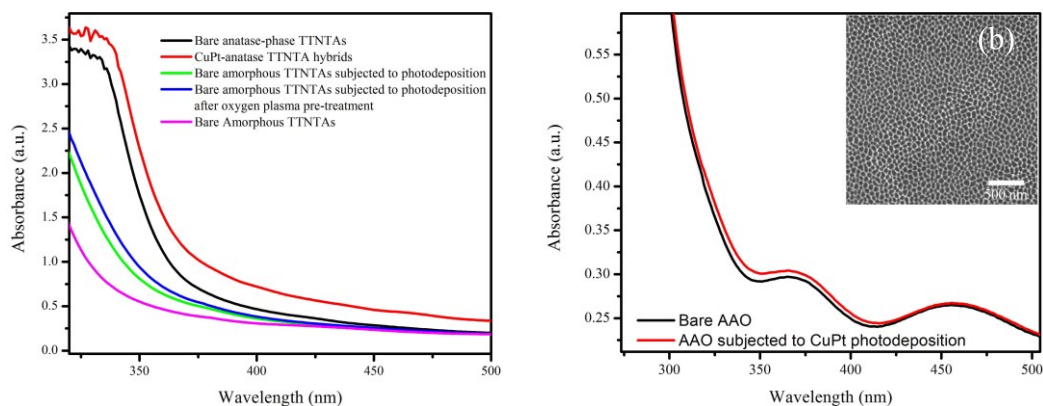


Figure 4-3. (a) Effect of CuPt photodeposition on the UV-Vis spectra of annealed, crystalline TTNTAs and un-annealed, amorphous TTNTAs (b) Nanoporous anodic aluminum oxide (AAO) on glass substrates before and after being subjected to CuPt photodeposition.

4.4 Morphology, structure and optical absorption of CuPt coated TTNTAs

The morphologies of the TTNTAs and CuPt-TTNTA hybrids were examined using a field emission scanning electron microscope (S-4800, Hitachi) operating at 5 kV accelerating voltage by secondary electron imaging. The morphology of the as-prepared TTNTAs was imaged using FESEM (**Figure 4-4**) where closed packed TTNTAs with an average outer diameter ~ 105 nm are seen. An inset image in top left corner of **Figure 4-4a** shows a cross section of TTNTAs with a tube-length of 1 μm . Not much change is observed in the morphology of TTNTAs after CuPt loading. The nanoparticles of bimetallic alloys that form CuPt-TTNTA hybrids are too small to be seen in SEM images.

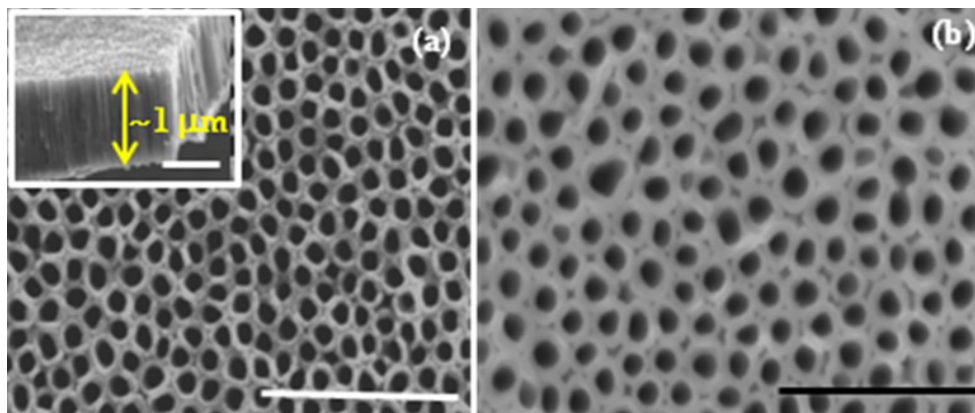


Figure 4-4. FESEM images display the morphological features of (a) TTNTAs, an inset image in the figure shows the cross-section of the arrays with the height of 1 micron and (b) CuPt-coated TTNTA hybrids. The scale bar refers to 500 nm for both the images.

Micro-Raman studies of the samples were carried out in back scattering mode (Nicolet Almega-XR). An excitation source of 532 nm with a beam spot of 2 micron was used to analyze the structure of the samples. MicroRaman spectroscopy is a sensitive and powerful technique to investigate defects, variations in local structure and phase transformations in TiO₂ based materials. The Raman spectra of TTNTAs and CuPt-TTNTA hybrids are shown in **Figure 4-5**. TTNTAs formed after anodization are amorphous in nature and their crystallization is achieved by annealing in air at 550°C. For crystalline anatase TiO₂ phase, six Raman active phonon modes are present that correspond to A_{1g}, B_{1g} and E_g modes, respectively.

Figure 4-5a shows a comparison of the Raman spectra of TTNTAs and CuPt-TTNTA hybrids. Raman spectra confirm the tetragonal anatase mode of TTNTAs with the presence of Raman active A_{1g}, B_{1g} and E_g modes.[172, 173] It can be seen that the most intense peak for TTNTAs appears at 130.4 cm⁻¹ corresponding to the E_g mode. In addition to the E_g mode, the other less intense peaks can be seen at 393.7 cm⁻¹, 513.1 cm⁻¹ and 636.5 cm⁻¹ confirming the presence of B_{1g}, A_{2g}

and E_g modes, respectively. A shift in a peak position of 7 cm^{-1} (137 cm^{-1}) is found for CuPt-TTNTA hybrids for main E_g mode with a small broadening. This shift in CuPt-TTNTA hybrids is due to dispersion of bimetallic CuPt NPs over TiO_2 producing a change in the local structure of TiO_2 . **Figure 4-5b** shows the Raman spectra of CuPt-TTNTA hybrids subjected to different irradiation times by the one sun output of a calibrated solar simulator together with heating at 100°C . Such a configuration to study the CuPt- TiO_2 interface was chosen keeping in mind the fact that both photochemical and thermochemical interfacial reactions are possible upon illumination in TTNTA photocatalysts.

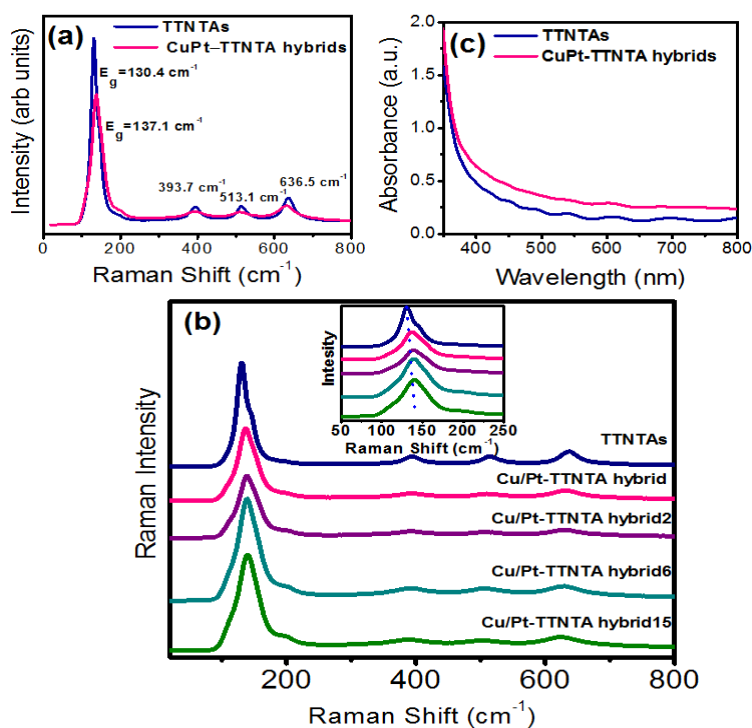


Figure 4-5. Counter-clockwise from top-left (a) Comparison of the room temperature Raman spectra of TTNTAs and CuPt-TTNTA hybrids (b) microRaman spectra of CuPt-TTNTA hybrids heated to 100°C with different light exposure times, here 2, 6 and 15 corresponds to hours of illumination; inset figure shows the broadening in the E_g peak of TiO_2 with time. (c) UV-Vis spectra of TTNTAs and CuPt-TTNTA hybrids.

The inset of **Figure 4-5b** shows the broadening of the main E_g peak in case of hybrids irradiated with different times in correspondence to the TTNTAs, which we associate with increasing structural disorder upon prolonged exposure to ultraviolet photons in simulated sunlight. UV-Vis spectra were collected in a Perkin-Elmer Lambda 1050 UV-Vis-NIR spectrophotometer equipped with a 150 mm integrating sphere to measure total diffuse reflectance. The UV-Vis spectra in **Figure 4-5c** show a strong sub-bandgap absorption in the bare TTNTAs due to an extended Urbach tail. No pronounced additional optical transitions were found in the CuPt-TTNTA hybrids. Intra- and interband absorption in CuPt NPs resulted in a slightly increased absorption of light throughout the visible spectra range in CuPt-TTNTA hybrids in comparison to TTNTAs.

The internal structure of samples were imaged using high resolution transmission electron microscopy (HRTEM) (JEOL 2200FS) operating at 200 kV, equipped with scanning transmission electron microscopy (STEM) and energy dispersive x-ray facility. TEM sample preparation of the CuPt-coated and uncoated nanotube cross sections was performed using focused ion beam etching in a SEM system (Hitachi-NB5000). Low and high resolution-TEM images and EDAX spectra of TTNTAs and their hybrids are displayed in **Figure 4-6**. A direct attachment of CuPt-NPs is clearly seen along the walls of TiO_2 nanotubes (**Figure 4-6a**). The encircled regions in this image indicate the CuPt NPs to be 2 - 5 nm in diameter, which is further confirmed through HRTEM images (**Figure 4-6c**). A high angle annular dark field scanning TEM (HAADFSTEM) image, shown in **Figure 4-6b** corresponds to the tiny bright spots demonstrating the dispersion of CuPt NPs on TTNTAs. A close knit attachment of CuPt NPs with the TTNTAs can be seen in **Figure 4-6c**, favoring the CuPt NPs and TiO_2 nanotube array structures to form hybrids with a strong interaction. EDX spectra,

shown in **Figure 4-6d** confirm the elemental state of Pt only, due to a very small concentration of Cu. However, the HRTEM images shown in **Figure 4-7** confirm the presence of CuPt bimetallic alloy.

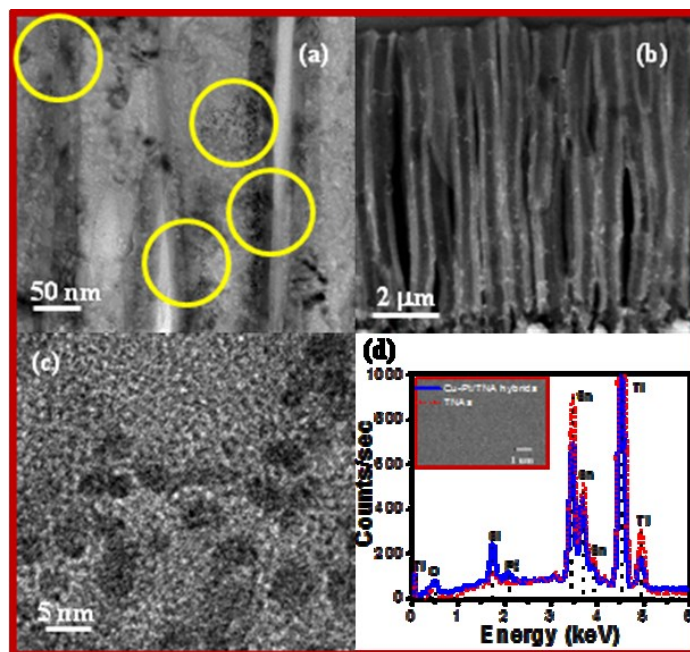


Figure 4-6. Low and high resolution transmission electron microscope images showing (a) Cu/Pt loaded TTNTAs, (b) HAAFD image in STEM mode presenting the TTNTA:CuPt-NP hybrids, (c) close knit attachment of CuPt nanoparticles along the walls of TTNTAs and (d) EDAX spectra confirming the presence of Pt.

Figure 4-7a-c display the auto correlated lattice spacing, analyzed from HRTEM pictures. The anatase phase of TiO_2 with d-spacing 0.34 nm corresponding to the (101) plane, is confirmed through high resolution lattice fringes (**Figure 4-7a**). The presence of Pt and CuPt alloy is also confirmed from the d-spacing of the lattice fringes to be 0.24 nm (111) and 0.22 nm (111), respectively (**Figure 4-7b-c**). The d-spacing of 0.22 nm from the lattice fringes reveals the formation of Pt rich alloy with very small concentrations of Cu. A complete chain of TTNTAs and the TTNTA:CuPt-NP hybrid structures with their corresponding d-spacing is summarized in **Figure 4-7d**. Thus, HRTEM results

confirm the intimate nature of the CuPt-TiO₂ hybrid structure interface that is the foundation for the further set of studies.

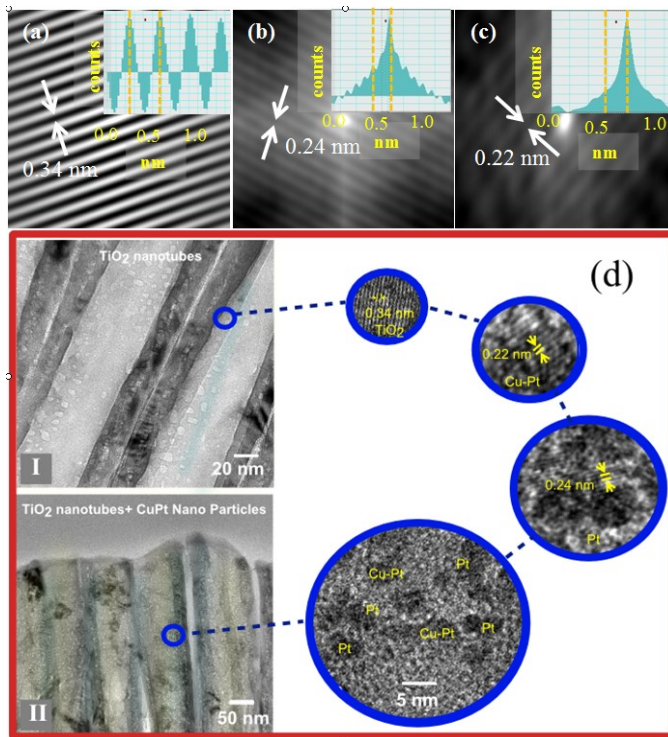


Figure 4-7. High-resolution autocorrelated images of (a) TiO₂ lattice planes (b) Pt NPs (c) CuPt NPs (d) HRTEM images displaying the crystalline planes for (I) TTNTAs and (II) CuPt-TTNTA hybrids.

XPS⁹, which is a highly surface sensitive technique, was carried out to investigate the difference in the chemical states of different elements present in TTNTAs and CuPt-TTNTA hybrids. XPS is also used as a means to understand the charge transfer and electronic interactions between the metal and the support in the mentioned hybrid structure (**Figure 4-10b-e**). The binding energies were

⁹ X-ray photoelectron spectroscopy (XPS) measurements were conducted out using Al K_α source with energy 1486.6 eV instrument (Axis-Ultra, Kratos Analytical) under UHV conditions (~10⁻⁸ Torr) with 0.3 eV resolution.

calibrated by the C 1s peak of the surface adventitious carbon at 284.6 eV (see **Figure 4-8** below). Acetylacetonate that is used for photodeposition process is the composition of C=O bonding (with binding energy of ~ 287.5) and as shown in **Figure 4-8** we do not observe any peak that corresponded to contamination due to presence of acetylacetonate or products of acetylacetonate decomposition.

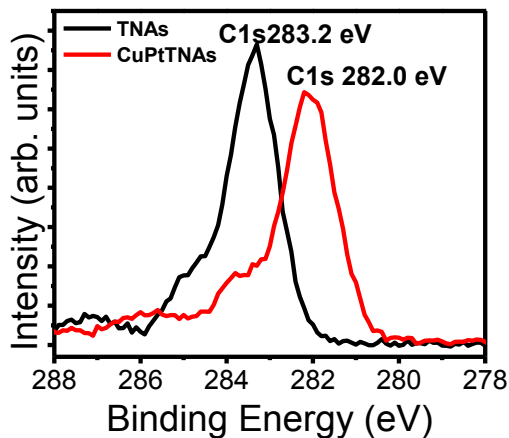


Figure 4-8. X-ray photoelectron spectra of TiO₂ nanotube arrays for C 1s

The survey scans on TTNTAs and CuPt-TTNTA hybrids confirm the presence of Ti, O and Pt. To confirm the presence of all materials along the length of TTNTs, time of flight-SIMS in depth profiling mode was performed on the sample. TOF-SIMS spectra (**Figure 4-9a**) confirm the presence of all the materials present in the sample along with the substrate up to a sputtering time of ~ 2600 s, which corresponds to the transition from the TiO₂ nanotube barrier layer to the FTO layer below. Furthermore, the intensities of Cu and Pt obtained through SIMS profiling correlate well with that of Ti, indicating a fairly uniform loading of Cu_{0.078}Pt_{0.92} NPs (**Figure 4-9b**) along the nanotube walls with a slight increase in Pt concentration closer to the barrier layer. The surface states of Ti, O and Pt are seen in **Figure 4-10b-d**. In **Figure 4-10**, the Ti 2p_{3/2} and Ti 2p_{1/2} states in TTNTAs present at 458.4 eV and 464.2 eV, respectively, correspond to Ti⁴⁺

states [174]. The Ti^{4+} surface state shifts to 457.8 eV and 463 eV in CuPt-TTNTA hybrids.

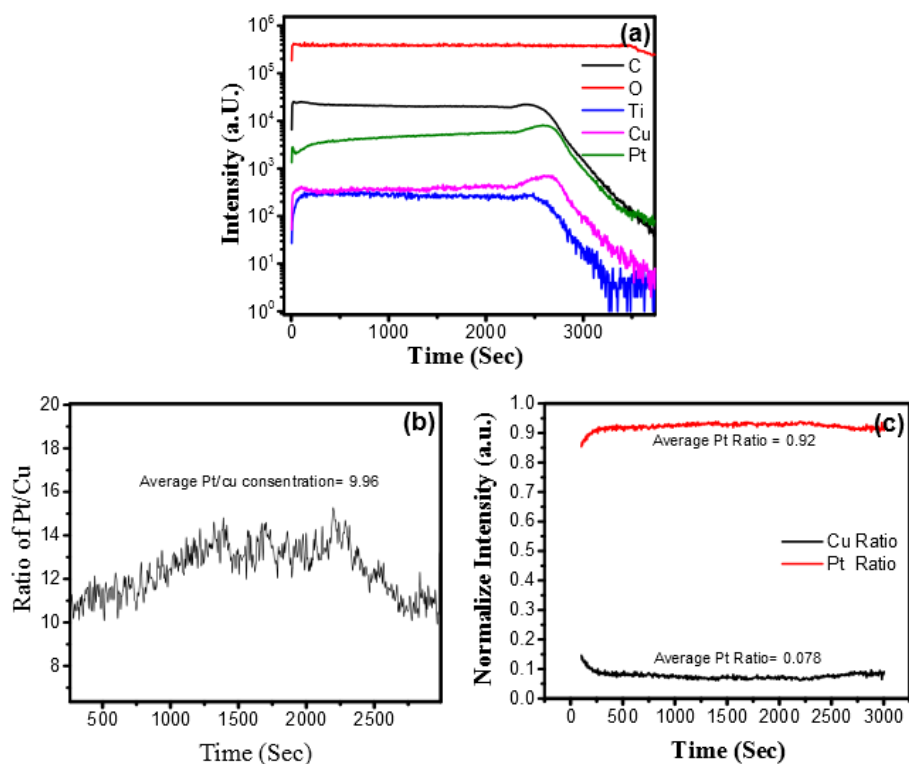


Figure 4-9 TOF-SIMS data from TTNTA:CuPt-NP hybrids(a)(b) ration of Pt to Cu along the length (c) atom fraction of Cu and Pt along the length

Figure 4-10c displays the O1s spectra with the presence of Ti-O peak at 529.63 eV and 529.45 eV for TTNTAs and for CuPt-TTNTA hybrids, respectively. While the binding energy shift in this case appears to be a mere -0.18 eV, measurements over a number of samples and peak decomposition of the resulting O1s spectra show that TTNTAs without an oxygen plasma treatment exhibit peaks at 531.90 eV and 530.14 eV, which correspond to Ti (3+) and HO-Ti (3+) respectively (**Figure 4-11a**).

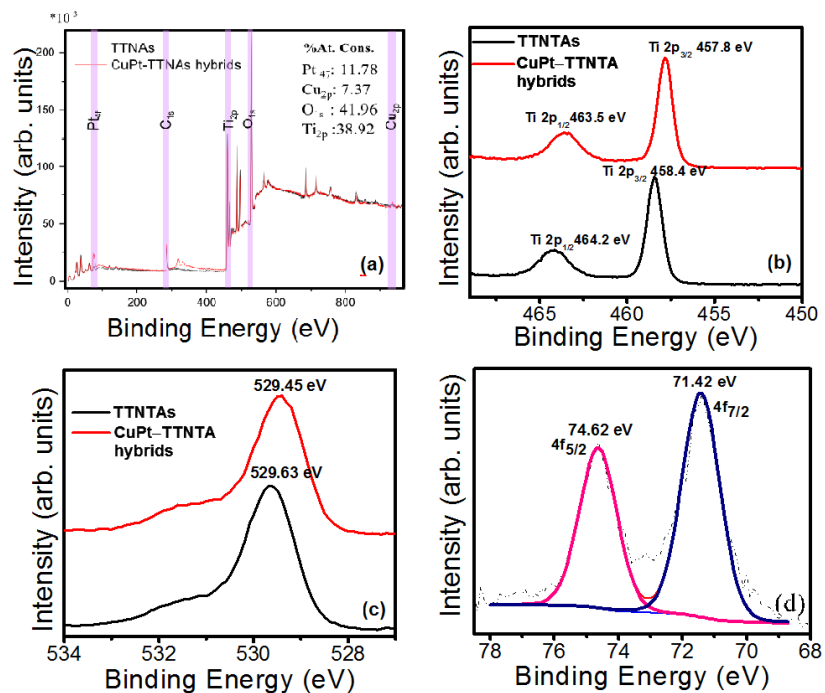


Figure 4-10. TTNTA:CuPt-NP hybrids (a) XPS survey and chemical composition of Pt, Cu, O, Ti (b) Ti2p (c) O1s and (d) Pt 4f.

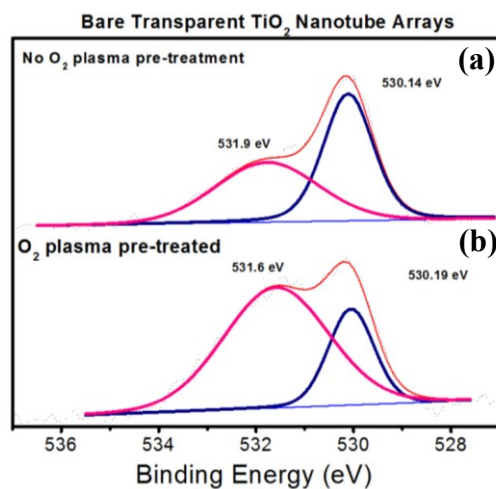


Figure 4-11. Peak decomposed O1s core level spectra for TTNTAs (a) without an oxygen plasma cleaning treatment and (b) with an oxygen plasma cleaning treatment.

Oxygen plasma treatment of the surface changes the relative weighting of the two peaks but leaves the peak positions almost unchanged (**Figure 4-11b**). On the

other hand, photodeposition of CuPt consistently shifts both the peaks constituting the O1s spectrum to lower binding energies (**Figure 4-12a**).

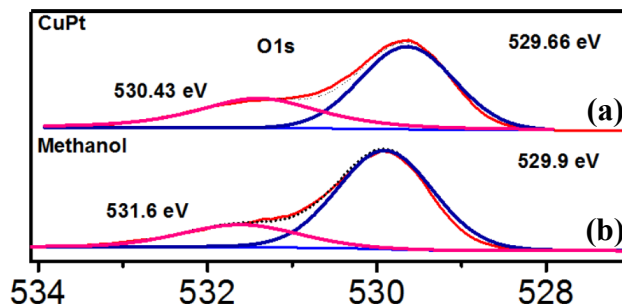


Figure 4-12. Peak decomposed O1s core level spectra for TTNTAs photodeposited with CuPt compared to TTNTAs subjected to AM1.5G illumination from a solar simulator in pure methanol.

This shift to lower binding energies after CuPt loading is characteristic of *n*-type semiconductors forming a Schottky junction, and occurs as a result of lattice distortion of TiO₂ surface that generates oxygen vacancies. The oxygen vacancies in TiO₂ correspond to the formation of Ti³⁺ states. Such a charge transfer process results in the shifting of binding energy of Ti to the lower energy side in CuPt-loaded TTNTAs. Measurements of multiple CuPt-TTNTA hybrid samples yielded band bending of 0.4-0.7 eV from the shifts in the Ti 2p core-level spectra.

Figure 4-13a displays the Pt 4f_{7/2} spectra with the presence of peak at 71.0 eV and 74.35 with well separation of spin-orbit component ($\Delta_{\text{metal}}=3.35$ eV) that is corresponded to the metal state of platinum. **Figure 4-13b** displays the Pt 4f_{7/2} spectra with the presence of peak at 72.7 eV that has a 1.7 eV shift compared to metallic state. As depicted in **Table 4-1** the binding energy that is corresponded to metal state for Pt4f_{7/2} is around 73.5±1.1eV and for platinum oxide (PtO₂) is around 74.85±0.75eV. This raises the question if part of this shift is due to the

oxidation state of platinum and chemisorption-induced shift or it's due to formation of nanocluster of platinum.

Table 4-1. Binding energy of common Pt-O [175] reproduced with permission from M. Peuckert et al., Surface Science, 1984. **145**(1): p. 239-259 © 1984 Published by Elsevier B.V.

Chemical state	Binding energy Pt4f _{7/2} eV	Binding energy Pt4f _{5/2} eV
Pt _{metal} (bulk)	71.015±0.285 [176-179]	74.35±0.15 [176, 180, 181]
PtO(bulk)	73.5±1.1 [248] [182-185]	74.5
PtO ₂ (bulk)	74.85±0.75[182-185]	77.4
Pt(OH) ₄	74.4	77.7
Pt O _{2-n/2} (OH) _n	74.3	77.6

As depicted in Ref [175] and [186] the chemical shift for platinum hydroxide/oxide (**Table 4-1**) is about 3 eV which is significantly higher than what we observed in photodeposited Cu_{0.078}Pt_{0.92} in comparison to bulk Platinum [186] and it indicate that this shift is not due to oxidation state of platinum.

The Pt 4f spectra can exhibit both initial and final state effects. The electric field due to the depletion region shifts the 4f_{7/2} and 4f_{5/2} peaks at 71.0 eV and 74.4 eV in bulk Pt to lower binding energies while the size-dependent screening effect shifts the peaks to higher binding energies. The width (FWHM) of the Pt 4f_{7/2} peak in bulk Pt is smaller than 0.5 eV. However, in **Figure 4-10d** and for other samples of photodeposited CuPt-TTNTA hybrids (see **Figure 4-13b**), the FWHM is ca. 1.5 eV which is indicative of the presence of Pt clusters of size 1 nm and smaller [186].

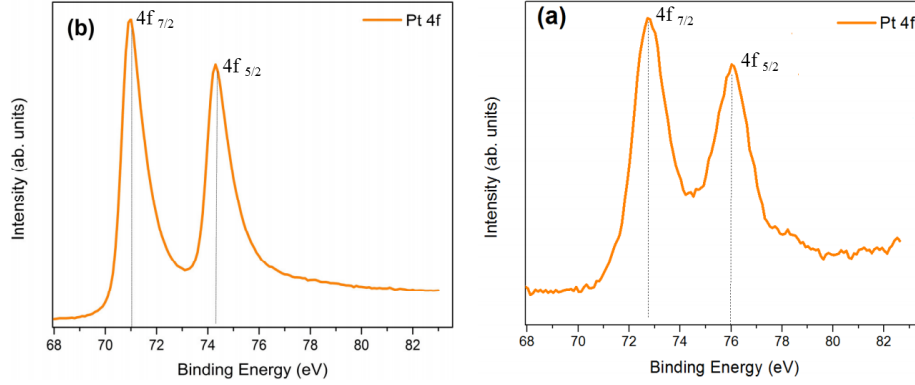


Figure 4-13. High resolution core level spectra showing the Pt $4f_{7/2}$ and Pt $4f_{5/2}$ peaks for (a) coated with CuPt nanoparticles by sputtering and (b) TTNTA samples coated with CuPt nanoparticles by photodeposition.

In **Figure 4-10d**, the binding energy shifts in the two Pt 4f peaks are +0.2 to +0.4 eV. However, for samples with band bending towards the lower end of the range (0.4-0.5 eV), the peak shifts are +1.2 to +1.5 eV as shown in **Figure 4-13b**, which we attribute to the final state effect being less obscured by the initial state effect [186]. The data obtained by us strongly indicates that metallic behavior is not fully developed in the photodeposited CuPt nanoparticles.

As shown in **Figure 4-9a-b** in order to qualify the relative concentration of Cu and Pt, the quantitative calculation has been applied on TOF-SIMS data and a ratio of 0.92: 0.078 for Pt:Cu has been calculated. However, using XPS binding energy which utilizes the peak area sensitivity is more accurate. In this method, the number of photoelectrons per second for any specific material is given by [187]:

$$I = n f \sigma \theta \gamma \lambda A T \quad (4-1)$$

Where 'n' is the number of atoms per cm^3 , ' σ ' is the photoelectric cross-section of the atomic orbital of interest in cm^2 , ' f ' is the X-ray flux, ' θ ' is the angular efficiency factor between the photon path and the detected electron, ' γ ' is the efficiency in the photoelectric

process, ' λ ' is the mean free path of the photoelectron, ' T ' is the detection efficiency and ' A ' is the area of the samples. The number of atom can be extract from equation (4-1) [187]:

$$n = \frac{I}{f\sigma\theta y\lambda AT} = \frac{I}{S} \quad (4-2)$$

Where ' s ' is atomic sensitivity. In this equation ' σ ' and ' λ ' will vary from material to material but ratio of ' σ_1/σ_2 ' and ' λ_1/λ_2 ' are nearly constant. And concentration ratio can be defined as [187]:

$$\frac{n_1}{n_2} = \frac{I_1/s_1}{I_2/s_2} \quad (4-3)$$

And atom fraction can be defined as [187]:

$$C_x = \frac{n_x}{\sum n_i} \quad (4-4)$$

We examined the specimens that were exposing to Uv and solar simulator, and we calculate atom fraction and atomic concentration of Cu and Pt by using equations (4-2) and (4-4). This result is presented in **Table 4-2**.

Table 4-2. atom fractions and concentration ratio of CuPt deposited by photodeposition method.

O ₂ plasma done	%At. Cons. of Cu	%At. Cons. of Pt	C _{cu}	C _{Pt}
CuPt _{solar simulator}	36.19	63.19	0.36	0.63
CuPt _{UV lamp}	13.28	86.72	0.13	0.86
O ₂ plasma done	C _{cu} ⁰	C _{cu} ⁺¹	C _{cu} ⁺²	C _{cu}
CuPt _{solar simulator}	11.57%	43.57%	44.84%	0.36
CuPt _{UV lamp}	17.5%	50.20%	32.47%	0.13
No- O ₂ plasma done	C _{cu} ⁰	C _{cu} ⁺¹	C _{cu} ⁺²	C _{cu}
CuPt _{solar simulator}	43.6%	37.76%	19.64%	0.36
CuPt _{UV lamp}	45.94%	37.38%	16.68%	0.13

4.5 Band alignment in CuPt coated TTNTAs

A clear difference in the UPS spectra of transparent TiO₂ nanotubes before and after the photodeposition of CuPt nanoparticles is evident in **Figure 4-14** with both the secondary electron cut-off and the valence band edge red-shifted to lower binding energies. The valence band maximum, which was previously located 3.25 eV below the Fermi level (E_f), is shifted to 2.76 eV below the Fermi level. By examining UPS spectra from multiple CuPt-TTNTA hybrid samples, a range of 0.49 - 0.67 eV was obtained for the observed band bending following CuPt photodeposition. The close agreement between the band-bending values obtained from XPS core-level spectra and UPS valence band spectra is noteworthy, and confirms the formation of a depletion region at the CuPt-TiO₂ interface following photodeposition.

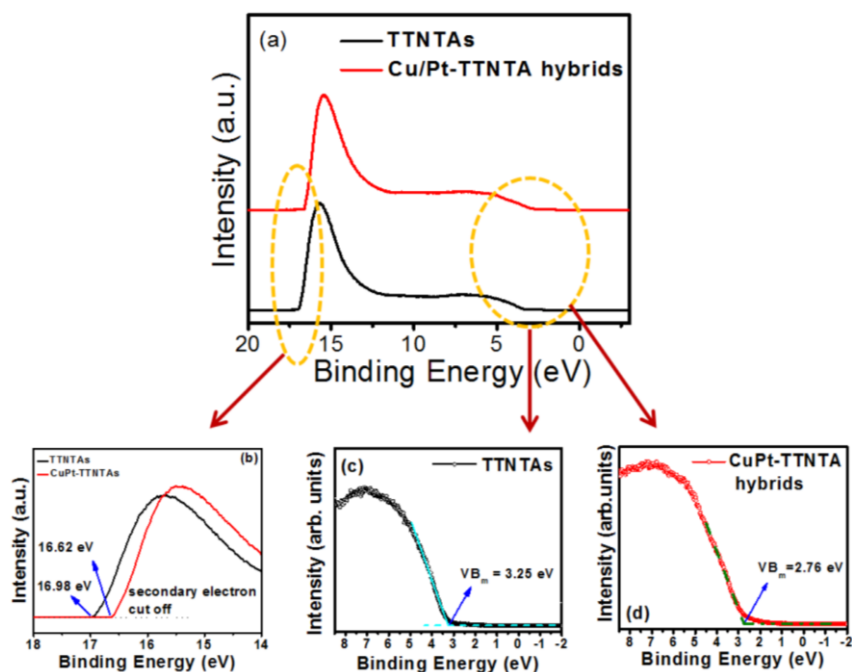


Figure 4-14. UPS data from TTNTA:CuPt-NP hybrids

The resolution of the UPS spectra is slightly superior to that of XPS spectra making the narrower UPS range more reliable. The work-function of a semiconductor surface is given by $\phi_s = h\nu - E_{SE}$ where the first term represents the energy of the photons used to probe the band-structure (He I:21.21 eV in our case) and the second term is the secondary electron cut-off transparent titania nanotubes is found to be 4.23 eV (implied electron affinity of 4.17 eV) [188] in agreement with most prior studies on anatase thin films and nanostructures, and increased by 0.36 eV upon photodeposition of CuPt to 4.59 eV. The difference of 0.13-0.31 eV between the estimated bandbending and the change in work-function indicates the formation of a surface dipole (Δ) at the CuPt nanoparticle-decorated TiO_2 surface (see **Figure 4-1**) [189].

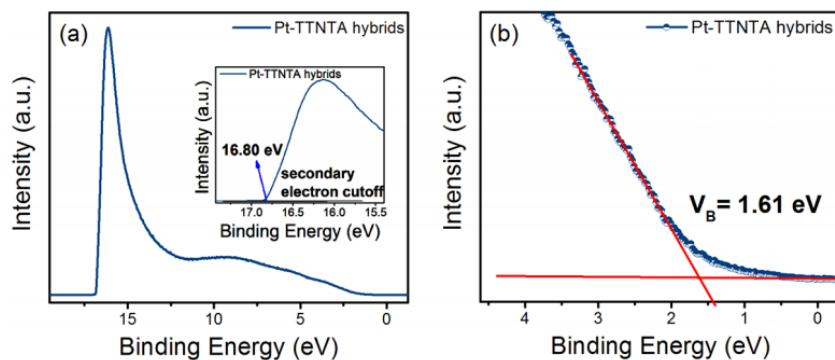


Figure 4-15. (a) UPS spectra of Pt-TTNTA hybrids with the inset showing the secondary electron cutoff region and (b) Zoomed in view of the low binding energy edge in the UPS spectrum shown in (a). The valence band maximum was estimated using the intercept on the abscissa obtained by extrapolating the low binding energy edge to the baseline.

To understand the effect of Cu in CuPt-TTNTA hybrids, UPS data were collected from Pt-TTNTA hybrids wherein TiO₂ nanotube arrays were coated with monometallic Pt nanoparticles using a near-identical photodeposition process. These data (see **Figure 2-14**) indicate the valence band edge in Pt-TTNTA hybrids to be shifted upward toward to the Fermi level by a much larger amount than in CuPt-TTNTA hybrids indicating a band bending as large as 1.6 eV. This observation can be rationalized using the Anderson model²⁹ based on the much higher work function of monometallic Pt which is reduced by the addition of Cu in bimetallic alloys.

4.6 Examination of the effect of illumination in pure methanol on the TTNTAs surface

Photodeposition was performed by us in a methanolic medium and involved the photocatalytic reduction of the noble metal precursors (acetylacetonate salts of Cu and Pt). A question that arises is whether the TiO₂ nanotubes also experience chemical reduction of the surface during this process through the ultraviolet

photon-mediated photocatalytic oxidation of methanol. The significance of this question lies in the determination of whether the observed Ti^{3+} states in CuPt-TTNTA hybrids arise from charge transfer to the metal or from reduction by methanol. Therefore photoemission spectroscopic measurements were performed in methanol under identical conditions without the metal precursors, and the resulting spectra were compared to TTNTAs and CuPt-TTNTA hybrids. The UPS spectra for methanol illuminated samples (**Figure 4-17**) are very dissimilar to those of TTNTAs and CuPt-TTNTA hybrids (**Figure 4-14**) with regards to the shape and locations of peaks and energy cut-offs. The valence band maximum for the methanol illuminated transparent titania nanotube array samples occurred at 3.10 eV, indicating a maximum band-bending of 0.15 eV produced by chemical reduction of the TiO_2 surface. For the same sample preparation and illumination conditions, the valence band maximum for CuPtTTNTA hybrids occurred at 2.76 eV.

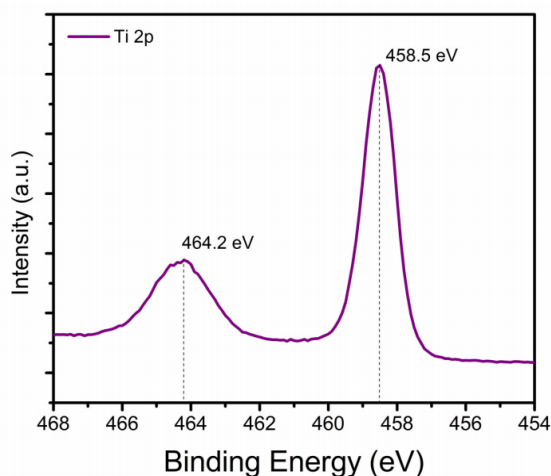


Figure 4-16. Ti 2p spectra for TTNTAs subjected to AM1.5G illumination from a solar simulator in pure methanol.

As seen in **Figure 4-16**, transparent TiO₂ nanotube samples illuminated in methanol under identical conditions but without the metal precursors do not show a shift unlike the CuPt-TTNTA hybrids in **Figure 4-14**. Thus significant band bending is indicated only in the presence of CuPt nanoparticles. The increase in work function of the methanol illuminated samples implied by the secondary electron cut-offs occurring at lower binding energies in the UPS spectrum of **Figure 4-17b** is attributed to surface adsorbates formed during the photochemical oxidation of methanol. The detailed study of such adsorbates is outside the scope of this work, but we will mention here that the dramatic attenuation of the secondary electron emission peaks in **Figure 4-17a** is a well-known sign of the presence of such adsorbates.[190, 191]

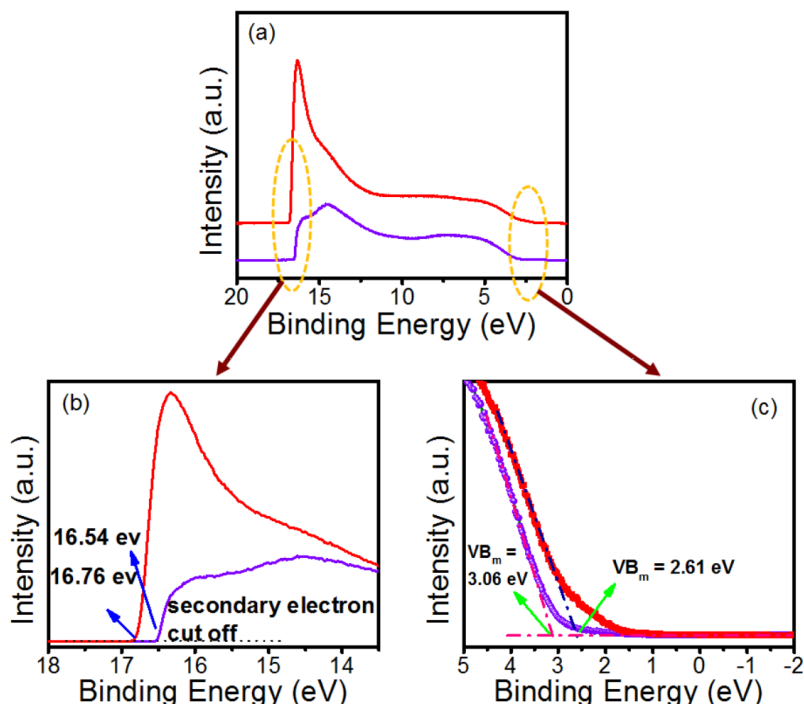


Figure 4-17. Counter-clockwise from top (a) whole UPS spectra (b) magnified view of secondary electron cut-off region and (c) valence band edges of transparent TiO₂ nanotube samples following photodeposition of CuPt NPs (red curve) and subsequent to illumination under identical conditions in methanol but without the presence of metal precursors (purple curve).

The deposition of CuPt nanoparticles is not purely a chemical reduction of the complexed Cu(II) and Pt(II) species in the respective acetylacetonates because the presence of ultraviolet radiation is essential. Therefore, the reaction is photo-induced, and it is possible to have one or both of photochemical reduction and photocatalytic deposition [192]. In photochemical reduction, the illuminated solvent (MeOH, a potent hole scavenger) is the reducing agent and it is conceivable that the TiO₂ too gets reduced in addition to the Cu(II) and Pt(II) ions. On the other hand, in photocatalytic deposition, it is illuminated TiO₂ that is the reducing agent (through photogenerated electrons). Therefore, TiO₂ can get oxidized at best but is more typically unchanged (since the reduction is performed by photogenerated excess charge carriers) [131]. The data presented here enables clear differentiation between the two phenomena under consideration. In particular, the band alignments produced by the photodeposition of CuPt on TiO₂ nanotube arrays are shown to be totally different from the corresponding alignment produced by pure photochemical reaction in methanol.

4.7 Comparison of photodeposited CuPt NPs to sputtered CuPt NPs

Figure 4-18 displays the transformation in the UPS valence band spectra of transparent TiO₂ nanotubes after the formation of 2-5 nm sized CuPt nanoparticles by sputtering. The morphology and structure of such vacuum deposited mono- and bimetallic noble metal nanoparticles deposited on to one-dimensional titania nanostructures have been reported on elsewhere [132, 155-160]. For sputtered CuPt, the UPS spectra at low binding energies show a clear Fermi edge close to $E_f = 0$ eV, which is a strong manifestation of metallic behavior. Likewise, the Pt 4f spectra in **Figure 4-13b** show peaks at 71.0 eV and 74.4 eV corresponding to

those of bulk platinum. These findings are in line with prior reports that show the metallic behavior of metal-semiconductor heterojunctions dominating at metal coverages exceeding 2 nm. The FWHM of the Pt 4f_{7/2} peak is ~1 eV for the sputtered CuPt NPs, less than that of photodeposited CuPt NPs by ~0.5 eV but not quite approaching the value of bulk Pt (0.5 eV).

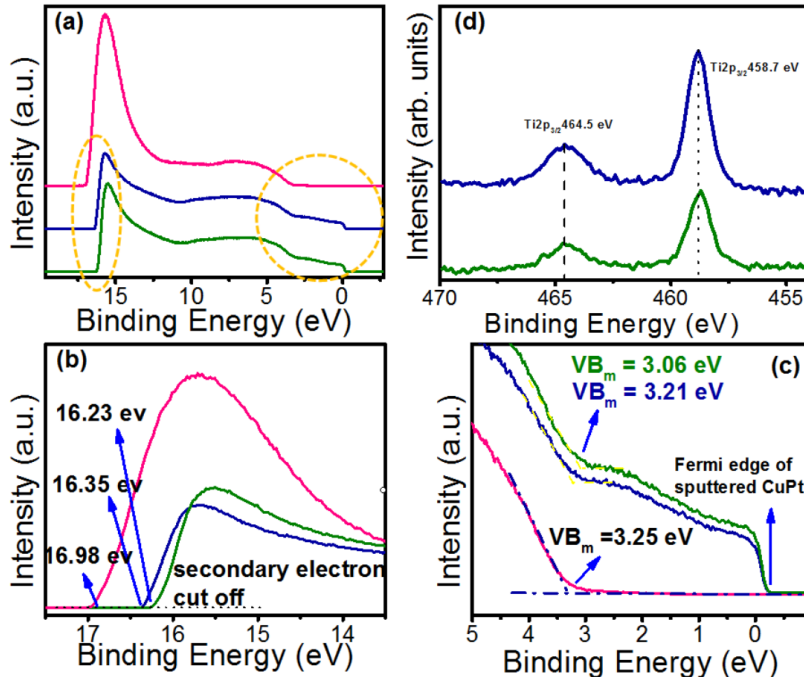


Figure 4-18. Counter-clockwise from top-right (a, b and c) Survey and magnified UPS valence band spectra of transparent TiO₂ nanotubes (pink-colored curve), sputtered CuPt nanoparticles formed on transparent TiO₂ nanotubes subsequent to an oxygen plasma clean (green-colored curves) and sputtered CuPt nanoparticles formed on transparent TiO₂ nanotubes without an oxygen plasma clean (blue-colored curves). In (d), the high resolution XPS core-level spectra of the Ti 2p peak is shown for sputtered CuPt nanoparticles formed on TiO₂ nanotube arrays.

In **Figure 4-18**, the valence band of TiO₂ is not completely obscured by the metallic behavior and is seen to be mostly unchanged by the formation of the heterojunction with sputtered CuPt. Furthermore, **Figure 4-19** highlights the vast

differences in the low binding energy XPS spectra of Sput-CuPt-TTNTA hybrids and the other types of TTNTAs studied in this report.

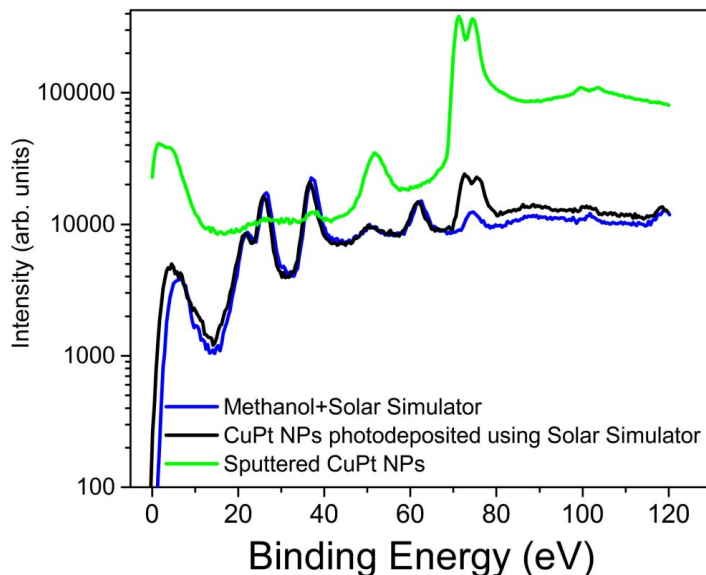


Figure 4-19. Magnified views of the low binding energy regions of the XPS spectra of TTNTAs subjected to bimetallic noble metal nanoparticle coating or ultraviolet treatment in methanol.

CuPt-TTNTA hybrids formed by photodeposition show a rich collection of features in the 0-60 eV binding energy range, rather similar to those exhibited by TTNTAs subjected to ultraviolet radiation in methanol albeit shifted. However, these features in the 0-60 eV spectral range are mostly absent or smeared out for the Sput-CuPt-TTNTA hybrids in **Figure 4-19**, which provides further confirmation of the manifestation of bulk metallic behavior in the sputtered samples and the lack thereof in the photodeposited samples. In **Figure 4-18d**, the Ti 2p binding energies for Sput-CuPt-TTNTA hybrids are slightly blue-shifted by 0.3 eV from the corresponding binding energies observed for bare TTNTAs in **Figure 4-10b**. In the absence of concomitant shifts in the Pt 4f spectra (**Figure 4-13b**) to support the formation of an accumulation layer (downward band-bending), such a shift may indicate a healing of the TiO₂ surface by

scavenging of remnant Ti^{3+} species by the deposited noble metal nanoparticles. Thus, the sputtered CuPt nanoparticles certainly do not exhibit upward band-bending (i.e. depletion) as manifested by shifts in either core-level spectra or the valence band spectra.

4.8 Work functions, Schottky barriers and surface dipoles at TTNTA surfaces

A number of samples examined in this study exhibit divergent behavior in their work-functions (as obtained from the secondary electron cut-off in the UPS spectra) and their band-bending (as obtained from shifts in the core-level binding energies and the UPS valence band edges). For instance, TTNTA samples illuminated by UV photons in methanol (**Figure 4-17c**), the valence band edge is slightly red-shifted by 0.19 eV to 3.06 eV from 3.25 eV in TTNTAs (**Figure 4-14c**) but with a red-shift of 0.44 eV in the secondary electron emission cut-off from 16.98 eV (**Figure 4-14b**) to 16.54 eV (**Figure 4-18b**). Therefore, the change in the work-function is significantly larger than the magnitude of the band-bending, and indicates the formation of a -0.25 eV surface dipole. The surface dipole does not affect the core-level binding energies of photoelectrons generated interior to itself. The absence of exact correlation between the work-function and the band-bending may be related to the orientation sensitivity of the work-function and the charge transfer. In polycrystalline TiO_2 nanotube arrays, the crystal planes exposed to the vacuum that determine the work function can be different from the crystal planes which have contributed the bulk of the transferred electronic charge. Sput-CuPt-TTNTA hybrid samples too exhibit significant shifts to higher work-functions with small or negligible band bending. However, these samples also show prominent bulk metallic character in their UPS

spectra as manifested by their Fermi edges. Therefore the work functions of 4.86-4.98 eV measured here (**Figure 4-18c**) are that of the bimetallic nanoparticles, and explained by the reduction of the platinum work-function of 5.5 eV due to the addition of lower work-function copper ($\phi_{Cu} = 4.6$ eV).

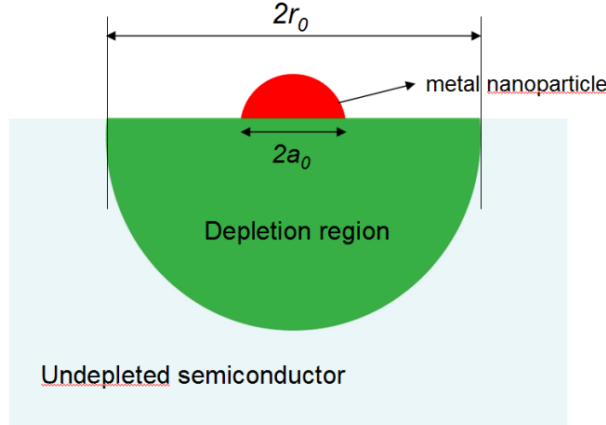


Figure 4-20. Unlike a continuous film, a discontinuous layer of metal nanoparticles decorating a surface does not produce a planar junction. For a hemispherical Schottky point-contact with a radius of a_0 , the radius (r_0) of the hemispherical depletion region formed in the semiconductor is given by $r_0 = \left(\frac{3a_0 \epsilon_r \epsilon_0 \phi_{bi}}{eN_d} \right)^{\frac{1}{3}}$ where e is the electron charge,

N_d is the carrier density in the n -type semiconductor, ϵ_r is the relative permittivity of the semiconductor, ϵ_0 is the permittivity of free-space and ϕ_{bi} is the built-in potential of the Schottky junction.

The Schottky barrier height is given by $\Phi_B = \phi_{bi} + \phi_n$ where $\phi_n (=E_c - E_f)$ depends on the intrinsic carrier concentration in the n -TiO₂ nanotubes and ϕ_{bi} is the maximum band-bending in the semiconductor. ϕ_{bi} is given by $kT \ln N_c/n$ where ' k ' is Boltzmann's constant and ' T ' is the absolute temperature, and estimated to be 0.06 eV at room temperature based on a conduction band density of states (N_c) of 10^{21} cm⁻³. In this study, we used TiO₂ nanotubes formed in ethylene glycol electrolytes and annealed in air, for which a carrier concentration (n) in the range 1.4×10^{19} – 3.5×10^{20} cm⁻³ has been measured [193, 194]. The bandgap (E_g) of anatase phase TiO₂ nanotubes (3.32 eV) is known to be slightly

larger than that of bulk anatase [195]. Thus, a range of 0.55-0.73 V is estimated for the Schottky barrier height. For a point-contact Schottky diode such as the one formed by isolated CuPt NPs decorating the walls of titania nanotube arrays, a hemispherical depletion region is obtained as shown in **Figure 4-20** [196]. We extracted the depletion region widths of such point-contact Schottky junctions with a barrier height of 0.4-0.7 V for 1 nm, 2 nm and 5 nm sized metal NPs for a range of equilibrium carrier concentrations in n-TiO₂ (**Figure 4-21**). The resulting depletion widths are 2-10 nm (inset of **Figure 4-21**). Since the wall-thickness of the TiO₂ nanotubes is in the range 25-35 nm, the nanotubes will not be fully depleted by the surface band bending.

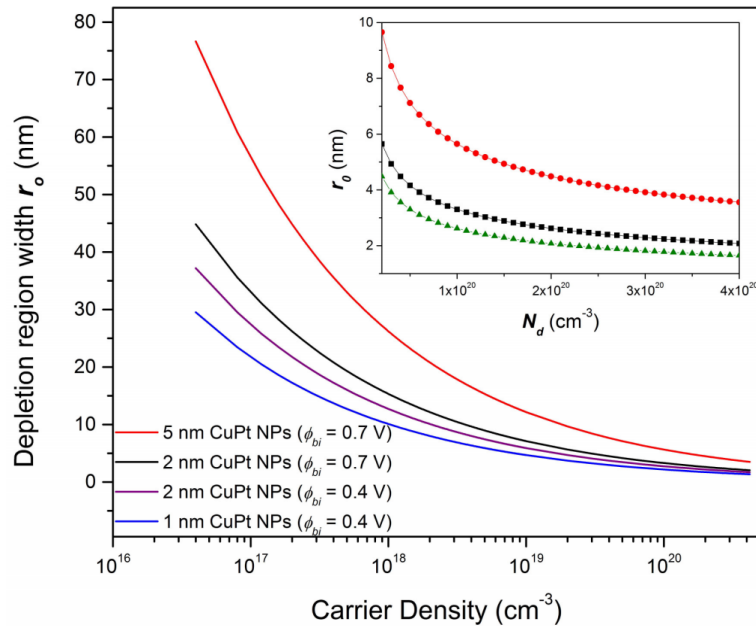


Figure 4-21. Depletion region widths for a point-contact Schottky junction between n-type anatase TiO₂ and CuPt NPs. The inset is a higher magnification view of the depletion widths obtained for the commonly observed carrier concentrations in TiO₂ nanotube arrays anodically formed in fluoride-ion containing ethylene glycol electrolytes for a band bending of 0.7 V; the depletion widths for 5 nm, 2 nm and 1 nm nanoparticles are represented by red, black and green curves respectively in the inset.

4.9 Schottky Barrier Electron Trapping?

The term "Schottky-Barrier Electron Trapping" is used quite frequently in the photocatalytic literature to describe the electron sink effect of noble metal nanoparticles [197-201]. But a Schottky barrier would indicate electron transfer to surface reactants on TiO₂ surfaces and hot hole injection into the CuPt NPs where they might participate in further reactions [202], opposite to the aforementioned electron sinking effect. At moderate incidence intensities of supra-bandgap photons (a carrier generation rate $< 10^{19} \text{ cm}^{-3}$), the term "Schottky-barrier electron trapping" would be wholly incorrect due to its implication that noble metal nanoparticles trap photogenerated electrons due to the built-in field of the Schottky junction when it is actually photogenerated holes that would be trapped by the noble metal. At high illumination intensities, flat band conditions are created which may favor electron trapping at the noble metal due to kinetic rather than energetic conditions if the hole is scavenged quickly enough by surfacebound species. But the electron trapping here would occur due to kinetic factors rather than the Schottky barrier. Likewise flat band conditions exist in very small anatase nanoparticles ($r < 20 \text{ nm}$) with a relatively low intrinsic carrier concentration that are unable to support a depletion region. But flat band conditions are unlikely to prevail in larger-sized, moderately-to heavily n-type TiO₂ crystallites or on single crystal anatase surfaces. Therefore we suggest that the term "Schottky-Barrier Electron Trapping" be used with extreme caution with *n*-type semiconductor photocatalysts if used at all. In the conventional understanding of photocatalysis, noble metal NPs act as electron sinks [203, 204] due to which transfer of photogenerated electrons to reactants occurs primarily on metal surfaces while the high oxidizing power of photogenerated holes is used in reactions on TiO₂ surfaces. The efficiency of charge-separation processes in such

a scenario is kinetically controlled by parameters such as the minority carrier diffusion length, photoinduced electron transfer rate to the metal, trapping crosssections and time-constants, etc. However, our XPS studies of the CuPt-TiO₂ interface in TTNTAs coated with photodeposited CuPt NPs (CuPt-TTNTA hybrids) show the existence of a depletion region with a built-in potential of 0.49-0.67 eV. Under actual photocatalytic reaction conditions, further variation of the interfacial electronic properties is possible due to adsorption of reactant species. Notwithstanding this, the Schottky barrier at the CuPt-TiO₂ interface detected by our studies would direct photoexcited electrons toward the TiO₂ and photoexcited holes toward the CuPt NPs (**Figure 4-1**), which would require a review of the commonly accepted mechanistic routes for various photocatalytic reactions that are almost exclusively based on hole-mediated oxidation on TiO₂ and electron-mediated reduction on the noble metal surface. The conventional model of noble metal electron sinks may still be applicable to the case of Sput-CuPt-TTNTA hybrids for which upward band bending was not detected.

Chapter 5

Wetting Phenomena using TNAs

5.1 Introduction

TiO₂ nanotube arrays (TNAs) are an intriguing class of nanomaterials. They combine the versatile application spectrum of TiO₂ with an ordered porous architecture that is easily achieved by the inexpensive process of electrochemical anodization [135]. The ability of TiO₂ to tether a wide range of biomolecules either directly or through linker monolayers in a stable fashion for extended durations, coupled with the large interfacial area and high effective refractive index of the nanotubes makes TNAs attractive for use in ultrasensitive labeled and label-free optical biosensors [205-207]. TNA-based drug-eluting bone implants utilize the non-toxic, chemically inert and mechanically robust nature of TiO₂, combined with high aspect ratio pores and the resulting diffusion-controlled release of molecules confined in the volume of the pores [208-213]. The *n*-type semiconducting behavior of TNAs concomitant with the position of the TiO₂ conduction band edge favoring ultrafast (fs) injection from a broad class of dyes, polymers and quantum dots is interesting from the perspective of constructing

ordered excitonic solar cells to overcome both the exciton diffusion bottleneck and to orthogonalize the competing processes of light absorption and charge separation [136, 214-219].

A key unifying theme in the above applications is that they all constitute hybrid devices, wherein interfaces involving the TNAs are critical. These include the dye-TNA, electrolyte-TNA and polymer-TNA interfaces in excitonic solar cells, osteoblast-TNA interface in bone implants, as well as the TNA-biomolecule, TNA-analyte and TNA-foulant interfaces in biosensors. Wetting of the TNA surface by liquids or gels is critical to the functioning of every one of the above-mentioned devices; however, such wetting behavior is currently inadequately understood and poorly optimized for peak device performance. For instance, the resilience of biomolecule-functionalized TNAs to fouling agents is controlled by the wetting characteristics of the surface. Likewise, the efficiency of the process of filling of *p*-type conjugated polymer(s) into TiO₂ nanotube arrays depends on the wetting properties of the pore-walls with respect to the polymer solution, which in turn dictates the imbibition dynamics of the polymer solution into the pores. In addition, mechanically robust, chemically inert, superamphiphobic coatings have applications in marine and industrial coatings, where the superamphiphobic coatings can retard both the nucleation of inorganic salt crystals and fouling by organic molecules. Despite such remarkable significance, issues concerning wetting rarely figure in the design of devices based on TiO₂ nanotube arrays, and consequently the existing device designs fail to take advantage of the full range of specifications, configurations and performance possibilities associated with the TNA architecture. Systematic and well-designed studies of the wetting behavior of functionalized, well-ordered TNAs are clearly needed to fill this void.

While nanoporous alumina has received some attention as an ordered porous structure for studies of wetting [220, 221], self-organized TiO₂ nanotube arrays with inner and outer wall surfaces and inter-tubular spaces present a different geometry, and potentially different wetting configurations from the hexagonal cylindrical channel architecture of nanoporous alumina. In this Chapter, we are motivated to generate and understand superamphiphobic surfaces using TiO₂ nanotube arrays. For this purpose, we functionalized titania nanotubes with perfluorinated monolayers since it is well-known that perfluorinated monolayers present the lowest energy surfaces obtainable by purely chemical surface modification [222, 223]. The low polarizability of the C-F bonds and the low overall dipole moment of perfluorinated molecules drastically reduce both Coulombic and Van der Waals interactions [224] – this is especially relevant given the high surface energy of the bare TiO₂ surfaces. The combination of chemical and geometric surface modification may be used to generate low energy liquid repellent surfaces with the added advantage of transparency [225], which are in great demand in diverse applications such as drag-free fluid flow in membranes, spatial confinement of the initiation of chemical reactions, prevention of biofouling, amelioration of fogging and freezing on mirrors and windows, etc. There exist both obvious and subtle differences in wetting phenomena on flat and nanotubular TiO₂ surfaces when functionalized using the same monolayer. For strongly lyophobic monolayers, the annular surfaces of the nanotubes reduce the effective contact area available for wetting and nearly eliminate hysteresis since any imbibition of the solvent droplet into the nanotubes encounters further repulsion from molecules adsorbed on the nanotube walls. On the other hand, in ambient conditions, the imbibition of solvent droplets into nanotubes derivatized by strongly lyophilic monolayers is constrained by the buoyant force of air trapped in the nanotubes [220]. In comparison to textured surfaces that use

microstructures, texturing-based on nanostructures is expected to reduce pinning and improve agreement with the Wenzel and Cassie-Baxter theories [226-228].

In this chapter, we study the wetting behavior of clean, unclogged, debris-free TNA surfaces coated with linear chain perfluorinated monolayers formed by self-assembly. Two different nanotube diameters and planar films were studied to understand geometric effects. In order to form a perfluorinated monolayer, we chose not to use the commonly employed perfluorinated alkyltrichlorosilane as the coupling agent, due to its well-known propensity to form three-dimensional multilayer polymer films (thus diminishing the structural effect of the nanotubes) and possessing only moderate binding strength to TiO_2 surfaces [229]. Instead, we used non-polymerizing perfluorinated alkanephosphonic acid and perfluorinated alkanecarboxylic acid, whose headgroups have high binding strength to TiO_2 surfaces. We examined many different classes of liquids including polar protic, polar aprotic and non-polar solvents to establish amphiphobicity. We also present a theoretical analysis of the wetting behavior, ensuring that the present work becomes the first systematic study on wetting properties of TNAs providing ample design specifications for future research.

TNAs have a hardness (> 1 GPa) [230, 231], Young's Modulus (23-44 GPa) [231, 232] and fracture toughness ($1-2.8 \text{ MPa}\cdot\text{m}^{1/2}$) [233] that is either comparable to or higher than films made of polytetrafluoroethylene (PTFE) and other polymers [234], which are currently the predominantly used hydrophobic and amphiphobic surfaces. Therefore, amphiphobic coatings and composites based on TiO_2 nanotube arrays offer the potential of more mechanical robustness, particularly for wear-resistant applications.

5.2 Theory behind wettability of TNAs

Wettability is defined by the interfacial equilibrium contact angle. As shown in **Figure 5-1**, when θ is larger than 90° , the liquid will not wet the surface and for θ less than 90° , the surface is partially or completely wettable. Surface energy is the most critical parameter in determining the wettability of the surface. If surface energy of the substrate is γ_{SA} , surface tension of liquid is γ_{LA} and interfacial tension is γ_{SL} , then spreading coefficient is stated as:

$$s = \gamma_{SA} - (\gamma_{LA} - \gamma_{SL}) \quad (5-1)$$

Spreading occurs when $\gamma_{SA} > \gamma_{SL} + \gamma_{LA}$. Based on spreading coefficient, it is observed that, there is a direct relation between the surface energy of the substrate and the surface tension of the liquid with contact angle. Surface energy of the substrate is controllable by functionalizing them with self-assembled monolayers or polymer coatings. In 2005, the wetting behavior of TNAs was investigated by Balaur et al [78, 235]. They functionalized the surface of nanotubes by octadecylphosphonic acid to make them hydrophobic.

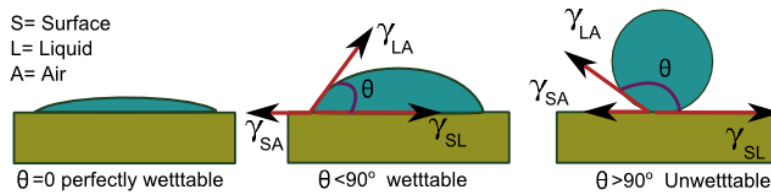


Figure 5-1. Schematic image for contact angles versus wettability

There is a direct relation between the number of carbon atoms in the carbon chain backbone and surface energy. Although, the surface energy will be decreased by increasing the number of carbon (due to improved close-packing of

the monolayer and restricted access to the underlying substrate), due to the nature of the terminal CH₂ and CH₃ groups, surface energy (γ_{SA}) will remain high. CH₂ and CH₃ terminal groups are non-reactive but strongly interact with hydrocarbon compounds through dispersive Van der Waals forces due to which their surface energies are in the range of 31 and 22 mN/m, respectively [236].

Fluorinated compounds form a chemical family with a carbon backbone where one or more hydrogen atoms are substituted by fluorine atoms. Perfluorinated compounds are those where the hydrogen atoms are fully substituted by fluorine atoms. Due to the low polarizability of the C-F bond, fluorinated hydrocarbons exhibit weak polar interactions as well as weak dispersive interactions thus rendering them repellent to both hydrocarbons and water (**Table 5-1**). Surface energies of perfluorinated compounds are estimated to be in the range 6 - 18 mN/m (CF₃, CF₂ terminations respectively).

Table 5-1. Chemical properties of organic solvents used in contact angle tests

Liquid	Surface tension @ 20 °C in mN/m	dispersion	Density (gr/ml)	Boiling point (°C)	Solubility in water gr/100 gr
Water	72.8	21.8	0.998	100	100%
Ethylene Glycol	47.7	21	1.115	197	Miscible
N,N-dimethyl formamide (DMF)	37.1	17.4	0.944	153	Miscible
Dimethyl sulfoxide	43.54	36	1.092	189	Miscible
Toluene	28.4	28.5	0.867	110.6	0.05
Diiodomethane	50.8	47.4	3.3254	182	0.124
n-Hexane	18.43	14.9	0.655	69	0.00%

Due to the higher phobicity of fluorinated hydrocarbons to water and oil, they are used in several industry and consumer products such as coated cookware, military uniforms, waterproof outdoor clothing, food handling equipment, fire

fighter foams and any water or oil repellent product. During the last two decades, a variety of studies have been conducted regarding the effect of using fluorinated compounds with different pendant functional groups. Based on the literature, by increasing the carbon chain length, the surface energy will be drastically decreased [236, 237].

5.3 Preparation of TNAs and planar TiO₂ thin films¹⁰

Titanium dioxide nanotube arrays were prepared by electrochemical anodization at room temperature using a two-electrode geometry [238]. Prior to anodization, titanium foil was degreased ultrasonically in acetone, DI water and methanol for 10 minutes each. The Ti foil was connected with the electrolyte by an O-ring and formed the anode; the cathode consisted of a piece of titanium with a surface area half time that of the Ti foil.

The distance between the Ti foil and the cathode was approximately 5 ± 0.1 cm. A DC power supply was used to drive the reaction. For growing highly ordered nanotubes, a two-step process involving pre-anodization in the first step, was used. In all steps, the electrolyte contained 0.3 wt% NH₄F and 4% DI water in

¹⁰ **Materials:** Linear chain perfluorononanoic acid (PFNA) with the molecular structure CF₃(CF₂)₇ COOH was purchased from Sigma Aldrich Corp. 1H, 1H', 2H, 2H'-perfluorodecyl phosphonic acid (PFDPA) with the molecular structure CF₃(CF₂)₉(CH₂)₂ PO₃H₂ was supplied by Aculon Inc. Methanol (99.8%), *n*-hexane (95%), N,N-Dimethylformamide (99.9%), dimethyl sulfoxide (99.9%), diiodomethane, toluene (99.5%), acetone (99.5%), ethylene glycol (99.9%) and ammonium fluoride (98.3%) were obtained from Fisher Scientific. Deionized (DI) water used for contact angle measurements was obtained from ELGA system (PURELAB Ultra, ELGA).

ethylene glycol. The pre-anodization step involved anodization of the Ti foil at 65 V for 2 hours followed by ultrasonic delamination of the oxide nanotube layer from the surface to leave a pattern of pits to nucleate ordered nanotubes in the second step. After the first step pre-anodization, the Ti foil was assembled back in the ethylene glycol electrolyte to perform the secondary anodization for another 24 hours. Before the formal anodization, the oxide layer was delaminated ultrasonically, and a pattern was left on the surface of foil.

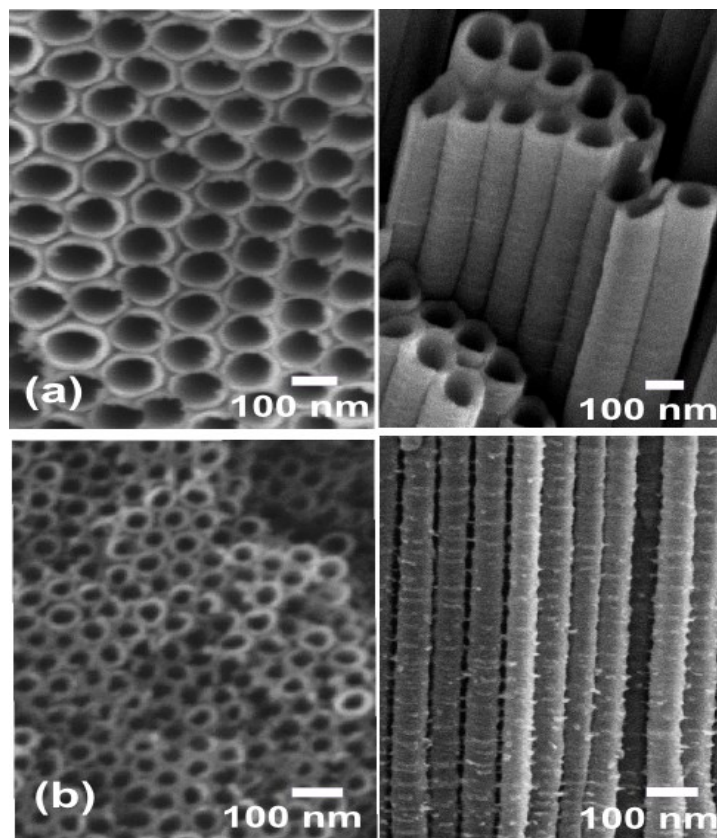


Figure 5-2. FESEM images of the two TiO_2 nanotube array geometries used in this study - (a) TNAs of 100 nm average inner diameter formed by anodization at 65 V and (b) TNAs of 30 nm average inner diameter formed by anodization at 20 V.

Subsequently, the exposed titanium was used for the first step formal anodization at 65 V for three hours followed by rinsing in methanol and drying by pressurized nitrogen. For anodizing small diameter nanotubes, Ti foils were

anodized for 72 hours at 20 V and since small diameter nanotubes are more difficult to delaminate, pre-anodization was not used. These TNAs are further treated with oxygen plasma in order to hydroxylate the surface. Concurrently, thin films of planar TiO₂ were prepared by annealing Ti foil overnight on a hot plate at 200° C. The cleaning steps for the Ti foil were identical to those used for the growth of TNAs.

5.3.1 Surface functionalization

Two different molecular monolayers were used to perform the functionalization of planar TiO₂ thin film (*TTF*), small diameter (*TNA_{Small}*) and big diameter (*TNA_{Large}*) titanium dioxide nanotube arrays. Functionalized surfaces were generated by 10 hour immersion in 1 mM solution of perfluorononanoic acid in n-hexane, and in 1 mM perfluorodecane phosphonic acid in methanol, respectively. Functionalization of nanotubes of two different diameters by PFNA and PFDPA resulted in four different kinds of substrates—*TNA_{Large}^{PFDPA}*, *TNA_{Large}^{PFNA}*, *TNA_{Small}^{PFDPA}* and *TNA_{Small}^{PFNA}*. Systematic wetting studies of TiO₂ thin films (*TTF*), bare nanotubes (*TNA_{Large}* and *TNA_{Small}*) and functionalized thin films, *TTF^{PFDPA}* and *TTF^{PFNA}* were performed prior to the measurements of contact angles on *TNA_{Large}^{PFDPA}*, *TNA_{Large}^{PFNA}*, *TNA_{Small}^{PFDPA}* and. Thus, we had in total nine substrates for the contact angle measurements. At least two samples of each type of substrate were used for contact angle measurements. The complete process flow for the generation functionalized TiO₂ thin films and nanotube arrays in illustrated in **Figure 5-3**.

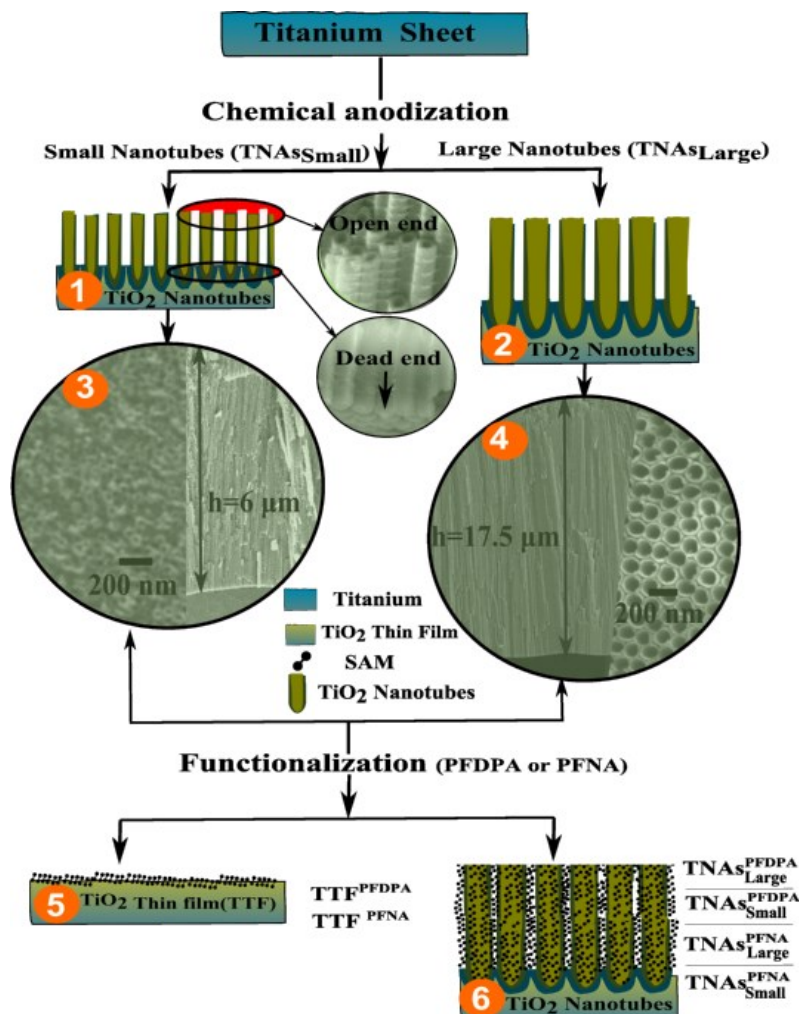


Figure 5-3. The process flow for the preparation of the TNAs coated with perfluoroalkyl monolayers. A Ti foil was used to synthesize the nanotubes by electrochemical anodization. The synthesized TNAs were of two different types – large and small which are numbered as 1($TNAs_{Small}$) and 2($TNAs_{Large}$), respectively. The encircled images beside the $TNAs_{Small}$ show the SEM images of the top and bottom of the nanotubes. The encircled images at the bottom of $TNAs_{Large}$ and $TNAs_{Small}$ (image 3 and 4) are the top and side views of the large and small nanotubes. Further, PFNA and PFDA were used obtain the two different kinds monolayers by self-assembly on planar TiO_2 thin films TTF –image 5) and $TNAs$ (image 6) substrates.

5.3.2 Characterization

The morphologies of the TNAs were imaged using a JEOL 6301F Field Emission Scanning Electron Microscope (FESEM). **Figure 5-2** shows top-views

and cross-sections of small diameter and large diameter nanotubes fabricated by the electrochemical anodization process at 65 V and 20 V, respectively. A Thermo Nicolet Nexus670 Fourier Transform Infrared (FTIR) spectrometer was used to obtain vibrational spectra from the sample surfaces in order to verify the presence of the monolayers. X-ray photoelectron spectroscopy (XPS, Kratos Analytical, Axis-Ultra) measurements were conducted out using Al K α source with energy 1486.6 eV under ultra-high vacuum (UHV) conditions ($\sim 10^{-8}$ Torr). The binding energies were calibrated by the C 1s peak of carbon at 284.6 eV. The static contact angle measurements were performed using a Drop Shape Analyzer (DSA) 100 (Krüss GmbH - Germany) and the wetting configuration of a 2 μ l drop was observed using an in-built CCD camera. The static contact angles were measured on two substrates of each kind (18 substrates in total) and a minimum of five measurements were performed at different locations on each substrate. In each case, the average contact angle was determined from a series of measurements to evaluate the consistency of wetting behavior on the studied substrate.

5.3.3 Results and Discussion

5.3.3.1 Verification of functionalization protocols

Figure 5-4 shows the XPS spectra of the functionalized TiO₂ thin films and large diameter TNAs. The high resolution spectra of Ti 2p (**Figure 5-4**) corresponds to two dominant doublet peaks at binding energies of 458.7 eV (Ti 2p_{3/2}) and 464.5 eV (Ti 2p_{1/2}), respectively for TTF^{PFDDPA} and TTF^{PFNA} [239]. This peak corresponds to the Ti⁴⁺ state of TiO₂. A minor shift of 0.2-0.3 eV is observed for TNA_{Large}^{PFDDPA} and TNA_{Large}^{PFNA} samples. A broadening in the core-level O 1s peak at 530.2 eV (**Figure 5-4b**) for TTF^{PFDDPA} and TTF^{PFNA} samples may be attributed to surface contamination.

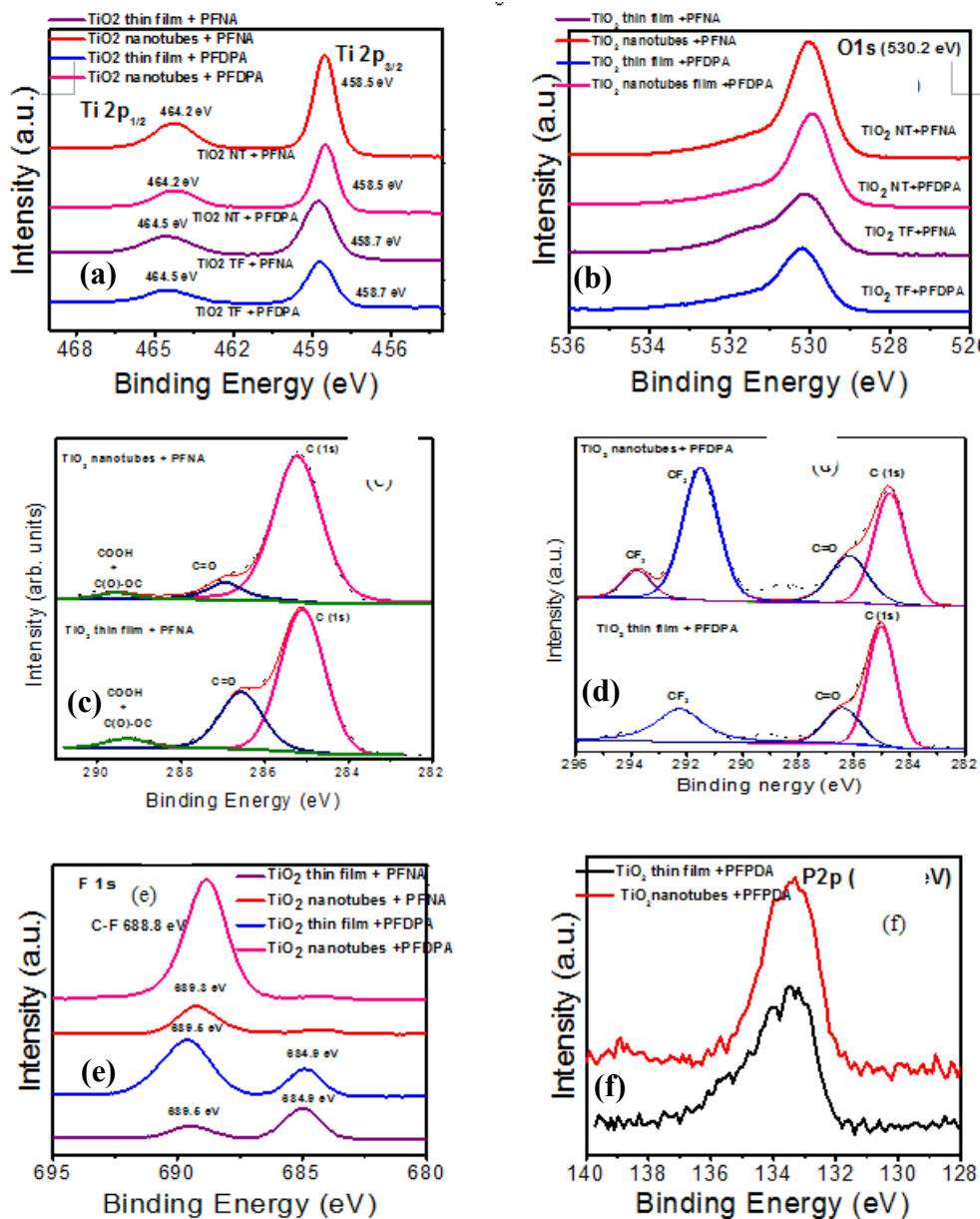


Figure 5-4. High resolution XPS spectra of TiO_2 thin films and TNALarge coated with PFNA and PFDPA.

The C 1s peaks on TiO_2 surface are deconvoluted into various peaks (**Figure 5-4c** and **d**). The tabulated details of the all the peaks present in the spectra may be found in **Table 5-2**. The main peak of carbon (C1s) is found at 284.6 ± 0.3 eV in all the samples except that of TTF^{PFNA} [240]. The C1s peak in the TTF^{PFNA} sample is shifted to 285.1 eV corresponding to C-H bonds on the

surface. The other peak found in the C1s region is at 286.4 ± 0.5 eV (C=O), which is found in all the samples. The presence of carboxyl and ester groups are seen at binding energies of 288.6 eV and 289.3 eV respectively for the PFNA-coated samples (TTF^{PFNA} and TNA_{Large}^{PFNA}) [240]. No such peak is observed in PFDPA-coated TiO₂ samples (TTF^{PFDPA} and TNA_{Large}^{PFDPA}). However, a prominent peak at a binding energy of 291.5 eV is seen in PFPDA-coated TiO₂ samples, corresponding to C-F bonds. This peak is found to be more intense in nanotube samples in comparison to thin films. The presence of C-F bonds is also seen in fluorine (F1s) XPS spectra at binding energy 689 ± 0.5 eV for all the samples (Figure 5-4e). Figure 5-4f, shows the P 2p spectra for TTF^{PFDPA} and TNA_{Large}^{PFDPA} .

Table 5-2. Identification and assignment of XPS peaks obtained from from TiO₂ thin films and nanotubes coated by PFNA and PDPFA monolayers

Samples	Elements (Region)	Peak Positions (eV)	Chemical entities
TiO ₂ –PFNA (thin films and nanotubes)	Ti	458.7 ± 0.2 eV (2p _{3/2}) 464.5 ± 0.3 eV (2p _{1/2})	TiO ₂
	O	530.2 eV (O1s)	-O-
	C(1s)	284.6 eV ± 0.3 eV (C1s)	graphitic carbon
	C	285.0 ± 0.5 eV	(C-H), sp ³ carbon
	C	286.4 ± 0.5 eV	(C=O), >C=O
	C	288.5 ± 0.5 eV	COOH + C(O)-OC
	F	689 ± 0.5 eV	C-F
	N	400 eV – 402 eV	-CN, N=O, -CONH ₂
TiO ₂ –PFDPA (thin films and nanotubes)	Ti	458.7 ± 0.2 eV (2p _{3/2}) 464.5 ± 0.3 eV (2p _{1/2})	TiO ₂
	O	530.2 eV (O1s)	-O-
	C(1s)	284.6 ± 0.3 eV (C1s)	graphitic carbon
	C	286.4 ± 0.5 eV	(C=O), >C=O
	C	292 ± 0.5 eV	CF ₂
	C	294 ± 0.5 eV	CF ₃
	F	689 ± 0.5 eV	C-F
	P	132.4 eV to 135.8 eV (as a function of oxygen environment)	P-C, P-O
N	400 eV – 402 eV	-CN, N=O, -CONH ₂	

The peak with binding energy 133.3 eV corresponds to P 2p_{3/2}, which is attributed to the pentavalent tetra coordinated phosphorous surrounded by a different chemical environment [241]. The 2p line at binding energy of 133.0 eV was reported on the surface of an alkane phosphonic acid complexed with zirconium, which was grafted on the native oxide of a Ti plate (TiO₂) [242]. A variation in binding energy of P 2p (132.4 eV to 135.8 eV) is found depending on the oxygen environment. A lowering in binding energy is reported in the P 2p when the P-OH bond (at *ca.* 134.5 eV) in, e.g., CH₃P(O)(OH)₂, is replaced by a P-C bond, as in Ph₂P-(O)OH (133.3 eV). No such peak is found in PFNA based TiO₂ samples [243, 244]. **Figure 5-5** shows the vibrational spectra of the functionalized TNAs. The bands at *ca.* 1241, 1210 and 1152 cm⁻¹ correspond to the -CF₂ stretches, thus confirming the presence of PFNA and PFDPA on the surface [245]. In **Figure 5-5b**, the strong -P=O bands in the 1230-1260 cm⁻¹ region are absent while bands in the 1000-1070 cm⁻¹ corresponding to the symmetric ν_sPO₂⁻ are prominent, pointing to a monodentate adsorption of the phosphonic acid headgroup.

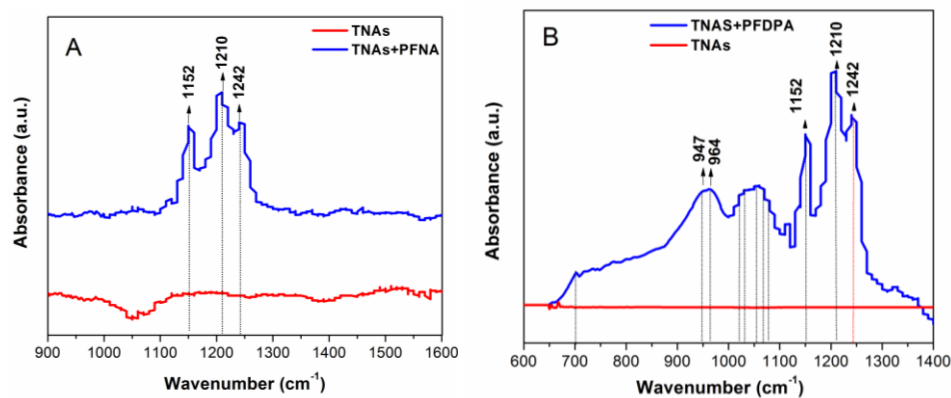


Figure 5-5. FTIR spectra of bare TiO₂ nanotube arrays (red), and subsequent to coating (blue) with a monolayer of perfluorononanoic acid (A) and perfluorodecylphosphonic acid (B).

Insight into the effect of nanostructuring was obtained by comparing the wetting characteristics of flat TiO₂ films to TNAs for identical functionalization and solvent(s). The packing density of alkanolic acid SAMs is positively correlated to the density of hydroxyl groups on the surface due to the participation of –OH groups in the bidentate binding of –COOH groups to the TiO₂. On the other hand, due to the much stronger interaction of the –PO₃H₂ headgroup with TiO₂, the packing density of alkanephosphonic acid SAMs is independent of the surface –OH group density, and equal to ~1 nmol cm⁻² on a flat TiO₂ substrate, corresponding to an area/molecule of 0.166 nm² [246].

5.3.3.2 Effect of surface morphology and surface chemistry on wetting behavior

Our main aim was to fabricate omniphobic substrates which repel a wide range of liquids or solvents. Therefore, we selected polar protic (deionized water, ethylene glycol), polar aprotic (dimethylformamide and dimethyl sulfoxide) and nonpolar (toluene and diiodomethane) solvents as working liquids for contact angle measurements to characterize the wetting properties of these disparate liquid classes on different chemically modified nanostructures. The measured contact angles for six different liquids on nine different substrates are shown in **Figure 5-6**. The exact values of contact angles with standard deviation in measurement for all six liquids on all nine substrates can be found in the **Table 5-3**. The data in **Figure 5-6**, and in **Table 5-3** provide evidence that the chemical treatment, i.e., monolayer formation is necessary for liquid repellence while geometric texturing via the creation of nanotubes generates extreme liquid repellence manifested by large static contact angles > 140°.

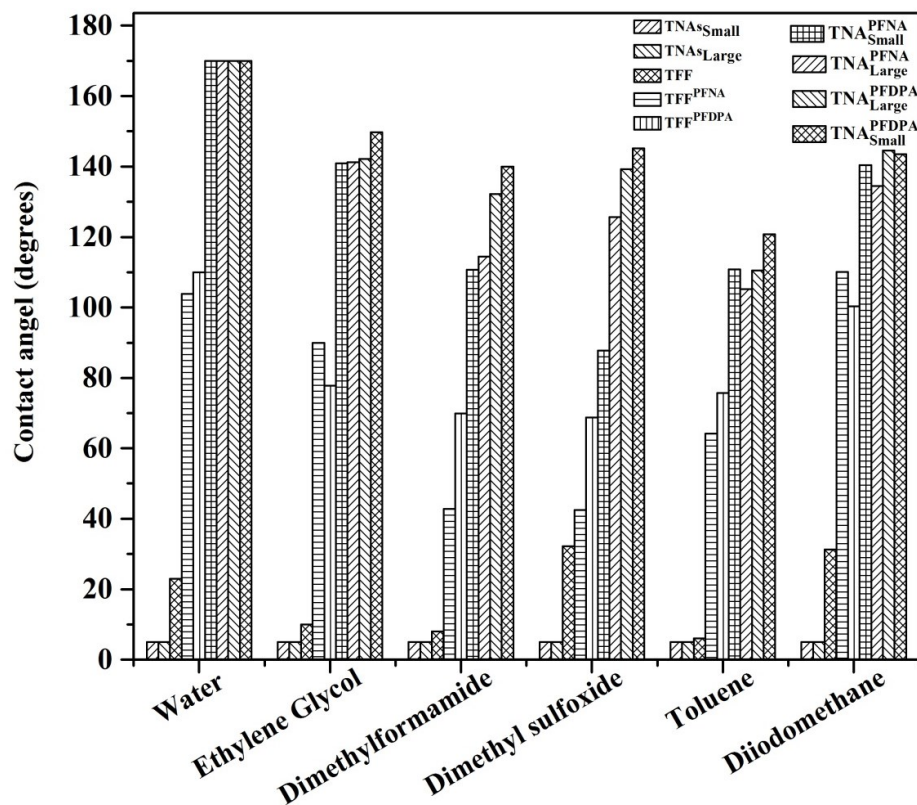


Figure 5-6. Equilibrium contact angles of different liquids on nine different substrates measured by the pendant drop technique are presented here. The bare TiO₂ thin film allows all liquids considered in this study, to spread easily; in nanotubular form (TNA_{Large} and TNA_{Small}), the substrates became more amphiphilic. The chemical treatment, namely functionalization by two different perfluorinated alkane chain-containing molecules (PFNA and PFDA) resulted in the bare flat TiO₂ thin films becoming hydrophobic surfaces (TTF^{PFDA} and TTF^{PFNA}). A similar treatment was performed on two different nanotubes (TNA_{Large} and TNA_{Small}) to generate four types of functionalized nanotube array samples (TNA_{Large}^{PFDA} , TNA_{Large}^{PFNA} , TNA_{Small}^{PFDA} and TNA_{Small}^{PFNA}), which showed distinctly different liquid-repellent characteristics compared to the bare nanotubes. The static contact angles obtained with these functionalized nanotubes are some of the highest observed for any surface.

The influence of the surface chemistry on wetting by particular liquids is commonly analyzed using the Owens-Wendt [247], Fowkes [248] or Van Oss-Good frameworks [249] in terms of the dispersive, polar and hydrogen-bonding components of the solid surface energy interacting with the corresponding

components of the liquid surface tension. We used the extended Fowkes theory [250] and the average values of the static contact angle observed using three prototypical liquids with known dispersive, polar and hydrogen-bonding components (diiodomethane, ethylene glycol and water) to determine the components of the solid surface energy, as per the following equations:

$$\begin{aligned}\gamma_L &= \gamma_L^d + \gamma_L^p + \gamma_L^h \\ \gamma_S &= \gamma_S^d + \gamma_S^p + \gamma_S^h \\ \gamma_L(1 + \cos \theta) &= 2\sqrt{\gamma_L^d \gamma_S^d} + 2\sqrt{\gamma_L^p \gamma_S^p} + 2\sqrt{\gamma_L^h \gamma_S^h}\end{aligned}\tag{5-2}$$

where γ represents the surface energy, the subscripts S and L denote solid and liquid, respectively while the superscripts d , p and h denote the dispersive, polar and hydrogen-bonding components of the surface energy, respectively. For both liquids and solid surfaces, the total surface energy is given by the sum of the dispersive, polar and hydrogen-bonding components.

While Owens-Wendt, Fowkes and Van Oss-Good theories are strictly applicable only for flat surfaces [251], applying them to nanostructured surfaces results in an estimate of the surface energy of a flat substrate that would produce the same static contact angle(s) and allows us predict the overall wetting behavior of nanotube arrays with different types of liquids [252]. The results of such an analysis are shown in **Table 5-3** and indicate a strong attenuation of the significant dispersive and hydrogen-bonding surface energies of bare (unfunctionalized) planar and nanotubular TiO₂ surfaces upon perfluoro-functionalization. The extended Fowkes analysis also indicates that nanostructuring the perfluorinated surface produces a near-complete attenuation

of polar and hydrogen bonding components of the surface energy. For example, while the polar component of the surface energy (γ_s^p) of the PFNA-functionalized flat TiO₂ sample (*TFF*) drops to 15.56 mN m⁻¹, γ_s^p for PFNA functionalized nanotube samples (TNA_{Small}^{PFNA} and TNA_{Large}^{PFNA}) is < 0.1 mN m⁻¹ (see **Table 5-3**).

A similar large drop in the hydrogen bonding component of the solid surface energy (γ_s^h) is seen for functionalized nanotube surfaces. Therefore, large static contact angles of wetting are expected for polar protic and polar aprotic solvents on nanotube surfaces, and this is indeed the case for all the polar solvents examined in this study. On the other hand, functionalized nanotube surfaces experienced only a modest decrease (< 3 mN m⁻¹) in the dispersive component (as shown in **Table 5-3**) of the surface energy in comparison to perfluorinated flat TiO₂ films.

If we closely look at **Table 5-3**, the total surface energies of the four functionalized nanotube samples (PFNA-large small and PFDPA large and small), are 2.35 mN m⁻¹, 1.03 mN m⁻¹, 0.74 mN m⁻¹ and 1.07 mN m⁻¹, respectively. The maximum difference in surface energy is 1.61 x 10⁻³ N/m, which could arise from the assumptions inherent in the extended Fowkes model and is well within the error range of the contact angle measurements. Therefore, while the Fowkes model is useful in understanding the chemical nature of the functionalized surfaces, the predictive value of the surface energy values in estimating the variations in wetting behavior as a function of nanotube morphology, type of functionalization and precise solvent, is quite limited.

Table 5-3. Contact angle (in degrees) for six different liquids on nine different substrates with the standard deviation determined from the average static contact angle. Also listed are the dispersive, polar and hydrogen-bonding components of the surface energy for each surface studied, calculating by the extended Fowkes method using the average contact angles for diiodomethane, ethylene glycol and water; $\gamma_s = \gamma_s^d + \gamma_s^p + \gamma_s^h$.

	<i>TFF</i>	<i>TFF^{PFNA}</i>	<i>TFF^{PFDA}</i>	<i>TNA_{Large}</i>	<i>TNA_{Small}</i>	<i>TNA_{Large}^{PFNA}</i>	<i>TNA_{Small}^{PFNA}</i>	<i>TNA_{Large}^{PFDA}</i>	<i>TNA_{Small}^{PFDA}</i>
Water	23.5° ±4.5°	103.9° ±15.5°	110.0° ±5.91°	< 5°	< 5°	> 170°	> 170°	> 170°	> 170°
Ethylene Glycol	< 10°	90.0° ±2.4°	77.8° ±4.99°	< 5°	< 5°	141.18° ±5.5°	140.9° ±4.5°	142.2° ±1.32°	149.7° ±0.2°
Dimethylformamide	< 10°	42.8° ±0.92°	69.9° ±2.58°	< 5°	< 5°	114.5° ±5.9°	110.7° ±2.5°	132.2° ±0.53°	140.0° ±4.92°
Dimethyl sulfoxide	32° ±2.2°	42.5° ±4.22°	68.7° ±4.93°	< 5°	< 5°	125.7° ±3.5°	87.8° ±23.3°	139.3° ±1.44°	145.2° ±2.61°
Toluene	< 5°	64.13±1.29°	75.7° ±2.46°	< 5°	< 5°	105.2° ±0.8°	110.8° ±3.44°	110.5° ±0.91°	120.8° ±2.17°
Diiodomethane	31.3±2.42°	110.1° ±3.31°	100.3° ±1.38°	< 5°	< 5°	134.5° ±1.59°	140.4° ±3.39°	144.6° ±0.38°	143.5° ±0.88°
Dispersive component of solid surface energy - γ_s^d (mN m ⁻¹)	33.27	1.65	2.92	> 43.12	> 43.12	1.40	0.59	0.30	0.64
Polar component of solid surface energy - γ_s^p (mN m ⁻¹)	14.60	15.56	21.05	> 8.36	> 8.36	0.06	0.08	0.24	0.06
Hydrogen-bonding component of solid surface energy - γ_s^h (mN m ⁻¹)	27.76	6.22	2.13	> 27.17	> 27.17	< 0.88	< 0.36	< 0.20	< 0.38
Total solid surface energy- γ_s (mN m ⁻¹)	75.63	23.42	26.10	> 78.65	> 78.65	< 2.35	< 1.03	< 0.74	< 1.07

5.3.3.3 Explanation of observed wetting behavior

As mentioned previously, aside from informing us that the functionalized nanotube surfaces have a low overall surface energy with their polar and dispersive components particularly attenuated w.r.t. functionalized flat TiO₂ surfaces, the extended Fowkes analysis of the previous section does not provide sufficient insight into the wetting configuration of different liquids on the various surfaces considered in this study. Therefore, we use a different to approach, outlined here, to analyze the observed wetting behavior. For substrates with geometric non-uniformity and chemical heterogeneity, Wenzel [253] and Cassie

[86] theories have been widely used to describe the wetting characteristics or contact angles on such substrates. Wenzel suggested that the contact angle of a liquid on a textured surface θ_r^w is a function of surface roughness and the equilibrium contact angle (θ_{flat}^e) on a flat substrate of the same material. This can be expressed as [253]

$$\cos \theta_r^w = r \cdot \cos \theta_{flat}^e \quad (5-3)$$

where r is the *surface roughness parameter* (ratio of the actual area to the projected area of the substrate containing the nanotextured surface). The theory proposed by Wenzel (Eq. (5-3)) indicates that surface roughness always magnifies the inherent wetting property of the substrate i.e. a lyophilic surface becomes even more lyophilic due to surface roughness and a lyophobic surface is rendered even more lyophobic. Therefore, we measured θ_{flat}^e on TiO₂ thin film substrates (*TTF*) and further determined θ_r^w . It was observed that, for all the liquids used in this study, the *TTF* surface is a liquid-attractive surface ($\theta_{flat}^e < 35^\circ$ for all liquids studied). This is attributed to the high surface energy of clean, bare TiO₂ due to dangling bonds and hydroxyl groups on the surface. Nanotubular TiO₂ has an even higher liquid-attractive nature, i.e., the contact angle is smaller than for flat TiO₂ surfaces for all liquids studied [35]. Thus, as predicted by Wenzel[253] a liquid-attractive bare amphiphilic surface becomes more amphiphilic with the increase in the surface roughness. This observation also implies that the drop placed on the nanotubes is in the Wenzel configuration.

As expected, the formation of a perfluorinated monolayer distinctly changes the wettability of *TTF* substrate. For example, bare *TTF* is hydrophilic, whereas

TTF^{PFDDPA} and TTF^{PFNA} are hydrophobic ($\theta_{flat}^{SAM} > 100^\circ$). However, it is highly challenging to obtain a flat monolayer-coated TiO_2 surface that is truly amphiphobic i.e. shows broad spectrum liquid repellence ($\theta_{flat}^{SAM} > 100^\circ$ for different classes of liquids). To achieve extremely liquid repellent surfaces, we need to obtain a surface where the liquid drop is in Cassie-Baxter or *fakir* state.[86] The *fakir* state is one that does not allow drop to collapse or spread (on the side walls of nano/micro structure) thereby allowing the liquid to rest at the tip of the asperities on the solid substrate. In such a scenario, the drop is suspended on the micro- or nano-scale asperities with the air underneath it. We performed similar functionalization of the nanotubes as we performed for TiO_2 thin films. It was observed by us that the nanotubes functionalized with perfluorinated monolayers showed extreme liquid repellence (**Figure 5-6**), for example TTF^{PFDDPA} is hydrophobic in nature but monolayer-coated TNAs (TNA_{Large}^{PFDDPA} , TNA_{Large}^{PFNA} , TNA_{Small}^{PFDDPA} and TNA_{Small}^{PFNA}) show superhydrophobic behavior ($\theta_{TNAs}^{SAM} > 170^\circ$). The detailed analysis and explanation of such behavior is provided in a later section.

5.3.3.4 Analysis of wetting properties and theoretical predictions of contact angle

In the case of a structurally heterogeneous surface, such as $TNAs_{Large}^{PFDDPA}$, $TNAs_{Large}^{PFNA}$, $TNAs_{Small}^{PFDDPA}$, and TNA_{Small}^{PFNA} , Cassie and Baxter reported that the contact angle of a liquid drop on a heterogeneous substrate in an air medium can be expressed as [86]:

(5-4)

$$\cos\theta_r^{CB} = f_{sl} (1 + \cos\theta_{flat}^e) - 1$$

where f_{sl} is the *contact area fraction parameter*, i.e., the ratio of the liquid-solid contact area and the projected area of the drop base. Titania nanotubes formed by anodization in ethylene glycol electrolytes are known to pack in a triangular lattice. The unit cell for the observed TiO_2 arrangements (see **Figure 5-2** and images (a) – (c) in **Figure 5-8**) can therefore be considered as an equilateral triangle, of side $2R_0$ (for nanotubes without any gap) or $2R_0+s$ (s is the inter-tubular gap) formed due to three hollow nanotubes. The representative unit cell considered for the analysis and the top view of this unit cell is shown in **Figure 5-8b**. For this case, the contact area fraction parameter (f_{sl} , f_{sl}) can be presented as Eq (5-5). Eq (5-5) was derived by considering first scenario. In **Figure 5-7**, the shaded area indicates the geometric area fraction occupied by TNAs. From symmetry considerations, each nanotube contributes $1/6^{\text{th}}$ of an annulus. The average value of all the above geometrical parameters, as estimated from scanning electron micrographs, were used to calculate the area fraction parameter f_{sl} .

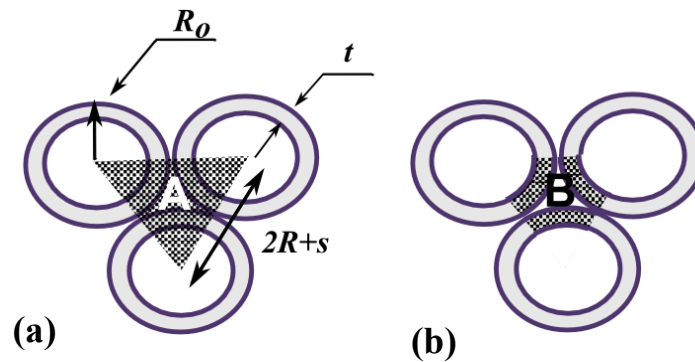


Figure 5-7. First scenario considered for the analysis: the unit cell consists of three hollow nanotubes with radius R_0 , wall-thickness t and inter-tube spacing s

$$f_{sl} = \frac{Area(B)}{Area(A)} = \frac{\frac{\pi}{2} [R_0^2 - (R_0 - t)^2]}{\frac{\sqrt{3}}{4} (2R_0 + s)^2}$$

$$f_{sl} = \frac{\frac{\pi}{2} [R_0^2 - R_0^2 + 2tR_0 - t^2]}{\frac{\sqrt{3}}{4} (2R_0 + s)^2} = \frac{\frac{\pi}{2} \left[\frac{2t}{R_0} - \left(\frac{t}{R_0} \right)^2 \right]}{\sqrt{3} R_0^2 \left(1 + \left(\frac{s}{2R_0} \right)^2 \right)}$$

(5-5)

$$f_{sl} = \frac{\frac{2t}{R_0} - \left(\frac{t}{R_0} \right)^2}{\frac{2\sqrt{3}}{\pi} \left[1 + \left(\frac{s}{2R_0} \right)^2 \right]}$$

where R_0 and t are the outer radius and wall thickness of an individual nanotube, respectively and s is the inter-tube spacing. For each of the two nanotube architectures studied, the values of R_0 , t and s were extracted using scanning electron micrographs, and are shown in **Table 5-3**. **Table 5-4** shows the comparison between the experimentally measured contact angle and the difference between the experimentally measured and theoretically predicted (using Eqs. (5-4) and (5-5)) contact angles. The subscript and superscript of the contact angle (θ) in **Table 5-4** represent the type of nanotube and the functionalization process, respectively. The value in the parenthesis represents the percentage difference between the theoretical predictions and experimentally observed contact angle measurements. It is evident that the $TNAs_{Small}^{PFDP}$ surface is the most liquid repellent surface with minimal deviation from the theoretical prediction. Both **Table 5-4** and **Table 5-3** show that PFDP-coated nanotube surfaces exhibit high contact angles ($> 130^\circ$) approaching superamphiphobic behavior for the four polar solvents examined in this study, namely water, EG, DMF and DMSO. PFNA-coated nanotube surfaces exhibit contact angles $> 140^\circ$

for the protic solvents (water and EG), and lower contact angles for the aprotic solvents, DMF and DMSO (Table 5-3).

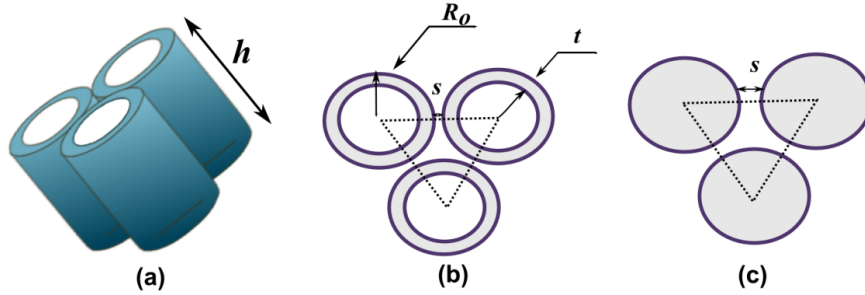


Figure 5-8. (a) The unit cell considered for the theoretical analysis assumes that the nanotubes are closely packed in a triangular lattice (b) First scenario considered for the analysis: the unit cell consists of three hollow nanotubes with height h , radius R_0 , wall-thickness t and inter-tube spacing s . (c) Second scenario considered for the analysis: The nanotubes are considered as solid nanorods of outer radius R_0 and there is a finite gap s in between them.

On the other hand, perfluoro-functionalized flat TiO_2 surfaces (TFF^{PFNA} and $\text{TFF}^{\text{PFDPA}}$) repel protic solvents and do not repel aprotic solvents (Table 5-3).

Table 5-4. The experimentally measured contact angle (θ) and deviation ($\Delta\theta$) from theoretically predicted value. The value in the parenthesis represents the percentage difference between the theoretically predicted and experimentally measured contact angle values.

Liquid	$\theta_{\text{Large}}^{\text{PFNA}}$ (°)	$\Delta\theta_{\text{Large}}^{\text{PFNA}}$ (°)	$\theta_{\text{Large}}^{\text{PFDPA}}$ (°)	$\Delta\theta_{\text{Large}}^{\text{PFDPA}}$ (°)
Ethylene Glycol	141.18±5.5	4.46(3.16)	142.2±1.32	11.20(7.87)
Dimethylformamide	114.5±5.9	6.01(5.25)	132.2±0.53	3.99(3.02)
Dimethyl sulfoxide	125.7±3.5	5.25(4.17)	139.3±1.44	11.50(8.25)
Toluene	105.2±0.8	21.31(20.29)	110.5±0.91	14.74(12.75)
Diiodomethane	134.5±1.59	9.95(7.40)	144.6±0.38	4.93(3.39)
Liquid	$\theta_{\text{Small}}^{\text{PFNA}}$	$\Delta\theta_{\text{Small}}^{\text{PFNA}}$	$\theta_{\text{Small}}^{\text{PFDPA}}$	$\Delta\theta_{\text{Small}}^{\text{PFDPA}}$
Ethylene Glycol	140.9±4.5	24.45(17.41)	149.7±.22	42.31(28.26)
Dimethylformamide	110.7±2.5	20.90(19.01)	140.0±4.92	37.15(26.53)
Dimethyl sulfoxide	87.8±23.3	1.89(2.14)	145.2±2.61	43.02(29.62)
Toluene	110.8±3.44	11.09(10.12)	120.8±2.17	14.64(12.21)
Diiodomethane	140.4±3.39	12.07(8.59)	143.5±0.88	21.854(15.22)

Thus for the polar aprotic solvents (DMF and DMSO), the liquid attractive behavior of the TFF^{PFNA} and TFF^{PFDDPA} transforms to liquid repellent behavior for the functionalized nanotubes, pointing to the likely emergence of Cassie-Baxter type wetting states. For polar protic solvents (Water and EG), the liquid-repellent behavior of TFF^{PFNA} and TFF^{PFDDPA} is amplified by nanostructuring, which could be caused by either Cassie-Baxter or Wenzel-type wetting states. Our subsequent analysis attempts to determine the nature of this wetting state. Keeping in mind that each nanotube behave as a closed pore and the inter-tube spaces act as an open space, we deduce that a liquid droplet may exist in three different configurations on the perfluorinated monolayer-coated nanotubes as shown in **Figure 5-9**. In each configuration, the local interaction between the individual nanotube and the liquid-air interface dictates the outcome of the drop configuration. In the first configuration, the drop does not spread locally on either the outer or inner surfaces of the nanotubes and consequently, we observe the failure in the drop deposition with the conventional pendant drop deposition technique [225]. The pendant drop deposition technique is a widely adopted technique to deposit the drop on the substrate for contact angle measurements where the needle with a liquid drop at its tip is brought near to the characterizing substrate and further allowed to get deposit on the substrate. During the deposition, the drop detaches from the needle and spreads on the substrate and finally one can determine the equilibrium contact angle of the drop which is in equilibrium condition on the substrate. It is to be noted that to determine the wetting characteristics of any low energy surface (the surface with very high contact angles) the drop volume needs to be smaller so that the contact angle measurements are performed without any influence of gravity [254]. This is achieved by maintaining the drop radius (R_c) much smaller than capillary length scale $l_c = \sqrt{\gamma_i/\rho g}$ where γ_i , ρ and g are the liquid surface tension, liquid density

and the gravitational acceleration respectively. In the case of very low energy surface such as functionalized *TNA* surfaces where the water drop of radius $\leq R_c$ remains attached to the needle and does not spread on the substrate. If we apply additional force on the drop through the needle to obtain the forceful spreading, first the drop rolls/slides on the characterizing surface and then climbs-up on the needle outer surface (Refer to Supplementary Video in Waghmare *et al* [255]). Since in our case the height of the nanotube is much larger than the radius h ($\sim 6-18 \mu\text{m}$) $\gg R_0$ (38-75 nm), the developed stresses at the three phase contact line (the portion at which drop is in contact with solid substrate) may disturb the nanotube arrangement [255, 256]. Moreover, if we perform the contact angle measurements on the drop that is attached to the needle, it may lead to wrong interpretation of the contact angles because the drop in this configuration always has affinity towards the needle. We have also maintained the drop-substrate contact for a longer time to allow the drop to spread without any additional force from the needle on the drop. But it was observed that the drop never spreads on the substrate and remained attached with the needle. Further, if the needle is retracted away from the characterizing substrate the drop travels along with the needle. For ultralyophobic surfaces, sessile drops of larger volume were used to observe the wetting behavior - but contact angles measured in such a configuration include the effect of gravity. For such ultralyophobic cases (e.g. water on functionalized nanotubes in this study) where a drop never gets deposited or spread on the surface, we have reported the contact angle $> 170^\circ$. In such a scenario, the drop neither stays in contact with any portion of the nanotube nor spreads locally as shown in the first configuration (image 1) of **Figure 5-9**.

For polar liquids other than water, we surmise that the liquid either spreads locally on the nanotube surface (image 2) or is in contact with a certain portion of

the nanotube to-surface (image 3) as shown in **Figure 5-9**. Whether the liquid just spreads on the tip of the nanotubes or if it imbibes in between the nanotubes or inside the nanotubes, is ambiguous. However, in our analysis thus far, we have strictly considered the drop is able to access only the top surface of the nanotubes for spreading, and therefore the geometric feature of the tip of the nanotubes (R_0 and t in Eq. (5-5)) decides the outcome of the drop configuration (using Eq. (5-4)).

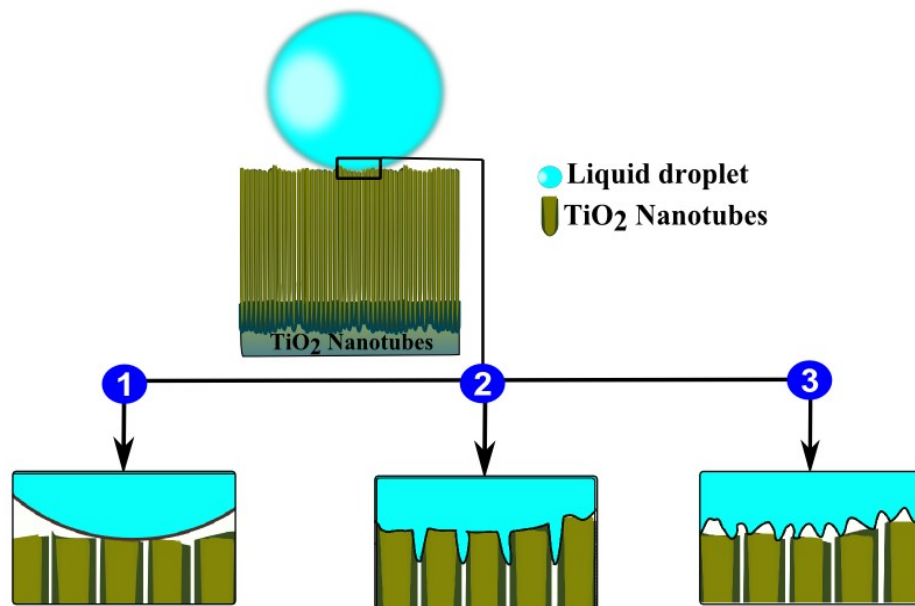


Figure 5-9. Possible drop configuration of liquids during the contact angle measurements. In the first case, the drop does not spread, whereas in the second and third cases the drop spreads over areas which are different from the area predicted by the contact area fraction parameter.

It is necessary to further investigate the local spreading of the drop to find out whether the drop has partially wetted the outer nanotube surface or whether it has imbibed inside the nanotubes. For this purpose, we have defined the experimental area fraction parameter (f_{sl}^{exp}) as follows [257]

(5-6)

$$f_{sl}^{\text{exp}} = \frac{1 + \cos \theta_{TNA_s}^e}{1 + \cos \theta_{flat}^e}$$

and compared it with the theoretically determined area fraction parameter (f_{sl}) provided in Eq. (5-5). In Eq. (5-6), $\cos \theta_{TNA_s}^e$ is the equilibrium contact angle measured on TNA surfaces. If $f_{sl}^{\text{exp}} > \dots$, then the drop wets the external surface (as shown in image 2 of **Figure 5-9**) in addition to the top surface of the pillar-like micro/nano structure. This results in over-prediction of the equilibrium contact angles. In the alternative case, where $f_{sl}^{\text{exp}} < \dots$, the drop is in contact with less area compared to the minimum available area to spread (as depicted in image 3 of Fig. **Figure 5-8**) or the area predicted by theory. The geometrical parameters (f_{sl}^{exp} and f_{sl}) for different nanotube configurations are presented in **Table 5-3**. The area fraction parameters for our cases are determined by using geometric parameters of nanotubes (Eq. (5-5) and Supplementary **Table 5-5**) and the experimentally observed contact angle values (Eq. (5-6) and Supplementary **Table 5-3**). The number in the parenthesis after the sample name in **Table 5-6** provides the theoretical area fraction parameter (f_{sl}) for four different configurations. Subsequently, the experimental area fraction parameter (f_{sl}^{exp}) for the same substrates with different liquids is also presented. It is to be noted that the experimental area fraction parameter (f_{sl}^{exp}) is determined from the contact angle values obtained from experiments and hence f_{sl}^{exp} is different for each liquid even though the drop is resting on the same geometric configuration whereas the theoretical area fraction parameter (f_{sl}) is purely a function of the geometrical parameters. It is clear from Table 2 that for the majority of studied substrate and liquid combinations $f_{sl}^{\text{exp}} < \dots$, which suggests that these liquids

prefer to be in contact with the air rather than the TiO₂ surface, and we infer that the drop is in a similar configuration to that presented in image 3 of **Figure 5-9**.

Table 5-5. Geometric parameters of nanotube-configurations studied here. The geometrical parameters of individual nanotube are obtained from SEM images.

	TNA_{Large}^{PFNA}	TNA_{Small}^{PFNA}	TNA_{Large}^{PFDDPA}	TNA_{Small}^{PFDDPA}
d (thickness of wall) nm	12	15	12	15
R (outer radius) nm	75	37.5	75	37.5
H (height) nm	17.5	6	17.5	6

Thus, we can infer the liquid drop to be in the *fakir* state, where the drop sticks to the surface but does not spread on the available surface. The reduction in contact area over and above that expected from purely geometrical considerations could be local surface roughness on the axial surface of the nanotubes and the type of molecular packing on the substrate. It is well-known that perfluorinated monolayers occupy an effective area 1.5 times that of the analogous alkane chains and are rigidly oriented almost orthogonally from the surface (i.e. parallel to the surface normal) due to the helical arrangement of CF₂ segments [258]. Due to the above mentioned larger spacing between adjacent molecules and the weaker Van der Waals interactions involving the less polarizable C-F bonds, the packing density of perfluorinated monolayers is smaller than that of alkyl chains. According to Hamaker theory [259, 260], close-packed monolayers experience stronger interactions with chemically similar molecules while a smaller molecular packing density results in weaker interactions, and therefore a larger contact angle than expected from purely chemical similarity between the molecules in the liquid and on the solid surface. These factors could explain why f_{sl}^{exp} is smaller than f_{sl} , and not equal to it. The clear exceptions to the plausible formation of *fakir* states are the wetting of toluene by TNA_{Large}^{PFNA} and TNA_{Large}^{PFDDPA} , and diiodomethane by

TNA_{Large}^{PFNA} . In these cases, $f_{sl}^{exp} > f_{sl}$ implying the liquid is wetting an area larger than dictated by the geometry of the nanotube top-surface. One may also argue that the base of the nanotube is always encapsulated, since the nanotube grows from the base, whereas the other end is always open (please see encircled SEM pictures in image 3 of **Figure 5-3**, i.e., open end and dead end).

Table 5-6. The area fraction parameter derived from experiments using Eq (5-5). And Eq (5-6). The corresponding theoretical values, are provided in parenthesis beside each different nanotube arrays.

Sample f_{sl}	(0.2842)	TNA_{Large}^{PFDA} (0.2842)	TNA_{Small}^{PFDA} (0.5803)	TNA_{Small}^{PFNA} (0.5803)
	f_{sl}^{exp}	f_{sl}^{exp}	f_{sl}^{exp}	f_{sl}^{exp}
Ethylene Glycol	0.23	0.18	0.05	0.23
Dimethylformamide	0.34	0.25	0.17	0.37
Dimethyl sulfoxide	0.24	0.18	0.13	0.60
Toluene	0.52	0.52	0.39	0.45
Diiodomethane	0.46	0.28	0.24	0.36

Thus, the entrapped air inside the nanotube pores may not find a way to get displaced if the liquid attempts to imbibe inside the nanotubes. In this situation the liquid may pressurize the entrapped air inside the nanotube instead of displacing it, and eventually the liquid may prefer the wetting of the external wall of nanotubes. The choice of configuration 2 (image 2 in **Figure 5-9**) as a possible alternative to the formation of *fakir* states is influenced by recent studies on closed pore structures [220, 261] strongly suggesting that trapped air does indeed resist the imbibition of liquid inside the pores. In such cases, one can consider the hollow tube act as a solid cylindrical pillar or as a nanorod, where the liquid can only spread on the outer surface of the nanorods. Owing to this argument, we have also performed the analysis for the case where we have assumed that the hollow nanotubes behave as a nanorod with a finite gap (s) in between them as

shown in **Figure 5-10**. The theoretical contact area fraction parameter (f_{sl}^{rod}) for such arrangement is

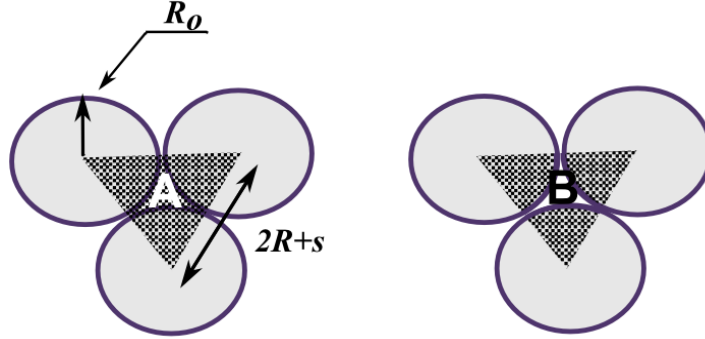


Figure 5-10. Second scenario considered for the analysis: The nanotubes are considered as solid nanorods of outer radius R_0 and there is a finite gap s in between them.

$$f_{sl}^{rod} = \frac{Area(B)}{Area(A)} = \frac{\frac{\pi}{2} [R_0^2]}{\frac{\sqrt{3}}{4} (2R_0 + s)^2} = \frac{\frac{\pi}{2} [R_0^2]}{\sqrt{3} \times R_0^2 \left(1 + \frac{s}{2R_0}\right)^2}$$

(5-7)

$$f_{sl}^{rod} = \frac{\pi}{2\sqrt{3}} \left(1 + \frac{s}{2R_0}\right)^{-2}$$

Here, the area fraction parameter of nanorods arranged in a triangular lattice is sought. The supplementary **Table 5-7** shows the difference between the measured contact angles and the theoretically determined contact angles, using Eqs. (5-7) and (5-4). It is distinctly clear that the deviation between the theoretical value and the experimentally measured contact angle for this case is much larger than the deviation observed in previous case (**Table 5-4**) i.e., the hollow nanotubes, lending further support to our speculation of drop configurations presented in

Figure 5-9 the formation of *fakir* states during wetting of functionalized nanotubes by polar liquids.

Table 5-7. Theoretically predicted contact angles (θ°) and the difference between the theory and the experimentally observed contact angle ($\Delta\theta^\circ$). Here it is assumed that the nanotubes behave like a nanorod and there is finite gap between them.

Liquid	TNA_{Large}^{PFNA}		TNA_{Small}^{PFNA}		TNA_{Large}^{PFDDPA}		TNA_{Small}^{PFDDPA}	
	θ	$\Delta\theta$	Θ	$\Delta\theta$	θ	$\Delta\theta$	θ	$\Delta\theta$
Ethylene Glycol	100.95	40.23	102.52	38.38	88.62	53.58	90.57	59.13
Dimethylformamide	62.24	52.26	65.35	45.35	82.19	50.01	84.36	55.64
Dimethyl sulfoxide	62.05	63.65	65.16	22.64	81.23	58.07	83.44	61.76
Toluene	77.62	27.38	79.98	30.82	86.89	28.61	88.90	31.90
Diiodomethane	116.43	18.07	117.61	22.79	107.80	37.20	109.19	34.31
Hexane	62.11	10.69	65.22	28.02	69.83	38.83	72.53	67.53

Now we try to understand the wetting configurations in **Table 5-6** that result in $f_{sl}^{exp} > f_{sl}$. In the case of the weakly polar liquids toluene and diiodomethane (DIM), wetting behavior different from that of polar liquids is encountered on the functionalized nanotube surfaces. **Table 5-2** shows that toluene wets flat TiO_2 (TFF), functionalized TiO_2 thin films – TFF^{PFNA} and TFF^{PFDDPA} (contact angles $< 90^\circ$) and bare nanotubes (TNA_{Large} and TNA_{Small}) whereas, it poorly wets functionalized TNAs (contact angles $> 90^\circ$). Such a transformation in wetting behavior is indicative of a Cassie-Baxter state, but the corresponding increase in the static contact angle falls significantly short of the minimum contact angles expected from the Cassie-Baxter relation for TNA_{Large}^{PFNA} and TNA_{Large}^{PFDDPA} . Flat, functionalized TFF surfaces repel DIM and this behavior is amplified in functionalized nanotubes, but likewise not to the extent expected from the Cassie-Baxter relation, for TNA_{Large}^{PFNA} . At the same time, the contact angles observed for this case diverge from the values expected for a classic Wenzel-state accounting for the complete surface area of the nanotubes. The results are suggestive of

partial imbibition of toluene and DIM into the nanotubes (image 2 in **Figure 5-8**), which corresponds to a transition between the Cassie-Baxter and Wenzel regimes. To obtain more information regarding the wetting configuration of apolar liquids on perfluorinated nanotube surfaces, we also examined the wetting behavior of hexane. Hexane is a low surface tension liquid with no purely dispersive interactions, due to which it is very difficult to construct surfaces that repel hexane. Typically a surface chemistry that results in a low energy surface needs to be coupled with a re-entrant profile to render a surface hexane-phobic.

Table 5-8. Experimentally contact angles (θ°) hexane on three non-chemically treated surface and six fluorinated surface. In all measurement $2\mu\text{l}$ droplet injected to the surface.

	TFF	TFF^{PFNA}	TFF^{PFDDPA}	TNA_{Large}	TNA_{Small}
Hexane	<10	42.6 ± 1.94	53.8 ± 3.17	<5	<5

	TNA_{Large}^{PFNA}	TNA_{Small}^{PFNA}	TNA_{Large}^{PFDDPA}	TNA_{Small}^{PFDDPA}	
Hexane	72.8 ± 4.8	37.2 ± 6.98	31.4 ± 1.56	<10	

Hexane wets TFF^{PFDDPA} and TFF^{PFNA} surfaces but $f_{sl}^{exp} > f_{sl}$ (f_{sl}^{exp} the area fraction that derived from experimental data [257] and f_{sl} is the area fraction that derived from geometrical structure of nanotubes (**Table 5-6**), ruling out a *fakir* state. Considering the large surface area of the nanotubes, and the corresponding large values of the surface area parameter r (> 100), a Wenzel state (contact angle $< 5^\circ$) resulting from complete imbibition into the nanotubes, is expected. But such a state is observed only for $S-TNAs^{PFDDPA}$ (**Table 5-8**). On the other hand, for $L-TNAs^{PFNA}$, the contact angle is 72.8° compared to 42.6° for TFF^{PFNA} . These effects can only be understood by taking into consideration the air trapped inside the nanotube pores. The balance between the capillary force and the force

resulting from the pressure of air trapped in the pore; result in a composite interface shown in **Figure 5-11** characterized by the following relationship:

$$\cos \theta_r = f_{sl} \cos \theta_{flat}^e + f_{lv} \cos \theta_{lv} + f_{ll} \cos \theta_{ll} \quad (5-8)$$

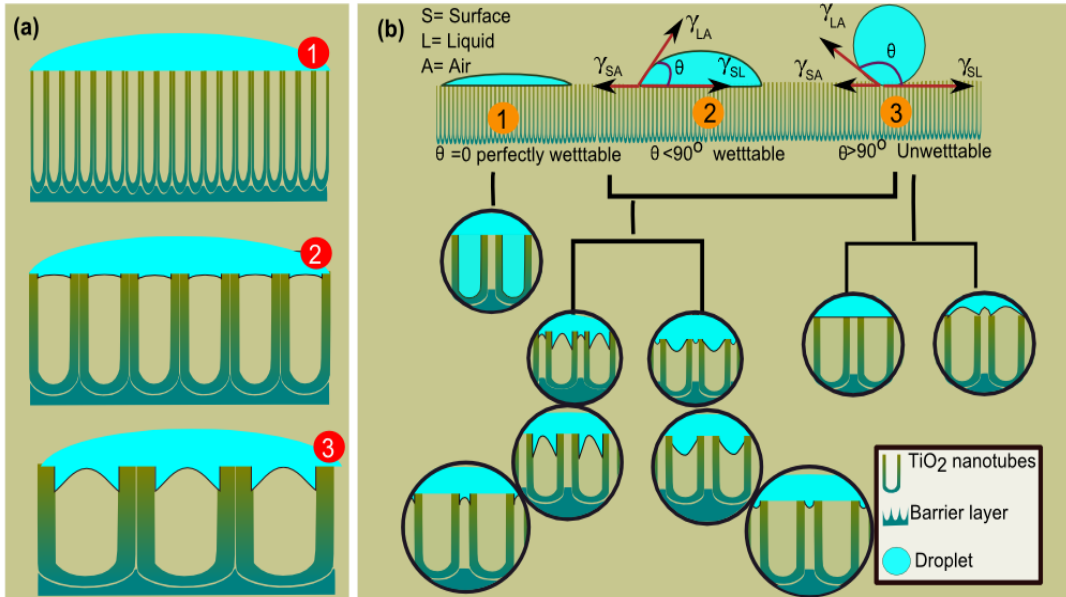


Figure 5-11. Schematic of wetting configurations of liquid droplet on a substrate containing closed nanopores. Configuration 1 depicts zero imbibition into the pores (*fakir* state), configuration 2 shows imbibition into the pores, but accompanied by only a small increase in the liquid-vapor area fraction while the configuration 3 illustrates imbibition along with a substantial increase in the liquid-vapor contact area fraction.

where as before, f_{sl} is the solid area fraction and θ_r is the contact angle of a liquid drop on the heterogeneous substrate. The new quantities introduced are the area fraction of the liquid in contact with the vapor (f_{lv}), the contact angle of wetting between the liquid and vapour ($\theta_{lv}=180^\circ$), the liquid-liquid contact fraction f_{ll} and the contact angle of wetting between the liquid and itself ($\theta_{ll}=0^\circ$). For the small diameter nanotubes in this study ($R_0 = 75$ nm), the solid area fraction f_{sl} is relatively high (> 0.5) and the capillary force given by

$F_c = \pi\gamma d_p \cos\theta_{flat}^e$ is relatively small, where d_p is the nanotube inner diameter, γ is the liquid surface tension and θ_{flat}^e is the Young's angle on the corresponding flat surface.

Consequently, liquid imbibes only a small distance into the nanopores and the increase in the liquid-vapor contact area fraction is not significant. The net result expected is a static contact angle of wetting similar to that obtained with the corresponding flat surface. Indeed, comparison of the relevant rows in **Table 5-8** shows this is exactly what is observed empirically for $S-TNAs^{PFNA}$. For the larger diameter nanotube diameters, the capillary force is larger and the liquid imbibes a considerable distance into the pores, a process that also increases the liquid-vapor contact fraction parameter whose effect is more significant. The net result expected is an increase in the static contact angle of wetting compared to smaller diameter nanotubes, which agrees perfectly with experimental observations for both $L-TNAs^{PFNA}$ and $L-TNAs^{PFDPA}$. In the nanotube architecture, due to the pressurization of trapped air in closed pores, liquid is expected to imbibe into the open inter-tubular spaces and preferentially wet the outer surfaces of the nanotubes resulting in a classic Wenzel state. But this is not observed to occur. In fact, the nanotubes studied by us behave akin to an ordered array of pores instead of an ordered array of tubes. The nanotube morphology is sensitive to the conditions of growth and the results might be telling us that under the conditions of growth employed in this study (anodization in ethylene glycol electrolytes), the inter-tubularspace is also acting as an encapsulated nanotube. But there still remains the issue of the significantly different behavior displayed by nanotubes functionalized with PFNA and PFDPA respectively, in their wettability toward hexane (**Table 5-8**), which requires understanding of the interplay of chemical and geometric factors.

For the more apolar liquids in this study (toluene, diiodomethane and hexane), dispersive interactions between the CF_2 - groups and solvent molecules can result in Wenzel-type wetting states or transition states between the Wenzel and Cassie-Baxter regimes. On flat TTF surfaces functionalized by both kinds of perfluorinated monolayers, the static contact angles of wetting for toluene and hexane (low surface tension liquids) are well below 90° due to such dispersive interactions. **Table 5-8** shows that PFDPA-coated small-diameter TNAs ($S\text{-TNAs}^{\text{PDPNA}}$) exhibit a static contact angle is much smaller ($<10^\circ$) with hexane, which is demonstrative of a Wenzel-type wetting state characterized by complete imbibition of hexane into the nanotubes. On the other hand, the contact angles with $S\text{-TNAs}^{\text{PFNA}}$ and $L\text{-TNAs}^{\text{PFNA}}$ show smaller and larger contact angles compared to the bare chemically treated surfaces (TTF^{PFNA} and $\text{TTF}^{\text{PFDPA}}$). PFNA-coated TNAs of 150 nm outer diameter, larger contact angles than PFNA-coated flat TiO_2 surfaces while PFNA-coated TNAs of 75 nm outer diameter, similar contact angles to PFNA-coated flat TiO_2 surfaces are observed.

The divergence between the wetting behaviors of hexane on PFNA- and PFDPA-coated surfaces may be rationalized on the basis of their differing molecular structures. Hexane has a lower surface tension and dispersive interactions dominate. Since both PFNA and PFDPA molecules are oriented almost normal to the surfaces on which they are anchored, imbibition of hexane into the nanopores or intertubular spaces brings hexane molecules into contact not merely with the terminal CF_3 and sub-terminal CF_2 groups but also exposes the molecular backbone to hexane molecules (see **Figure 5-12**). In PFNA, every hydrogen atom in the carbon chain is substituted by fluorine atoms (100 % fluorination) resulting in the molecular backbone being presenting a very low surface energy to hexane molecules due to non-optimal dispersive interactions

between fluorocarbons and hydrocarbons. In PFDPA, the two CH_2 groups in the backbone buried below the perfluorinated segment become exposed to the hexane molecules and experience wetting due to strong dispersive interactions.

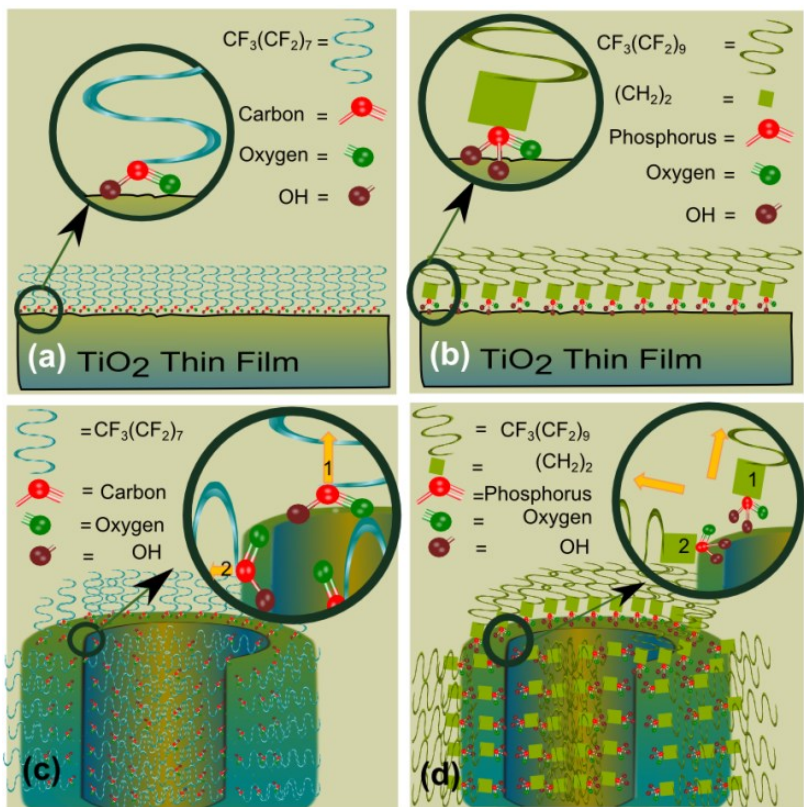


Figure 5-12. Packing, orientation and exposed terminal groups for PFNA and PFDPA self-assembled monolayers on planar and nanotubular TiO_2 surfaces.

5.3.3.5 Contact Angle Sustainability

Nanotube arrays were immersed in 35 cm of water and ethylene glycol. The static contact angle was measured. For PFDPA monolayers that underwent 24 hour immersion, the contact angle was unchanged due to the immersion treatment. For PFNA monolayers, the surface became hydrophilic after being immersed for only a few minutes, indicating the carboxylic acid to metal oxide bonds were

being broken. Images for titanium dioxide nanotubes with PFDPA monolayers before and after immersion treatment are shown below (Figure 5-13)

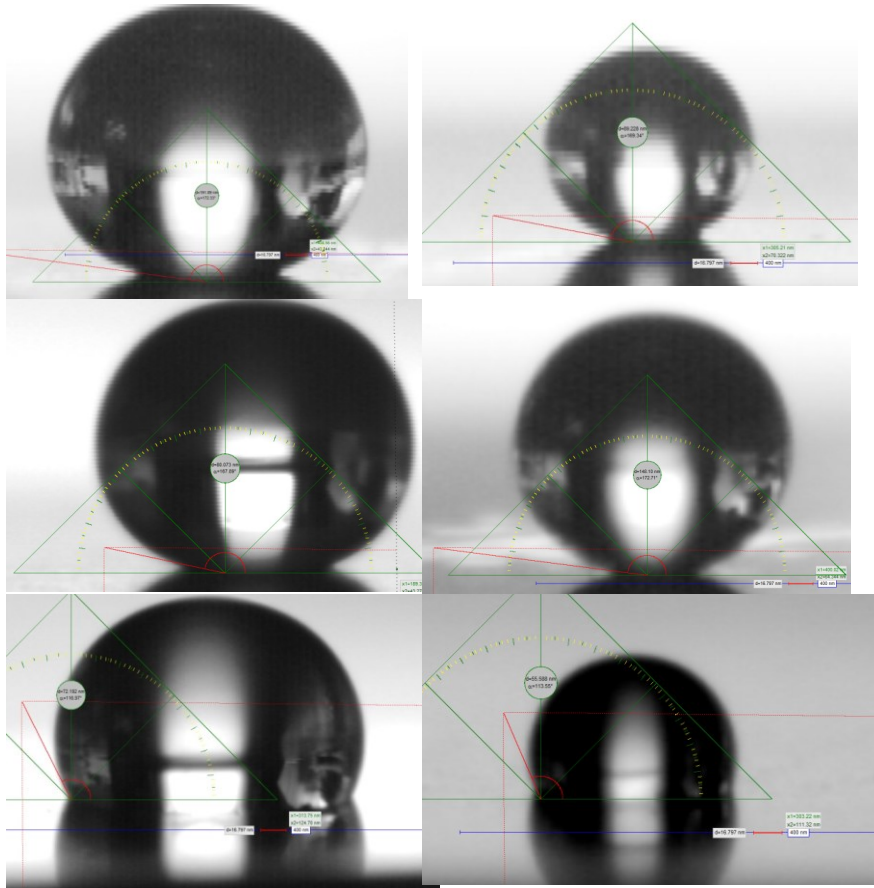


Figure 5-13. Static contact angles of water on large diameter nanotube arrays (a), small diameter nanotube arrays (b), and TiO₂ thin films (c) all treated with PFDPA. Images on left are pre-immersion treatment, on the right are post-immersion treatment in water. The contact angle is unchanged.

For additional tests of stability, S-TNAs_{PFNA}, L-TNA_{PFNA}, S-TNAs_{PFDPA} and L-TNA_{PFDPA} were immersed in oil sands process waters (OSPW) for 21 days. Due to imperfection in the SAM layer, water penetrates in S-TNAs_{PFNA} and L-TNA_{PFNA} through the monolayer and chemical reaction takes place with carboxylic acid group, and monolayer was removed in 10 minutes. The large

diameter $\text{TNA}_{\text{PFDPA}}$ showed best stability after 21 days in comparison to small diameter TNAs.

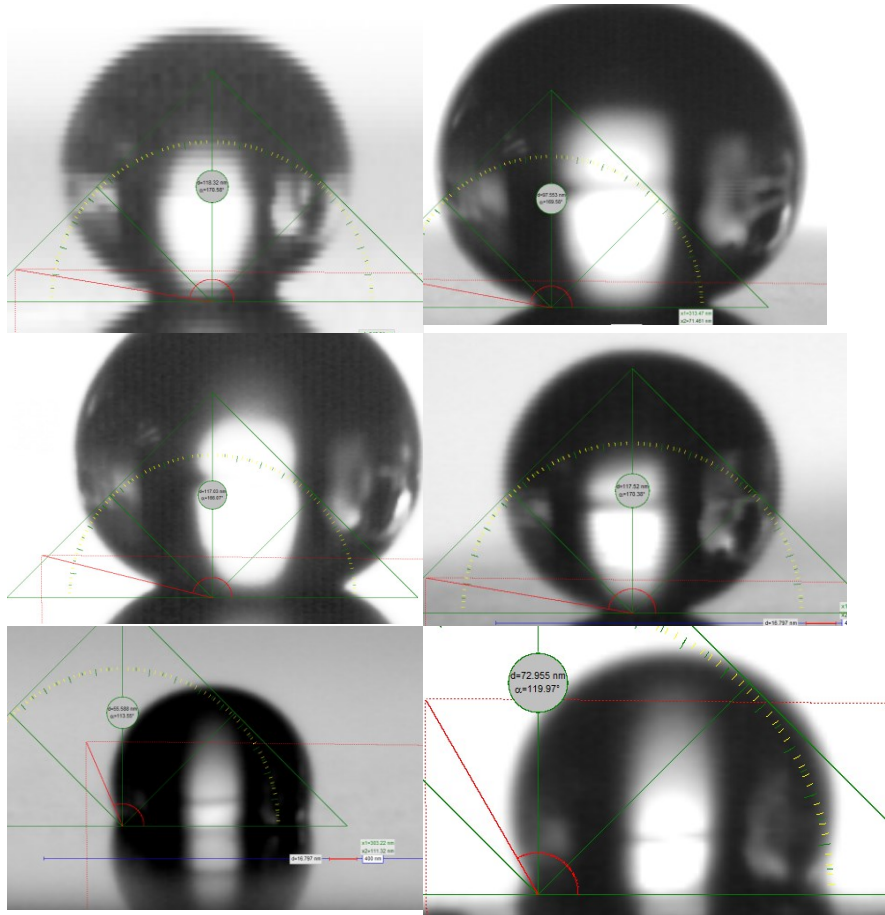


Figure 5-14. Static contact angles of water on large diameter nanotube arrays (a), small diameter nanotube arrays (b), and TiO_2 thin films (c) all treated with PFDPA. Images on left are pre-immersion treatment, on the right are post-immersion treatment in ethylene glycol. The contact angle is unchanged.

Chapter 6

Conclusion and Future Work

6.1 TNAs on non-native substrate

By varying the conditions of thin film growth over a large range of parameters, and correlating the structure and morphology of the thin films obtained to the nanostructures that resulted upon anodization, we obtained the insight that the formation of ordered nanotube arrays as opposed to disordered and irregular nanoporous structures, depends critically on the pore nucleation processes, which in turn depend on the surface roughness and grain structure of the precursor Ti films. Evaporated Ti films were found to possess small grain size and high local surface roughness, which resulted in nanotubes with extremely rough sidewalls. Ti thin films formed by Ar⁺ ion sputtering at commonly used chamber pressures of 7-20 mTorr at substrate temperatures ranging from room-temperature to 250°C possessed a highly rough surface and three-dimensional grains, which precluded the formation of ordered nanotubes upon anodization due to highly non-uniform pore nucleation processes. In contrast, Ti thin films sputtered at low chamber pressures of 0.8-2 mTorr had low surface roughness due to the atomic peening process. Such films, even when deposited at room temperature, resulted in ordered nanotube arrays upon anodization.

6.1.1 Future work in the area of TNAs on non-native substrates

TiO₂ nanotube arrays, due to high refractive index, vectorial charge transport pathways, mechanical robustness, orthogonalization of light absorption and charge transfer, acting as a host crystal lattice for intercalation of ions, being transparent in visible region and possessing a high surface area, are a promising structure and material for different optoelectronic applications including solar cells, lithium-ion batteries and photocatalysts. In this thesis, the successful growth of titania nanotubes was demonstrated on a variety of substrates (polyimide, glass, fluorine-doped tin oxide coated glass, stainless steel and SU-8) at room temperature by employing the atomic peening mechanism. This opens the way forward to fabricate nanotubes of increasing compositional or structural complexity on non-native substrates.

Niobium (Nb) is known to be a shallow donor in TiO₂. The formation of TNAs heavily doped with Nb on glass or polymer substrates could be interesting for transparent conductive oxide applications. The merger of Nb nano-precipitates in the walls of the nanotube will improve the conductivity of TiO₂ nanotube arrays that can then be used in any device that involves vectorial transport of charge. Thus one future research project could involve the controlled electrochemical anodization of co-sputtered Ti-Nb films to form nanotubes on any transparent substrate. The morphology and optical properties of anodized samples will have to be characterized using scanning and transmission electron microscopy, spectrophotometry and ellipsometry. XPS will need to be performed to study the chemical composition of the referred sample while four-point probe and other electrical measurements will be needed to determine the electrical properties.

6.2 Electronic Properties of the interfaces of TNAs with promoter noble metallic nanoparticles

The structure and electronic properties of the TiO₂-noble metal interface are important in both photocatalysis and conventional catalysis. Most of the work in this area considers TiO₂ nanoparticles - reports on TiO₂ nanotubes are scarce. Likewise, the majority of photoemission spectroscopic studies consider metal nanoparticles or films deposited under high vacuum conditions. However alternative methods of noble metal impregnation such as electrodeposition, photodeposition and colloidal synthesis are being extensively used to prepare photocatalysts. Anodically formed TiO₂ nanotube arrays coated with noble metal nanoparticles (NPs) formed by non-vacuum processes are being researched intensively for photocatalytic applications and have shown exceptional performance in recent studies. In the conventional understanding of photocatalysis, noble metal NPs act as electron sinks [262, 263] due to which transfer of photogenerated electrons to reactants occurs primarily on metal surfaces while the high oxidizing power of photogenerated holes is used in reactions on TiO₂ surfaces. The efficiency of charge-separation processes in such a scenario is kinetically controlled by parameters such as the minority carrier diffusion length, photoinduced electron transfer rate to the metal, trapping cross-sections and time-constants, etc. Therefore, it is vital to know and understand the band-alignment at the TiO₂-noble metal promoter interface.

Our XPS and UPS studies of the CuPt-TiO₂ interface in transparent TiO₂ nanotube arrays (TTNTAs) coated with photodeposited CuPt NPs (CuPt-TTNTA hybrids) showed the existence of a depletion region with a built-in potential of at least 0.6-0.7 eV. Under actual photocatalytic reaction conditions, further

variation of the interfacial electronic properties is possible due to adsorption of reactant species. Notwithstanding this, the Schottky barrier at the CuPt-TiO₂ interface detected by our studies would direct photoexcited electrons toward the TiO₂ and photoexcited holes toward the CuPt NPs, which would require a review of the commonly accepted mechanistic routes for various photocatalytic reactions. A Schottky barrier would indicate electron transfer to surface reactants on TiO₂ surfaces and hot hole injection into the CuPt NPs where they might participate in further reactions [202]. In the event of a low intrinsic electron concentration, the nanotube wall might be fully depleted and separation of the photogenerated charge would occur due to the built-in electric field of the Schottky barrier instead of being kinetically controlled.

6.2.1 Future work

In this study we measured the work function, binding energy, Schottky barrier potential and valence band position (with respect to the vacuum level) of polycrystalline anatase TiO₂ nanotubes decorated with CuPt bimetallic alloy by using XPS and UPS. Since polycrystalline anatase was used as the host material, the effect of crystallographic orientation and the effect of different crystal planes on formation of a Schottky barrier interface was not studied in this dissertation. As future work, rutile nanowire or monocrystalline anatase nanostructures can be used as a host material in order to study effect of crystal plane(s) on the formation of different interfaces. On the other hand, in the current study, we used CuPt bimetallic alloy as a guest material and the effect of the presence of Cu-NPs and Pt-NPs is not well known in band bending. As a future plan we suggest promoting TTNA by Cu-NPs and Pt-NPs separately in order to clarify the effect of the bimetallic NPs.

6.3 Wetting properties of the interfaces of TNAs with liquids

Applications of TNAs in biosensors, liquid junction solar cells, photocatalysts dispersed in liquids, photoelectrochemical water-splitting, etc. involve interactions of the titania nanotubes with various liquids, yet systematic studies of the wetting behavior of TNAs exposed to a large number of liquids from different solvent families (e.g. polar protic, polar aprotic, non-polar) are rare. It is well understood that the chemical heterogeneity and surface topography significantly influence the wetting characteristics of the substrate. The chemical heterogeneity is either achieved by chemical treatment [219] or heat treatment [264] whereas specific surface topographies are obtained by texturing the surface by fabricating micro/nanostructures [120]. However, obtaining a superomniphobic surface i.e. one that can repel a wide range of liquids (such as polar, non-polar, protic, aprotic, organic, non-organic, etc.), is still an unresolved issue. Here, we have attempted to produce a substrate that repels a wide range of liquids. We combined both approaches – the geometric texturing (by growing TNAs on the substrates) and chemical heterogeneity (by functionalizing the TiO₂ surface with liquid-repellent monolayers) to achieve this goal. The necessity of such a combined approach was validated by presenting the wetting characteristics of two different configurations of TNAs with and without chemical treatment. Secondly, the highly ordered nanotube architecture presents a model system to study wetting and imbibition processes. The functionalization of TiO₂ nanotube arrays with perfluorodecanephosphonic acid generated a surface which can be considered an omniphobic surface since it repelled a wide range of liquids (polar protic, polar aprotic and select non-polar solvents).

Wenzel [253] and Cassie-Baxter [86] theories were applied for theoretical contact angle calculations for titanium thin film (TTF) and TNAs. Transitions

from Wenzel-state to *fakir* or Cassie-states were observed in close-ended nanotubes. Small diameter TNAs exhibited higher contact angles as compared to the other substrates with minimal deviation from experimental result. By using Cassie theories, it is shown that we achieved the liquid drop in fakir or Cassie-Baxter state. The fakir state suggests that liquid doesn't spread on the surface nor stick to it. Superamphiphobic surfaces are typically designed using slender conical upright structures, which are difficult to fabricate and mechanically vulnerable. Our results indicate that the mechanically robust architecture of metal oxide nanotubes/nanopore arrays could also be used to construct superamphiphobic surfaces in a more facile way by (i) choosing appropriate surface modification and (ii) optimizing the diameter of the pores to maximize the effect of the trapped air pressure in resisting liquid imbibition into the closed pores.

6.3.1 Future work 1

TNAs have potent application in the area of pH-sensors. TNAs sensitized by pH-sensitive dyes form robust colorimetric and fluorimetric pH sensors. Initially, dye incorporated TNAs are hydrophobic in nature and cannot be used in oilsands fluid streams. The fluid stream in oilsands upgrading plants and tailings ponds contains a combination of corrosive ions and organic particulate fouling agents that are very sticky. As a result, commercially available pH sensors fare poorly in such an environment due to fouling and leaching of pH-sensitive dyes. In order to address these problems, a second non-optically active monolayer is coated to make the nanotubes amphiphobic (repellent to both water and oils) so that it may block the fouling agents from oilsands process waters (OSPW) while retaining its pH responsivity. Therefore, engineering the wettability of TNAs is important for such applications.

The future work aims to make a TNA-based pH sensor by attaching a pH-sensitive dye molecule onto them. Initially, dye incorporated TNAs are hydrophilic in nature and cannot be used for pH sensing applications in the oil sands industry. The OSPW contains some fouling agents that are very sticky with an approximate composition of 30-70% water, 2-30% bituminous solids and 20-40 % clay-type fine solids. In order to use TNAs for sensing and antifouling applications in the oilsands industry, another monolayer is coated to make it amphiphobic so that it may block the fouling agents in the OSPW. The process involves the deposition of high quality titanium (Ti) thin film on stainless steel by sputtering. The Ti foil will be used as a substrate for anodization to grow TNAs.

These TNAs are further treated with oxygen plasma in order to populate the surface with a high density of OH⁻ groups that can participate in binding. The resulting hydrophilic TNAs are immersed in a pH-sensitive dye molecule in order to attach these molecules to the exposed surfaces of the TNAs. However, because of the hydrophilic character of these dye- incorporated TNAs, they cannot be used in OSPW, where they will be subject to near immediate fouling and leaching away of the dye molecules. To prevent fouling and dye leaching, TNAs are further treated with oxygen plasma in order to remove the dye molecule only from the superficial regions of the nanotubes and then bound to a perfluorinated monolayer resulting in a repellent surface. Such amphiphobic TNAs can be used in the oilsands industry for sensing and anti-fouling applications.

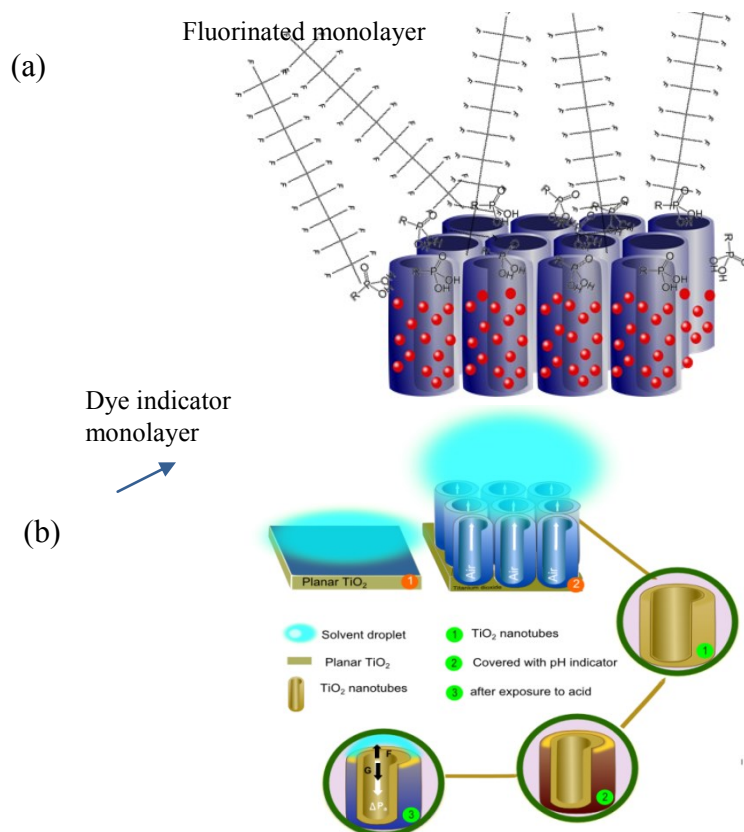


Figure 6-1. (a, b) Process flow for making a dye-based pH-sensor with an amphiphobic surface

6.3.2 Future work 2

The objective of this project will be to improve the surface properties and corrosion resistance of stainless steel, by functionalizing the surface and making it more hydrophobic for easy transport of fluids in oil industry without using vacuum deposition processes. For achieving the desired water-repellency, forming a layer of perfluorinated TiO₂ nanotubes on the steel substrates is proposed since TNAs have a high surface-to-volume ratio with hollow structures. The idea behind this is to form self-assembled monolayers (SAM) on stainless steel (with two phosphonic functional groups) and uniformly bind the perfluorinated discrete TiO₂ nanotubes to the second functional group. Spectroscopic techniques such as

FTIR will be applied to understand the nature of the bonds between the oxide layer and the monolayer.

References

1. Ma, X.Q., et al., *Preparation and characterization for depositing platinum on TiO₂ nanotubes*. Journal of Inorganic Materials, 2003. **18**(5): p. 1131-1134.
2. Varghese, O.K., et al., *Hydrogen sensing using titania nanotubes*. Sensors and Actuators B-Chemical, 2003. **93**(1-3): p. 338-344.
3. Mor, G.K., et al., *A self-cleaning, room-temperature titania-nanotube hydrogen gas sensor*. Sensor Letters, 2003. **1**(1): p. 42-46.
4. Mor, G.K., et al., *A room-temperature TiO₂-nanotube hydrogen sensor able to self-clean photoactively from environmental contamination*. Journal of Materials Research, 2004. **19**(2): p. 628-634.
5. Adachi, M., et al., *Formation of titania nanotubes and applications for dye-sensitized solar cells*. Journal of the Electrochemical Society, 2003. **150**(8): p. G488-G493.
6. Mor, G.K., et al., *Photoelectrochemical properties of titania nanotubes*. Journal of Materials Research, 2004. **19**(10): p. 2989-2996.
7. Chen, Y.X., K. Wang, and L.P. Lou, *Photodegradation of dye pollutants on silica gel supported TiO₂ particles under visible light irradiation*. Journal of Photochemistry and Photobiology a-Chemistry, 2004. **163**(1-2): p. 281-287.
8. Liang, H.C., X.Z. Li, and J. Nowotny, *Photocatalytical Properties of TiO(2) Nanotubes*, in *Solid State Chemistry and Photocatalysis of Titanium Dioxide*, M.K. Nowotny and J. Nowotny, Editors. 2010, Trans Tech Publications Ltd: Stafa-Zurich. p. 295-328.
9. Wang, N., et al., *Evaluation of bias potential enhanced photocatalytic degradation of 4-chlorophenol with TiO₂ nanotube fabricated by anodic oxidation method*. Chemical Engineering Journal, 2009. **146**(1): p. 30-35.
10. Imai, H., et al., *Morphology transcription with TiO(2) using chemical solution growth and its application for photocatalysts*. Solid State Ionics, 2002. **151**(1-4): p. 183-187.
11. Wang, K.H., et al., *The pH and anion effects on the heterogeneous photocatalytic degradation of o-methylbenzoic acid in TiO₂ aqueous suspension*. Chemosphere, 2000. **40**(4): p. 389-394.
12. Hoyer, P., *Formation of a titanium dioxide nanotube array*. Langmuir, 1996. **12**(6): p. 1411-1413.
13. Hoyer, P., *Semiconductor nanotube formation by a two-step template process*. Advanced Materials, 1996. **8**(10): p. 857-&.
14. Wisnet, A., et al., *Nanoscale investigation on large crystallites in TiO₂ nanotube arrays and implications for high-quality hybrid photodiodes*. Journal of Materials Science. **47**(17): p. 6459-6466.

15. Imai, H., et al., *Direct preparation of anatase TiO₂ nanotubes in porous alumina membranes*. Journal of Materials Chemistry, 1999. **9**(12): p. 2971-2972.
16. Sun, J., L.A. Gao, and Q.H. Zhang, *TiO₂ tubes synthesized by using ammonium sulfate and carbon nanotubes as templates*. Journal of Materials Science Letters, 2003. **22**(5): p. 339-341.
17. Lou, X.W. and H.C. Zeng, *Complex alpha-MoO₃ nanostructures with external bonding capacity for self-assembly*. Journal of the American Chemical Society, 2003. **125**(9): p. 2697-2704.
18. Peng, T.Y., et al., *Fabrication of titania tubules with high surface area and well-developed mesostructural walls by surfactant-mediated templating method*. Chemistry of Materials, 2003. **15**(10): p. 2011-2016.
19. Zhang, M., Y. Bando, and K. Wada, *Sol-gel template preparation of TiO₂ nanotubes and nanorods*. Journal of Materials Science Letters, 2001. **20**(2): p. 167-170.
20. Zhang, M., Y. Bando, and K. Wada, *Synthesis of coaxial nanotubes: Titanium oxide sheathed with silicon oxide*. Journal of Materials Research, 2001. **16**(5): p. 1408-1412.
21. Shin, H.J., et al., *Formation of TiO₂ and ZrO₂ nanotubes using atomic layer deposition with ultraprecise control of the wall thickness*. Advanced Materials, 2004. **16**(14): p. 1197-+.
22. Zwillling, V., et al., *Structure and physicochemistry of anodic oxide films on titanium and TA6V alloy*. Surface and Interface Analysis, 1999. **27**(7): p. 629-637.
23. Gong, D., et al., *Titanium oxide nanotube arrays prepared by anodic oxidation*. Journal of Materials Research, 2001. **16**(12): p. 3331-3334.
24. Shankar, K., et al., *Cation effect on the electrochemical formation of very high aspect ratio TiO₂ nanotube arrays in formamide - Water mixtures*. Journal of Physical Chemistry C, 2007. **111**(1): p. 21-26.
25. Ruan, C.M., et al., *Fabrication of highly ordered TiO₂ nanotube arrays using an organic electrolyte*. Journal of Physical Chemistry B, 2005. **109**(33): p. 15754-15759.
26. Yoriya, S., et al., *Fabrication of vertically oriented TiO₂ nanotube arrays using dimethyl sulfoxide electrolytes*. Journal of Physical Chemistry C, 2007. **111**(37): p. 13770-13776.
27. Lawandy, N.M., et al., *LASER ACTION IN STRONGLY SCATTERING MEDIA*. Nature, 1994. **368**(6470): p. 436-438.
28. Usami, A., *Theoretical study of application of multiple scattering of light to a dye-sensitized nanocrystalline photoelectrochemical cell*. Chemical Physics Letters, 1997. **277**(1-3): p. 105-108.
29. Chou, T.P., et al., *Hierarchically structured ZnO film for dye-sensitized solar cells with enhanced energy conversion efficiency*. Advanced Materials, 2007. **19**(18): p. 2588-+.
30. Zhang, Q., et al., *Polydisperse aggregates of ZnO nanocrystallites: A method for energy-conversion-efficiency enhancement in dye-sensitized solar cells*. Advanced Functional Materials, 2008. **18**(11): p. 1654-1660.

31. Yu, J.G., Q.L. Li, and Z. Shu, *Dye-sensitized solar cells based on double-layered TiO₂ composite films and enhanced photovoltaic performance*. *Electrochimica Acta*, 2011. **56**(18): p. 6293-6298.
32. Macak, J.M., et al., *Multilayer TiO₂-nanotube formation by two-step anodization*. *Electrochemical and Solid State Letters*, 2007. **10**(7): p. K28-K31.
33. Grimes, C.A. and G.K. Mor, *TiO₂ Nanotube Arrays Synthesis, Properties, and Applications Introduction*. *TiO₂ Nanotube Arrays - Synthesis, Properties, and Applications*. 2009, New York: Springer. XIII-XXVII.
34. Lee, W., et al., *Fast fabrication of long-range ordered porous alumina membranes by hard anodization*. *Nature Materials*, 2006. **5**(9): p. 741-747.
35. Lee, W., R. Scholz, and U. Goesele, *A continuous process for structurally well-defined Al₂O₃ nanotubes based on pulse anodization of aluminum*. *Nano Letters*, 2008. **8**(8): p. 2155-2160.
36. Mizeikis, V., et al., *Optical characteristics of two-dimensional photonic crystals in anodic aluminum oxide films*. *Japanese Journal of Applied Physics Part 1-Regular Papers Short Notes & Review Papers*, 2004. **43**(6A): p. 3643-3647.
37. Wang, B., et al., *Preparation of photonic crystals made of air pores in anodic alumina*. *Nanotechnology*, 2007. **18**(36).
38. Su, Y., et al., *Controllable preparation of the ordered pore arrays anodic alumina with high-quality photonic band gaps*. *Materials Letters*, 2011. **65**(17-18): p. 2693-2695.
39. Yan, P., et al., *Fabrication of one-dimensional alumina photonic crystals with a narrow band gap and their application to high-sensitivity sensors*. *Journal of Materials Chemistry C*, 2013. **1**(8): p. 1659-1664.
40. Shang, G.L., et al., *Preparation of narrow photonic bandgaps located in the near infrared region and their applications in ethanol gas sensing*. *Journal of Materials Chemistry C*, 2013. **1**(34): p. 5285-5291.
41. Lin, J., K. Liu, and X. Chen, *Synthesis of Periodically Structured Titania Nanotube Films and Their Potential for Photonic Applications*. *Small*, 2011. **7**(13): p. 1784-1789.
42. Yip, C.T., et al., *Direct and Seamless Coupling of TiO₂ Nanotube Photonic Crystal to Dye-Sensitized Solar Cell: A Single-Step Approach*. *Advanced Materials*, 2011. **23**(47): p. 5624-+.
43. Wang, J. and Z.Q. Lin, *Freestanding TiO₂ nanotube arrays with ultrahigh aspect ratio via electrochemical anodization*. *Chemistry of Materials*, 2008. **20**(4): p. 1257-1261.
44. Scanlon, D.O., et al., *Band alignment of rutile and anatase TiO₂*. *Nature Materials*. **12**(9): p. 798-801.
45. Mohammadpour, A. and K. Shankar, *Anodic TiO₂ nanotube arrays with optical wavelength-sized apertures*. *Journal of Materials Chemistry*. **20**(39): p. 8474-8477.
46. Gonzalez, R.J., R. Zallen, and H. Berger, *Infrared reflectivity and lattice fundamentals in anatase TiO₂*. *Physical Review B*, 1997. **55**(11): p. 7014-7017.

47. Jeong, B.S., D.P. Norton, and J.D. Budai, *Conductivity in transparent anatase TiO₂ films epitaxially grown by reactive sputtering deposition*. Solid-State Electronics, 2003. **47**(12): p. 2275-2278.
48. Wang, J. and Z.Q. Lin, *Anodic Formation of Ordered TiO₂ Nanotube Arrays: Effects of Electrolyte Temperature and Anodization Potential*. Journal of Physical Chemistry C, 2009. **113**(10): p. 4026-4030.
49. Bandara, J., et al., *Integration of TiO₂ nanotube arrays into solid-state dye-sensitized solar cells*. European Physical Journal-Applied Physics. **53**(2): p. 6.
50. Varghese, O.K., M. Paulose, and C.A. Grimes, *Long vertically aligned titania nanotubes on transparent conducting oxide for highly efficient solar cells*. Nature Nanotechnology, 2009. **4**(9): p. 592-597.
51. Lai, Y.K., et al., *Optical and electrical characterization of TiO₂ nanotube arrays on titanium substrate*. Applied Surface Science, 2005. **252**(4): p. 1101-1106.
52. Premchand, Y.D., et al., *Fabrication of self-organized TiO₂ nanotubes from columnar titanium thin films sputtered on semiconductor surfaces*. Electrochemistry Communications, 2006. **8**(12): p. 1840-1844.
53. Mor, G.K., et al., *Fabrication of hydrogen sensors with transparent titanium oxide nanotube-array thin films as sensing elements*. Thin Solid Films, 2006. **496**(1): p. 42-48.
54. Mor, G.K., et al., *A review on highly ordered, vertically oriented TiO₂ nanotube arrays: Fabrication, material properties, and solar energy applications*. Solar Energy Materials and Solar Cells, 2006. **90**(14): p. 2011-2075.
55. Chu, S.Z., et al., *Highly porous TiO₂/Al₂O₃ composite nanostructures on glass by anodization and the sol-gel process: fabrication and photocatalytic characteristics*. Journal of Materials Chemistry, 2003. **13**(4): p. 866-870.
56. Yu, X.F., et al., *Formation of nanoporous titanium oxide films on silicon substrates using an anodization process*. Nanotechnology, 2006. **17**(3): p. 808-814.
57. Vomiero, A., et al., *Flexible dye sensitized solar cells using TiO₂ nanotubes*. Energy & Environmental Science. **4**(9): p. 3408-3413.
58. Galstyan, V., et al., *Vertically Aligned TiO₂ Nanotubes on Plastic Substrates for Flexible Solar Cells*. Small. **7**(17): p. 2437-2442.
59. Zheng, H.D., et al., *Fast formation of thick and transparent titania nanotubular films from sputtered Ti*. Electrochemistry Communications, 2009. **11**(6): p. 1308-1311.
60. Mor, G.K., et al., *Transparent highly ordered TiO₂ nanotube arrays via anodization of titanium thin films*. Advanced Functional Materials, 2005. **15**(8): p. 1291-1296.
61. Paulose, M., et al., *Anodic growth of highly ordered TiO₂ nanotube arrays to 134 μ m in length*. Journal of Physical Chemistry B, 2006. **110**(33): p. 16179-16184.

62. Kalantar-Zadeh, K., et al., *Effect of crystallographic orientation on the anodic formation of nanoscale pores/tubes in TiO₂ films*. Applied Surface Science, 2009. **256**(1): p. 120-123.
63. Shankar, K., et al., *Recent Advances in the Use of TiO₂ Nanotube and Nanowire Arrays for Oxidative Photoelectrochemistry*. Journal of Physical Chemistry C, 2009. **113**(16): p. 6327-6359.
64. Centi, G. and S. Perathoner, *Catalysis: Role and Challenges for a Sustainable Energy*. Topics in Catalysis, 2009. **52**(8): p. 948-961.
65. Centi, G. and S. Perathoner, *Opportunities and prospects in the chemical recycling of carbon dioxide to fuels*. Catalysis Today, 2009. **148**(3-4): p. 191-205.
66. Roy, S.C., et al., *Toward Solar Fuels: Photocatalytic Conversion of Carbon Dioxide to Hydrocarbons*. ACS Nano, 2010. **4**(3): p. 1259-1278.
67. Mallouk, T.E., *The emerging technology of solar fuels*. The Journal of Physical Chemistry Letters, 2010. **1**(18): p. 2738-2739.
68. Mohamed, H.H. and D.W. Bahnemann, *The role of electron transfer in photocatalysis: Fact and fictions*. Applied Catalysis B: Environmental, 2012. **128**(0): p. 91-104.
69. Valencia, S., et al., *A new kinetic model for heterogeneous photocatalysis with titanium dioxide: Case of non-specific adsorption considering back reaction*. Applied Catalysis B: Environmental, 2011. **104**(3-4): p. 300-304.
70. Li, K., et al., *A critical review of CO₂ photoconversion: Catalysts and reactors*. Catalysis Today, 2014. **224**(0): p. 3-12.
71. Dey, G.R., *Chemical Reduction of CO₂ to Different Products during Photo Catalytic Reaction on TiO₂ under Diverse Conditions: an Overview*. Journal of Natural Gas Chemistry, 2007. **16**(3): p. 217-226.
72. He, H., et al., *Enhanced Charge Separation in Nanostructured TiO₂ Materials for Photocatalytic and Photovoltaic Applications*. Industrial & Engineering Chemistry Research, 2012. **51**(37): p. 11841-11849.
73. Sheen, Y.C., et al., *New approach to fabricate an extremely super-amphiphobic surface based on fluorinated silica nanoparticles*. Journal of Polymer Science Part B-Polymer Physics, 2008. **46**(18): p. 1984-1990.
74. Tuteja, A., et al., *Designing superoleophobic surfaces*. Science, 2007. **318**(5856): p. 1618-1622.
75. Zhang, J. and S. Seeger, *Superoleophobic Coatings with Ultralow Sliding Angles Based on Silicone Nanofilaments*. Angewandte Chemie-International Edition, 2011. **50**(29): p. 6652-6656.
76. Deng, X., et al., *Candle Soot as a Template for a Transparent Robust Superamphiphobic Coating*. Science, 2012. **335**(6064): p. 67-70.
77. Kim, H., et al., *Extreme Superomniphobicity of Multiwalled 8 nm TiO₂ Nanotubes*. Langmuir, 2011. **27**(16): p. 10191-10196.
78. Balaur, E., et al., *Wetting behaviour of layers of TiO₂ nanotubes with different diameters*. Journal of Materials Chemistry, 2005. **15**(42): p. 4488-4491.

79. Barthwal, S., Y.S. Kim, and S.-H. Lim, *Fabrication of amphiphobic surface by using titanium anodization for large-area three-dimensional substrates*. Journal of Colloid and Interface Science, 2013. **400**(0): p. 123-129.
80. Lai, Y.K., et al., *Superhydrophilic-superhydrophobic micropattern on TiO₂ nanotube films by photocatalytic lithography*. Electrochemistry Communications, 2008. **10**(3): p. 387-391.
81. Lai, Y.K., et al., *Electrophoretic deposition of titanate nanotube films with extremely large wetting contrast*. Electrochemistry Communications, 2009. **11**(12): p. 2268-2271.
82. Navarrini, W., et al., *Anti-fingerprints fluorinated coating for anodized titanium avoiding color alteration*. Journal of Coatings Technology and Research, 2011. **8**(2): p. 153-160.
83. Vanithakumari, S.C., R.P. George, and U. Kamachi Mudali, *Influence of silanes on the wettability of anodized titanium*. Applied Surface Science, 2014. **292**(0): p. 650-657.
84. Barthwal, S., Y.S. Kim, and S.H. Lim, *Fabrication of amphiphobic surface by using titanium anodization for large-area three-dimensional substrates*. Journal of Colloid and Interface Science, 2013. **400**: p. 123-129.
85. Xi, J.M., L. Feng, and L. Jiang, *A general approach for fabrication of superhydrophobic and superamphiphobic surfaces*. Applied Physics Letters, 2008. **92**(5): p. 3.
86. Cassie, A.B.D. and S. Baxter, *Wettability of porous surfaces*. Transactions of the Faraday Society, 1944. **40**: p. 0546-0550.
87. Farsinezhad, S., et al., *Transparent Anodic TiO₂ Nanotube Arrays on Plastic Substrates for Disposable Biosensors and Flexible Electronics*. Journal of Nanoscience and Nanotechnology. **13**(4): p. 2885-2891.
88. Zhang, X.J., et al., *Photocatalytic Conversion of Diluted CO₂ into Light Hydrocarbons Using Periodically Modulated Multiwalled Nanotube Arrays*. Angewandte Chemie-International Edition. **51**(51): p. 12732-12735.
89. Lu, K., Z.P. Tian, and J.A. Geldmeier, *Polishing effect on anodic titania nanotube formation*. Electrochimica Acta. **56**(17): p. 6014-6020.
90. Albertin, K.F., A. Tavares, and I. Pereyra, *Optimized Ti polishing techniques for enhanced order in TiO₂ NT arrays*. Applied Surface Science. **284**: p. 772-779.
91. Lee, B.G., et al., *Electropolishing for the formation of anodic nanotubular TiO₂ with uniform length and density*. Applied Surface Science. **257**(16): p. 7190-7194.
92. Mizushima, W., *A STUDY OF THE FORMATION OF ANODIC OXIDE FILMS ON TITANIUM*. Journal of the Electrochemical Society, 1961. **108**(9): p. 825-829.
93. Macak, J.M., H. Tsuchiya, and P. Schmuki, *High-aspect-ratio TiO₂ nanotubes by anodization of titanium*. Angewandte Chemie-International Edition, 2005. **44**(14): p. 2100-2102.

94. Cai, Q.Y., et al., *The effect of electrolyte composition on the fabrication of self-organized titanium oxide nanotube arrays by anodic oxidation*. Journal of Materials Research, 2005. **20**(1): p. 230-236.
95. Allam, N.K., K. Shankar, and C.A. Grimes, *Photoelectrochemical and water photoelectrolysis properties of ordered TiO₂ nanotubes fabricated by Ti anodization in fluoride-free HCl electrolytes*. Journal of Materials Chemistry, 2008. **18**(20): p. 2341-2348.
96. Mor, G.K., et al., *Fabrication of tapered, conical-shaped titania nanotubes*. Journal of Materials Research, 2003. **18**(11): p. 2588-2593.
97. Varghese, O.K., et al., *Crystallization and high-temperature structural stability of titanium oxide nanotube arrays*. Journal of Materials Research, 2003. **18**(1): p. 156-165.
98. Macak, J.M., et al., *Smooth anodic TiO₂ nanotubes*. Angewandte Chemie-International Edition, 2005. **44**(45): p. 7463-7465.
99. Macak, J.M. and P. Schmuki, *Anodic growth of self-organized anodic TiO₂ nanotubes in viscous electrolytes*. Electrochimica Acta, 2006. **52**(3): p. 1258-1264.
100. Shir, D., et al., *Performance of Ultrathin Silicon Solar Microcells with Nanostructures of Relief Formed by Soft Imprint Lithography for Broad Band Absorption Enhancement*. Nano Letters. **10**(8): p. 3041-3046.
101. Zhang, Q.F., et al., *Polydisperse aggregates of ZnO nanocrystallites: A method for energy-conversion-efficiency enhancement in dye-sensitized solar cells*. Advanced Functional Materials, 2008. **18**(11): p. 1654-1660.
102. Chou, T.P., et al., *Hierarchically structured ZnO film for dye-sensitized solar cells with enhanced energy conversion efficiency*. Advanced Materials, 2007. **19**(18): p. 2588-+.
103. Yin, H., H. Liu, and W.Z. Shen, *The large diameter and fast growth of self-organized TiO₂ nanotube arrays achieved via electrochemical anodization*. Nanotechnology, 2010. **21**(3).
104. Arpin, K.A., et al., *Multidimensional Architectures for Functional Optical Devices*. Advanced Materials. **22**(10): p. 1084-1101.
105. Sulka, G.D. and K. Hnida, *Distributed Bragg reflector based on porous anodic alumina fabricated by pulse anodization*. Nanotechnology, 2012. **23**(7).
106. Farsinezhad, S., et al., *Amphiphobic surfaces from functionalized TiO₂ nanotube arrays*. Rsc Advances, 2014. **4**(63): p. 33587-33598.
107. Wang, L.P., et al., *Influence of temperature and ion kinetic energy on surface morphology of CeO₂ films prepared by dual plasma deposition*. Materials Science and Engineering a-Structural Materials Properties Microstructure and Processing, 2002. **336**(1-2): p. 75-80.
108. Paulose, M., et al., *Application of highly-ordered TiO₂ nanotube-arrays in heterojunction dye-sensitized solar cells*. Journal of Physics D-Applied Physics, 2006. **39**(12): p. 2498-2503.
109. Wood, R.M., *The Lattice Constants of High Purity Alpha Titanium*. Proceedings of the Physical Society, 1962. **80**(3): p. 783.

110. Messier, R., A.P. Giri, and R.A. Roy, *REVISED STRUCTURE ZONE MODEL FOR THIN-FILM PHYSICAL STRUCTURE*. Journal of Vacuum Science & Technology a-Vacuum Surfaces and Films, 1984. **2**(2): p. 500-503.
111. Abelmann, L. and C. Lodder, *Oblique evaporation and surface diffusion*. Thin Solid Films, 1997. **305**(1-2): p. 1-21.
112. Wood, R.M., *LATTICE CONSTANTS OF HIGH PURITY ALPHA TITANIUM*. Proceedings of the Physical Society of London, 1962. **80**(515): p. 783-&.
113. Semaltianos, N.G., *Thermally evaporated aluminium thin films*. Applied Surface Science, 2001. **183**(3-4): p. 223-229.
114. Qui, H., et al., *Effect of deposition rate on structural and electrical properties of Al films deposited on glass by electron beam evaporation*. Thin Solid Films, 2002. **414**(1): p. 150-153.
115. Chu, S.Z., et al., *Synthesis and characterization of titania nanostructures on glass by Al anodization and sol-gel process*. Chemistry of Materials, 2002. **14**(1): p. 266-272.
116. Lin, C.H., et al., *Photocatalytic generation of H₂ gas from neat ethanol over Pt/TiO₂ nanotube catalysts*. Catalysis Letters, 2004. **98**(1): p. 61-66.
117. Macak, J.M., et al., *On wafer TiO₂ nanotube-layer formation by anodization of Ti-films on Si*. Chemical Physics Letters, 2006. **428**(4-6): p. 421-425.
118. Stergiopoulos, T., et al., *Dye-sensitization of self-assembled titania nanotubes prepared by galvanostatic anodization of Ti sputtered on conductive glass*. Nanotechnology, 2009. **20**(36).
119. Galstyan, V., et al., *TiO₂ nanotubular and nanoporous arrays by electrochemical anodization on different substrates*. Rsc Advances, 2011. **1**(6): p. 1038-1044.
120. Farsinezhad, S., et al., *Transparent Anodic TiO₂ Nanotube Arrays on Plastic Substrates for Disposable Biosensors and Flexible Electronics*. Journal of Nanoscience and Nanotechnology, 2013. **13**(4): p. 2885-2891.
121. Tao, J., T. Wu, and P. Gao, *Fast Fabrication of Long TiO₂ Nanotube Array with High Photoelectrochemical Property on Flexible Stainless Steel*. Journal of Nanoscience and Nanotechnology, 2012. **12**(3): p. 1852-1858.
122. Ji, Y.J., et al., *Fabrication of double-walled TiO₂ nanotubes with bamboo morphology via one-step alternating voltage anodization*. Electrochemistry Communications, 2011. **13**(9): p. 1013-1015.
123. Roy, P., S. Berger, and P. Schmuki, *TiO₂ Nanotubes: Synthesis and Applications*. Angewandte Chemie-International Edition, 2011. **50**(13): p. 2904-2939.
124. Su, Z.X., et al., *Formation of anodic TiO₂ nanotube arrays with bimodal pore size distribution*. Electrochemistry Communications, 2013. **31**: p. 67-70.
125. Mohammadpour, A., et al., *Anodic Growth of Large-Diameter Multipodal TiO₂ Nanotubes*. Acs Nano, 2010. **4**(12): p. 7421-7430.

126. Chen, B. and K. Lu, *Hierarchically Branched Titania Nanotubes with Tailored Diameters and Branch Numbers*. Langmuir, 2011. **28**(5): p. 2937-2943.
127. Macak, J.M., et al., *Multilayer TiO₂-Nanotube Formation by Two-Step Anodization*. Electrochemical and Solid-State Letters, 2007. **10**(7): p. K28-K31.
128. Albu, S.R., D. Kim, and P. Schmuki, *Growth of aligned TiO₂ bamboo-type nanotubes and highly ordered nanolace*. Angewandte Chemie-International Edition, 2008. **47**(10): p. 1916-1919.
129. Mun, K.-S., et al., *A Stable, Label-free Optical Interferometric Biosensor Based on TiO₂ Nanotube Arrays*. ACS Nano, 2010. **4**(4): p. 2070-2076.
130. Lin, J., K. Liu, and X.F. Chen, *Synthesis of Periodically Structured Titania Nanotube Films and Their Potential for Photonic Applications*. Small, 2011. **7**(13): p. 1784-1789.
131. Yip, C.T., et al., *Direct and Seamless Coupling of TiO₂ Nanotube Photonic Crystal to Dye-Sensitized Solar Cell: A Single-Step Approach*. Advanced Materials, 2011. **23**(47): p. 5624+.
132. Guo, M., et al., *Design and coupling of multifunctional TiO₂ nanotube photonic crystal to nanocrystalline titania layer as semi-transparent photoanode for dye-sensitized solar cell*. Energy & Environmental Science, 2012. **5**(12): p. 9881-9888.
133. Zhang, X., et al., *Photocatalytic Conversion of Diluted CO₂ into Light Hydrocarbons Using Periodically Modulated Multiwalled Nanotube Arrays*. Angewandte Chemie International Edition, 2012: p. n/a-n/a.
134. Sergentu, V.V., et al., *Prediction of negative index material lenses based on metallo-dielectric nanotubes*. physica status solidi (RRL) – Rapid Research Letters, 2008. **2**(5): p. 242-244.
135. Shankar, K., *TiO₂ Nanotube Arrays: Growth and Application*, in *Encyclopedia of Nanotechnology*, B. Bhushan, Editor. 2012, Springer Netherlands. p. 2742-2755.
136. Shankar, K., et al., *Effect of device geometry on the performance of TiO₂ nanotube array-organic semiconductor double heterojunction solar cells*. Journal of Non-Crystalline Solids, 2008. **354**(19-25): p. 2767-2771.
137. Macak, J.M., S.P. Albu, and P. Schmuki, *Towards ideal hexagonal self-ordering of TiO₂ nanotubes*. Physica Status Solidi-Rapid Research Letters, 2007. **1**(5): p. 181-183.
138. Stepniowski, W.J., et al., *Fast Fourier transform based arrangement analysis of poorly organized alumina nanopores formed via self-organized anodization in chromic acid*. Materials Letters, 2014. **117**(0): p. 69-73.
139. Sulka, G.D., et al., *Fabrication of nanoporous TiO₂ by electrochemical anodization*. Electrochimica Acta, 2010. **55**(14): p. 4359-4367.
140. Sulka, G.D., et al., *Through-hole membranes of nanoporous alumina formed by anodizing in oxalic acid and their applications in fabrication of nanowire arrays*. Electrochimica Acta, 2010. **55**(14): p. 4368-4376.

141. Moayed, M.H. and R.C. Newman, *Evolution of current transients and morphology of metastable and stable pitting on stainless steel near the critical pitting temperature*. Corrosion Science, 2006. **48**(4): p. 1004-1018.
142. Isaacs, H.S., *The localized breakdown and repair of passive surfaces during pitting*. Corrosion Science, 1989. **29**(2-3): p. 313-323.
143. Scher, H. and E.W. Montroll, *Anomalous transit-time dispersion in amorphous solids*. Physical Review B, 1975. **12**(6): p. 2455-2477.
144. Habazaki, H., et al., *Fast migration of fluoride ions in growing anodic titanium oxide*. Electrochemistry Communications, 2007. **9**(5): p. 1222-1227.
145. Bhargava, Y.V., Q.A.S. Nguyen, and T.M. Devine, *Initiation of Organized Nanopore/Nanotube Arrays in Titanium Oxide II. Nanopore Size and Spacing*. Journal of the Electrochemical Society, 2009. **156**(3): p. E62-E68.
146. Nguyen, Q.A.S., Y.V. Bhargava, and T.M. Devine, *Initiation of Organized Nanopore/Nanotube Arrays in Anodized Titanium Oxide I. Criterion for Initiation*. Journal of the Electrochemical Society, 2009. **156**(3): p. E55-E61.
147. Yang, D.J., et al., *Vertically oriented titania nanotubes prepared by anodic oxidation on Si substrates*. Ieee Transactions on Nanotechnology, 2008. **7**(2): p. 131-134.
148. Chappanda, K.N., et al., *Growth and characterization of TiO₂ nanotubes from sputtered Ti film on Si substrate*. Nanoscale Research Letters, 2012. **7**.
149. Marasso, S.L., G. Canavese, and M. Cocuzza, *Cost efficient master fabrication process on copper substrates*. Microelectronic Engineering. **88**(8): p. 2322-2324.
150. Crawford, G.A. and N. Chawla, *Tailoring TiO₂ nanotube growth during anodic oxidation by crystallographic orientation of Ti*. Scripta Materialia, 2009. **60**(10): p. 874-877.
151. Leonardi, S., et al., *TiO₂ Nanotubes: Interdependence of Substrate Grain Orientation and Growth Characteristics*. The Journal of Physical Chemistry C, 2011. **116**(1): p. 384-392.
152. Mie, G., *Contributions to the optics of turbid media, particularly of colloidal metal solutions*. Contributions to the optics of turbid media, particularly of colloidal metal solutions Transl. into ENGLISH from Ann. Phys.(Leipzig), v. 25, no. 3, 1908 p 377-445, 1976. **1**: p. 377-445.
153. Gans, R., *Über die Form ultramikroskopischer Goldteilchen*. Annalen der Physik, 1912. **342**(5): p. 881-900.
154. Li, L., P.A. Salvador, and G.S. Rohrer, *Photocatalysts with internal electric fields*. Nanoscale, 2014. **6**(1): p. 24-42.
155. Zhang, X., et al., *Photocatalytic Conversion of Diluted CO₂ into Light Hydrocarbons Using Periodically Modulated Multiwalled Nanotube Arrays*. Angewandte Chemie, 2012. **124**(51): p. 12904-12907.
156. Amirsolaimani, B., et al., *Effect of the Nature of the Metal Co-Catalyst on CO₂ Photoreduction Using Fast-Grown Periodically Modulated Titanium*

- Dioxide Nanotube Arrays (PMTiNTs)*. MRS Online Proceedings Library, 2013. **1578**: p. null-null.
157. Wang, W.-N., et al., *Size and Structure Matter: Enhanced CO₂ Photoreduction Efficiency by Size-Resolved Ultrafine Pt Nanoparticles on TiO₂ Single Crystals*. Journal of the American Chemical Society, 2012. **134**(27): p. 11276-11281.
 158. Feng, X.J., et al., *Synthesis and deposition of ultrafine Pt nanoparticles within high aspect ratio TiO₂ nanotube arrays: application to the photocatalytic reduction of carbon dioxide*. Journal of Materials Chemistry, 2011. **21**(35): p. 13429-13433.
 159. Raja, K.S., et al., *CO₂ Photoreduction in the Liquid Phase over Pd-Supported on TiO₂ Nanotube and Bismuth Titanate Photocatalysts*. Electrochemical and Solid State Letters, 2011. **14**(5): p. F5-F8.
 160. Zhang, Q.H., et al., *Photocatalytic reduction of CO₂ with H₂O on Pt-loaded TiO₂ catalyst*. Catalysis Today, 2009. **148**(3-4): p. 335-340.
 161. Anderson, R.L., *Experiments on Ge-GaAs heterojunctions*. Solid-State Electronics, 1962. **5**(5): p. 341-351.
 162. Park, J.Y., et al., *Probing Hot Electron Flow Generated on Pt Nanoparticles with Au/TiO₂ Schottky Diodes during Catalytic CO Oxidation*. Nano Letters, 2008. **8**(8): p. 2388-2392.
 163. Chen, H., et al., *Fabrication of TiO₂-Pt Coaxial Nanotube Array Schottky Structures for Enhanced Photocatalytic Degradation of Phenol in Aqueous Solution*. The Journal of Physical Chemistry C, 2008. **112**(25): p. 9285-9290.
 164. Anpo, M., *Photocatalysis on titanium oxide catalysts: Approaches in achieving highly efficient reactions and realizing the use of visible light*. Catalysis Surveys from Asia, 1997. **1**(2): p. 169-179.
 165. Gomathi Devi, L. and S. Girish Kumar, *Strategies developed on the modification of titania for visible light response with enhanced interfacial charge transfer process: an overview*. Central European Journal of Chemistry, 2011. **9**(6): p. 959-961.
 166. Kim, J., J. Lee, and W. Choi, *Synergic effect of simultaneous fluorination and platinization of TiO₂ surface on anoxic photocatalytic degradation of organic compounds*. Chemical Communications, 2008(6): p. 756-758.
 167. Liu, M., et al., *Cu(II) Oxide Amorphous Nanoclusters Grafted Ti³⁺ Self-Doped TiO₂: An Efficient Visible Light Photocatalyst*. Chemistry of Materials, 2011. **23**(23): p. 5282-5286.
 168. Kim, S., S.-J. Hwang, and W. Choi, *Visible Light Active Platinum-Ion-Doped TiO₂ Photocatalyst*. The Journal of Physical Chemistry B, 2005. **109**(51): p. 24260-24267.
 169. Farsinezhad, S., A.N. Dalrymple, and K. Shankar, *Toward single-step anodic fabrication of monodisperse TiO₂ nanotube arrays on non-native substrates*. physica status solidi (a), 2014: p. 1-9.
 170. Mills, A. and S.K. Lee, *Platinum Group Metals and Their Oxides in Semiconductor Photosensitisation* **BASIC PRINCIPLES, METAL**

- PHOTODEPOSITION AND WATER PHOTOSPLITTING REACTIONS.* Platinum Metals Review, 2003. **47**(1): p. 2-12.
171. Rodríguez, J.L., et al., *Photocatalytic Deposition of Nickel Nanoparticles on Titanium Dioxide.* MRS Online Proceedings Library, 2010. **1279**: p. null-null.
 172. Parayil, S.K., et al., *Synthesis-Dependent Oxidation State of Platinum on TiO₂ and Their Influences on the Solar Simulated Photocatalytic Hydrogen Production from Water.* The Journal of Physical Chemistry C, 2013. **117**(33): p. 16850-16862.
 173. Zhang, J., et al., *UV Raman Spectroscopic Study on TiO₂. I. Phase Transformation at the Surface and in the Bulk.* The Journal of Physical Chemistry B, 2005. **110**(2): p. 927-935.
 174. Wang, G., et al., *Hydrogen-Treated TiO₂ Nanowire Arrays for Photoelectrochemical Water Splitting.* Nano Letters, 2011. **11**(7): p. 3026-3033.
 175. Peuckert, M. and H.P. Bonzel, *CHARACTERIZATION OF OXIDIZED PLATINUM SURFACES BY X-RAY PHOTOELECTRON-SPECTROSCOPY.* Surface Science, 1984. **145**(1): p. 239-259.
 176. Romeo, M., et al., *PHOTOEMISSION-STUDY OF PT ADLAYERS ON NI(111).* Surface Science, 1990. **238**(1-3): p. 163-168.
 177. Baudoing-Savois, R., et al., *Co ultra-thin films on Pt(111) and Co-Pt alloying: a LEED, Auger and synchrotron x-ray diffraction study.* Journal of Physics-Condensed Matter, 1999. **11**(43): p. 8355-8375.
 178. Thiele, J., et al., *AN EXPERIMENTAL-STUDY OF THE GROWTH OF CO/PT(111) BY CORE-LEVEL PHOTOEMISSION SPECTROSCOPY, LOW-ENERGY-ELECTRON DIFFRACTION AND AUGER-ELECTRON SPECTROSCOPY.* Journal of Physics-Condensed Matter, 1994. **6**(27): p. 5025-5038.
 179. Alnot, M., et al., *A STUDY OF THE GROWTH-MECHANISM OF PLATINUM ON RE(0001) BY PHOTOEMISSION OF ADSORBED XENON.* Surface Science, 1985. **162**(1-3): p. 886-890.
 180. Rogers, J.D., et al., *HIGH-RESOLUTION STUDY OF THE M45N67N67 AND M45N45N67 AUGER TRANSITIONS IN THE 5D SERIES.* Journal of Physics F-Metal Physics, 1982. **12**(9): p. 2097-2102.
 181. Duckers, K., H.P. Bonzel, and D.A. Wesner, *SURFACE CORE LEVEL SHIFTS OF PT(111) MEASURED WITH Y-M-ZETA-RADIATION (132.3 EV).* Surface Science, 1986. **166**(1): p. 141-158.
 182. Fierro, J.L.G., J.M. Palacios, and F. Tomas, *AN ANALYTICAL SEM AND XPS STUDY OF PLATINUM RHODIUM GAUZES USED IN HIGH-PRESSURE AMMONIA BURNERS.* Surface and Interface Analysis, 1988. **13**(1): p. 25-32.
 183. Kim, K.S., N. Winograd, and R.E. Davis, *ELECTRON SPECTROSCOPY OF PLATINUM-OXYGEN SURFACES AND APPLICATION TO ELECTROCHEMICAL STUDIES.* Journal of the American Chemical Society, 1971. **93**(23): p. 6296-&.

184. Bancroft, G.M., et al., *ESCA STUDY OF SPUTTERED PLATINUM FILMS*. Analytical Chemistry, 1975. **47**(3): p. 586-588.
185. Juarez, J.M., M.B. Gomez Costa, and O.A. Anunziata, *Synthesis and characterization of Pt-CMK-3 hybrid nanocomposite for hydrogen storage*. International Journal of Energy Research, 2015. **39**(1): p. 128-139.
186. Eberhardt, W., et al., *PHOTOEMISSION FROM MASS-SELECTED MONODISPERSED PT CLUSTERS*. Physical Review Letters, 1990. **64**(7): p. 780-784.
187. Moulder, J.F., *Handbook of X-ray Photoelectron Spectroscopy: A Reference Book of Standard Spectra for Identification and Interpretation of XPS Data*. reissue ed. 1995: Physical Electronics, 1995.
188. Park, M.-H., et al., *Doping of the Metal Oxide Nanostructure and its Influence in Organic Electronics*. Advanced Functional Materials, 2009. **19**(8): p. 1241-1246.
189. Moench, W., *Interface-induced gap states and band-structure lineup at TiO₂ heterostructures and Schottky contacts*. Journal of Applied Physics, 2010. **107**(1).
190. Henrist, B., et al., *The secondary electron yield of TiZr and TiZrV non-evaporable getter thin film coatings*. Applied Surface Science, 2001. **172**(1-2): p. 95-102.
191. Chen, J., et al., *Secondary electron yield measurements of carbon covered multilayer optics*. Applied Surface Science, 2010. **257**(2): p. 354-361.
192. Camacho, R., et al., *Preparation and Characterization of Pt/C and Pt/TiO₂ Electrocatalysts by Liquid Phase Photodeposition*. Topics in Catalysis, 2011. **54**(8-9): p. 512-518.
193. Pu, P., et al., *Relation between morphology and conductivity in TiO₂ nanotube arrays: an electrochemical impedance spectrometric investigation*. Journal of Solid State Electrochemistry, 2013. **17**(3): p. 817-828.
194. Kar, P. and K. Shankar, *Lumped Modeling of the Electrochemical Impedance Spectroscopic Data of Anodic TiO₂ Nanotube Arrays*. 2014. **In Preparation**.
195. Kurian, S., H. Seo, and H. Jeon, *Significant Enhancement in Visible Light Absorption of TiO₂ Nanotube Arrays by Surface Band Gap Tuning*. Journal of Physical Chemistry C, 2013. **117**(33): p. 16811-16819.
196. Lyeo, H.K., et al., *Profiling the thermoelectric power of semiconductor junctions with nanometer resolution*. Science, 2004. **303**(5659): p. 816-818.
197. Kim, J., D. Monllor-Satoca, and W. Choi, *Simultaneous production of hydrogen with the degradation of organic pollutants using TiO₂ photocatalyst modified with dual surface components*. Energy & Environmental Science, 2012. **5**(6): p. 7647-7656.
198. Park, H.W., J.S. Lee, and W.Y. Choi, *Study of special cases where the enhanced photocatalytic activities of Pt/TiO₂ vanish under low light intensity*. Catalysis Today, 2006. **111**(3-4): p. 259-265.

199. Choi, W., *Pure and modified TiO₂ photocatalysts and their environmental applications*. Catalysis Surveys from Asia, 2006. **10**(1): p. 16-28.
200. Lee, J.S. and W.Y. Choi, *Photocatalytic reactivity of surface platinumized TiO₂: Substrate specificity and the effect of Pt oxidation state*. Journal of Physical Chemistry B, 2005. **109**(15): p. 7399-7406.
201. Kim, S., S.J. Hwang, and W.Y. Choi, *Visible light active platinum-ion-doped TiO₂ photocatalyst*. Journal of Physical Chemistry B, 2005. **109**(51): p. 24260-24267.
202. Zhdanov, V.P. and B. Kasemo, *Substrate-mediated photoinduced chemical reactions on ultrathin metal films*. Surface Science, 1999. **432**(3): p. L599-L603.
203. Zhao, W., et al., *Photodegradation of sulforhodamine-B dye in platinumized titania dispersions under visible light irradiation: Influence of platinum as a functional co-catalyst*. Journal of Physical Chemistry B, 2002. **106**(19): p. 5022-5028.
204. Sangpour, P., F. Hashemi, and A.Z. Moshfegh, *Photoenhanced Degradation of Methylene Blue on Cosputtered M:TiO₂ (M = Au, Ag, Cu) Nanocomposite Systems: A Comparative Study*. Journal of Physical Chemistry C, 2010. **114**(33): p. 13955-13961.
205. Mun, K.S., et al., *A Stable, Label-free Optical Interferometric Biosensor Based on TiO₂ Nanotube Arrays*. ACS Nano, 2010. **4**(4): p. 2070-2076.
206. Song, Y.Y., et al., *TiO₂ Nano Test Tubes as a Self-Cleaning Platform for High-Sensitivity Immunoassays*. Small, 2010. **6**(11): p. 1180-1184.
207. Kar, P., et al., *Ultrahigh sensitivity assays for human cardiac troponin I using TiO₂ nanotube arrays*. Lab on a Chip, 2012. **12**(4): p. 821-828.
208. De Santo, I., et al., *Exploring doxorubicin localization in eluting TiO₂ nanotube arrays through fluorescence correlation spectroscopy analysis*. Analyst, 2012. **137**(21): p. 5076-5081.
209. Gulati, K., et al., *Biocompatible polymer coating of titania nanotube arrays for improved drug elution and osteoblast adhesion*. Acta Biomaterialia, 2012. **8**(1): p. 449-456.
210. Kazemzadeh-Narbat, M., et al., *Multilayered coating on titanium for controlled release of antimicrobial peptides for the prevention of implant-associated infections*. Biomaterials, 2013. **34**(24): p. 5969-5977.
211. Liang, K., X.C. Li, and B.K. Tay, *Study of Bone Morphogenetic Protein-2 Delivery with Different TiO₂ Nanotube Structures*. Nanoscience and Nanotechnology Letters, 2013. **5**(2): p. 162-166.
212. Oh, S., et al., *Visible Light Irradiation-Mediated Drug Elution Activity of Nitrogen-Doped TiO₂ Nanotubes*. Journal of Nanomaterials, 2013.
213. Popat, K.C., et al., *Titania nanotubes: A novel platform for drug-eluting coatings for medical implants?* Small, 2007. **3**(11): p. 1878-1881.
214. Luo, L., et al., *Effects of aggregation and electron injection on photovoltaic performance of porphyrin-based solar cells with oligo(phenylethynyl) links inside TiO₂ and Al₂O₃ nanotube arrays*. Physical Chemistry Chemical Physics, 2010. **12**(5): p. 1064-1071.

215. Sun, W.T., et al., *CdS quantum dots sensitized TiO₂ nanotube-array photoelectrodes*. Journal of the American Chemical Society, 2008. **130**(4): p. 1124-+.
216. Yang, H.H., et al., *Heterojunction Engineering of CdTe and CdSe Quantum Dots on TiO₂ Nanotube Arrays: Intricate Effects of Size-Dependency and Interfacial Contact on Photoconversion Efficiencies*. Advanced Functional Materials, 2012. **22**(13): p. 2821-2829.
217. Ziolk, M., et al., *Femtosecond to millisecond studies of electron transfer processes in a donor-(π -spacer)-acceptor series of organic dyes for solar cells interacting with titania nanoparticles and ordered nanotube array films*. Physical Chemistry Chemical Physics, 2012. **14**(8): p. 2816-2831.
218. Shankar, K., et al., *Highly efficient solar cells using TiO₂ nanotube arrays sensitized with a donor-antenna dye*. Nano Letters, 2008. **8**(6): p. 1654-1659.
219. Kim, S., et al., *Broad Spectrum Light Harvesting in TiO₂ Nanotube Array - Hemicyanine Dye-P3HT Hybrid Solid-State Solar Cells*. Ieee Journal of Selected Topics in Quantum Electronics, 2010. **16**(6): p. 1573-1580.
220. Li, Z., et al., *Closed-air induced composite wetting on hydrophilic ordered nanoporous anodic alumina*. Applied Physics Letters, 2010. **97**(23): p. -.
221. Smirnov, S., et al., *Water Confinement in Hydrophobic Nanopores. Pressure-Induced Wetting and Drying*. Acs Nano, 2010. **4**(9): p. 5069-5075.
222. Schulman, F. and W.A. Zisman, *The spreading of liquids on low-energy surfaces. V. Perfluorodecanoic acid monolayers*. Journal of Colloid Science, 1952. **7**(5): p. 465-481.
223. Hare, E.F., E.G. Shafrin, and W.A. Zisman, *Properties of Films of Adsorbed Fluorinated Acids*. The Journal of Physical Chemistry, 1954. **58**(3): p. 236-239.
224. Cheng, D.F., et al., *Smooth Perfluorinated Surfaces with Different Chemical and Physical Natures: Their Unusual Dynamic Dewetting Behavior toward Polar and Nonpolar Liquids*. Langmuir, 2013. **29**(36): p. 11322-11329.
225. Waghmare, P.R., S. Das, and S.K. Mitra, *Under-water superoleophobic Glass: Unexplored role of the surfactant-rich solvent*. Scientific Reports, 2013. **3**.
226. Joanny, J.F. and P.G. de Gennes, *A model for contact angle hysteresis*. The Journal of Chemical Physics, 1984. **81**(1): p. 552-562.
227. Brandon, S., et al., *Partial wetting of chemically patterned surfaces: The effect of drop size*. Journal of Colloid and Interface Science, 2003. **263**(1): p. 237-243.
228. Wolansky, G. and A. Marmur, *Apparent contact angles on rough surfaces: the Wenzel equation revisited*. Colloids and Surfaces A: Physicochemical and Engineering Aspects, 1999. **156**(1-3): p. 381-388.
229. Hutchins, D.O., et al., *Solid-state densification of spun-cast self-assembled monolayers for use in ultra-thin hybrid dielectrics*. Applied Surface Science, 2012. **261**(0): p. 908-915.

230. Smith, B.S., et al., *Hemocompatibility of titania nanotube arrays*. Journal of Biomedical Materials Research Part A, 2010. **95A**(2): p. 350-360.
231. Crawford, G.A., et al., *Microstructure and deformation behavior of biocompatible TiO₂ nanotubes on titanium substrate*. Acta Biomaterialia, 2007. **3**(3): p. 359-367.
232. Shokuhfar, T., et al., *Direct Compressive Measurements of Individual Titanium Dioxide Nanotubes*. ACS Nano, 2009. **3**(10): p. 3098-3102.
233. Zou, J.-p. and R.-z. Wang, *Crack initiation, propagation and saturation of TiO₂ nanotube film*. Transactions of Nonferrous Metals Society of China, 2012. **22**(3): p. 627-633.
234. Ashby, M.F., *Overview No. 80: On the engineering properties of materials*. Acta Metallurgica, 1989. **37**(5): p. 1273-1293.
235. Balaur, E., et al., *Tailoring the wettability of TiO₂ nanotube layers*. Electrochemistry Communications, 2005. **7**(10): p. 1066-1070.
236. Zenasni, O., A.C. Jamison, and T.R. Lee, *The impact of fluorination on the structure and properties of self-assembled monolayer films*. Soft Matter. **9**(28): p. 6356-6370.
237. Graupe, M., et al., *Oriented surface dipoles strongly influence interfacial wettabilities*. Journal of the American Chemical Society, 1999. **121**(13): p. 3222-3223.
238. Mohammadpour, A. and K. Shankar, *Anodic TiO₂ nanotube arrays with optical wavelength-sized apertures*. Journal of Materials Chemistry, 2010. **20**(39): p. 8474-8477.
239. Wang, D.A., et al., *Spontaneous Phase and Morphology Transformations of Anodized Titania Nanotubes Induced by Water at Room Temperature*. Nano Letters, 2011. **11**(9): p. 3649-3655.
240. Puziy, A.M., et al., *XPS and NMR studies of phosphoric acid activated carbons*. Carbon, 2008. **46**(15): p. 2113-2123.
241. Ariza, M.J., et al., *X-ray photoelectron spectroscopy analysis of di-(2-ethylhexyl) phosphoric acid activated membranes*. Journal of Colloid and Interface Science, 2000. **226**(1): p. 151-158.
242. Gawalt, E.S., et al., *Enhanced bonding of alkanephosphonic acids to oxidized titanium using surface-bound alkoxyzirconium complex interfaces*. Langmuir, 1999. **15**(26): p. 8929-8933.
243. Nefedov, V.I., et al., *X-ray electron study of transition-metal complexes with phosphorus-containing acids*. Zhurnal Neorganicheskoi Khimii, 1974. **19**(5): p. 1416-1417.
244. Viornery, C., et al., *Surface modification of titanium with phosphonic acid to improve bone bonding: Characterization by XPS and ToF-SIMS*. Langmuir, 2002. **18**(7): p. 2582-2589.
245. Kruszewski, K.M. and E.S. Gawalt, *Perfluorocarbon Thin Films and Polymer Brushes on Stainless Steel 316 L for the Control of Interfacial Properties*. Langmuir, 2011. **27**(13): p. 8120-8125.
246. Silverman, B.M., K.A. Wieghaus, and J. Schwartz, *Comparative properties of siloxane vs phosphonate monolayers on a key titanium alloy*. Langmuir, 2005. **21**(1): p. 225-228.

247. Owens, D.K. and R.C. Wendt, *Estimation of the surface free energy of polymers*. Journal of Applied Polymer Science, 1969. **13**(8): p. 1741-1747.
248. Fowkes, F.M., *Attractive Forces at Interfaces*. Industrial & Engineering Chemistry, 1964. **56**(12): p. 40-52.
249. Van Oss, C.J., R.J. Good, and M.K. Chaudhury, *Additive and nonadditive surface tension components and the interpretation of contact angles*. Langmuir, 1988. **4**(4): p. 884-891.
250. Hata, T., Y. Kitazaki, and T. Saito, *Estimation of the Surface Energy of Polymer Solids*. The Journal of Adhesion, 1987. **21**(3-4): p. 177-194.
251. Doganci, M.D., et al., *Combined XPS and contact angle studies of flat and rough ethylene-vinyl acetate copolymer films*. Journal of Applied Polymer Science, 2012. **124**(3): p. 2100-2109.
252. Lai, Y., et al., *Markedly Controllable Adhesion of Superhydrophobic Spongelike Nanostructure TiO₂ Films*. Langmuir, 2008. **24**(8): p. 3867-3873.
253. Wenzel, R.N., *Resistance of solid surfaces to wetting by water*. Industrial and Engineering Chemistry, 1936. **28**: p. 988-994.
254. De Gennes, P.-G., F. Brochard-Wyart, and D. Quéré, *Capillarity and wetting phenomena: drops, bubbles, pearls, waves*. 2004: Springer.
255. Waghmare, P.R., S. Das, and S.K. Mitra, *Drop deposition on under-liquid low energy surfaces*. Soft Matter, 2013. **9**(31): p. 7437-7447.
256. Waghmare, P.R., S. Das, and S.K. Mitra, *Drop deposition on under-liquid low energy surfaces*. Soft Matter. **9**(31): p. 7437-7447.
257. Erbil, H.Y. and C.E. Cansoy, *Range of Applicability of the Wenzel and Cassie-Baxter Equations for Superhydrophobic Surfaces*. Langmuir, 2009. **25**(24): p. 14135-14145.
258. Zenasni, O., A.C. Jamison, and T.R. Lee, *The impact of fluorination on the structure and properties of self-assembled monolayer films*. Soft Matter, 2013. **9**(28): p. 6356-6370.
259. Israelachvili, J.N., *Intermolecular and surface forces: revised third edition*. 2011: Academic press.
260. Johnson, R.E. and R.H. Detre, in *Wettability*, J.C. Berg, Editor. 1993, Marcel Dekker: New York.
261. Ran, C., et al., *Wetting on Nanoporous Alumina Surface: Transition between Wenzel and Cassie States Controlled by Surface Structure*. Langmuir, 2008. **24**(18): p. 9952-9955.
262. Sangpour, P., F. Hashemi, and A.Z. Moshfegh, *Photoenhanced Degradation of Methylene Blue on Cosputtered M:TiO₂ (M = Au, Ag, Cu) Nanocomposite Systems: A Comparative Study*. The Journal of Physical Chemistry C, 2010. **114**(33): p. 13955-13961.
263. Zhao, W., et al., *Photodegradation of Sulforhodamine-B Dye in Platinized Titania Dispersions under Visible Light Irradiation: Influence of Platinum as a Functional Co-catalyst*. The Journal of Physical Chemistry B, 2002. **106**(19): p. 5022-5028.

264. Sun, R.-D., et al., *Photoinduced Surface Wettability Conversion of ZnO and TiO₂ Thin Films*. The Journal of Physical Chemistry B, 2001. **105**(10): p. 1984-1990.
265. Ghosh, G., *Sellmeier coefficients and dispersion of thermo-optic coefficients for some optical glasses*. Applied Optics, 1997. **36**(7): p. 1540-1546.
266. Tompkins, H.G. and E.A. Irene, *Handbook of Ellipsometry*. William Andrew Publishing/Noyes.

Appendix A- Absorption Coefficient

The refractive index of a material determines how much light will be reflected when entering into the material from vacuum and is defined as ' $n=c/v$ ' where ' n ' stands for refractive index, ' c ' is the speed of light in vacuum and ' v ' is speed of light in that material. In general, the refractive index varies as a function of wavelength (or frequency) and is given by the square-root of the complex dielectric constant ($\epsilon=n^2$). The high-frequency dielectric constant of a medium through which light propagates can be defined by various empirical dispersion relations such as Sellmeier (non-absorbing media), Lorentz Drude (lossy media), Tauc-Lorentz (semiconductors) and so on.

$$\epsilon_r = \epsilon_{r0} + \sum_{i=1}^M \frac{A_i \lambda^2}{\lambda^2 + j\Gamma_i \lambda - \lambda_i^2} \quad (\text{A- 1}) \text{ Sellmeier Equation}$$

Here ' ϵ_r ' is the permittivity of the material, ' ϵ_{r0} ' is permittivity at the reference wavelength, ' A_i ' is the component strength, ' T_i ' is damping factor and ' λ_i ' is the oscillation wavelength. Sellmeier equation was proposed by Wilhelm Sellmeier in 1871 for a particular transparent medium for dispersion modeling [265]. In the lossy medium case, the Sellmeier equation can be written in a more general form which is called the Lorentz dispersion equation.

$$\epsilon_r^b = \sum_{m=1}^M \frac{\Omega_p^2}{\omega_m^2 - \omega^2 + j\omega\Gamma_m} \quad (\text{A- 2}) \text{ Lorentz Dispersion}$$

In Lorentz dispersion, the underlying physical assumptions are that the atom is more massive than electron, and that the system exhibits the behavior of a Coulombic simple harmonic oscillator with characteristic resonances. In this situation, the electric field will vary with angular frequency ' ω ' [2]. For metals

which consist of large numbers of free electrons, a superior dispersion expression is given by the Drude model:

$$\varepsilon_r^f = 1\varepsilon_{r0} + \frac{\Omega_p^2}{j\omega\Gamma_0 - \omega^2} \quad (\text{A- 3) Drude Model}$$

The Drude model is a classical model that is based on kinetic theory and electron bouncing and re-bouncing behavior [266]. In the case of real metals and surface plasmons, the Lorentz-Drude model is used which incorporates both the behavior of a free electron gas and characteristic resonances. The Drude model is used for intraband (free electron effect) part of the dielectric function and the Lorentz is used for interband (bounded electron effect) part of the dielectric function.

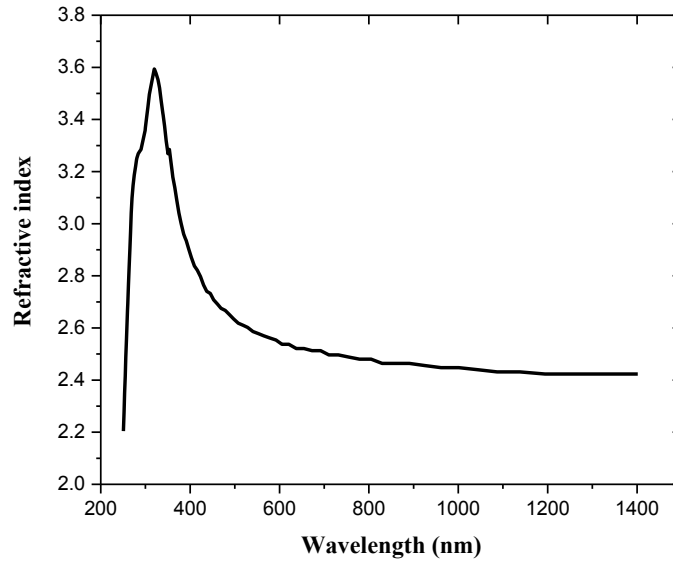


Figure A- 1. TiO₂ anatase ‘n’ value versus wavelength.

The refractive index of a metal is a complex number since some part of the light is absorbed by free electrons in the metal. The real part of the refractive index is related to the imaginary part of the refractive index through the Kramers-Kronig relation¹¹:

$$\operatorname{Re} \varepsilon(\omega) = 1 + \frac{2}{\pi} \mathcal{P} \int_0^{+\infty} \frac{\Omega \operatorname{Im} \varepsilon(\Omega)}{\Omega^2 - \omega^2} d\Omega \quad (\text{A- 4})$$

where $\operatorname{Re} \varepsilon(\omega)$ is the permittivity of the material at optical frequencies and $\operatorname{Im} \varepsilon(\omega)$ is the dielectric loss. The overall refractive index in lossy media is a complex value:

$$n' = n - i\kappa \quad (\text{A- 5})$$

Where ' n ' is the refractive index and ' κ ' is the extinction coefficient. By definition, in a plane wave with wave number ' k ':

$$k = n'k_0 = n' \left(\frac{2\pi}{\lambda_0} \right) \quad (\text{A- 6})$$

For a monochromatic plane wave:

$$E(z, t) = E_0 \exp[i(\omega t - kz)] \quad (\text{A- 7})$$

Using (A-6) in (A-7) gives:

¹¹ Kramers-Kronig is a mathematical relation that is used to calculate the imaginary part of refractive index from the real part and vice versa.

$$E(z, t) = E_0 \exp \left[i(\omega t - \left(\frac{2\pi}{\lambda_0} \right) z) \right] \exp \left[-\frac{2\pi}{\lambda_0} \kappa z \right] \quad (\text{A- 8})$$

The power carried by a plane wave in a lossy medium is proportional to $|E_0|^2$ where E_0 is the complex electric field. Therefore $|E_0|^2$ decays as:

$$\exp \left[-2 \frac{2\pi}{\lambda_0} \kappa z \right] \quad (\text{A- 9})$$

In other words, for plane wave propagation along the z direction in a lossy media:

$$I(z) = I(0) \exp[-\alpha z] \quad (\text{A- 10})$$

$I(0)$ is intensity at $z=0$. By comparing equation (A-9) and (A-10):

$$\alpha = 2 \frac{2\pi}{\lambda_0} \kappa = 2k_0 \kappa \quad (\text{A- 11})$$

Where ' k ' is the wave number and ' κ ' is the extinction coefficient. For any material, α varies by several orders of magnitude with λ_0 . Every material has a transparency window ($\alpha \ll 1$). Aside from absorption a light beam can also lose energy due to scattering processes in a material.

Appendix B - (List of Publication)

B-1 Refereed Publications

1. Zarifi M, Farsinezhad S, Daneshmand M, Shankar K, Selective microwave sensors exploiting the interaction of analytes with trap states in TiO₂ nanotube arrays, Nano Letters (under review) (2015).
2. Benlamri M, Farsinezhad S, Barlage D. W and Shankar K “Low Doped ZnO Films for Electronic Devices by Cathodic Electrodeposition”, submitted to Journal of Materials Chemistry C (under review) (2016).
3. Adl A. H, Farsinezhad S, Sharma H, and Shankar K, “Effect of Sol Stabilizer on the Structure and Electrical Properties of Solution-Processed ZnO thin Films”, RSC Advances, 5, 87007 - 87018, (2015).
4. Farsinezhad S, Sharma H and Shankar K “Interfacial Band Alignment for Photocatalytic Charge Separation in TiO₂ Nanotube Arrays Coated with CuPt Nanoparticles”, Physical Chemistry Chemical Physics, DOI: 10.1039/C5CP05679A, (2015).
5. Sharma H, Krabbe JD, Farsinezhad S, van Popta AC, Wakefield NG, Fitzpatrick GA and Shankar K, “Mapping Stresses in High Aspect Ratio Polysilicon Electrical Through-Wafer Interconnects (ETWIs)”, Journal of Micro/Nanolithography, MEMS, and MOEMS (JM3) (2015) .

6. Zarifi MH, Farsinezhad S, Shankar K and Daneshmand M, "Liquid Sensing Using Active Feedback Assisted Co-Planar Microwave Resonator", IEEE Microwave and Wireless Components Letters, 25, 621-623 (2015).
7. Zarifi M, Mohammadpour A, Farsinezhad S, Wiltshire BD, Nosrati M, Askar S, Daneshmand M, Shankar K, "TRMC Using Planar Microwave Resonators: Application to the Study of Long-lived Charge Pairs in Photoexcited Titania Nanotube Arrays", 119, 14358-14365, The Journal of Physical Chemistry (2015).
8. Gang He, B. D. Wiltshire, P. Choi, A. Savin, Sh. Sun, A. Mohammadpour, M. J Ferguson, R. McDonald, S. Farsinezhad, A. Brown, K. Shankar and E. Rivard, "Phosphorescence within Benzotellurophenes and Color Tunable Tellurophenes under Ambient Conditions", Chemical Communications (2015).
9. Piyush Kar, Samira Farsinezhad, Xiaojiang Zhang and Karthik Shankar, "Anodic Cu₂S and CuS Nanorod and Nanowall Arrays: Preparation, Properties and Application in CO₂ Photoreduction", Nanoscale, 6, 14305-14318 (2014).
10. Farsinezhad S, Prashant W, Wiltshire BD, Amiri S, Sushanta KM, Shankar K, "Amphiphobic surfaces from functionalized TiO₂ nanotube arrays", RSC Advances, 4, 33587-33598 (2014).
11. Farsinezhad S, Dalrymple AN and Shankar K, Towards Single-Step Anodic "Fabrication of Monodisperse TiO₂ Nanotube Arrays on Non-Native

- Substrates", *Physica Status Solidi A: Applications and Materials Science*, 211, 113-121 (2014).
12. Mohammadpour A, Farsinezhad S, Wiltshire BD and Shankar K, "Majority Carrier Transport in Single Crystal Rutile Nanowire Arrays", *Physica Status Solidi - Rapid Research Letters* (accepted for inclusion in Focus Issue on Functional Oxides), 8, 512-516, (2014).
 13. Zhang X, Han F, Shi B, Farsinezhad S, Dechaine GP and Shankar K, "Photocatalytic Conversion of Diluted CO₂ into Light Hydrocarbons Using Periodically Modulated Multiwalled Nanotube Arrays", *Angewandte Chemie*, 51, 12732-12735 (2013).
 14. Farsinezhad S, Mohammadpour A, Dalrymple AN, Geisinger J, Kar P, Brett MJ and Shankar K, "Transparent anodic TiO₂ nanotube arrays on plastic substrates for disposable biosensors and flexible electronics", *Journal of Nanoscience and Nanotechnology* 13, 2885-2891 (2013).

B-2 Conference Proceedings Papers

1. Benlamri M, Farsinezhad S, Barlage D. W and Shankar K ,” High performance solution-processed ZnO thin films on flexible substrate”, *The Proceedings of the ASME 2015 International Mechanical Engineering Congress & Exposition* (2015).
2. Farsinezhad S, Prashant W, Wiltshire BD, Amiri S, Sushanta KM, Shankar K, “The wetting behavior of TiO₂ nanotube arrays with perfluorinated surface functionalization”, *The Proceedings of the ASME 2014 International Mechanical Engineering Congress & Exposition* (2014).

3. Ahmad Adl , Mourad Benlamri, Samira Farsinezhad, Himani Sharma and Karthik Shankar, "High performance ZnO TFTs through improved material processing and device design", The Proceedings of the ASME 2014 International Mechanical Engineering Congress & Exposition (2014).
4. Amirsolaimani B, Zhang X, Han F, Farsinezhad S, Mohammadpour A, Dechaine GP and Shankar K, "Effect of the Nature of the Metal Co-Catalyst on CO₂ Photoreduction Using Fast-Grown Periodically Modulated Titanium Dioxide Nanotube Arrays (PMTiNTs)", Proceedings of the Materials Research Society, vol. 1578 : Titanium Dioxide - Fundamentals and Applications (2013).
5. Mohammadpour A, Farsinezhad S, Hsieh LH and Shankar K, "Multipodal and Multilayer TiO₂ Nanotube Arrays: Hierarchical Structures for Energy Harvesting and Sensing", Proceedings of the Materials Research Society, vol. 1552 : Nanostructured Metal Oxides for Advanced Applications (2013).

B-3 Presentations and Posters

1. (Oral presentation) "The Wetting of Self-Assembled Monolayer-coated TiO₂ Nanotube and Nanorod Arrays", S. Farsinezhad, B. D. Wiltshire, P.R. Waghmare, S. K. Mitra, and K. Shankar, International Conference on MEMS and Sensors (*ICMEMSS 2014*), IIT-Madras, India, December 2014.
2. (Oral presentation) "Microstrip-coupled Open Loop Microwave Resonators Integrated With 1-D Semiconductor Nanostructures for Sensing", Mohammad Zarifi, Samira Farsinezhad, Benjamin D. Wiltshire, Arash Mohammadpour, Mojgan Daneshmand and Karthik Shankar, International

Conference on MEMS and Sensors (*ICMEMSS 2014*), IIT-Madras, India, December 2014.

3. (Oral presentation) "Enhanced CO₂ photoreduction catalysts using noble metal and alloy nanoparticles grafted on to TiO₂ nanotubes", Samira Farsinezhad, Uchenna Obuekwe, Himani Sharma, Jing Shen, Natalia Semagina and Karthik Shankar, *23rd Canadian Symposium on Catalysis*, Edmonton, May 2014.
4. (Oral presentation) Himani Sharma, Samira Farsinezhad and Karthik Shankar "TiO₂ Nanotube Arrays with Periodically Modulated Diameters for Photonic & Energy Harvesting Applications" *IMECE2014*.
5. (Oral presentation) "Investigations into the electronic properties of the nanoparticle-TiO₂ nanotube array interface for photocatalytic applications", Himani Sharma, Samira Farsinezhad and Karthik Shankar, *23rd Canadian Symposium on Catalysis*, Edmonton, May 2014.
6. (Oral presentation) Ahmad Adl, Mourad Benlamri, Samira Farsinezhad, Himani Sharma and Karthik Shankar, "High performance ZnO TFTs through improved material processing and device design", *IMECE2014*.
7. (Oral presentation) Samira Farsinezhad, Uchenna Obuekwe, Himani Sharma, Jing Shen, Natalia Semagina and Karthik Shankar, "Enhanced CO₂ photoreduction catalysts using noble metal and alloy nanoparticles grafted on to TiO₂ nanotubes", *23rd Canadian Symposium on Catalysis* (May 11-14, 2014).

8. (Poster) "Vertically oriented copper sulfide nanorod arrays for high-rate visible-responsive reductive photocatalysis", Samira Farsinezhad, Piyush Kar, Xiaojiang Zhang, Babak Amirsolaimani, Ling Hsuan-Hsieh, Arash Mohammadpour and Karthik Shankar, *Spring Meeting of the Materials Research Society*, San Francisco, (April 2013).

9. (Oral Presentation) "Three-dimensionally ordered films of TiO₂ nanotubes for non-lithographically fabricated photonic crystals", Xiaojiang Zhang, Samira Farsinezhad, Arash Mohammadpour and Karthik Shankar, *Photonics North (SPIE)*, Montreal, (June 2012).

10. (Oral Presentation) "Use of multilayer structures to engineer the optical properties of TiO₂ nanotube arrays for light harvesting applications", Samira Farsinezhad, Xiaojiang Zhang, Arash Mohammadpour and Karthik Shankar, *Photonics North (SPIE)*, Montreal, (June 2012).